Edited by
James B. Elsner
Robert E. Hodges
Jill C. Malmstadt
Kelsey N. Scheitlin

HURRICANES AND CLIMATE CHANGE

Volume 2

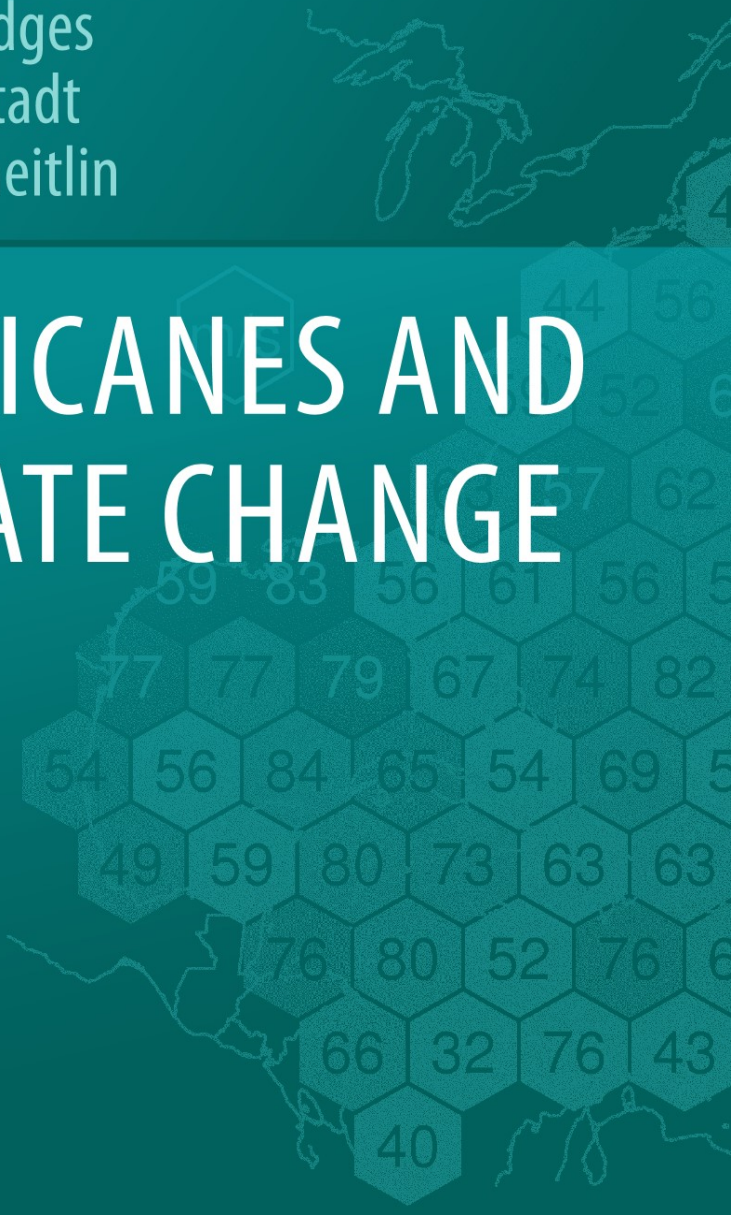

Aegean Conferences

Springer

Hurricanes and Climate Change

James B. Elsner • Robert E. Hodges
Jill C. Malmstadt • Kelsey N. Scheitlin
Editors

Hurricanes and Climate Change

Volume 2

Springer

Editors
James B. Elsner
Florida State University
Department of Geography
Ferndale Drive 114
32306 Tallahassee, Florida
USA
jelsner@fsu.edu

Robert E. Hodges
Florida State University
Department of Geography
Ferndale Drive 114
32306 Tallahassee, Florida
USA

Jill C. Malmstadt
Florida State University
Department of Geography
Ferndale Drive 114
32306 Tallahassee, Florida
USA

Kelsey N. Scheitlin
Florida State University
Department of Geography
Ferndale Drive 114
32306 Tallahassee, Florida
USA

ISBN 978-90-481-9509-1 e-ISBN 978-90-481-9510-7
DOI 10.1007/978-90-481-9510-7
Springer Dordrecht Heidelberg London New York

Library of Congress Control Number: 2010934734

© Springer Science+Business Media B.V. 2010
No part of this work may be reproduced, stored in a retrieval system, or transmitted in any form or by any means, electronic, mechanical, photocopying, microfilming, recording or otherwise, without written permission from the Publisher, with the exception of any material supplied specifically for the purpose of being entered and executed on a computer system, for exclusive use by the purchaser of the work.

Cover illustration: Frequency and intensity of hurricanes at lifetime maximum intensity over the North Atlantic. The color scale is linear from 1 (blue) to 15 (yellow) indicating the number of hurricanes reaching lifetime maximum (first time only) within the hexagon. The value inside the hexagon is the maximum intensity (m/s) of all lifetime maximum values in the bin. The analysis is done on a Mollweide projection so that the hexagons have equal area. Data source: U.S. National Hurricane Center best-track, 1943-2008.

Cover design: deblik

Printed on acid-free paper

Springer is part of Springer Science+Business Media (www.springer.com)

Preface

Hurricanes are among nature's most destructive agents. Widespread interest surrounds the possibility that they might even get more damaging in the future. Some policy makers consider it a call to action. Financial want to know when and by how much. And scientists are certainly challenged by the range and interactions of the processes involved. This book, arising from the Second International Summit on Hurricanes and Climate Change (31 May through 5 June 2009 in Corfu, Greece), contains new research since the First Summit (2007 in Crete) on topics related to hurricanes and climate change. Chapters are grouped into studies using global climate models and those taking empirical and statistical approaches. The latter include investigations of basin-wide and regional tropical cyclone activity.

The book opens with a review of progress on an international project to compare global climate models on their ability to generate tropical cyclones. Chapter 2 highlights predictions of tropical cyclone activity under global warming using a cloud-resolving climate model. Chapter 5 discusses the potential insights of considering tropical cyclone activity as critical phenomenon. Chapter 6 highlights the importance of sea-surface temperature in driving the amount of monetary losses from hurricanes (but not the frequency of loss events) affecting the United States. This is important as most of the literature on this subject, including that written by some of the insurance companies, has failed to do a credible job with this issue. We know greater monetary losses occur with stronger hurricanes. We know hurricanes can become more intense when they are over warmer waters. So we expect the probability of a large loss to be higher when the oceans warm. Interestingly, results show that when sunspots are few there is a higher probability of at least one loss event.

The intriguing finding of a solar signal in hurricane activity is taken up in more detail in Chapter 7. Statistical evidence of a linkage between the solar cycle and major hurricanes over the eastern North Pacific and hurricanes along the U.S. coast is presented. These results are particular salient given that the sun may be going through an extended period of inactivity. The record of coastal hurricanes is sometimes invoked as evidence that climate change plays no significant role in modulating hurricane activity. But other factors could mitigate against a climate signal in these hurricanes. For instance, evidence presented in Chapter 10 is consistent with the hypothesis that hurricanes near land may be increasingly affected by continental aerosols. Also, modeling studies show increasing carbon dioxide

causes the stratosphere to cool leading to a faster jet stream and a tendency for more frequent positive phases of the North Atlantic Oscillation. It is well known that a positive North Atlantic Oscillation tends to steer the hurricanes away from the United States.

Return periods of high winds from hurricanes in the vicinity of Florida are estimated in Chapter 11. Historically the state was affected by hurricane winds of 60 m s^{-1} once every 2 years, but there is evidence that the strongest hurricanes may be getting stronger in this part of the world as well. Chapter 13 provides a methodology for producing a track-relative climatology. This is a novel way to examine hurricane activity, and it is applied toward understanding the risk of high winds to Eglin Air Force Base in northern Florida.

Although much has been written on hurricanes and climate change, the chapters in this volume represent some of the more interesting and innovative new research on this important topic. The Summit, which had participants from 17 different countries, was sponsored by Aegean Conferences, the Risk Prediction Initiative, and Climatek. Plans are underway to hold the Third International Summit on the island of Rhodes in the summer of 2011.

Tallahassee, Florida
April 2010

James B. Elsner
Robert E. Hodges
Jill C. Malmstadt
Kelsey N. Scheitlin
The Editors

Contents

1 **The Tropical Cyclone Climate Model Intercomparison Project** 1
Kevin Walsh, Sally Lavender, Hiroyuki Murakami, Enrico Scoccimarro, Louis-Phillipe Caron, and Malek Ghantous

2 **Change of Tropical Cyclone and Seasonal Climate State in a Global Warming Experiment with a Global Cloud-System-Resolving Model** 25
Kazuyoshi Oouchi, Masaki Satoh, Yohei Yamada, Hirofumi Tomita, and Wataru Yanase

3 **Role of the SST Anomaly Structures in Response of Cyclogenesis to Global Warming** 39
Fabrice Chauvin and Jean-François Royer

4 **Tropical Cyclone Rainfall in the Observations, Reanalysis and ARPEGE Simulations in the North Atlantic Basin** 57
Anne S. Daloz, Fabrice Chauvin, and Frank Roux

5 **Tropical Cyclones as a Critical Phenomenon** 81
Álvaro Corral

6 **Environmental Signals in Property Damage Losses from Hurricanes** 101
Thomas H. Jagger, James B. Elsner, and R. King Burch

7 **A Statistical Analysis of the Frequency of United States and Eastern North Pacific Hurricanes Related to Solar Activity** 121
Robert E. Hodges and James B. Elsner

8 Regional Typhoon Activity as Revealed by Track Patterns and Climate Change 137
Pao-Shin Chu, Xin Zhao, and Joo-Hong Kim

9 Climatic Features and Their Relationship with Tropical Cyclones Over the Intra-Americas Seas 149
Jorge A. Amador, Eric J. Alfaro, Erick R. Rivera, and Blanca Calderón

10 On the Increasing Intensity of the Strongest Atlantic Hurricanes 175
James B. Elsner and Thomas H. Jagger

11 Frequency and Intensity of Hurricanes Within Florida's Threat Zone 191
Jill C. Malmstadt, James B. Elsner, and Thomas H. Jagger

12 Linking Tropical Cyclone Number Over the Western North Pacific with Sea Surface Temperatures 205
Chongjian Liu, Liping Ma, Ying Liu, Zhexian Luo, Xiaotu Lei, Xiaogang Zhou, Donghai Wang, and Hui Xu

13 A Track-Relative Climatology of Eglin Air Force Base Hurricanes in a Variable Climate 217
Kelsey N. Scheitlin and James B. Elsner

14 Estimating the Impact of Climate Variability on Cumulative Hurricane Destructive Potential Through Data Mining 231
Roshanak Nateghi, Steven M. Quiring, and Seth D. Guikema

Index 253

Chapter 1
The Tropical Cyclone Climate Model Intercomparison Project

Kevin Walsh, Sally Lavender, Hiroyuki Murakami, Enrico Scoccimarro, Louis-Phillipe Caron, and Malek Ghantous

Abstract In this chapter, a review is given of progress to date on an intercomparison project designed to compare and evaluate the ability of climate models to generate tropical cyclones, the Tropical Cyclone climate Model Intercomparison Project (TC-MIP). Like other intercomparison projects, this project aims to evaluate climate models using common metrics in order to make suggestions regarding future development of such models. A brief summary is given of the current ability of these models and some initial conclusions are made. Coarser-resolution climate models appear to have difficulty simulating tropical formation in the Atlantic basin, but simply increasing the resolution of such models does not necessarily lead to improved simulations in this region. The choice of convective scheme is also important in determining the tropical cyclone formation rate. There appears to be little relationship between the simulated details of the large-scale climate and model tropical cyclone formation rates, and possible reasons are given for this. Recent fine-resolution models have shown considerable improvement in their simulation of both global and Atlantic tropical cyclone formation, leading to the possibility that such models could be used for detection and attribution studies of the causes of observed changes in tropical cyclone formation rate, particularly in the Atlantic basin.

Keywords Tropical cyclone · Climate model · Global warming · Intercomparison

K. Walsh (✉), S. Lavender, and M. Ghantous
School of Earth Sciences, University of Melbourne, Melbourne, Australia
e-mail: kevin.walsh@unimelb.edu.au; sallyl@unimelb.edu.au; malek.ghantous@gmail.com

H. Murakami
Meteorological Research Institute, Tsukuba, Ibaraki, Japan
e-mail: himuraka@mri-jma.go.jp

E. Scoccimarro
Istituto Nazionale di Geofisica e Vulcanologia (INGV), Bologna, Italy
e-mail: scoccimarro@bo.ingv.it

L.-P. Caron
CRCMD Network, UQAM, Montreal, Canada
e-mail: lpcaron@sca.uqam.ca

J.B. Elsner et al. (eds.), *Hurricanes and Climate Change: Volume 2*,
DOI 10.1007/978-90-481-9510-7_1, © Springer Science+Business Media B.V. 2010

1 Introduction

The possible effect of climate change on tropical cyclones remains one of the most controversial topics in modern meteorology. Opinions on this issue range from flat denial that there could be any effect to predictions of large increases in tropical cyclone incidence and intensity that are already detectable in the observed record. A range of techniques have been used to make inferences about this topic, ranging from purely statistical analyses to sophisticated fine-resolution models to fundamental theories of atmospheric behaviour.

Some years ago, the debate about the effects of climate change on overall global warming went through the same stage as the current controversy about its effects on tropical cyclones. In both topics, initial theoretical work established that such an effect was consistent with our understanding of atmospheric physics – for tropical cyclones and climate change, this was the work of Emanuel (1987). For global climate change, this was followed by a period of model development and experimentation, accompanied by argument over both the existence and the magnitude of the possible climate change signal. This debate is now essentially over: there are few serious climate scientists who still believe that there is no significant global effect. Numerous detection and attribution studies have shown that the observed twentieth and early twenty-first century warming is consistent with climate model predictions based on the observed increases in greenhouse gas concentration in the atmosphere (Hegerl et al. 2007). These same climate models project even larger changes later this century (IPCC 2007).

In contrast, for tropical cyclones and climate change, the debate continues. There are fundamental reasons why this is so. Most climate data consists of daily records, whereas tropical cyclones are considerably rarer events. Unlike the global climate record of (for example) land-based screen temperature, there is considerable controversy about the consistency of the tropical cyclone record, due to significant changes in observing systems over several decades (Kossin et al. 2007). Unlike the land-based temperature record, the main tropical cyclone records, the best track data, were never intended to be used as climate data sets. As a result, little attention was paid to ensuring that the techniques used to construct them were consistent from year to year. The other issue limiting scientific conclusions from this debate is that until very recently, climate model simulations of the observed distribution of tropical cyclone extreme wind speeds were poor (e.g. Walsh 2008). This is also in contrast to the quality of the simulation of global average temperature: since this is considerably easier to simulate, its quality has always been better (IPCC 2007). One of the crucial steps in the debate on the causes of the observed increase in global average temperature over the past century or so was the development of an ability to simulate that increase and the relative contributions of the various climate forcings (aerosols, solar radiance, greenhouse gas concentrations) to observed climate change (e.g. Stott et al. 2001). Thus the causes of global climate change were able to be identified, through the process of detection and attribution.

Recent improvements in climate model simulations of tropical cyclones have the same potential to resolve arguments about the causes of observed trends in tropical cyclone characteristics, provided of course that there is agreement on the magnitude

and direction of observed trends. Leaving aside the question of observed trends for the moment, this article focuses on recent developments in tropical cyclone climate models.

2 Tropical Cyclones as Simulated by Climate Models

2.1 Current-Climate Simulation

A recent review of the quality of tropical cyclone simulation in climate models is contained in Walsh (2008). In a nutshell, this paper concluded that the simulation of tropical cyclone formation and tracks by the best climate models is reasonable. In contrast, the simulation of tropical cyclone intensity distributions is inadequate, largely as a result of coarse resolution. While the simulation of tropical cyclone formation and tracks does not depend so much on model resolution as intensity does, there is still considerable room for improvement in climate model simulations of these variables. This is important as there have been observed trends in tropical cyclone formation that are less controversial than trends in observed wind speeds (e.g. Kossin et al. 2007). Thus climate models used for attribution studies need the best possible simulation of these trends that can be obtained.

Recent climate models have continued to demonstrate improvement in their ability to simulate tropical cyclones. In particular, Knutson et al. (2008) employ a regional climate model of 18 km resolution to demonstrate an excellent ability to simulate the year-to-year variations of tropical cyclone formation in the Atlantic basin, when forced with NCEP reanalyses. This model uses a form of internal nudging to ensure that the larger scale features of the regional model solution in the interior of the domain remain similar to the large-scale forcing outside of the domain. The regional climate model study of Semmler et al. (2008) employed a resolution of 28 km over an Atlantic domain, giving a good simulation of both the mean and the interannual variability of tropical cyclone formation in this basin. No internal nudging was used in this model simulation.

Global model simulations have also been improving. Bengtsson et al. (2007) used the ECHAM5 atmosphere-only model, run with observed interannually-varying sea surface temperatures, to generate large numbers of simulated tropical cyclones, although numbers were lower than observed in the Atlantic basin. Gualdi et al. (2008) used a T106 (about 125 km resolution) version of the SINTEX-G coupled ocean-atmosphere model and examined the tropical cyclone climatology. This model employs the mass flux convection scheme of Nordeng (1994), as adapted from the previous work of Tiedtke (1989). Numbers of tropical cyclones generated globally were less than observed but still good in the Atlantic region. The statistical-deterministic model of Emanuel et al. (2008) also generates reasonable numbers of storms in the Atlantic and has a good representation of the interannual variability of storm formation. The global 50 km resolution model of Zhao et al. (2010) used observed SSTs as a lower boundary condition, running four realisations of the period 1981–2005. The model produced realistic simulations of the observed

trends in tropical cyclone frequency over that period of time, including the upward trend in numbers in the Atlantic basin. While correlations between simulated and observed interannual variation were good in the Atlantic, they were not as good in other tropical cyclone formation basins, with the Indian Ocean displaying a poor relationship. In all of these simulations, however, the simulated distribution of tropical cyclone intensity remains inadequate, with much fewer high-intensity storms simulated than observed.

As model resolution increases and experience is gained in constructing the best model formulation required to generate tropical cyclones, the simulation of tropical cyclone climatology will improve. But high-resolution global model runs remain very expensive, so most climate simulations during the next few years will continue to be of coarser resolution (100–200 km). It would be best if the climate model that is used for prediction of future global or regional temperature and precipitation also had a reasonable climatology of tropical cyclone formation, as this would demonstrate that the model is performing well at most spatial and time scales. Nevertheless, one issue that was identified by Walsh et al. (2007) was that many climate model studies of tropical cyclones had been performed to date but that almost all of them used different criteria to define a model-generated tropical cyclone. One way to circumvent this issue would be to define a simulated tropical cyclone in the same way that observed tropical cyclones are defined: by simply counting all of the storms that had 10 m wind speeds in excess of 17.5 ms^{-1} and had the warm core structure of tropical cyclones, similar to the method used by Zhao et al. (2010) for their 50 km resolution global model simulations. Even so, this is a very severe test for a climate model of coarser resolution, indeed an unfair test as it compares a model of limited resolution with reality, which has effectively unlimited resolution. Climate models are usually validated by comparing their performance against observations that have been degraded to a resolution similar to that of the model. Walsh et al. (2007) proposed the same process for tropical cyclone simulation: to degrade data from weak, observed tropical cyclones to the resolution of the climate model and determine what are their maximum wind speeds at that resolution. Additionally, this serves as a way of comparing the results of climate models running at slightly different resolutions. In this way, the native ability of the model to generate tropical cyclones is assessed in a resolution-appropriate fashion.

This was the philosophy behind the proposed Tropical Cyclone climate Model Intercomparison Project (TC-MIP).[1] Like all intercomparison projects, this project proposes and defines common metrics for the assessment of climate models of tropical cyclones (e.g. Camargo et al. 2007; Yokoi et al. 2009). Ideally, at this stage in the intercomparison project, it would be best if there were numerous recent high-resolution global model experiments that could all be analysed using consistent methodologies. Such model output does not yet exist, but the proposed CMIP5 archive may eventually provide such a resource. In the meantime, building on similar previous projects, we reanalyse the CMIP3 model output and some recent high-resolution climate models, using common metrics for all models, including two separate detection routines.

[1] www.earthsci.unimelb.edu.au/∼kwalsh/tcmip_index.html

3 Model Description

The CMIP3 climate model archive (www-pcmdi.llnl.gov) was established to enable further analysis of output produced for the IPCC Fourth Assessment Report (IPCC 2007). The simulations analysed here are the climate of the twentieth century experiments (20c3 m), for the model years 1980–1999. In these runs, coupled ocean-atmosphere models are forced with the observed increase in greenhouse gas concentrations over the twentieth century. The models analysed (Table 1) have

Table 1 List of models analysed from CMIP3 archive. Resolution is in degrees

No.	Model	Institution	Resolution
1	BCCR-BCM2.0	Bjerknes Centre for Climate Research	2.8 × 2.8
2	CGCM3.1(T47)	Canadian Centre for Climate Modelling & Analysis	3.75 × 3.75
3	CGCM3.1(T63)	Canadian Centre for Climate Modelling & Analysis	2.8× 2.8
4	CNRM-CM3	Météo-France/Centre National de Recherches Météorologiques	2.8 × 2.8
5	CSIRO-Mk3.0	CSIRO Atmospheric Research	1.9 × 1.9
6	CSIRO-Mk3.5	CSIRO Atmospheric Research	1.9 × 1.9
7	GFDL-CM2.0	US Department of Commerce/NOAA/Geophysical Fluid Dynamics Laboratory	2.5 × 2.0
8	GFDL-CM2.1	US Department of Commerce/NOAA/Geophysical Fluid Dynamics Laboratory	2.5 × 2.0
9	GISS-AOM	NASA/Goddard Institute for Space Studies	4.0 × 3.0
10	GISS-EH	NASA/Goddard Institute for Space Studies	5.0 × 4.0
11	GISS-ER	NASA/Goddard Institute for Space Studies	5.0 × 4.0
12	FGOALS-g1.0	LASG/Institute of Atmospheric Physics	2.8 × 3.0
13	INM-CM3.0	Institute for Numerical Mathematics	5.0 × 4.0
14	IPSL-CM4	Institut Pierre Simon Laplace	3.75 × 2.5
15	MIROC3.2(hires)	University of Tokyo, National Institute for Environmental Studies, and JAMSTEC	1.1 × 1.1
16	MIROC3.2(medres)	University of Tokyo, National Institute for Environmental Studies, and JAMSTEC	2.8 × 2.8
17	ECHAM5/MPI-OM	Max Planck Institute for Meteorology	1.9 × 1.9
18	MRI-CGCM2.3.2	Meteorological Research Institute	2.8 × 2.8
19	NCAR-CCSM3	National Center for Atmospheric Research	1.4 × 1.4
20	NCAR-PCM1	National Center for Atmospheric Research	2.8 × 2.8
21	UKMO-HadCM3	Hadley Centre for Climate Prediction and Research/Met Office	3.75 × 2.5
22	UKMO-HadGEM1	Hadley Centre for Climate Prediction and Research/Met Office	1.9 × 1.25

a range of resolutions, from 1° × 1° to 5° × 4°. While none of these models have resolutions that are genuinely suitable for the generation of intense tropical cyclones, the techniques developed as part of this project for examining the interrelationships between model formulation, model large-scale climate and model generation of tropical cyclones are directly applicable to similar comparisons of the results of high-resolution models.

Two recent high-resolution models have been analysed using the TC-MIP common metrics. The MRI/JMA 20-km global mesh model (Mizuta et al. 2006) is run using a timeslice method for model years 1979–2003. The model is hydrostatic, with 60 vertical levels, uses a semi-Lagrangian time integration scheme and a prognostic Arakawa-Schubert cumulus convection scheme (Randall and Pan 1993). The CMCC-INGV model is a fully coupled general circulation model without flux adjustments using a T159 (about 80 Km) atmospheric component (Roeckner et al. 2003). The parameterization of convection is based on the mass flux concept (Tiedtke 1989), modified following Nordeng (1994). The global ocean model used is a 2° resolution global ocean model (Madec et al. 1998) with a meridional refinement near the equator, to 0.5°. The CMCC-INGV data used in this work are obtained running the model over the period 1970–1999 using twentieth century (20C3 M) atmospheric forcings as specified by the IPCC (http://www-pcmdi.llnl.gov/ipcc/about_ipcc.php).

4 Methodology

4.1 Large-Scale Climate Variables

One of the primary goals of the intercomparison project is to identify relationships between simulated large-scale climate variables and simulated tropical cyclone formation. As part of the TC-MIP project, the following climate variables are examined, as they have been shown in previous observational studies to influence tropical cyclone formation and characteristics (e.g. intensity, size):

- Mean sea level pressure
- Precipitation
- Convective precipitation
- Sea surface temperature
- Maximum potential intensity
- Genesis potential index
- Relative humidity
- Wind shear
- Surface latent heat flux

The definition of most of these variables is self-explanatory, but explanation is needed of some of them. Convective precipitation is the model's estimate of that portion of the precipitation that is convective rather than stratiform. Numerous

observations had shown that the presence of persistent deep convection is a prerequisite for tropical cyclone formation (e.g. McBride 1995). It is recognized, though, that the quality of model simulation of this quantity varies greatly between models, as it is determined by the model's convective parameterisation. Maximum potential intensity (potential maximum wind speed and potential minimum pressure) is based on based the formulation of Bister and Emanuel (1998). The genesis potential index (GP) is that of Emanuel and Nolan (2004):

$$GPI = \left|10^5\,\eta\right|^{3/2} \left(\frac{\mathrm{H}}{50}\right)^3 \left(\frac{V_{pot}}{70}\right)^3 (1 + 0.1\,\mathrm{V}_{shear})^{-2}$$

where η is the absolute vorticity at 850 hPa in s^{-1}, H is the relative humidity at 700 hPa in percent, V_{pot} is the potential maximum wind speed in metres per second and V_{shear} is the magnitude of the vertical wind shear between 850 and 200 hPa, also in metres per second.

Not all of these variables will be discussed in this chapter, as a full analysis of the interrelationships has yet to be performed. This chapter will focus on the relationship between the genesis potential and model-generated tropical cyclone formation, as the GP includes several of the large-scale variables analysed.

4.2 Detection of Tropical Cyclones in Model Output

Two detection methods are used for the identification of tropical cyclones in the climate model output. The CSIRO detection scheme (Walsh et al. 2007) defines a low-level wind speed threshold for tropical cyclone identification that is resolution-dependent. The resolution-dependent thresholds are derived from the maximum 10 m winds seen in high-resolution analyses of weak tropical cyclones that are degraded to various coarser resolutions. In this way, the output of a coarser-resolution model is compared with reality degraded to the same resolution. For models of horizontal resolution finer than about 30 km, the detection threshold becomes the same as the observed definition: 17.5 m s^{-1} wind speeds at a height of 10 m. At a climate model resolution of 200 km, the threshold becomes about 13 m s^{-1}. The advantage of this scheme is that enables the results of climate models of different resolutions to be compared. A disadvantage is that it does not account for the non-linear interaction inherent in climate models between resolution and storm development.

In addition, the detection scheme of Camargo and Zebiak (2002) was employed. In this scheme, joint probability distribution functions of quantities important for tropical cyclone detection, such as low-level vorticity, are constructed for each tropical cyclone formation basin. Based on these probability distributions, tropical cyclones are declared to be those lows that have values of these quantities in excess of a pre-defined statistical threshold. The advantage of this scheme is that it partially corrects for model biases and thus gives a better indication of the pattern of model formation in regions where storms might be weak, while still giving an indication of

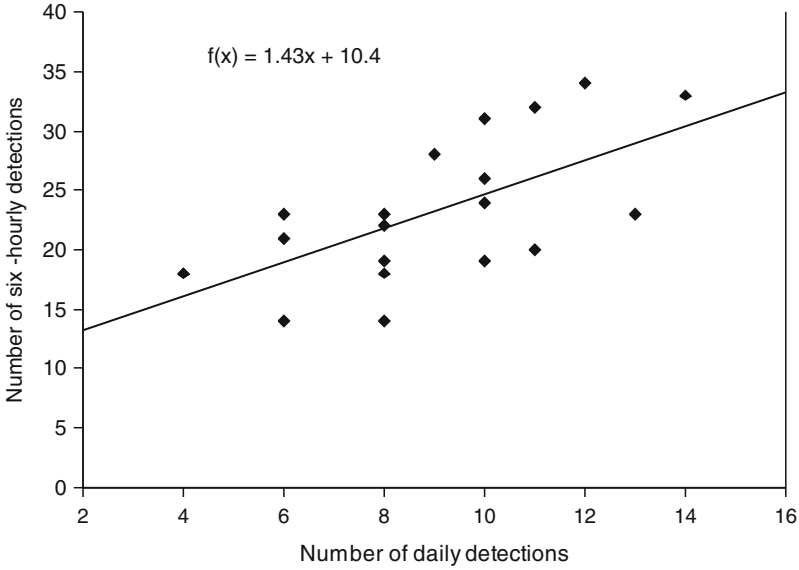

Fig. 1 Comparison of number of detections from four-times daily NCEP-2 reanalyses versus detectionsfrom the same data daily averaged. Only one detection per individual storm track is made

the differences in formation rates between basins. A disadvantage is that because the thresholds vary between basins and between models, it becomes harder to compare model results using this scheme.

One issue that needs to be addressed for this type of scheme is that the CMIP3 archive consists almost entirely of daily-average data rather than instantaneous fields. This causes tropical cyclones in the models to be smeared over an area rather than detected at a specific location. For example, Fig. 1 shows a comparison between detection of storms using the CSIRO detection scheme for four times daily instantaneous NCEP-2 reanalyses versus the same data daily averaged. Only one count per individual storm track is made so that a direct comparison can be made between formation rates in the two datasets. It is clear that applying the CSIRO detection scheme to daily average data results, as expected, in a considerable undercount of detections. Thus as an approximate correction for this effect, we multiply detected numbers of storms in the daily-average data using the CSIRO detection scheme by a factor of 2.5, commensurate with the relationship shown in Fig. 1. This approximate factor has been chosen because the linear relationship shown in Fig. 1 cannot be used precisely, as it implies that zero daily detections must be accompanied by roughly ten 6-h detections, which is unphysical.

5 Results

5.1 CMIP3 Model Output

5.1.1 Large-Scale Fields: Emanuel Genesis Parameter

Figure 2 shows a compilation of genesis parameter results, for January–March (Fig. 2a) and July–September (Fig. 2b), with models arranged down the page from highest to lowest resolution. For January–March (Fig. 1a), almost all models display higher GP than derived from the NCEP-2 reanalysis (top figure). Further analysis of the reasons for this systematic model bias indicate that almost all models have higher 700 hPa relative humidity values than observed in a broad band across the regions close to the location of the monsoonal trough. Since the GP is related to the cube of the relative humidity, this largely explains the overestimate in almost every model of the NCEP-based GP.

The reasons for this bias are unclear at this time. The representation of the boundary-layer physics in a model with relatively coarse vertical resolution is necessarily fairly crude, and it is possible that this leads to an excessive vertical transport of moisture in these models, particularly in the tropics. Alternatively, there may be a systematic dry bias in the NCEP-2 reanalysis over the monsoon trough regions. Trenberth (2005) note that the precipitable water content in the NCEP-2 reanalysis over the tropics is dry compared with the ERA-40 reanalysis, and also dry compared with RSS SSM/I data. In general, the spatial pattern of the GP produced by the higher-resolution models is mostly superior to that produced by the lower-resolution models. Calculations of GP using the ERA-40 given a much better agreement with model-simulated GP (not shown).

Figure 2b shows similar results for July–September. Once again, the GP shows general higher values than those derived from the NCEP reanalysis.

5.1.2 Comparison Between Results of Two Detection Schemes

Figure 3 shows a comparison between the two detection schemes. Tropical cyclone formation for the months January–March, from the IBtracs best track data (Knapp et al. 2009) (top), and from the CSIRO Mk3.5 model output for the CSIRO detection scheme (middle) and basin-dependent detection scheme. The best track data shows the well-known pattern of observed tropical cyclone in the Southern Hemisphere summer months: maximum formation occurs in regions off the northeast and northwest coasts of Australia and east of Madagascar. The CSIRO detection scheme shows that the CSIRO Mk 3.5 model appears to be simulating about the correct number of formations, although the pattern of formation has some deficiencies: there is little formation in the eastern South Pacific region, for instance. Comparing these detections to those determined using the basin-dependent detection scheme, the patterns are similar. A small amount of formation that is not observed is indicated

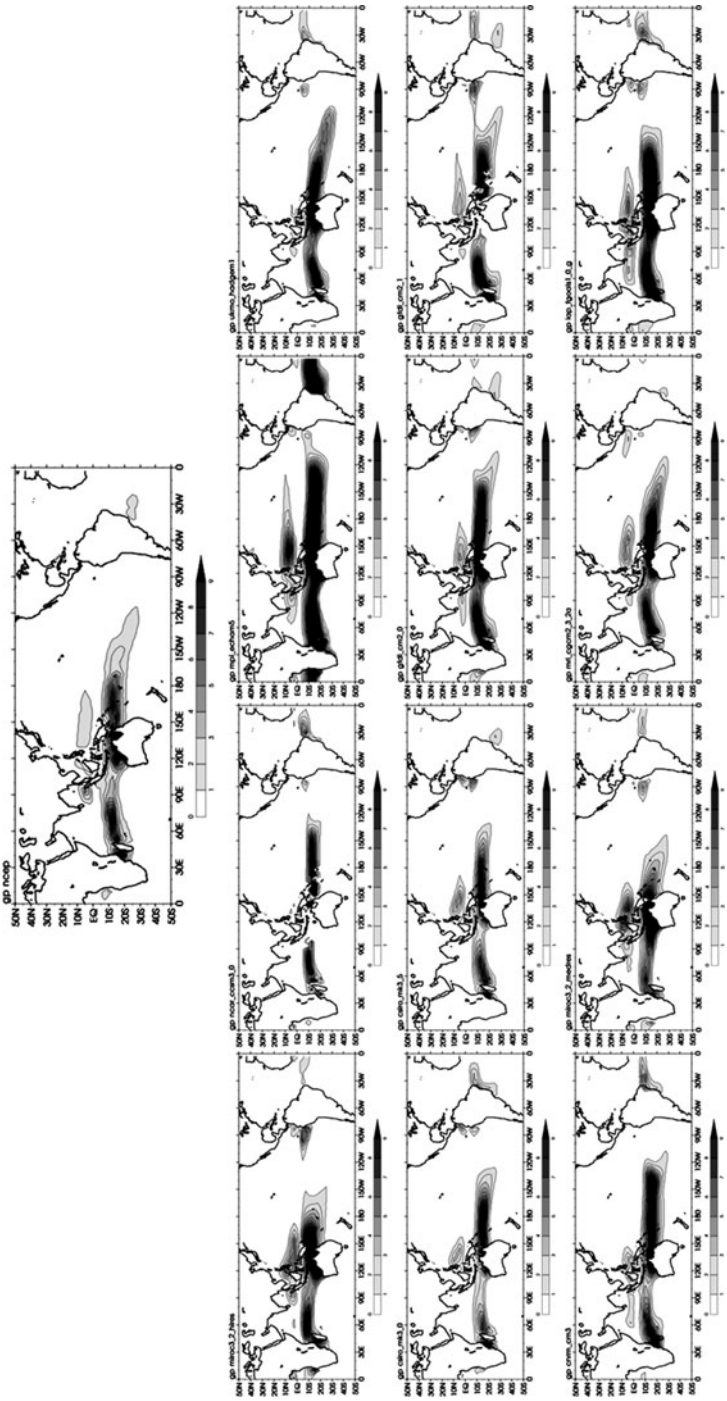

Fig. 2a Emanuel genesis parameter fields for higher-resolution CMIP3 models, January–March. Formation rate is per $2.5^\circ \times 2.5^\circ$ grid box per 20 years

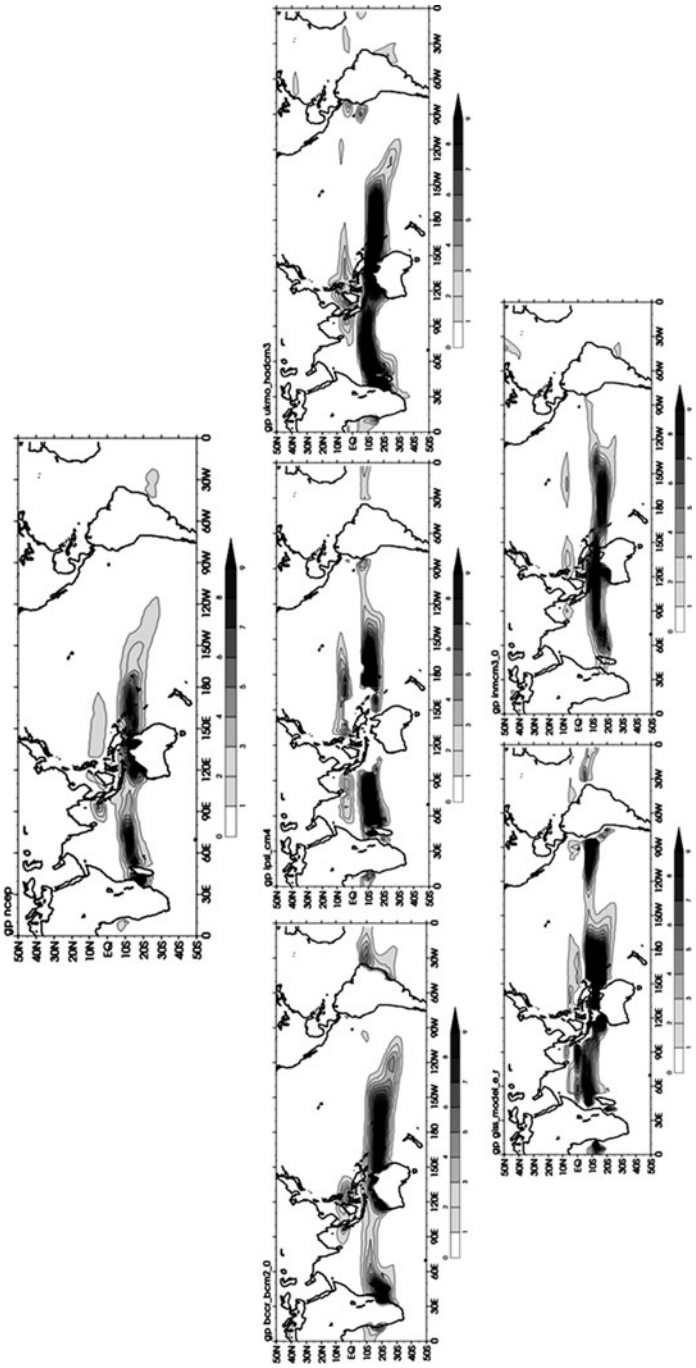

Fig. 2a (continued) For lower-resolution models

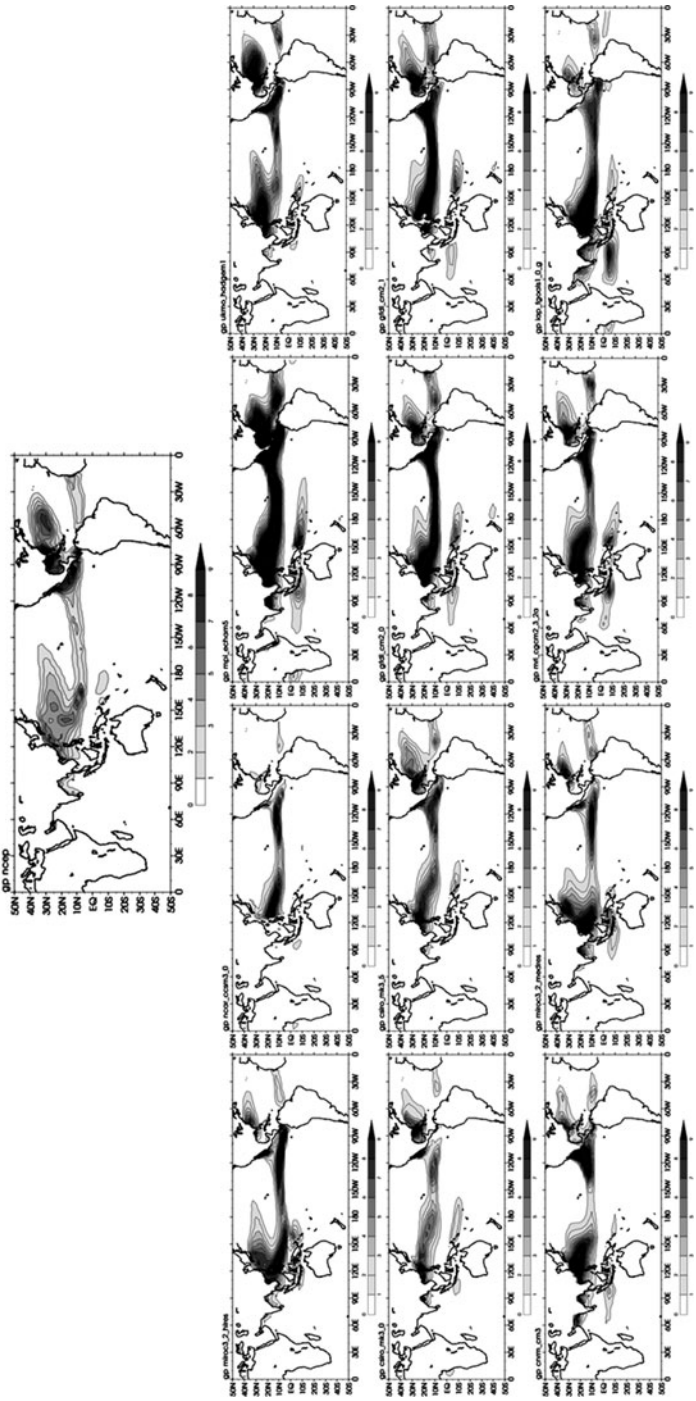

Fig. 2b The same as Fig. 2a for July–September

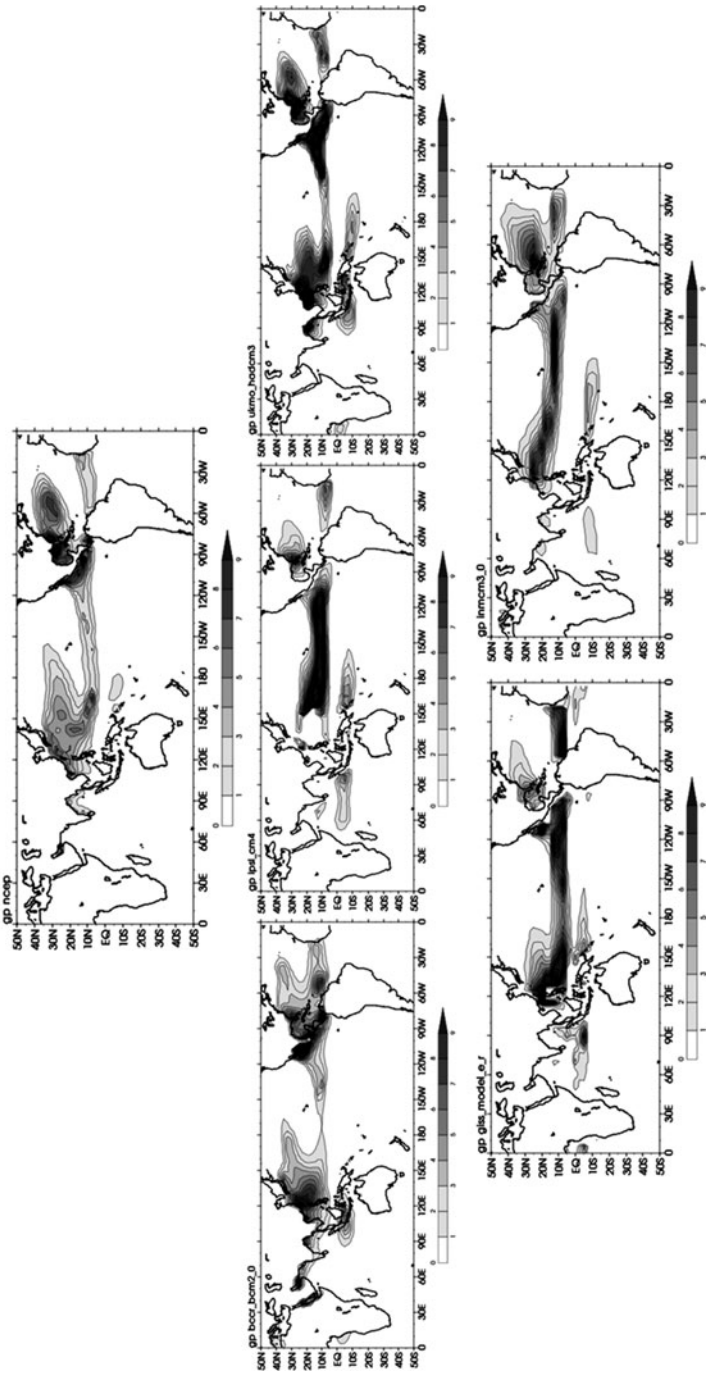

Fig. 2b (continued)

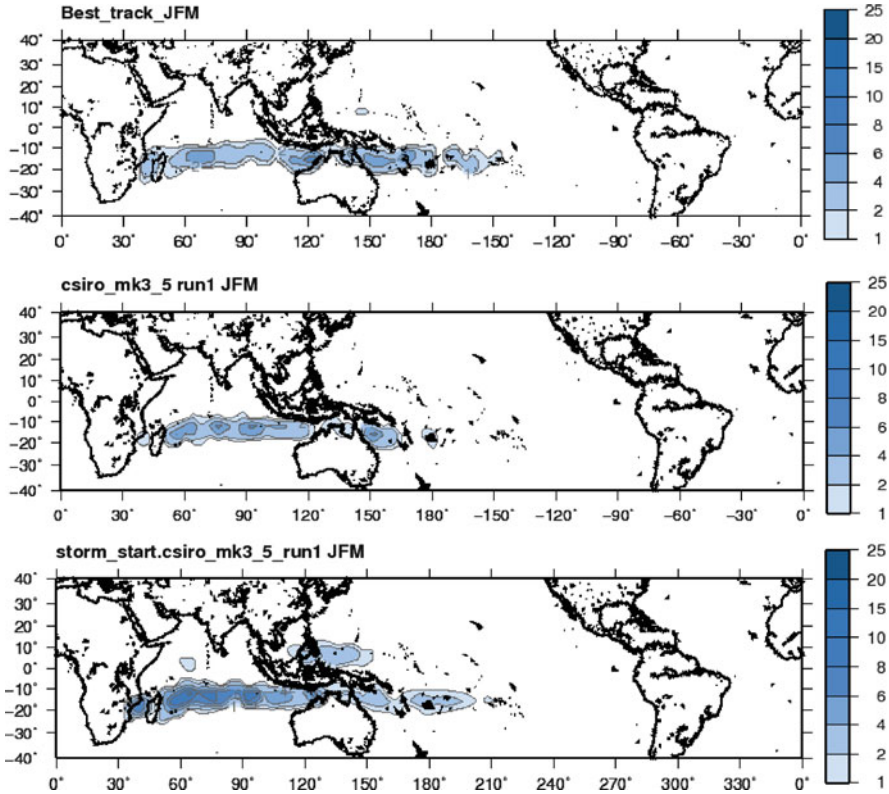

Fig. 3 Global tropical cyclone genesis for JFM from (*top*) IBTracs best track data; and as generated by the CMIP3 CSIRO Mk 3.5 data from (*middle*) the CSIRO detection scheme; and (*bottom*) the basin-dependent detection scheme. Formation rate is per $2.5° \times 2.5°$ grid box per 20 years

in the basin-dependent scheme in the north Indian Ocean. The differences between the results from the two schemes are partly due to the higher sensitivity of the basin-dependent scheme; further analysis of the CSIRO detection results indicates that it also detects some formation in the north Indian Ocean, but at a lower rate.

5.1.3 PCMDI Model Tropical Cyclone Generation

Results using the CSIRO detection scheme from those higher-resolution PCMDI models that have sufficient daily data to enable tropical cyclone detection are shown in Figs. 4 and 5. In general, results from lower-resolution models tend to be poorer (not shown). Figure 4 shows results for January–March. The same arrangement of models is made as for the GP results of Fig. 1. Comparing Fig. 1 to Figs. 4 and 5, there appears to be little relationship between the GP and the actual rate of model

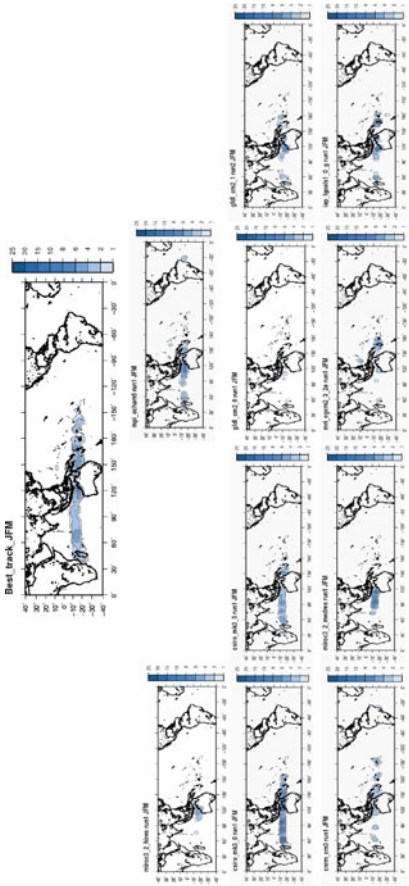

Fig. 4 Detected model tropical cyclone formation rate using the CSIRO detection scheme, for January–March. Units are the same as Fig. 1 (higher resolution models only)

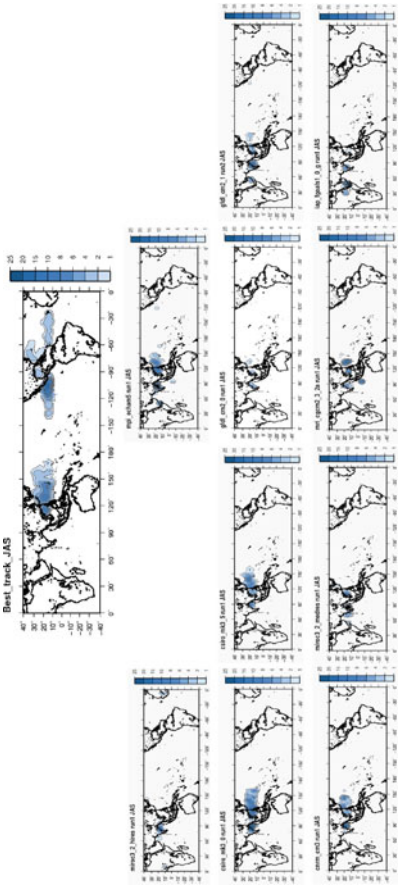

Fig. 5 The same as Fig. 4 but for July–September

formation of storms. For example, the ECHAM5 model (second row, third from the left) has a very large value of GP, but the formation rate is not that high. In contrast, the CSIRO models (third row) have a more realistic GP and a relatively realistic formation rate. Both Camargo et al. (2007) and Yokoi et al. (2009) also found little relationship between the GP and tropical cyclone formation. There are a priori reasons to believe why these relationships might differ from model to model. For instance, models have different representations of horizontal diffusion and diffusive processes that are either explicitly specified in their dynamical formulation or implicit in that formulation – for instance, a model that employs semi-Lagrangian advection has an inherently more diffusive structure than one that uses a more explicit advection scheme. Part of the process of model intercomparison is identifying such model-dependent issues as a way of making recommendations for improvements in model formulation.

The results of Figs. 4 and 5 show that there are substantial differences between the formation rates of cyclones from model to model. There appears to be a slight tendency for lower-resolution models to have lower rates of formation, but this is certainly not systematic: for instance, the MIROC high-resolution model has relatively low rates of cyclone formation despite it being the highest resolution model in the PCMDI suite. A comparison of Figs. 4 and 5 shows that formation rates are consistent from model to model despite the different season: if a model has a larger formation rate in one season than other models, it also has a larger formation rate in the other season.

Some systematic biases are evident in cyclone formation common across most models. For instance, Fig. 5 shows that there is little formation in any model in the Atlantic basin in June–September, even in models like the CSIRO models that have considerable formation in other tropical cyclone basins. The observed formation rate in the Atlantic is consistently lower than in the northeast and northwest Pacific, suggesting that this could be a threshold effect: it can be argued that because the North Atlantic is the only tropical cyclone basin not associated with a monsoon trough, and because the seasonal mean flow has a westerly vertical shear, formation of tropical cyclones is inherently more difficult in the Atlantic (McBride 1995). Thus, in coarse-resolution models, few (or none) are formed. Certainly, finer-resolution models implemented in the Atlantic have little difficulty in generating tropical cyclones (e.g. Knutson et al. 2008), although as discussed later, this is not solely a function of resolution.

6 High-Resolution Global Model Output

Some preliminary results have been obtained from high-resolution model output. The JMA-GSM 20-km global mesh model and the CMCC-INGV 80-km GCM results are shown in Figs. 6 and 7. Both models appear to have a good pattern of cyclone formation compared with observations, although both also have fewer

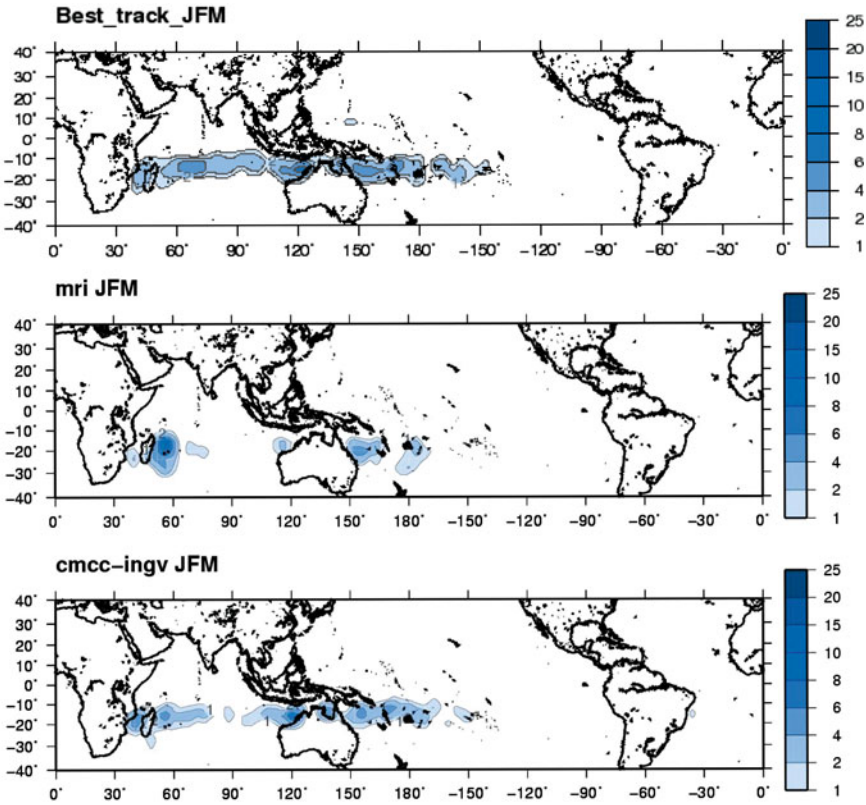

Fig. 6 The same as Fig. 3 for (*top*) the MRI model and (*bottom*) the CMCC-INGV model as described in the text, using the CSIRO detection scheme

than observed tropical cyclone formations. Again, neither model simulates sufficient storm formation in the Atlantic. In the case of the results from the MRI model, it is believed that the specification of the convection scheme in the model is causing the number of tropical cyclones to be less than observed (H. Murakami, 2009, personal communication). For the CMCC-INGV model, the data analysed here are daily average data, which as Fig. 1 shows would lead to an underestimate by at least a factor of 2 on average in the number of detected storms. More recent analysis of the CMCC-INGV model output is shown in Fig. 8, where four-times daily data were analysed. The number of storms generated in the Atlantic basin is considerably larger than in the daily average data, although still less than observed. Numbers in most other basins are good, however.

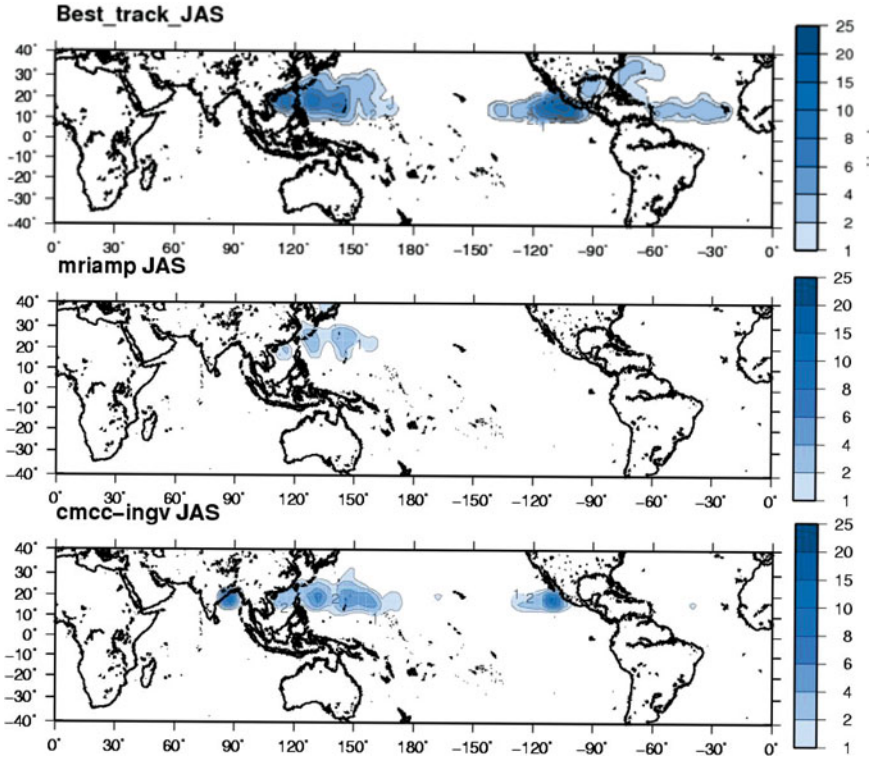

Fig. 7 The same as Fig. 6 for July–September

7 Regional Climate Model Results

One of the persistent biases even in the high resolution global models examined here is the undersimulation of tropical cyclone formation in the Atlantic. Nevertheless, regional models implemented over the Atlantic have been shown to achieve excellent results when nested within reanalyses (Knutson et al. 2008). Results are shown here from the Canadian Regional Climate Model (GEM). GEM is a fully non-hydrostatic model, employing an advanced semi-implicit, semi-Lagrangian dynamical core (Zadra et al. 2008). The model uses a hybrid-terrain-following vertical coordinate with 53 levels (top at 10 hPa) and uses the Kain-Fritsch parameterization scheme (Kain and Fritsch 1990) for deep convection and the Kuo transient scheme (Kuo 1965; Bélair et al. 2005) for shallow convective processes. The lateral boundaries are forced using a one-way nesting technique and the lateral boundary conditions are derived from the European Centre for Medium-Range Weather Forecasts (ECMWF) Reanalysis data (ERA-40; Uppala et al. 2005) for the 1979–2001 period and the ECMWF uninitialized global analyses for the 2002–2006 period. No spectral nudging toward the pilot large-scale fields is performed.

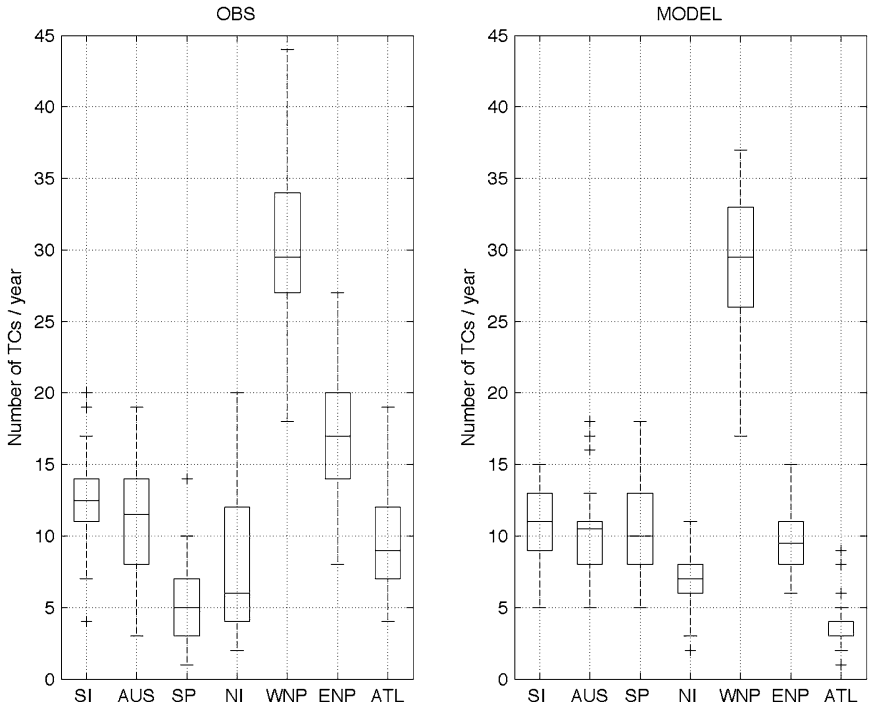

Fig. 8 Box plot of yearly tropical cyclone numbers, CSIRO detection scheme, for the CMCC-INGV model, four times daily data, current climate, compared with observations

Over the entire period of simulation, GEM produced a total of 357 Atlantic tropical cyclones, slightly more than the 318 storms observed during the same period. The geographical distribution of the simulated storms is shown in Fig. 9, which displays the mean number of cyclogenesis events over a 2.5° × 2.5° area per decade. There appears to be good concordance between actual cyclogenesis locations and high ASO Genesis Potential Index values seen in Fig. 9.

Both this model and the ZETAC model employed by Knutson et al. (2008) cannot simulate the strongest tropical cyclones, however. In this model, there were no hurricanes stronger than Saffir-Simpson category 1, while Knutson et al. (2008) showed a similar intensity distribution in their 18-km resolution model.

8 Discussion and Conclusion

A number of issues have been identified in this intercomparison process to date. Many of the CMIP3 models simulate fewer than observed systems in the Atlantic basin. The more recent experience of Zhao et al. (2010) may give some guidance

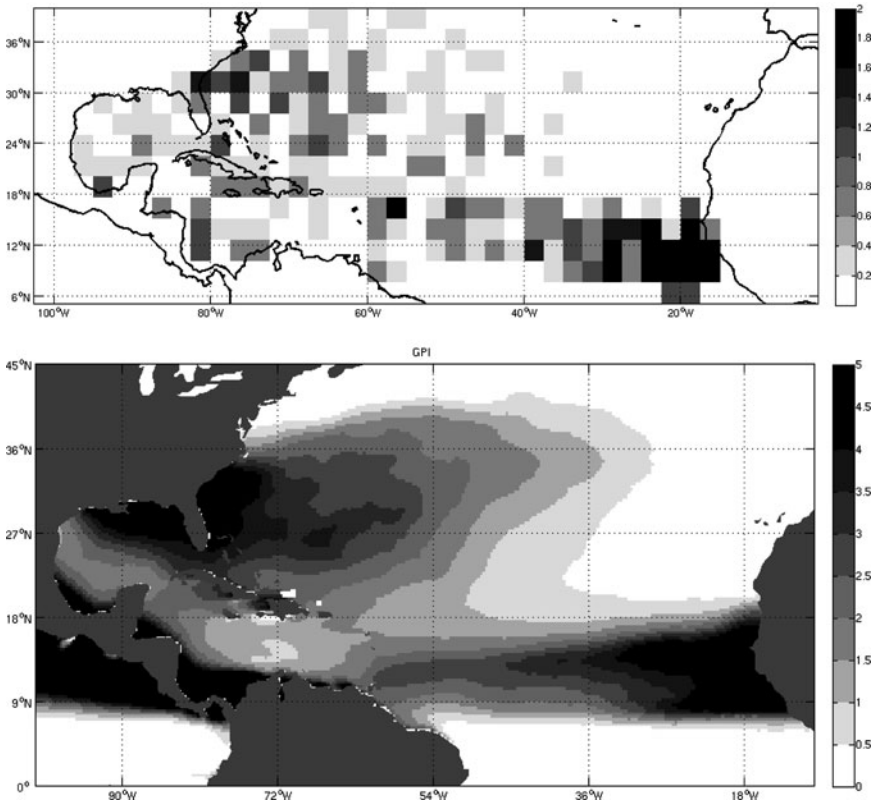

Fig. 9 *Top*: Model formation rate (formation per 2.5° × 2.5° box per decade); *bottom*: Emanuel GP

regarding how this problem may be addressed. The issue appears not to be simply a matter of increasing resolution: Zhao et al. (2010) found that a previous version of their model run at the same 50 km resolution as their recently published simulations was unable to generate sufficient numbers of storms in the Atlantic. They made several significant changes to this model, including the implementation of a new dynamical core; an increase in the number of vertical levels; the introduction of a diagnostic cloud scheme that assumed a sub grid-scale distribution of water; and the replacement of the Arakawa-Schubert convection scheme by a shallow convection scheme based on that of Bretherton et al. (2004). Testing showed that the main reason that a better climatology of tropical cyclones was produced was the replacement of the convective parameterization (M. Zhao, 2009, personal communication). This emphasizes the importance of the specification of the convection scheme for the generation of tropical cyclones, as also illustrated in Figs. 6 and 7 in this study.

Thus it is important to emphasize that higher resolution alone will not enable a better climatology of tropical cyclones to be produced. In developing a good climate model of tropical cyclone formation, it is clear that in addition to having a good

simulation of the large-scale tropical climate, a model needs to generate realistic small-scale variance. It is tempting to assume that the simulated detailed pattern of large-scale variables, as for instance represented by genesis parameters, will necessarily have a good relationship to tropical cyclone formation. But as shown by some previous work and also in this study, there appears to be little relationship between the chosen genesis parameter and the actual simulated rate of tropical cyclone formation, at least at the typical resolution of the CMIP3 models. This is a significant issue because it would be preferable not to have to take the model that is used for mean climate prediction and tune or modify it into a special version that is used for tropical cyclone climate prediction. If this is done, it reduces the confidence in these predictions.

There are nevertheless good reasons to be optimistic regarding the future quality of tropical cyclone climate predictions. It is clear that models are continuing to improve. A near-term goal may be the confident attribution of the recent observed increase in tropical cyclone formation in the Atlantic ocean, in other words determining the relative contribution of global warming and natural variability (Emanuel 2007). The TC-MIP project, by suggesting common ways in which such models can be improved, will aid in this process.

Acknowledgments The authors would like to thank the Australian Research Council Network for Earth System Science (ARCNESS) and Woodside Energy for supplying funding for the creation of the data sets analysed in this project. We would like to thank Aurel Moise, Aaron McDonough and Peter Edwards of the CSIRO's Advanced Scientific Computing group for assistance in creating a subset of the PCMDI data set, and the CSIRO Climate Adaptation Flagship for supplying funding for a related project. We would like to thank Damien Irving of CSIRO, who worked on an earlier version of this document. The authors would also like to thank their respective institutions for supporting this work. This chapter is a considerably extended version of a paper presented at the Centre for Australian Weather and Climate Research (CAWCR) Modelling Workshop, held November 25–28, 2009.

References

Bélair S, Mailhot J, Girard C, Vaillancourt P (2005) Boundary layer and shallow cumulus clouds in a medium-range forecast of a large-scale weather system. Mon Wea Rev 133:1938–1959

Bengtsson L, Hodges KI, Esch M (2007) Tropical cyclones in a T159 resolution global climate model: comparison with observations and reanalyses. Tellus 59:396–496

Bister M, Emanuel KA (1998) Dissipative heating and hurricane intensity. Met Atmos Phys 52:233–240

Bretherton CS, McCaa JR, Grenier H (2004) A new parameterization for shallow cumulus convection and its application to marine subtropical cloud-topped boundary layers. Part I: Description and 1-d results. Mon Wea Rev 132:864–882

Camargo SJ, Zebiak SE (2002) Improving the detection and tracking of tropical storms in atmospheric general circulation models. Wea Forecast 17:1152–1162

Camargo SJ, Barnston AG, Emanuel KA (2007) Tropical cyclone genesis potential in climate models. Tellus 59A:428–443

Emanuel KA (1987) The dependence of hurricane intensity on climate. Nature 326:483–485

Emanuel KA (2007) Environmental factors affecting tropical cyclone power dissipation. J Climate 22:5497–5509

Emanuel KA, Nolan DS (2004) Tropical cyclone activity and global climate. In: Proceedings of 26th conference on hurricanes and tropical meteorology, American Meteorological Society, pp 240–241

Emanuel K, Sundararajan R, Williams J (2008) Hurricanes and global warming: Results from downscaling IPCC AR4 simulations. Bull Am Meteor Soc 89:347–367

Gualdi S, Scoccimarro E, Navarra A (2008) Changes in tropical cyclone activity due to global warming: Results from a high-resolution coupled general circulation model. J Climate 21:5204–5228

Hegerl GC, Zwiers FW, Braconnot P, Gillett NP, Luo Y, Marengo Orsini JA, Nicholls N, Penner JE, Stott PA (2007) Understanding and attributing climate change. In: Solomon S, Qin D, Manning M, Chen Z, Marquis M, Averyt KB, Tignor M, Miller HL (eds) Climate change 2007: The physical science basis. Contribution of Working Group I to the Fourth Assessment Report of the Intergovernmental Panel on Climate Change. Cambridge University Press, Cambridge/New York, pp 663–745

IPCC (2007) Climate change 2007: The physical science basis. Contribution of Working Group I to the Fourth Assessment Report of the Intergovernmental Panel on Climate Change. In: Solomon S, Qin D, Manning M, Chen Z, Marquis M, Averyt KB, Tignor M, Miller HL (eds) Cambridge University Press, Cambridge/New York, 996 pp

Kain JS, Fritsch JM (1990) A one-dimensional entraining/detraining plume model and application in convective parameterization. J Atmos Sci 47:2784–2802

Knapp KR, Kruk MC, Levinson DH, Gibney EJ (2009) Archive compiles new resource for global tropical cyclone research. Eos Trans 90:doi:10.1029/2009EO060002

Knutson TR, Sirutis JJ, Garner ST, Vecchi GA, Held IM (2008) Simulated reduction in Atlantic hurricane frequency under twenty-first-century warming conditions. Nat Geosci 1:479–483

Kossin JP, Knapp KR, Vimont DJ, Murnane RJ, Harper BA (2007) A globally consistent reanalysis of hurricane variability and trends. Geophys Res Lett 34:L04815. doi:10.1029/2006GL028836

Kuo HL (1965) On formation and intensification of tropical cyclones through latent heat release by cumulus convection. J Atmos Sci 22:40–63

Madec G, Delecluse P, Imbard M, Levy C (1998) OPA 8.1 Ocean General circulation model reference manual, Internal Rep. 11, Institut Pierre-Simon Laplace, Paris, France

McBride JL (1995) Tropical cyclone formation. In: Elsberry RL (ed) Global perspectives on tropical cyclones. WMO/TD-No. 693

Mizuta R, Oouchi K, Yoshimura H, Noda A, Katayama K, Yukimoto S, Hosaka M, Kusunoki S, Kawai H, Nakagawa M (2006) 20-km-mesh global climate simulations using JMA-GSM model: Mean climate states. J Met Soc Japan 84:165–185

Nordeng TE (1994) Extended versions of the convective parameterization scheme at ECMWF and their impact on the mean and transient activity of the model in the Tropics. ECMWF Research Department Technical Memo 206, 41 pp

Randall D, Pan D-M (1993) Implementation of the Arakawa-Schubert cumulu parameterization with a prognostic closure. In: Emanuel KA, Raymond DJ (eds) The representation of cumulus convection in numerical models. Meteor Monogr, Am Meteor Soc 46:137–144

Roeckner E, Bäuml G, Bonaventura L, Brokopf R, Esch M, Giorgetta M, Hagemann S, Kirchner I, Kornblueh L, Manzini E, Rhodin A, Schlese U, Schulzweida U, Tompkins A (2003) The atmospheric general circulation model ECHAM5. Part I: Model description. Rep. No. 349, Max-Planck-Institut für Meteorologie, Hamburg, Germany, 127 pp

Semmler T, Varghese S, McGrath R, Nolan P, Wang S, Lynch P, O'Dowd C (2008) Regional climate model simulations of North Atlantic cyclones: frequency and intensity changes. Clim Res 36:1–16

Stott PA, Tett SFB, Jones GS, Allen MR, Ingram WJ, Mitchell JFB (2001) Attribution of twentieth century temperature change to natural and anthropogenic causes. Clim Dyn 18:1–21

Tiedtke M (1989) A comprehensive mass flux scheme for cumulus parameterization in large–scale models. Mon Wea Rev 117:1779–1800

Trenberth KE, Fasullo J, Smith L (2005) Trends and variability in column-integrated water vapour. Clim Dyn 24:741–758

Uppala SM and Coauthors (2005) The ERA-40 reanalysis. Quart J Roy Meteor Soc 131:2961–3012

Walsh K (2008) The ability of climate models to generate tropical cyclones: implications for prediction. In: Peretz L (ed) Climate change research progress, Nova, New York, pp 313–329

Walsh K, Fiorino M, Landsea C, McInnes K (2007) Objectively-determined resolution-dependent threshold criteria for the detection of tropical cyclones in climate models and reanalyses. J Clim 20:2307–2314

Yokoi S, Takayabu Y, Chan J (2009) Tropical cyclone genesis frequency over the western North Pacific simulated in medium-resolution coupled general circulation models. Clim Dyn:doi 10.1007/s00382-009-0593-9

Zadra A, Caya D, Côté J, Dugas B, Jones C, Laprise R, Winger K, Caron L-P (2008) The next Canadian Regional climate model. Phys Can 64:75–83

Zhao M, Held I, Lin S-J, Vecchi GA (2010) Simulations of global hurricane climatology, interannual variability, and response to global warming using a 50km resolution GCM. J Clim 22:6653–6678

Chapter 2
Change of Tropical Cyclone and Seasonal Climate State in a Global Warming Experiment with a Global Cloud-System-Resolving Model

Kazuyoshi Oouchi, Masaki Satoh, Yohei Yamada, Hirofumi Tomita, and Wataru Yanase

Abstract Recent increase in computation power allows a use of high-resolution global model to investigate possible future change of tropical cyclones. In this chapter, we propose a new approach here to pursue the issue: the use of global cloud- system resolving model (GCRM).[1] It is the model designed with the clear aim of resolving cloud cluster, an essential component of tropical cyclogenesis, and therefore expected to provide a new result for the projection of future change of tropical cyclone. This chapter highlights our first attempt of time-slice prediction of future tropical cyclone (TC) under a global warming condition and associated climate change of season-long period with 14-km mesh version of Nonhydrostatic ICosahedral Atmospheric Model (NICAM), a prototype GCRM. Notable changes in the seasonal-mean state include decrease in outgoing longwave radiation (OLR) in the western to central Pacific, in particular east of the maritime continent, and increase in OLR and decrease in outgoing shortwave radiation in the mid and high latitudes. The former (the latter) is associated with an enhanced activity of precipitation (decrease in cloud amount) over the region. Global frequency of TCs in the

[1] "Cloud-system-resolving model" here refers specifically to a characteristic of the model in which gross effects of mesocale ensemble of convection that plays important role in tropical cyclone are represented. This type of model is capable of representing tropical cyclone viewed as a convective system built up of mesoscale ensemble of cumulus convection, if not the details of processes associated with inner cumulus clouds or cumulus convection.

K. Oouchi (✉), M. Satoh, Y. Yamada, and H. Tomita
Research Institute for Global Change, Japan Agency for Marine-Earth Science and Technology, 3173-25 Showamachi, Kanazawa-ku, Yokohama-Shi, Kanagawa 236-0001, Japan
e-mail: k-ouchi@jamstec.go.jp; yoheiy@jamstec.go.jp; htomita@jamstec.go.jp

M. Satoh
Atmosphere and Ocean Research Institute, The University of Tokyo, 5-1-5 Kashiwanoha, Kashiwa-Shi, Chiba 277-8568, Japan
e-mail: satoh@aori.u-tokyo.ac.jp

W. Yanase
Atmosphere and Ocean Research Institute, The University of Tokyo, 5-1-5 Kashiwanoha, Kashiwa-Shi, Chiba 277-8568, Japan
e-mail: yanase@aori.u-tokyo.ac.jp

J.B. Elsner et al. (eds.), *Hurricanes and Climate Change: Volume 2*,
DOI 10.1007/978-90-481-9510-7_2, © Springer Science+Business Media B.V. 2010

seasonal period is projected to decrease, in agreement with the general statement in the Intergovernmental Panel on Climate Change Fourth Assessment Report. On a regional basis, the frequency decreases over the North Atlantic, and remains almost unchanged in the western Pacific. The tendency of global frequency is found to be insensitive to detection threshold of the surface wind speed in the tropical cyclone tracking algorithm. The control experiment is designed for the particular year of 2004, which had a more El Nino flavor than normal year; therefore some caution is necessary in interpreting the results for this particular choice of experimental design.

Keywords Tropical cyclone change · Global warming experiment · Global cloud-resolving model

1 Introduction

High-resolution climate modeling is a general trend in the climate modeling community across worldwide. The 20-km mesh atmospheric general circulation model developed in Meteorological Research Institute/Japan Meteorological Agency of Japan is one of the highest resolution hydrostatic models (Mizuta et al. 2006). On the other hand, global cloud-resolving modeling has recently opened a new era to global modeling of tropical weather and short-term climate states. The Nonhydrostatic ICosahedral Atmospheric Model (NICAM, Satoh et al. 2008; Tomita and Satoh 2004) is a prototype of such kind of model, and has demonstrated simulations of tropical weather events in which mesoscale clouds and convection play vital role, such as Madden-Julian Oscillation (MJO; Miura et al. 2007) and tropical cyclone (Fudeyasu et al. 2008; Oouchi et al. 2009a) and boreal summer Indo-Asian monsoon (Oouchi et al. 2009b).

This chapter shows some results from another new attempt to apply NICAM to the study of future change of tropical cyclone activity and the associated seasonal climate states. The time-slice experiment is performed with the boundary condition provided by World Climate Research Program (WCRP) Coupled Model Inter-comparison Project phase 3 (CMIP3) coordinated activity. Results from another comprehensive analysis on the projected tropical cyclone change are discussed in Yamada et al. (2010). This chapter is organized as follows: Section 2 overviews design of the experiments. Section 3 discusses the results, and summary and additional remarks are described in Section 4.

2 Experimental Design

The model configuration of NICAM is the same as that used by Oouchi et al. (2009a). The horizontal grid spacing is approximately 14 km. Although the resolution is coarser for cloud-resolving model, it is chosen partly because the

multi-months time integration with much finer resolution is very computationally demanding, and partly because this is a first step to investigate this problem using global nonhydrostatic model and identify an overall performance of the approach. The resolution can capture mesoscale convection and cloud cluster and their interaction with tropical disturbances such as Madden-Julian Oscillation (MJO) that play important role in tropical cyclogenesis (Miura et al. 2007; Oouchi et al. 2009a). The experiment follows a time-slice approach (Bengtsson et al. 1996) consisting of a control (CTL) experiment for the period of June–October 2004 and a future GW experiment for the period of May–October at the end of the twenty-first century. May for GW is regarded as a spin-up period and excluded from the analysis.

Due to the large computational burden of GCRM approach, time integration is limited to one season, and statistical reliability of the projected TC changes remains as a topic of future research. The purpose of this experiment is therefore to see general feasibility of GCRM to approach the problem of future TC change under a particular boundary condition (such as sea surface temperature) as well as the associated climate components, to provide a general background to see merit and demerit of the GCRM approach for this purpose against conventional climate models. The intention here is not to provide general conclusion regarding the future tropical cyclone change, but rather to provide a case study of future change with a particular set of CTL and future experiment conditions. For CTL, the boundary conditions of sea surface temperature (SST) and sea ice concentration (SIC) are the same as those in the boreal summer 2004 experiment of Oouchi et al. (2009a). The conditions for GW are created using the dataset of the World Climate Research Program (WCRP) Coupled Model Inter-comparison Project phase 3 (CMIP3) with the method of Mizuta et al. (2008). The climate forcing for GW is created by adding the SST and SIC differences between the present-day (1979–2003) and GW (2075–2099) periods to the CTL. The pattern of SST forcing is El-Nino like and details are discussed in Yamada et al. (2010). The carbon dioxide concentration in GW is uniformly twice that in CTL, following the A1B scenario of the Intergovernmental Panel on Climate Change (IPCC)'s Special Report on Emissions Scenarios (SRES). The initial conditions for GW are taken from a present-day National Centers for Environmental Prediction (NCEP) reanalysis dataset for 0:00 UTC 1 May 2004. The model TCs are tracked using the methodology described by Sugi et al. (2002) and Oouchi et al. (2006). We compare the simulated TCs with an observational TC dataset (OBS) provided by the Unisys Corporation (http://weather.unisys.com/hurricane/) and IBTrACS (International Best Track Archive for Climate Stewardship). We use 17.5 m s^{-1} at 1,000 hPa as the wind speed threshold for TC definition; no artificial tuning of thresholds is required for the 14-km mesh simulation (Walsh et al. (2007).

3 Results

3.1 Changes in Mean Climate Features

A possible change in tropical cyclone under future climate condition has been investigated by many types of numerical models with multi-year time integration. The results discussed in this chapter are based on seasonal-long analysis (3 months), and therefore they cannot be extrapolated beyond the context of seasonal long projection. Yet, as GCRM has strength in treating mesoscale organization of clouds and convection (Satoh et al. 2008), it is as such expected to convey more reliable information regarding the tropical cyclone genesis, its development and the associated cloud climatology than in the conventional climate models. Its potential merits further investigation.

Figures 1–4 show the horizontal distribution (left) and zonal mean (right) of the seasonal (3-months) averaged Outgoing Shortwave Radiation (OSR), OLR, surface precipitation rate, and surface temperature for the control (CTL), global warming experiments (GW), and the difference as GW minus CTL. In terms of general characteristics, two features are to be mentioned here. First, OLR decreases for GW in the northern Indian Ocean, and the east of the maritime continent. This can be due to the enhanced precipitation activity over the region, which can be confirmed in Fig. 3. Second, OLR increases and OSR decreases in the mid latitudes over 30–60° N. This feature is likely to result from decrease in cloud amount (not shown), which is suggested by decrease in OSR and the increase in OLR as a manifestation of the surface temperature increase over the region (Fig. 4).

For regional characteristics, a precipitation increase under GW condition is dominant, in particular over the western Pacific. Across the central to eastern Pacific east of 120–150° W, significant increase is detected in the latitudinal belt around 5–10° N. On its poleward and equatorward sides, precipitation is found to decrease. This suggests a meridional shift or change in the width of the active precipitation band corresponding to the intertropical convergence zone.

3.2 Changes in Tropical Cyclones Tracks Frequency and Maximum Wind Speed

The changes in seasonal mean features discussed in the previous sub-section are the background climate states on which disturbances such as tropical cyclones are embedded. This subsection treats some simulated changes in tropical cyclone activity. The tropical cyclone tracks during the 3 months period for CTL and GW experiments, and the best track dataset are shown in Fig. 5, wherein distribution of the period-averaged sea surface temperature are superimposed on the plots. We can see that the tracks in CTL experiment are generally consistent with those in the observation (Figs. 5a and 5b). There is little deficiency over the north western Pacific, which

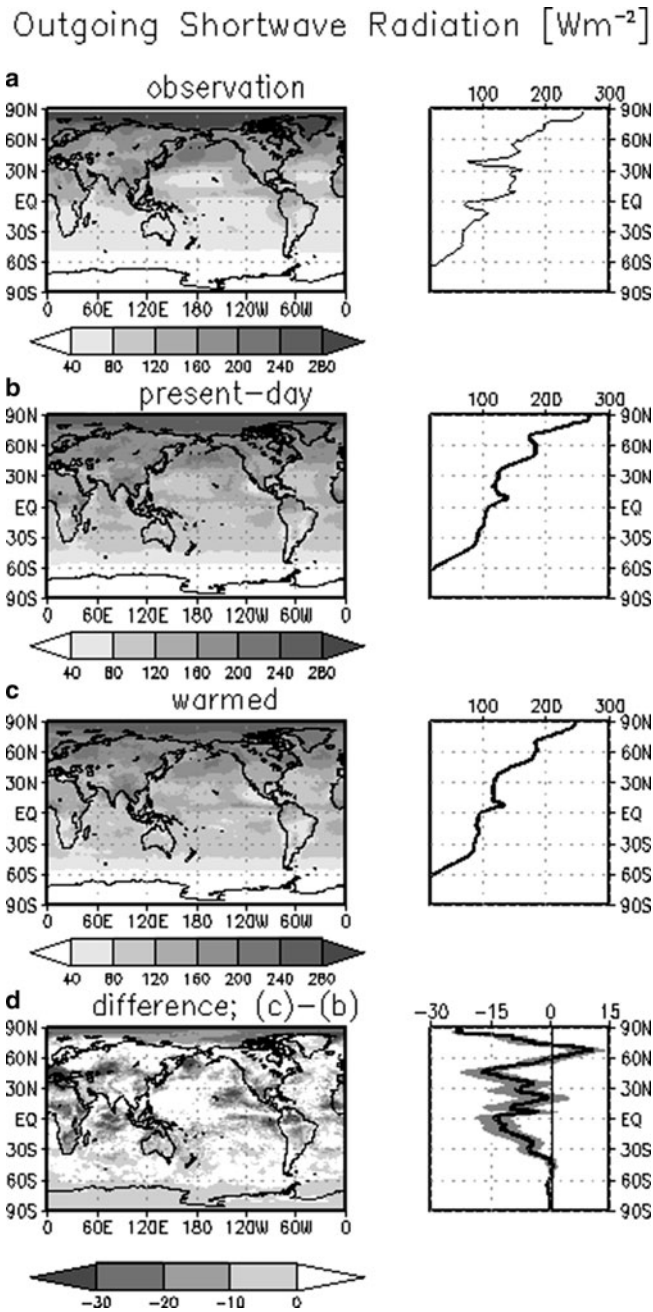

Fig. 1 Horizontal distribution of outgoing shortwave radiation ($W\,m^{-2}$) averaged over the 3 months period, JJA (*left*), and its zonal average (*right*) for (**a**) from Observation from NCEP Reanalysis, (**b**) control experiment (CTL), (**c**) global warming experiment (GW), and (**d**) the difference as GW minus CTL. Error bars are included for the difference (GW minus CTL) of the zonal average (**d**)

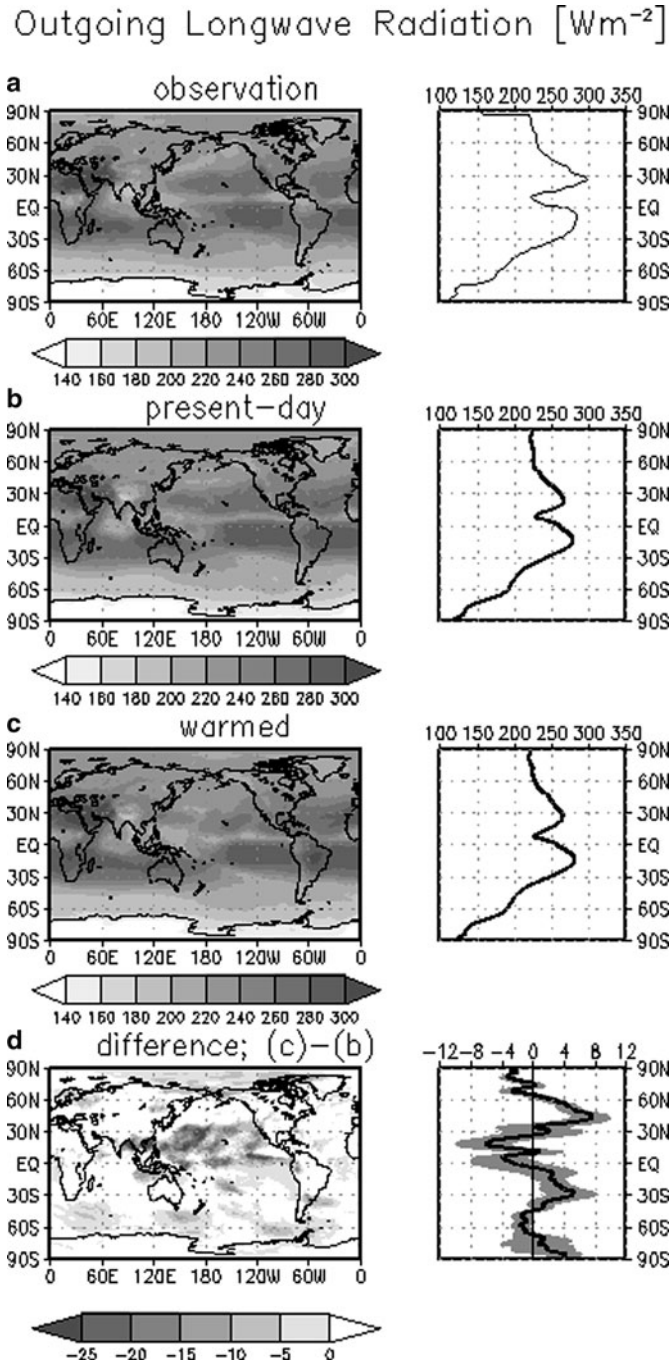

Fig. 2 Same as Fig. 1 but for outgoing longwave radiation (W m^{-2})

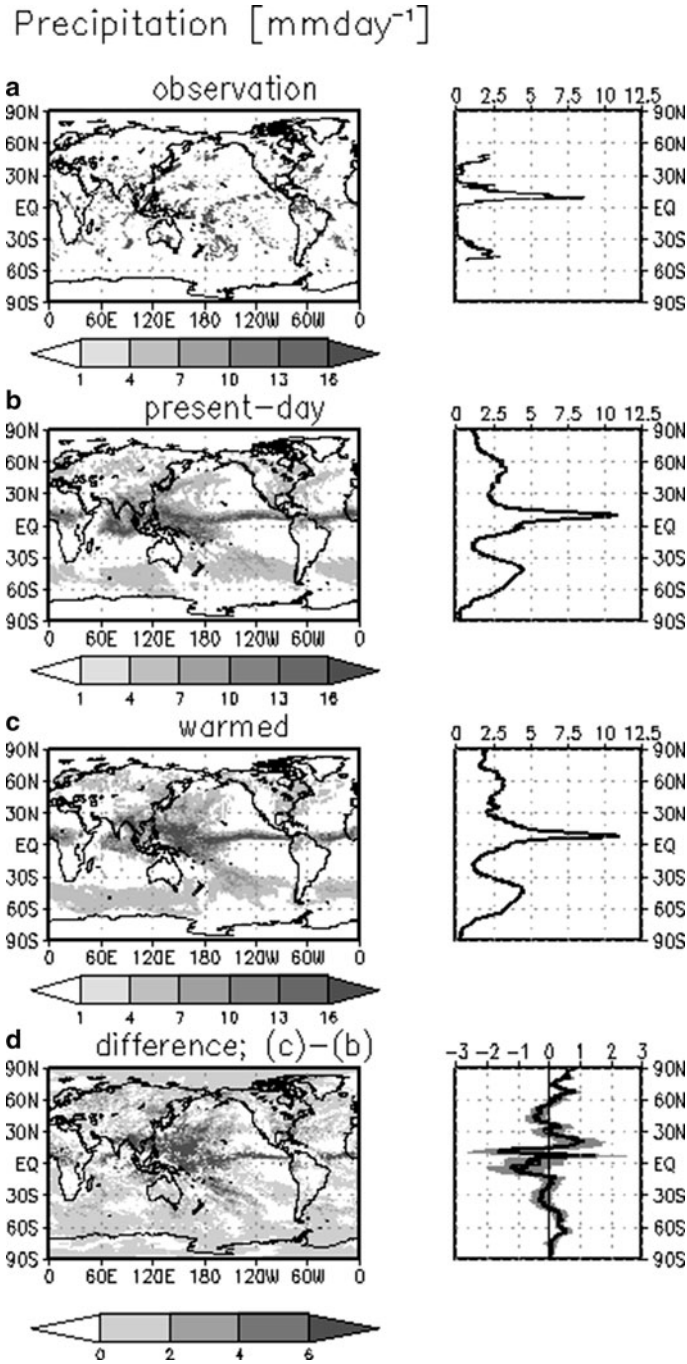

Fig. 3 Same as Fig. 1 but for surface precipitation rate (mm day^{-1}). Observation (**a**) is from the Tropical Rainfall Measuring Mission 3B42 dataset

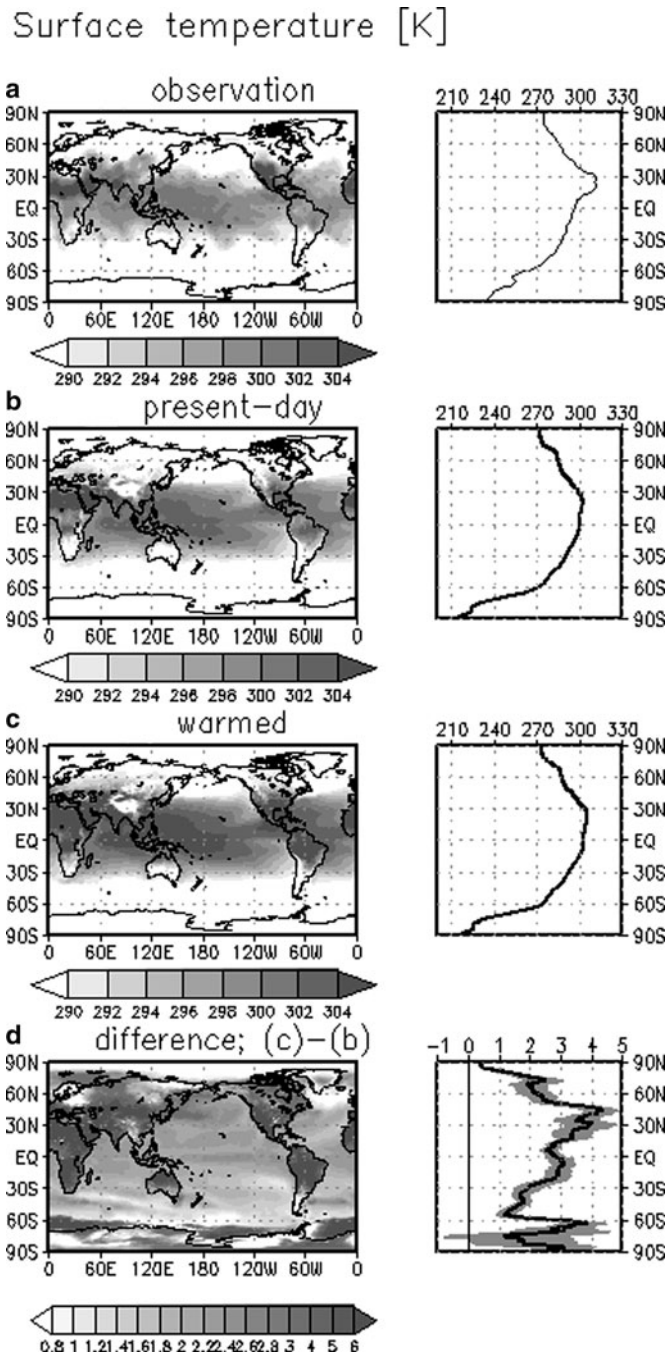

Fig. 4 Same as Fig. 1 but for surface temperature (K)

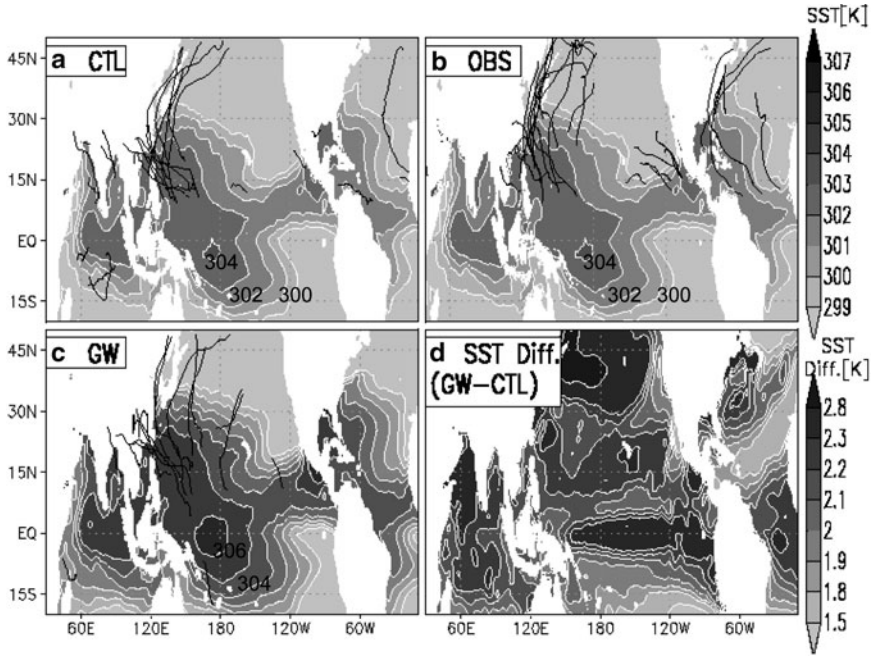

Fig. 5 Tropical cyclone tracks (*black*) from June to August, and sea surface temperature (*shade*) averaged over the period for (**a**) CTL experiment, (**b**) Unisys best track, and (**c**) GW experiment. (**d**) sea surface temperature difference as GW minus CTL. White contours in (**a–c**) are every 1 K

Table 1 The tropical cyclone numbers for the globe and each ocean basin during June, July and August of 2004 for observations (best track database from Unisys and IBTrACS), CTL experiment and a future 3-month period under GW experiment. Each oceanic basin is defined as in Oouchi et al. (2006); Indian Ocean (30–100°E); Western Pacific Ocean (100–180°E); Eastern Pacific Ocean (180–90°W); Atlantic Ocean (90°W–0)

	Indian Ocean	W. Pacific	E. Pacific	Atlantic	Globe (JJA)
OBS (Unisys)	3	15	7	8	33
OBS (IBTrACS)	0	16	7	8	31
CTL	8	12	3	3	26
GW	2	13	3	1	19

is usually the case in most of conventional climate models (Oouchi et al. 2006). In the GW experiment, tropical cyclones become active over the western Pacific and quiescent over the Atlantic ocean (Yamada et al. 2010). Table 1 summarizes the tropical cyclone frequency for each oceanic basin and the globe for OBS, CTL, and GW. The global number (26) for CTL is close to the observed number of 33 (Unisys) or 31 (IBTrACS). This particular experiment with 14-km mesh GCRM therefore reproduces the global tropical cyclone number for this particular season (JJA of 2004) close to observation without artificial tuning of the threshold for TC definition. However, model underpredicts the count over the Atlantic Ocean and the

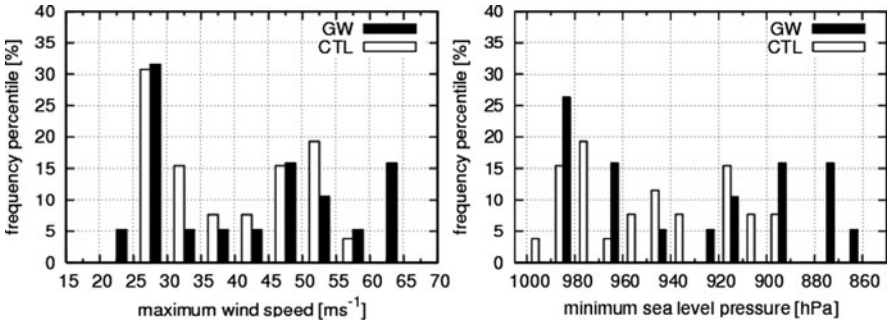

Fig. 6 Frequency percentile for CTL and GW as a function of the maximum wind speed at 1,000 hPa (*left panel*) and minimum sealevel pressure (*right panel*) for each of the 3-month experiment

Eastern Pacific, and overpredicts it over the Indian Ocean. Improvement of these biases are important for accurate projection of tropical cyclone change, which we are intensely working on. In terms of future change, the global frequency is reduced from 26 to 19 (by about 30%), but the change depends on the ocean basin. The frequency is decreased over the Indian Ocean and the North Atlantic Ocean, whereas it remains almost unchanged over the western Pacific and the eastern Pacific.

The change in intensity of TCs in GW condition is investigated, and the histograms of the maximum wind speed and the minimum sea-level pressure are displayed in Fig. 6. Overall, TCs of intense class (such as wind speed higher than 55 m s^{-1} and the pressure lower than 900 hPa) are found to increase in GW, compared to the TCs of weaker class; for example, the pressure of the most intense TC is about 871 hPa in GW while it is 902 hPa in CTL. The tendency of increase in intense TCs under GW condition is in agreement with past studies with high-resolution climate model (e.g., Oouchi et al. 2006).

How to specify threshold values in physical parameters in detecting tropical cyclone in a given model is a key problem for model inter-comparison. Figure 7 shows the sensitivity of the global tropical cyclone numbers to threshold values of the wind speed. It is demonstrated that global reduction tendency in GW is robust for any given surface wind speed threshold. It turned out that the robustness of the reduction in the tropical cyclone number holds even when the other thresholds (such as warm core criterion) are changed. The graphs also suggest that storm of tropical depression type (with the maximum wind speed being less than 17 m s^{-1}) occupies about 47% and 40% of the total storms that reached the wind speed of more than 10 m s^{-1} for CTL and GW experiment, respectively. Therefore, it is hypothesized that the GW atmosphere can be generally unfavorable for increasing frequency of diabatically sustained vortex disturbances of weaker intensity class, in spite of increase in moisture compared to present-day climate condition. On the contrary, it is favorable for increasing frequency of intense tropical cyclone (Yamada et al. 2010), which supports the 20-km mesh GCM study (Oouchi et al. 2006) and recent observational study (Elsner et al. 2008). Walsh et al. (2007) suggested that most of the

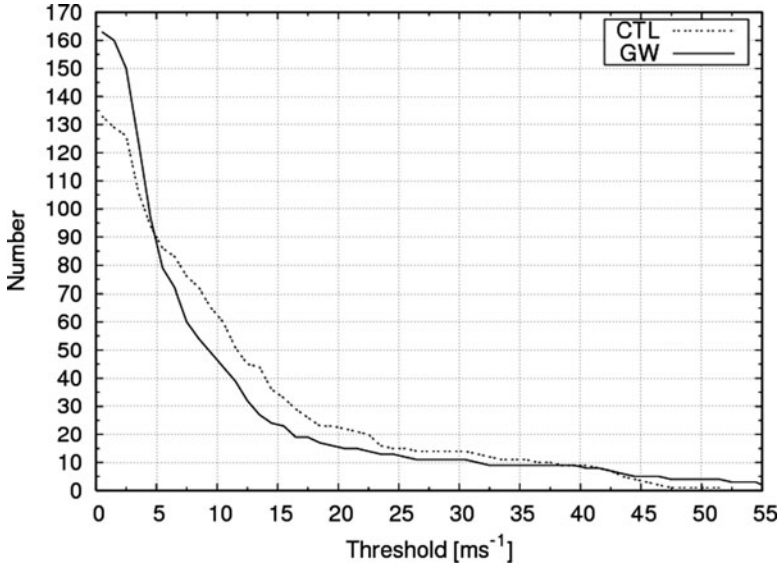

Fig. 7 Tropical cyclone numbers for CTL and GW experiments with varying maximum wind speed thresholds

conventional climate models used different criteria for detecting tropical cyclone, and therefore it has been difficult to extract unified information by inter-model comparisons. It is pointed out that the threshold varies roughly linearly with resolution. According to their results, the 17.5 m s^{-1} threshold used in this experiment can provide reasonable assessment to detect tropical cyclone with the grid spacing of 14-km used in this experiment.

4 Summary and Remarks

This chapter reports our attempt to use GCRM to investigate changes in tropical cyclones (TCs) under future global warming conditions by discussing highlights of some simulated results. The use of GCRM can be a new, promising strategy for a scenario-driven estimate of future climate that would benefit most from the expected future high-end computation environment.

We found that the projected TC changes are consistent with findings of the IPCC-4th Assessment Report (IPCC 2007) in terms of a global reduction of frequency and global increase of more intense TCs under the global warming climate condition (Yamada et al. 2010). In each oceanic basin, the model projects little change over the western Pacific, and noticeable reduction in the North Atlantic, although its statistical robustness remains to be fully evaluated in future work with the extension of time integration period. Over the western Pacific, TC genesis is merely

shifted eastward due to the prescribed SST of El-Nino-like pattern, leading to little change in frequency, and reduction in the North Atlantic is also associated with change in the atmospheric circulation pattern that is mostly ascribed to El-Nino-like SST forcing (Yamada et al. 2010). The result also suggests that the projected TC change in the western Pacific and the Atlantic Ocean is sensitive to the way SST forcing is given, as pointed out by Sugi et al. (2009). It is necessary to investigate how sea surface temperature change affects future tropical cyclone activity; an evidence was demonstrated by satellite-derived observation study (Elsner et al. 2008).

It is important to note that, although the present work projects global reduction in future TC frequency being consistent with the IPCC AR4, the underlying physical implications are far-reaching; GCRM is capable of tracking the majority of convection-coupled seed vortices that can develop into TCs, and these are the processes inadequately represented in conventional GCMs due to uncertainty in cumulus convection schemes (Oouchi et al. 2009a). The subsequent aim of the present work is therefore to clarify the mechanism of the projected change in TCs, making use of the strength of GCRM that resolves with fidelity cloud system. To obtain statistical robustness of TC characteristics, time integration needs to be extended beyond one season, which is another direction we should take in a future work. Climate variability on different time scale, such as decadal change in SST, complicates the real picture and clear understanding on causal relationship between SST change and tropical cyclone activity change (Knutson et al. 2007). Discrimination of these processes spanning different time scales is difficult by the present study with the limited time integration period, and nor can we plan to clarify this type of problem using GCRM under the current computational power. We may ultimately need to incorporate some ocean–atmosphere interaction processes for accurate projection of future change, which should be an important research theme in a near future.

An ongoing analysis plan with the current dataset is to investigate change in triggering disturbances such as MJO and easterly and equatorial waves. It will help understand the two distinguishing questions of "how tropical cyclones intensify in future" and "how tropical cyclones are initiated in future." This is an important subject that has not been systematically investigated using conventional GCMs, and GCRM can provide a comprehensive understanding on this problem.

Acknowledgments K. Oouchi thanks the conference organizers of the Second International Summit on Hurricanes and Climate Change for their supports and the participants for valuable discussions. The numerical experiments were performed on the Earth Simulator of JAMSTEC under the framework of KAKUSHIN project funded by the Ministry of Education, Culture, Sports, Science and Technology (MEXT), Japan. The analysis of NICAM data was supported also by the Core Research for Evolutional Science and Technology (CREST) of the Japan Science and Technology Agency. The Climate Model Intercomparison Project 3 (CMIP3) SST and SIC dataset was provided by Drs. Mizuta, Adachi, and Kitoh (Meteorological Research Institute). Constructive comments by a reviewer were beneficial for improving the presentation.

References

Bengtsson L, Botzet M, Esch M (1996) Will greenhouse-induced warming over the next 50 years lead to higher frequency and greater intensity of hurricanes? Tellus 48A:57–73

Elsner J, Kossin J, Jagger T (2008) The increasing intensity of the strongest tropical cyclones. Nature 455:92–95

Fudeyasu H., Wang Y, Satoh M, Nasuno T, Miura H, Yanase W (2008) The global cloud-system-resolving model NICAM successfully simulated the life cycles of two real tropical cyclones. Geophys Res Lett 35:L22808. doi:10.1029/2008GL0360033

Intergovernmental Panel on Climate Change (2007) Chapter 8: Climate models and their evaluation: 8.5.3 Tropical cyclones. Contribution of working Group 1 to the Fourth Assessment Report of the Intergovernmental Panel on Climate Change. In: Solomon S et al. (eds) Climate change 2007: The physical science basis. Cambridge University Press, Cambridge, pp 628

Knutson T, Sirutis J, Garner S, Held I, Tuleya R (2007) Simulation of the recent multidecadal increase of Atlantic hurricane activity using an 18-km-grid regional model. Bull Am Meteorol Soc 88(10). doi:10.1175/BAMS-88–10–1549

Miura H, Satoh M, Nasuno T, Noda A, Oouchi K (2007) A Madden-Julian Oscillation event simulated using a global cloud-resolving model. Science 318:1763–1765

Mizuta R, Oouchi K, Yoshimura H, Noda A, Katayama S, Yukimoto S, Hosaka M, Kusunoki S, Kawai H, Nakagawa M (2006) 20-km mesh global climate simulations using JMA-GSM model. -Mean Climate States- J Meteor Soc Jpn 84:165–185

Mizuta R, Adachi Y, Yukimoto S, Kusunoki S (2008) Estimation of the future distribution of sea surface temperature and sea ice using the CMIP3 multi-model ensemble mean, Tech. Rep. 56, Meterol. Res. Inst., Tsukuba, Japan

Oouchi K, Yoshimura J, Yoshimura H, Mizuta R, Kusunoki S, Noda A (2006) Tropical cyclone climatology in a global-warming climate as simulated in a 20-km-mesh global atmospheric model: Frequency and intensity analysis. J Meteor Soc Japan 84:259–276

Oouchi K, Noda A, Satoh M, Wang B, Xie S, Takahashi H, Yasunari T (2009a) Asian summer monsoon simulated by a global cloud system-resolving model: diurnal to intra-seasonal variability. Geophys Res Lett 36:L11815. doi:10.1029/2009GL038271

Oouchi K, Noda A, Satoh M, Miura H, Tomita H, Nasuno T, Igaz S (2009b) A simulated preconditioning of typhoon genesis controlled by a boreal summer Madden-Julian Oscillation event in a global cloud-system-resolving model. SOLA 5:065–068. doi:10.2151/sola.2009–017

Satoh M, Matsuno T, Tomita H, Miura H, Nasuno T, Iga S (2008) Nonhydrostatic icosahedral atmospheric model (NICAM) for global cloud resolving simulations. J Comp Phys 227:3486–3514

Sugi M, Noda A, Sato N (2002) Influence of global warming on tropical cyclone climatology: an experiment with JMA global climate model. J Meteor Soc Jpn 80:249–272

Sugi M, Noda A, Murakami H, Yoshimura J (2009) A reduction in global tropical cyclone frequency due to global warming. SOLA 5:164–167. doi:10.2151/sola.2009–042

Tomita H, Satoh M (2004) A new dynamical framework of nonhydrostatic global model using the icosahedral grid. Fluid Dyn Res 34:357–400

Walsh K, Fiorino M, Landsea C, McInnes K (2007) Objectively determined resolution-dependent threshold criteria for the detection of tropical cyclones in climate models and reanalysis. J Clim 20:2307–2314

Yamada Y, Oouchi K, Satoh M, Tomita H, Yanase W (2010) Projection of changes in tropical cyclone activity and cloud height due to greenhouse warming: Global cloud-system-resolving approach, Geophys Res Lett 37: L07709. doi:10.1029/2010GL042518

Chapter 3
Role of the SST Anomaly Structures in Response of Cyclogenesis to Global Warming

Fabrice Chauvin and Jean-François Royer

Abstract Projections of future changes in tropical cyclone genesis are still subject to debate since no consensus has been reached, yet, among the General Circulation Models which participated in the last IPCC Assessment Report (AR4). Making the hypothesis that the main reason for such a dispersion in the responses come from the diversity of sea surface temperature anomaly structures obtained in the coupled atmosphere/ocean systems, an ensemble of experiments has been conducted with the CNRM/Météo-France ARPEGE/Climate model, forced with climatological sea surface temperatures (SST) issued from 15 of the 22 coupled models of the AR4. In this chapter, responses in the original AR4 simulations and ARPEGE experiments were compared for two indices representing global cyclogenesis of tropical cyclones: the Convective Yearly Genesis Parameter and the Genesis Potential Index. CYGP responses in the ARPEGE experiment present a dispersion similar to the one from original AR4 scenarios, suggesting that the SST anomaly structures play a significant role in these responses. Additional experiments, using year-to-year varying SST, suggested that the interannual variability of SST cannot explain the dispersion. Additionally, looking at the mean ensemble response for original AR4 and ARPEGE SST forced simulations, tropical Indian Ocean and parts of the West Pacific, North of 20°N, appear to deliver a consistent response, which ARPEGE is able to reproduce and even to enhance. This implies that use of a single model in sensitivity experiments may be an interesting approach in suppressing all dependencies on the models characteristics and configurations.

Keywords Sea surface temperature · Cyclogenesis index · ARPEGE/Climate

F. Chauvin (✉) and J.-F. Royer
GAME/CNRM (Météo-France/CNRS), 42 Avenue Coriolis 31057 Toulouse Cedex 01, France
e-mail: fabrice.chauvin@meteo.fr; jean-francois.royer@meteo.fr

J.B. Elsner et al. (eds.), *Hurricanes and Climate Change: Volume 2*,
DOI 10.1007/978-90-481-9510-7_3, © Springer Science+Business Media B.V. 2010

1 Introduction

According to last Assessment Report (AR4) of the IPCC (Solomon et al. 2007), a synthesis of the model results to date indicates that, for a future warmer climate, coarse-resolution models show few consistent changes in tropical cyclones, with results dependent on the model (WG1, Chapter 10). Due to the complexity of the climate and its representation by models of different complexity, different reasons may be emphasized to explain such a spread in the response of the models. The model resolution is probably the most important, since most of the models participating in the last IPCC exercise show resolutions between 500 and 120 km which are not sufficient to represent correctly all the dynamics or mechanisms of the tropical cyclones. Moreover, assuming that tropical cyclones could be represented, their characteristics will depend largely on the model physical parameterizations, which determine how convection organizes. A third reason for the discrepancy between models lies on the structures of the sea surface temperatures (SST) calculated by the coupled systems. Indeed, while all the IPCC models indicate a substantial rise in the global mean SSTs, spatial and temporal patterns of change can differ greatly from one system to another. These differences may arise from ocean model, atmospheric model and/or surface fluxes at the interface between the two. Chauvin et al. (2006), using high-resolution atmospheric configuration of the ARPEGE/Climat model forced with two sets of SST anomalies, showed that the response of the tropical Atlantic cyclonic activity to global warming depended strongly on the spatial structure of these anomalies, more than the magnitude of the warming. The reason for such a dependency to SST anomaly patterns was found to be the mean response of the atmosphere to differential heating at the surface, through vertical shear of the horizontal wind, particularly.

Due to the low resolution of the models used to simulate present and future climate, tropical cyclones cannot be explicitly tracked in most AR4 climate scenarios. One way to deal with this discrepancy is to assess large-scale conditions which are thought to favor cyclogenesis. Early works of Gray (1968, 1975) suggested some large-scale indices combining several variables leading to enhancement of cyclogenesis. Among these variables, one can distinguish between dynamical and thermal conditions. Dynamical conditions include the Coriolis effect, the vertical shear of horizontal wind between low and high troposphere and relative vorticity in low levels, while thermal conditions account for the instability of the atmosphere as well as the oceanic heat content, through mid-level relative humidity, lapse rate and difference between SST and 26°C, a threshold widely accepted as a condition of formation of cyclones after the works of Palmen (1948). Combination of these variables led to the building of a Yearly Genesis Parameter, calibrated to account for a 20-year genesis climatology. This index was used by Ryan et al. (1992) and Watterson et al. (1995) to demonstrate that it allowed to diagnose, in General Circulation Models, climatology and interannual variability of cylogenesis. In 1998, Royer et al. showed that the Gray's formulation as it was defined, could not be used to address climate change They proposed a refinement of the YGP to represent the thermal component through the use of convective precipitation, which can be seen as an integration of all the thermal effects in play inside the model. The

Convective YGP (CYGP) was thus used to address the impact of anthropogenic global warming in model scenarios. This new index has been largely used in a number of studies (McDonald et al. 2005; Chauvin et al. 2006; Royer and Chauvin 2008; Caron and Jones 2008). Since then, Emanuel and Nolan (2004) have proposed a new formulation of what is called the Genesis Potential Index (GPI), based on broadly the same dynamical component as the YGP but using relative humidity and the concept of Potential Intensity (PI, Bister and Emanuel 1997) to account for thermal conditions. This index has been described and validated in Camargo et al. (2007a, b). It is important to mention that one does not really know whether large-scale indices represent the favourable conditions for cyclogenesis or traces of the tropical cyclone activity on the large-scale conditions. Indeed, few attempts have been made to assess the interannual variability of indices in relation with ENSO patterns (Camargo et al. 2007a). On the contrary, most studies related to indices have described climatological relationships between large-scale conditions and genesis.

Relationship between SST and cyclonic activity have been largely debated in the past. Early works of Palmen (1948) related cyclonic activity with SST and further works have emphasized the role of SST in the development of tropical cyclones (Emanuel 1986; Holland 1997). Beyond the direct effect linking SST to tropical cyclone activity (Saunders and Lea 2008), another relationship may occur through atmospheric circulation induced by SST anomaly structures. The impact of ENSO on cyclonic activity, notably, is important in modifying the distribution of favorable regions of cyclogenesis (Camargo et al. 2007a).

2 Definitions of the Cyclogenesis Indices

2.1 Convective Yearly Genesis Parameter (CYGP)

The CYGP has been defined by Royer et al. (1998) to solve the problem of Gray's YGP to account for climate change scenarios.

The dynamical potential was the same as in the YGP, defined as the product of the three original factors:

$$\mathrm{CYGP} = \mathrm{f}\,(\zeta_\mathrm{r}\,\mathrm{f}/|\mathrm{f}| + 5)\,(|\delta\mathrm{V}/\delta\mathrm{P}| + 3)^{-1}\,\mathrm{P_c},$$

where $\mathrm{f} = 2\Omega\,.\,\sin\varphi$ is the Coriolis parameter, φ is the latitude and Ω the angular velocity of the Earth in $10^{-5}\,\mathrm{s}^{-1}$, ζ_r is the low level relative vorticity at 950 hPa in $10^{-6}\,\mathrm{s}^{-1}$, $\delta\mathrm{V}/\delta\mathrm{P}$ is the vertical shear of the horizontal wind (V) between the pressure (P) levels 950 and 200 hPa, in m s^{-1}/750 hPa and $\mathrm{P_c}$ is the convective precipitation which exceeds a given threshold.

The complete thermal potential of Gray's YGP has been replaced by one based on the convective precipitation diagnosed by the models. In order to avoid that cyclogenesis is diagnosed over regions of shallow convection, a threshold was introduced in the formulation of the thermal potential, i.e. if convective precipitations are under this amount, the convective potential is set to 0. The choice of the threshold

has been made empirically, in such a way that the ERA40 spatial repartition of the CYGP corresponds fairly to global observations. A basic threshold of 3 mm day^{-1} was fixed for ERA40. Without taking into account the 3 mm day^{-1} threshold, near mid-latitudes cyclogenesis is artificially diagnosed while the conditions are generally not favorable over these regions.

Since the total convective precipitation varies from model to model, depending on the convective precipitation scheme, we made the convective threshold model-dependent and proportional to the total oceanic convective precipitation simulated by each model between the latitudes 35°S and 35°N. The complete description of the calculation appears in Royer et al. (1998) and Royer and Chauvin (2008).

2.2 Genesis Potential Index (GPI)

The GPI of Emanuel and Nolan (2004) is defined as follows:

$$\mathrm{GPI} = |10^5\ \zeta_a|^{3/2}\ (\mathrm{H}/50)^3\ (\mathrm{V_{pot}}/70)^3\ (1 + 0.1\mathrm{V_{shear}})^{-2},$$

where ζ_a is the absolute vorticity at 850 hPa, H the relative humidity, Vpot is the maximum PI wind speed and V_{shear} is the vertical shear of the horizontal wind between 850 and 200 hPa.

The PI used in this index has been studied from a long time by Emanuel (1995) and Bister and Emanuel (1997) and aims at representing the stability of the atmosphere, given the SST, MSLP and lapse rate. The GPI index has been used in climate studies by Camargo et al. (2007a, b) and Nolan et al. (2007).

2.3 Calibration

To allow comparison between all the indices from all the models, a convention was adopted which ensures that the global number of cyclogenesis is equal to 84 systems in the present climate. Thus, the model-dependent calibrating factor is applied to indices for future climate in the same way as in the present one. We choose to perform a global instead of per-oceanic-basin calibration to let each simulation produce its proper distribution of cyclogenesis around the world. When looking at basin number of cyclogenesis, one should keep in mind that numbers are representative of the part of cyclogenesis calculated in the basin relative to the total number.

3 Objectives of the Study

In order to try to understand why models give such different responses to global warming, we undertook a set of simulations with the help of ARPEGE/Climat model of the CNRM. Use of a unique model allows to address the impact of SST anomaly

patterns in a forced configuration and at a constant resolution. This is an attempt to isolate the only SST effect from the complete set of IPCC AR4 models.

From 15 of the 22 models archived in the IPCC database, we calculated the present (1990–1999) and future (2090–2099) climatologies of SST, taken from the control and SRESA2 scenarios for each and we performed present and future runs of 10 years each with these climatologies as a forcing. No interannual variability was considered in this ensemble of simulations due to the computational cost of such experiments. Additional four 30-year simulations were nevertheless performed with interanually varying SSTs to address the sensitivity of the results to this timescale variability. These additional simulations were forced by SSTs over the periods 1970–1999 and 2070–2099. ARPEGE/Climat was run in a T63 truncation, associated with a physical grid of approximately 2°8 × 2°8. The vertical resolution consists in 31 atmospheric levels, mainly distributed in the troposphere but nevertheless representing the stratosphere quite well. The convective scheme is from Bougeault (1985). For all the simulations, CYGP and GPI were calculated on the base of monthly means and averaged over the same periods of 10 years to calculate the annual number of cyclogenesis. Figure 1 shows the 15 SST anomalies taken from the original AR4 models. It can be seen, from Fig. 1 that there is a large variety of SST patterns, even though general patterns seem to emerge: positive anomalies over equatorial Pacific and global Indian Ocean and negative ones over southeastern Pacific. Over the Atlantic, no common feature emerges.

The hypothesis that we want to test here is that the dispersion in cyclogenesis activity, at least as measured by CYGP and GPI, is due to the variety of SST anomaly patterns structure. For this, we eliminate all the other sources of dispersion by using the same physics and resolution, through the use of a unique model. Another source of dispersion has been suppressed, in the first part of the study, interannual variability of the surface boundary forcings. In a second part, we performed some experiments to assess the sensitivity of the cyclogenesis response to interannually varying SSTs.

4 Global Results

Table 1 shows the correlations for the two cyclogenesis indices and for each AR4 model between the climatological response in the original simulation and in the ARPEGE forced simulation. The first notable feature in Table 1 is that the GPI correlations are much stronger that the CYGP correlations. To understand this relationship more clearly between the ARPEGE and original simulations, one should remember that the two indices differ largely in their definition of the thermal potential. Indeed, for the GPI, the PI concept is largely dependent on SST while the CYGP is essentially based on convective precipitation. The latter is more variable and highly dependent on the convective scheme used in the model. It is thus not surprising that the thermal potential obtained with ARPEGE can differ greatly from the original one. Indeed, the ARPEGE simulated CYGP anomaly is quite better

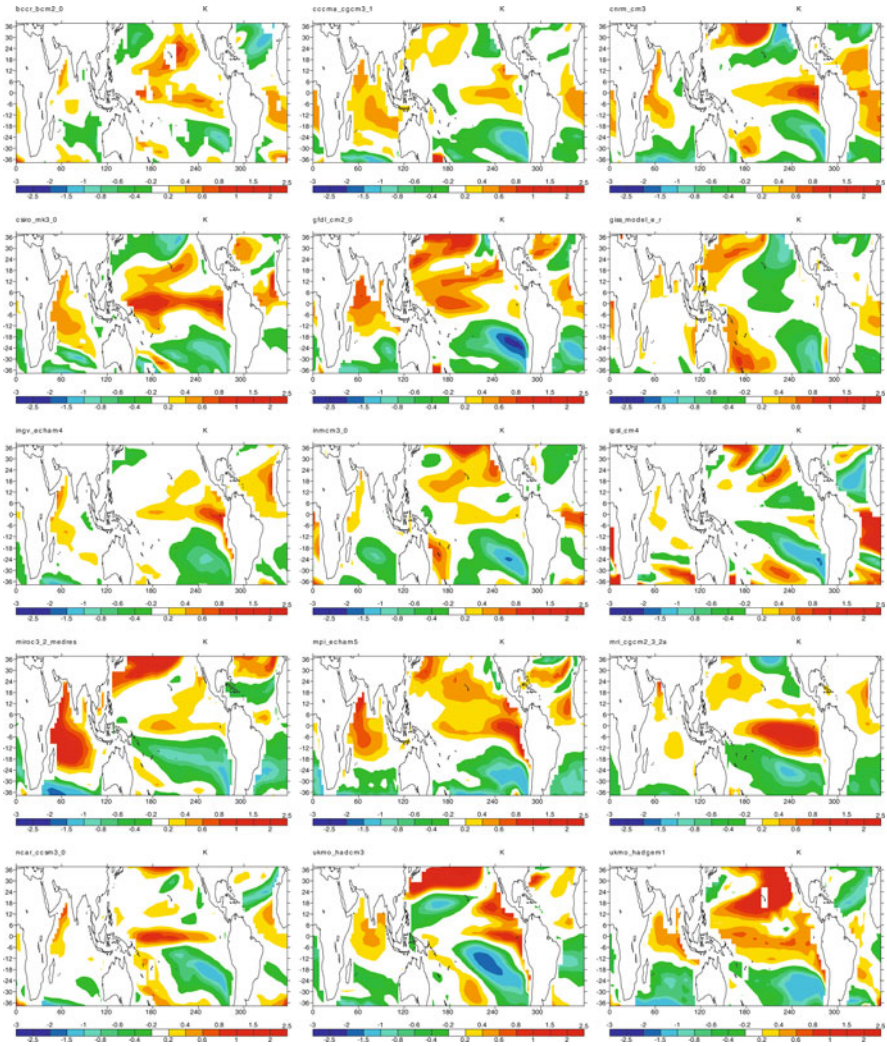

Fig. 1 Normalized SST anomaly patterns for the 15 models. Red to yellow colors are associated with positive anomalies and blue to green to negative ones. The periods of averaging for climatologies are respectively 1990–1999 and 2090–2099. Units are in degree Celsius

correlated to the original CNRM-CM3 (0.38) than to the other models, since the same convective scheme is used for original and forced simulations. The most striking feature in the CYGP correlations is the good correlation for the other French model from IPSL. Although the two models are completely different in their constitution (ARPEGE is spectral while the IPSL model is performed in grid-point) as well as in their parameterizations, their respective correlations appear equal, far higher than the other models. The MPI model is also distinct from the other models

Table 1 IPCC AR4 name and horizontal resolution of the models selected for this study, and spatial correlations between responses in coupled AR4 models and ARPEGE simulations for CYGP and GPI. Numbers in parentheses are for interannual varying SST experiments

Model	Resolution	CYGP	GPI
INMcm3_0	5° × 4°	0.05	0.44
GISS_model_e_r	5° × 4°	0.11	0.49
CCMA_cgcm3_1	T47	0.17	0.46
IPSL_cm4	3.75° × 2.5°	0.38 (*0.41*)	0.61
UKMO_hadcm3	3.75° × 2.5°	0.11 (*0.07*)	0.25
MRI_cgcm2_3_2_a	T42	0.12	0.31
MIROC3_2_medres	T42	0.21	0.44
BCCR_bcm2_0	T63/G42	0.04	0.44
CNRM_cm3	T63/G42	0.38 (*0.51*)	0.44
GFDL_cm2_0	2.5° × 2°	0.07 (*–0.06*)	0.47
CSIRO_mk3_0	T63	0.00	0.26
MPI_echam5	T63	–0.07	0.00
UKMO_hadgem1	1.875° × 1.25°	–0.06	0.16
NCAR_ccsm3_0	T85	0.15	0.32
INGV_echam4	T106	0.10	0.34

in that the ARPEGE simulations fails at reproducing both CYGP and GPI anomalies obtained with the original run. Since the two indices present the same discrepancy, one may think that the problem lies in the dynamical potential. We verified that in the original AR4 simulations with MPI model, response in dynamical variables is weaker than in the other models.

As an illustration, Fig. 2 shows the original AR4 and ARPEGE simulated anomalies in CYGP for the models from CNRM, GFDL, IPSL and UKMO which will be studied in more details in the next section. The two French models show some strong similarities in the anomalies in the South Indian Ocean (SIO) and, in parts of the Arabian Sea. In other part of the world, the patterns differ and each of the models present their own particularities. CNRM reproduces relatively well the Northern Pacific tropical band as well as the South Pacific West/East dipole, while IPSL does a good job for North Pacific subtropical dipole and tropical Atlantic. On the contrary, GFDL and UKMO models show several parts of the world were the patterns differ substantially, even if by some places, results are in agreement. For the GPI index, as said earlier, similarities are higher between original and forced simulations (Fig. 3).

According to correlations shown in Table 1, SST anomaly patterns between present and future climate in the original scenarios of the AR4 cannot account for the entire response of cyclogenesis, as hypothesized in Section 3. On the other hand, Figs. 2 and 3 suggest that dispersion in the SST anomaly patterns prescribed in the ARPEGE simulations leads to quite different cyclogenesis anomalies. Thus, in agreement with Chauvin et al. (2006), SST plays an important role in the cyclogenesis response to climate change even though it cannot explain the whole response. In Section 3, we mentioned that four additional experiments were performed in order

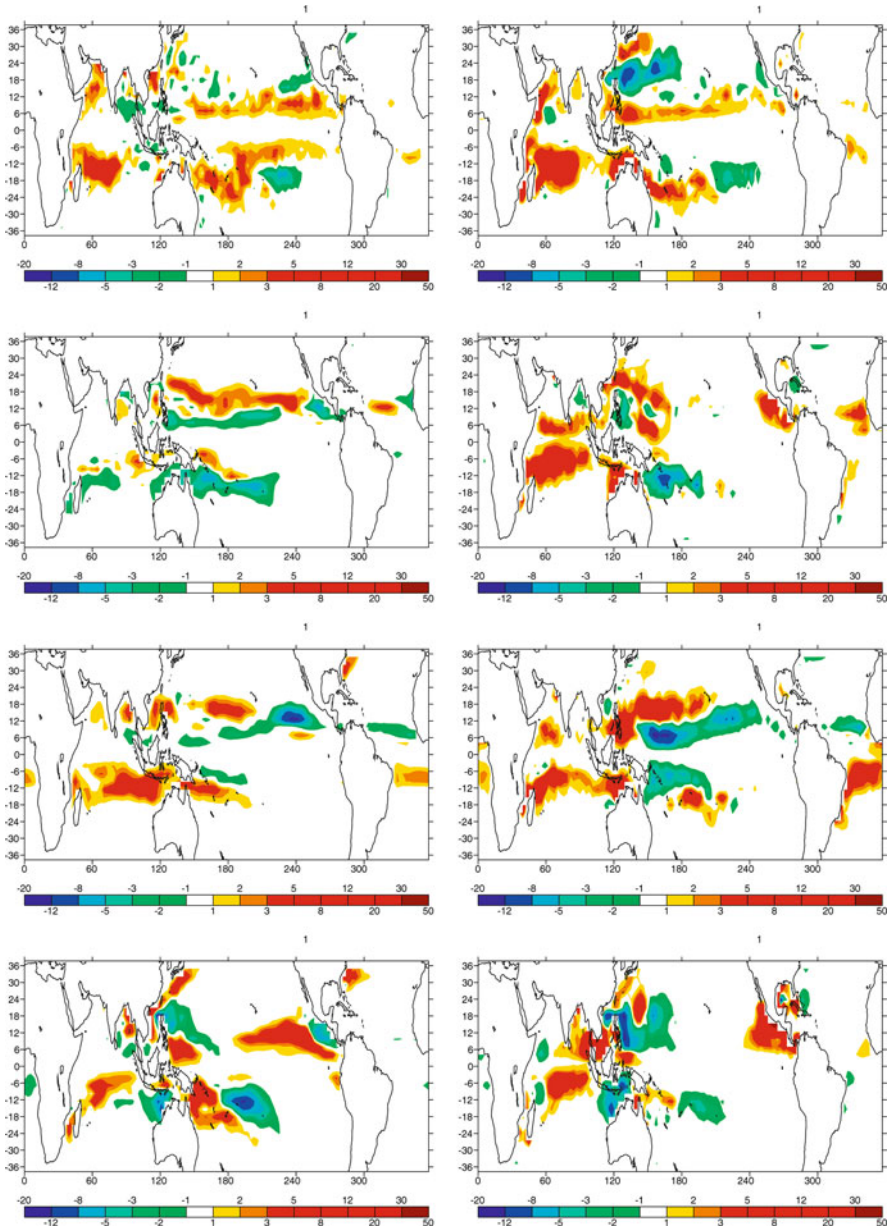

Fig. 2 Future minus present climate CYGP anomaly for original scenarios (*left*) and ARPEGE SST-forced simulations (*right*). Climatologies have been computed over periods 1970–1999 and 2070–2099 for AR4 original models and over the ten climatological years for ARPEGE. Units are in number of cyclogenesis per 5° per 20 years. Models retained are CNRM, GFDL, IPSL and UKMO (hadcm3)

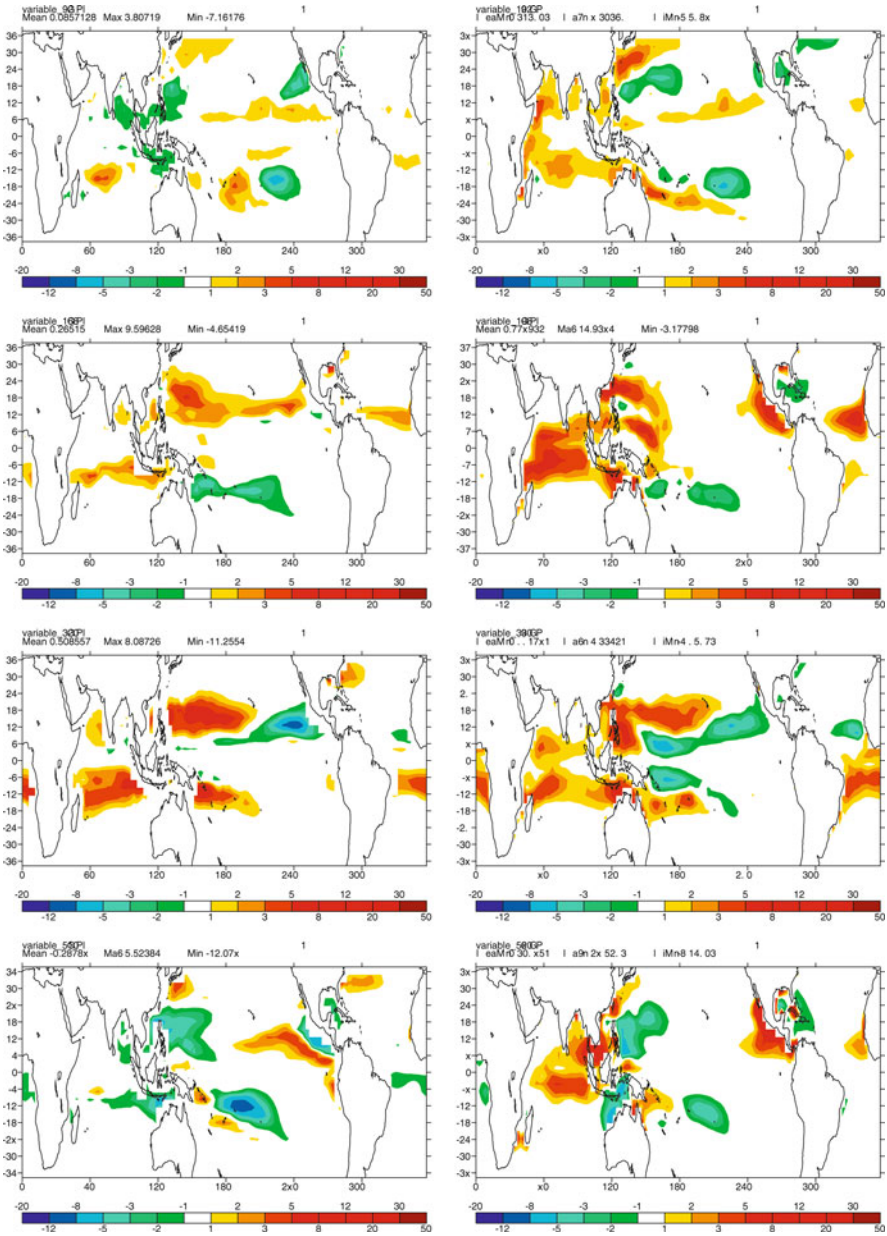

Fig. 3 Same as Fig. 2 for GPI

to assess the sensitivity of ARPEGE response to the year-to-year varying SSTs. We performed 30-year simulations for both present and future climate SSTs from each of the four models presented in Fig. 2. CYGP anomalies are presented in Fig. 4.

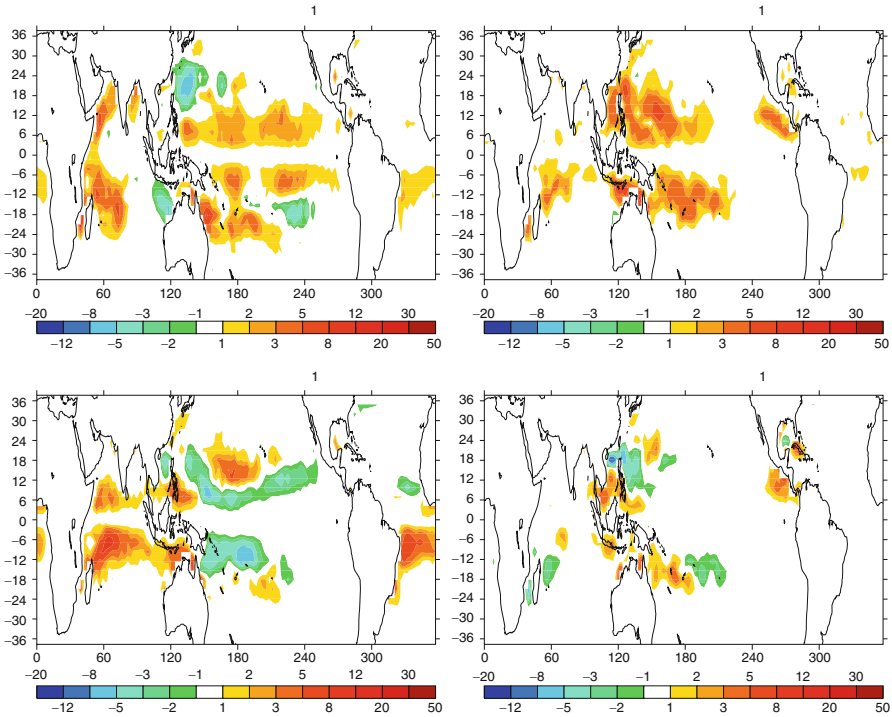

Fig. 4 Future minus present climate for ARPEGE year-to-year varying SST-forced simulations. Climatologies have been computed over periods 1970–1999 and 2070–2099 for both original AR4 and ARPEGE simulations. Units are in number of cyclogenesis per 5° per 20 years. Models retained are CNRM, GFDL, IPSL and UKMO (hadcm3)

For the CNRM SST anomaly, including interannual variability makes the CYGP response closest to the coupled scenario than using the mean anomaly. Correlation reaches 0.51 instead of 0.38 for the mean SST experiment (correlation was performed with a 30-year climatology of the original AR4 model instead of the 10-year climatology used to compare mean SST experiments). Nevertheless, the major discrepancy in the WNP basin between 15°N and 30°N persists though less marked. For the other models, no significant increase can be detected in the year-to-year varying SST experiments. This is not surprising since ARPEGE model has no reason to respond to interannual SST varying in the same way as original AR4 models. Thus, except for the CNRM model, performing the year-to-year varying SST experiments has not really improved the correlations between ARPEGE experiments and original AR4 models. This implies that lack of interannual variability cannot explain the weak correlations between ARPEGE and original AR4 anomalies. Since all the simulations have been calibrated relatively to the same number of global cyclogeneses, all the responses from the original AR4 models can be averaged for CYGP and GPI, and thus compared with the mean ensemble response from ARPEGE. Figure 5 shows the resulting CYGP (top) and GPI (bottom), for original AR4 (left)

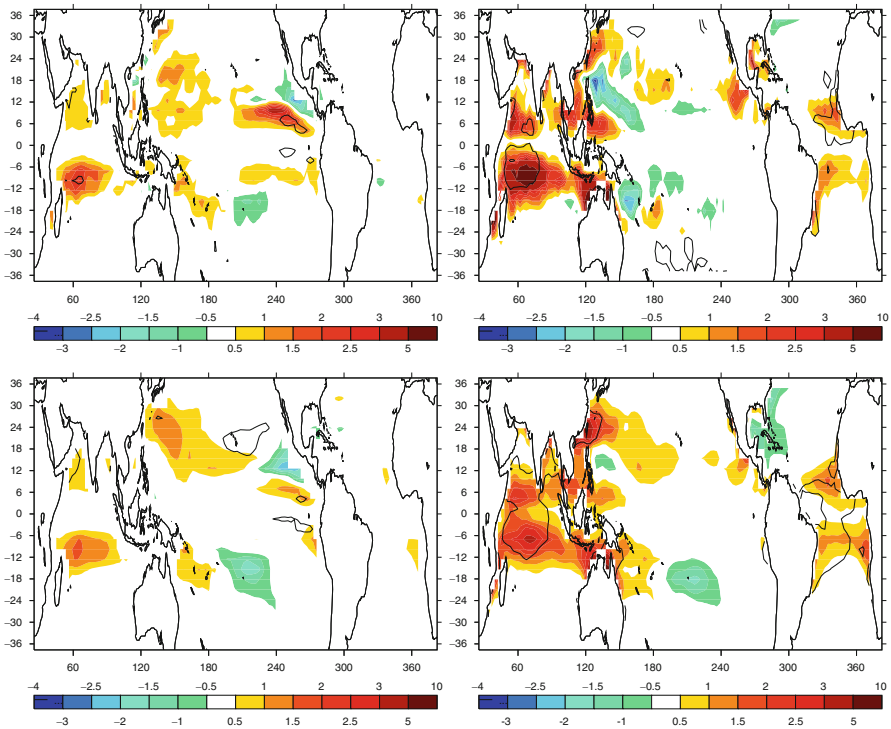

Fig. 5 Future minus present climate mean anomaly of CYGP (*top*) and GPI (*bottom*) calculated from the 15 models. On the left, anomalies are for the original AR4 scenarios and on the right for ARPEGE climatological SST-forced simulations. Climatologies have been computed as in Fig. 2. Units are in number of cyclogenesis per 5° per 20 years. Black contour delineate regions were the difference is significant at 90% in a Student's t-test

and ARPEGE (right) simulations. Black contour represents the regions were the mean response is significant at the 90% level, according to a Student's t-test. From Fig. 5 left panels, it can be seen that most basins show coherent responses for both CYGP and GPI in the original AR4 models. Among all the basins, some show some significant responses: North Indian Ocean and tropical North East Pacific for both CYGP and GPI, and South Indian Ocean for CYGP. From Fig. 5 right panels, some regions show robustness of the mean ARPEGE ensemble simulations over Indian Ocean and, in a lesser extent, over West North Pacific, North of 20°N. On the contrary, North East Pacific is no more coherent while tropical Atlantic shows a coherent response where original AR4 models did not converge. Strength of the response in the Indian Ocean is higher than for original AR4 models.

5 Results for the Different Oceanic Basins

To assess cyclogenesis in a more integrated point of view, we calculated the mean number of cyclogeneses (NC) for each of the original AR4 and ARPEGE simulations, from both CYGP and GPI. 6 basins were considered: North Indian Ocean (NIO), South Indian Ocean (SIO), West North Pacific (WNP), North East Pacific (NEP), South West Pacific (SWP) and Atlantic (ATL). Table 2 indicates the limits of the basins.

Figure 6 shows a scatter plot of NC in ARPEGE versus original AR4, for each basin. Dots are for present and triangles for future climate and the left figure shows the results for the CYGP and the right one for the GPI. For both CYGP and GPI in the present climate, the respective NC for each basin is preserved when using ARPEGE, that is the CNRM model does not bias the cyclonic activity toward a particular basin when forced by the original AR4 SST. Looking in more detail shows that ARPEGE tends, nevertheless, to overestimate cyclonic activity over NWP and ATL, and to underestimate it over NEP and SWP, for the two indices. In the Indian

Table 2 Limits of the oceanic basins

Basin	Limits
North Indian Ocean	40–100°E 0–35°N
South Indian Ocean	20–100°E 0–45°S
West North Pacific	100–180°E 0–55°N
North East Pacific	180°W to American coast 0–55°N
South West Pacific	100–200°E 0–50°S
Atlantic	American coast-Greenwich 0–55°N

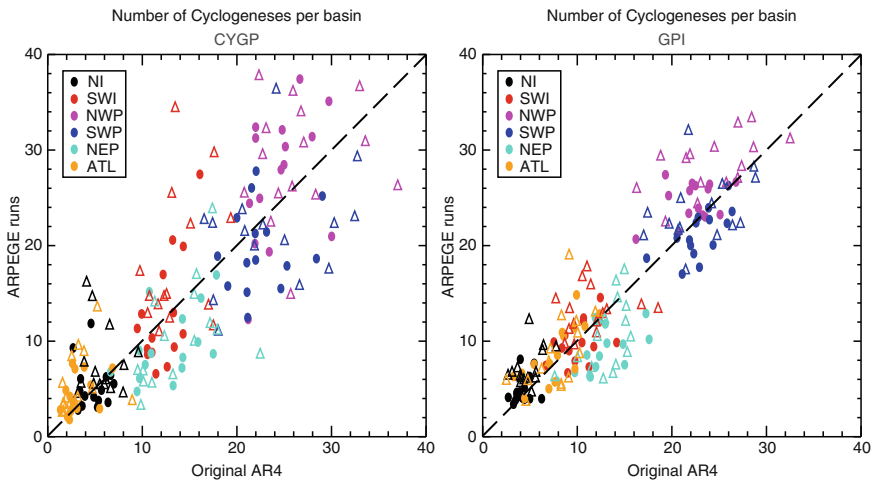

Fig. 6 Scatter plot of the numbers of cyclogenesis per basin and per model. Each symbol represents the number of cyclogenesis calculated from original AR4 model in abscissa and ARPEGE forced simulation in ordinate. Dots are for present and triangles up for future climate

Ocean, SWI is well reproduced by ARPEGE while NI is overestimated for GPI and underestimated for CYGP. In agreement with correlations showed in Table 1, GPI index shows a smaller dispersion than CYGP.

Concerning the response to global warming, comparison of ARPEGE simulations with original AR4 runs differs from indices and basins. For the CYGP (Fig. 5 left), and in agreement with Fig. 5, future NC in ARPEGE simulations tends to be greater than present NC over NIO and SIO, as well as Atlantic basin. For the latter, original mean AR4 models did not show any consensus. For Indian basins, the increase in the future was already present in original AR4 even though not as strong and significant than in ARPEGE. For the NWP, ARPEGE shows no preferred scenario while original AR4 tended to increase NC, although results were not significant. For the NEP and SWP, ARPEGE agrees with original AR4 on no consensual change. The results obtained for the GPI are sensibly the same as for the CYGP except for the SWP were ARPEGE clearly shows an increasing NC while original AR4 were less conclusive.

From Figs. 5 and 6, thus, it can be concluded that Indian Ocean has a particular status among the other basins in the sense that original AR4 models seem to present some coherent tendencies well reproduced by ARPEGE.

To understand this relative consensus on the Indian Ocean response to anthropogenic warming, we distinguished between thermal and dynamical components of CYGP and GPI. Thermal potential appears to be the component which explains the mean behavior of the indices. For CYGP, this potential is based on the convective precipitation (P_c), while for GPI, this is the product of the PI and relative humidity. Only the PI and P_c show a mean response structure coherent with the whole CYGP and GPI mean responses. The anomalies of thermal potential in CYGP and PI term in GPI are represented in Fig. 6. Relative humidity, vorticity and vertical shear do not show such structures which could explain the consensus (not shown). Both terms show a largely positive response everywhere except in the central South Pacific, and this structure is in good agreement with the mean SST response shown in Fig. 8. Indeed, Fig. 7 shows a mean positive anomaly over all the tropical band, Arabian Sea, North Eastern Pacific and Gulf of Mexico and a negative anomaly over South Central Pacific and North Atlantic. It is not surprising that P_c and PI show the structure similar to SST since these are directly dependent on air-sea interactions: P_c, through convective parameterization schemes and PI, through its formulation (Bister and Emanuel 1997). The association between dynamical variables and SST are more subtle and relative humidity results from evaporation but also from advective processes.

6 Discussion

Royer and Chauvin (2008) have emphasized the lack of common CYGP response of AR4 models. They did not investigate the reasons for such discrepancies nor the ensemble mean response of cyclogenesis. Nevertheless, they brought a methodology

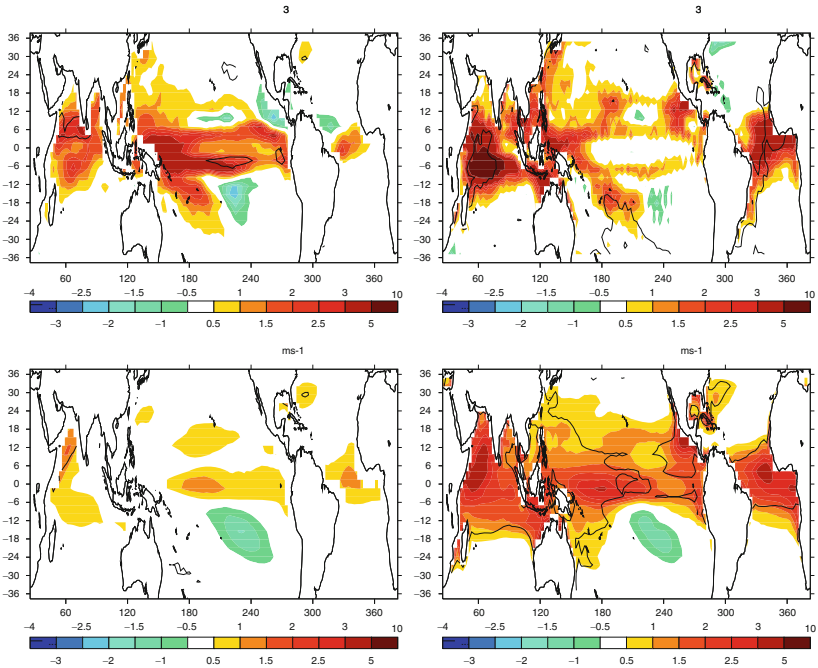

Fig. 7 Same as Fig. 5 for CYGP thermal potential term and PI term in GPI

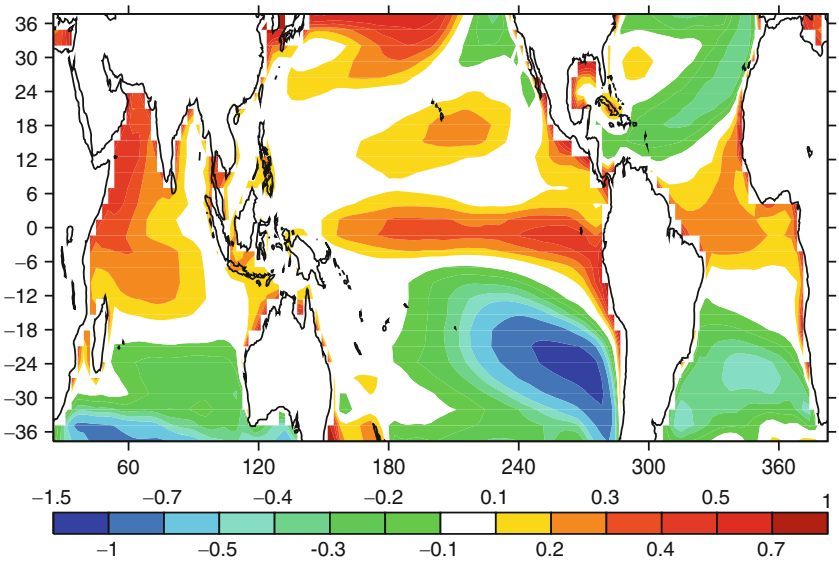

Fig. 8 Ensemble mean SST anomaly between 2090–2099 and 1990–1999 from the 15 AR4 scenarios. Units are in degree Celsius

which allowed to make possible the comparison between the models, through a calibrating process which has been applied by Caron and Jones (2008) in a more systematic comparison of CYGP for all the AR4 scenarios and models. The latter come to the same conclusions that there is a large dispersion in the models responses, at least in the large-scale conditions which are thought to be favourable for cyclogenesis. For each AR4 model SST conditions, the CYGP and, to a lesser extent, the GPI responses are not the same when forcing ARPEGE than in the original AR4 scenarios. The lack of interannual variability cannot account for these differences since the four models for which we have performed year-to-year varying SST forcing did not show real increase of the correlation between original AR4 and ARPEGE anomalies. In fact, the relation between SST and cyclonic activity is probably much more complex than a purely passive response of cyclogenesis to SST anomaly and cutting the coupling between the two processes leads to different responses of cylogenesis. Nevertheless, even without coupling process, SST anomaly structure plays a non negligible role in the response of cyclogenesis. One can remind the relatively good correlation between original and forced ARPEGE CYGP anomalies (0.38 in Table 1). This correlation, while not so high, is far higher than the other correlations, except the second French model for an unexplained reason. It is not surprising that ARPEGE forced run better reproduces the CYGP anomaly pattern when forced with SST anomaly from the original coupled simulation, since the same atmospheric component has been used in the two simulations. This correlation can be interpreted as a measure of the forcing contribution of SST to the CYGP anomaly. For the other models, it cannot really be expected to reproduce the same response due to large differences in physics and dynamics of the AR4 models. In other words, the forcing contribution of SST anomalies is masked by the existing differences between ARPEGE and original AR4 models. If the same set of experiments had been performed with another model of the AR4 database, we would probably observe a better correlation between CYGP patterns for this model.

Another interesting result obtained in this study is illustrated in Fig. 9, which represents model-to-model anomaly spatial correlations for original AR4 and ARPEGE experiments. Left panel shows that for CYGP, ARPEGE shows the same dispersion as the original AR4 scenarios did, with a slight tendency to bias the correlations toward positive values. This is not the case for GPI since ARPEGE tends to produce essentially positive correlations while original AR4 correlations were more widely distributed in negative values. This means that for the GPI, the use of a single model forced with different SST patterns reduces the dispersion of responses. Our feeling is that use of PI theory in the GPI index may be the clue for this behavior. Its too strong dependence in SST probably explains why the SST-forced experiments bias the inter-model correlations toward positive values.

As mentioned earlier, when forcing ARPEGE with the SST anomaly produced by the CNRM-CM3 coupled system (with the same atmospheric component), the correlation between CYGP anomaly patterns is the highest although not very high. Comparison of responses in Fig. 2 shows that the WNP response in the ARPEGE forced experiment is quite different from the response in the original CNRM-CM3. The reasons for such differences should be searched in the coupling process which

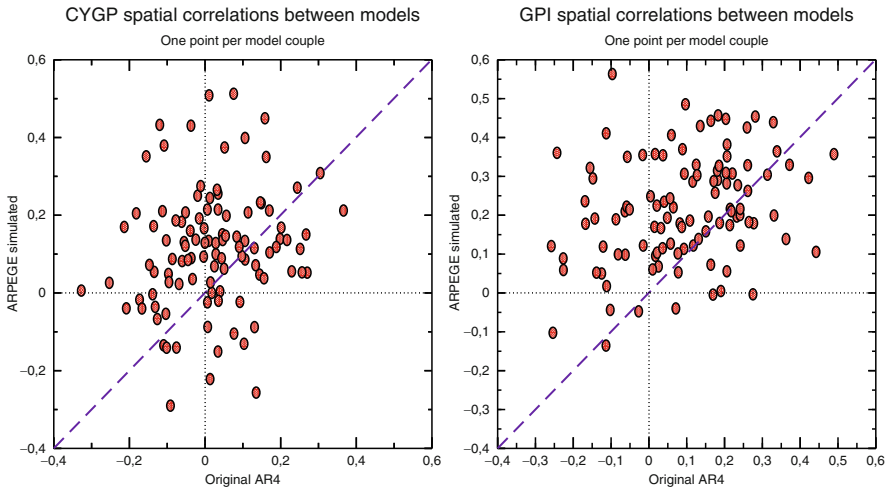

Fig. 9 Scatter plots representing model-to-model anomaly spatial correlations for original (*abscissa*) and forced (*ordinate*) experiments. Left panel is for CYGP and right panel is for GPI

takes into account the interactions between atmospheric conditions and underlying ocean. WNP is the region of the world of highest cyclogeneses. The cumulated effect of tropical cyclones may play an active role in the modulation of SSTs which may no more be seen as a purely forcing effect. Indeed, even though resolution of the original AR4 models is not sufficient to explicitly represent such systems, large scale systems occur nevertheless and contribute to modify SSTs, through heat exchange and upwelling of cooler water. Therefore, forcing the atmosphere with the resulting SST anomalies cannot lead to the same CYGP patterns as the original coupled model. The fact that largest discrepancies in CYGP patterns occur over the most active basin in the world agrees with the interaction between SST and CYGP.

7 Conclusion

This study investigated the dispersion of the AR4 models in representing tropical cyclone genesis through large-scale dynamical and thermal conditions. Previous studies (Royer and Chauvin 2008; Caron and Jones 2008) emphasized the lack of consensus between AR4 models in the response of CYGP in the scenarios of global warming. We tried, here, to extend the comparison, by using both CYGP and GPI in original AR4 models and in idealized ARPEGE atmospheric simulations where SST were prescribed according to the original AR4 SST anomalies between future and present climate.

Main results of the present study confirm that SST anomaly spatial structures play an important role in the CYGP and GPI response to global warming, even

though, the link between the two indices and underlying surface conditions cannot be simply summarized in a passive response of cyclognesis to SST. Indeed, the use of ARPEGE/Climat to simulate the atmospheric response to the different SST anomalies shows that a large diversity of responses may be obtained. Interestingly, as a sensitivity experiment, the actual study demonstrated that the use of a single atmospheric model in a forced configuration, can account for the large variability of responses obtained with the ensemble of AR4 models, at least for the CYGP index. For the GPI, this conclusion is not so evident, due to its too strong dependency on SST anomalies, thus leading to a reduction of degrees of freedom in the ensemble simulations.

Finally, another important result found here, is that, even though original AR4 models globally differ in their response of the cyclogenesis activity to global warming, some regions of the world seem to be more consensual than others. Indian Ocean shows a fairly coherent positive response in AR4 models, in relation to the coherent warming between most of the coupled models. This response is even reinforced in the ARPEGE ensemble simulation. On the contrary the Western North Pacific region seems to be very dependent on the coupling processes, since even when forcing ARPEGE with SST anomalies produced by the original CNRM-CM3, large discrepancies still exist in the cyclogenesis response between the two simulations.

It appears that for the major part of the world, atmosphere/ocean coupling may be crucial in the representation of the cyclonic activity response to global warming. Future simulations should take into account the entire atmosphere/ocean system with high resolutions to explicitly represent tropical cyclones. Thus, retroactions of tropical cyclones over ocean could be investigated.

References

Bister M, Emanuel KA (1997) Dissipative heating and hurricane intensity. Meteorol Atmos Phys 65:233–240

Bougeault P (1985) A simple parameterization of the large-scale effects of cumulus convection. Mon Wea Rev 113:2108–2121

Camargo SJ, Emanuel KA, Sobel AH (2007a) Use of a genesis potential index to diagnose ENSO effects on tropical cyclone genesis. J Clim 20:4819–4834

Camargo SJ, Sobel AH, Barston AG, Emanuel KA (2007b) Tropical cyclone genesis potential index in climate models. Tellus A 59:4428–4443

Caron L-P, Jones CG (2008) Analysing present, past and future tropical cyclone activity as inferred from an ensemble of Coupled Global Climate Models. Tellus 60A:80–96

Chauvin F, Royer JF, Déqué M (2006) Response of hurricane-type vortices to global warming as simulated by ARPEGE-Climat at high resolution. Climate Dyn 27:377–399

Emanuel KA (1986) An air-sea interaction theory for tropical cyclones, Part I: Steady-state maintenance. J Atmos Sci 43:585–604

Emanuel KA (1995) Sensitivity of tropical cyclones to surface exchange coefficients and a revised steady-state model incorporating eye dynamics. J Atmos Sci 52:3969–3976

Emanuel KA, Nolan DS (2004) Tropical Cyclones and the global climate system. In preprints for 26th Conference on Hurricanes and Tropical Meteorology. Miami Florida. Am Meteorol Soc Boston

Gray WM (1968) Global view of the origin of tropical disturbances and storms. Mon Wea Rev 96:669–700

Gray WM (1975) Tropical cyclone genesis. Department of Atmospheric Science Paper No. 234. Colorado State University, Fort Collins, CO

Holland GJ (1997) The maximum potential intensity of tropical Cyclones. J Atmos Sci 54: 2519–2541

McDonald RE, Bleaken DG, Cresswell DR, Pope VD, Senior CA (2005) Tropical storms: Representation and diagnosis in climate models and the impacts of climate change. Clim Dyn 25:19–36

Nolan DS, Rappin ED, Emanuel KA (2007) Tropical cyclogenesis sensitivity to environmental parameters in radiative-convective equilibrium. Quart J Meteorol Soc 133:2085–2107

Palmen E (1948) On the formation and structure of tropical cyclones. Geophysica 3:26–38

Royer JF, Chauvin F (2008) Response of tropical cyclogenesis to global warming in an IPCC AR-4 scenario assessed by a modified yearly genesis parameter. In: Elsner JB, Jagger TH (eds) Hurricanes and climate change. Springer, Berlin, Germany, pp 213–234

Royer JF, Chauvin F, Timbal B, Araspin P, Grimal D (1998) A GCM study of the impact of greenhouse gas increase on the frequency of occurrence of tropical cyclones. Clim Change 38:307–343

Ryan BF, Watterson IG, Evans JL (1992) Tropical cyclone frequencies inferred from Gray's yearly genesis parameter: Validation of GCM tropical climates. Geophys Res Lett 19:1831–1834

Saunders MA, Lea AS (2008) Large contribution of sea surface warming to recent increase in Atlantic hurricane activity. Nature 451:557–560

Solomon S, Qin D, Manning M, Chen Z, Marquis M, Averyt KB, Tignor M, Miller HL (eds) (2007) Contribution of Working Group I to the Fourth Assessment Report of the Intergovernmental Panel on Climate Change. Cambridge University Press, Cambridge/New York, pp 996

Watterson IG, Evans JL, Ryan BF (1995) Seasonal and interannual variability of tropical cyclogenesis: Diagnostics from large-scale fields. J Clim 8:3052–3066

Chapter 4
Tropical Cyclone Rainfall in the Observations, Reanalysis and ARPEGE Simulations in the North Atlantic Basin

Anne S. Daloz, Fabrice Chauvin, and Frank Roux

Abstract In this chapter, we performed a climatological study of the tropical cyclone (TC) precipitation in the satellite observations and the reanalysis from the ECMWF and NCEP/NCAR centers over the North Atlantic (NATL) basin. Using the recently developed best track IBTrACS (Kruk et al. 2009; Knapp et al. 2009) we derived the mean daily TCs rainfall within 10°×10° box around the center of the TCs, the fraction of TCs rainfall to total rainfall and the TCs precipitation efficiency (TCPE). These variables were used to assess the ability of the reanalysis to represent the impact of TCs in altering the total rainfall over the North Atlantic basin. The main results show that:

- The maximum of cyclonic precipitation is located in the Caribbean Sea and the Gulf of Mexico, for the observation and the reanalysis.
- TCs contribute to a maximum of precipitation (between 15° and 25°N) over the Southern Gulf of Mexico, the Caribbean Sea and the West Atlantic Ocean for the observation and the reanalysis.
- The most efficient TCs are located in the Gulf of Mexico, the Caribbean Sea and the West Atlantic Ocean for the observation and the reanalysis.

We used a high resolution (0.5°) stretched atmospheric global climate model (GCM) ARPEGE to simulate the present and future TCs rainfall.The tracking of TCs was realized with the method of Chauvin et al. (2006). With the present integration, we assessed the ability of ARPEGE in simulating the TCs rainfall and the fraction and the efficiency of TCs rainfall. Future simulation has also been produced to study the possible evolution of those variables. The main results for the present and future simulations over the North Atlantic basin indicate that:

A.S. Daloz (✉) and F. Chauvin
CNRM, 42 av. G. Coriolis, 31057 Toulouse Cedex 1, France
e-mail: anne-sophie.daloz@cnrm.meteo.fr; fabrice.chauvin@meteo.fr

F. Roux
OMP, 22 av. E. Belin, 31400 Toulouse, France
e-mail: frank.roux@aero.obs-mip.fr

J.B. Elsner et al. (eds.), *Hurricanes and Climate Change: Volume 2*,
DOI 10.1007/978-90-481-9510-7_4, © Springer Science+Business Media B.V. 2010

- ARPEGE detects the maxima obtained by the observations and the reanalysis for the TCs rainfall and the fraction. However, it overestimates them.
- ARPEGE obtains sparser results than the observations and the reanalysis for the efficiency of TCs, but detects the maxima over the West and East NATL Ocean.
- ARPEGE presents a sensitivity to the time period, consistent with the real variation of TCs activity.
- The difference between the future and present integration shows a decreasing contribution of the TCs rainfall and an increasing efficiency of TCs.

Keywords Tropical cyclone · Rainfall · Reanalysis · Climate model

1 Introduction

Tropical cyclones (TCs) have a great impact on the environment. Rodgers and Adler (2001) showed in the NATL basin, that precipitation associated to TCs represents a small but significant amount of the total annual rainfall. Flooding produced by the TCs rainfall can be quite destructive; they are currently the leading cause of hurricane-related fatalities in the United States (Fitzpatrick 2006). Coastal communities devastated by strong hurricanes usually take years to recover. Inland flooding associated with TCs accounted for a majority (57%) of the 600 US deaths due to hurricanes between 1970 and 1999 (Rappaport 2000).

In the North Atlantic basin, the official hurricane season begins June 1 and ends November 30, although activity has been observed outside this time frame. Due to the changes of genesis location during the hurricane season (Neumann et al. 1999), the genesis patterns in the Atlantic and the Gulf of Mexico can be divided in tree categories (Fitzpatrick 2006): early season (June 1–July 15), mid-season (July 16–September 20), and late season (September 21–November 30). In the early-season, storms mostly occur in the Western Caribbean Sea and the Gulf of Mexico. Midseason storms originate in the main basin of the tropical Atlantic Ocean even if genesis still occur in the Gulf of Mexico, but not in the majority of cases, and is virtually nonexistent in the Caribbean Sea. The mid-summer genesis lull in the Caribbean Sea is possibly due to local enhancement of trade winds mixing the ocean in the area (Inoue et al. 2008) or because conditions favorable for dynamic instability only occur in the early and late season (Molinari et al. 1997). Genesis in the tropical Atlantic Ocean peaks in the midseason. Water temperatures are warm enough to immediately impact tropical waves propagating off the African continent. The late season witnesses a quick decline in the main basin of the tropical Atlantic Ocean. However the Gulf of Mexico experiences a more gradual decline and the Caribbean Sea a revival of storm formation.

According to the Fourth Intergovernmental Panel on Climate Change (IPCC 2007), it is difficult to distinguish any man-induced long-term trend of the cyclonic activity and scenarios for a warmer climate do not converge on any trend in the intensity or number of TCs. Most recent studies assessing the associated precipitation to TCs in the NATL basin indicate that an increase may be induced by a warmer

climate (Lau et al. 2008). However, questions remain concerning the ability of the reanalysis and the global climate models (GCMs, General Circulation Models) to simulate the amount that TCs contribute to the total rainfall, how the cyclonic precipitation is distributed geographically or the precipitation efficiency of the TCs.

Rodgers and Adler (1999) first estimated monthly TC rainfall using Special Sensor Microwave Imager (SSM/I) satellite data in the Western North Pacific (WNP) Ocean. They indicated that about 7% of the rainfall to the entire domain of the WNP from June to November is due to TCs and also that TCs rainfall contribute to a maximum of 40% off the lower Baja California. They also studied the impact of El Niño on the TCs rainfall, and they noticed that in general, TCs rainfall is enhanced during El Niño years. Dedicated to the WNP basin, Ren et al. (2006) studied the TCs rainfall using stations observations in China. They showed that in most of the southeastern regions, TCs rainfall accounts for more than 20–40% of the total annual precipitation. They suggested that China has experienced decreasing TCs rainfall influence over the past 48 years, presenting downwards trends of the TCs rainfall volume, the annual frequency of torrential events and the contribution of TCs rainfall. Wu et al. (2007) confirmed the decreasing influence of the TCs rainfall using station observations in the Hainan Islands. In the WNP basin, Kubota (2009) investigate the effects of TCs on seasonal and interannual rainfall variability by using rainfall data in stations. They showed that, in some regions, TC rainfall exceed 60% of the total rainfall. They also found that the interannual variability of the TC rainfall is primarily modulated by El Niño-Southern Oscillation (ENSO). Hasegawa and Emori (2005) used a relatively high resolution (1.1°) atmospheric GCM to simulate TCs rainfall within the WNP basin under present day and doubled CO_2 climates. They found an increase in mean TCs rainfall over Japan with doubling CO_2 despite an accompanying decrease in the frequency and intensity of TCs. In the NATL basin, Rodgers and Adler (2001) showed that the contribution was around 4% for the entire basin, but regionally could reach 30% in the northeast of Puerto Rico, 15°W, 55°W and off the west coast of Africa. During warm El Niño events TCs rainfall is inhibited. Larson (2004) used gridded daily rainfall analysis based on rain gauge observations and found that landfalling TCs contribute up to 15–20% of rainfall along the US Gulf and Mexican coast on average. Moreover they noted that tropical cyclone activity was modulated on both seasonal and intraseasonal time scales by the Arctic Oscillation (AO) and El Niño. During La Niña conditions with AO positive conditions, the atmospheric circulation is more conducive to activity in the main development region. Sheperd et al. (2007) studied the contribution of tropical cyclones to extreme rainfall in four mini-basins near coastal southeastern United States using satellite precipitation dataset (TRMM). They noticed that major hurricanes produce the most extreme rainfall days, but tropical depression/storm days contribute most significantly to cumulative seasonal rainfall (8–17%) and are thus more critical to assess trends. Lau et al. (2008) conducted a study with GPCP and TRMM rainfall data on the relationship between TCs and extreme rain events in the NATL and WNP basins. Results show that climatologically, TCs contribute to 8% of rain events and 17% of total rain amount in NATL, compared to 9% of rain events and 21% of rain amount in WNP. In the NATL basin, there is a positive trend in the contribution

of TCs to extreme events. The last result is confirmed by Knight and Davis (2009) for the Southeastern United States where they studied the contribution of tropical cyclones to extreme rainfall with surface observation station. They attributed this increase to the storm wetness (precipitation per storm), the storm frequency and storm duration driven by natural decadal oscillations or by large-scale warming of the environment. Based on the TRMM database, Jiang and Zipser (2009) studied the global, seasonal and interannual variations of the monthly TCs rainfall in the six basins of tropical cyclogenesis. For the NATL basin they found that, TCs contribute 8–9%, with a maximum contribution in September and more generally during La Niña years.

The next question that should be addressed is the manner in which reanalysis and GCMs simulate the influence of the TCs to the total North Atlantic rainfall. In a first part, we focus on the study of the TCs rainfall from the satellite observation and the reanalysis. The mean daily North Atlantic TCs rainfall is determined using the recently developed best track, IBTrACS. We also established two quantitative metrics for the cyclonic rainfall associated with tropical systems; the mean precipitation distribution of the TCs and the precipitation efficiency of the TCs. The second section is dedicated to the analysis of high resolution present and future (0.5°) stretched grid experiment using the tracking method presented in Chauvin et al. (2006). The final section provides conclusion and discussions.

2 Observation and Reanalysis

2.1 Datasets and Tracking Methodology

2.1.1 Datasets

Satellite Observations

- TRMM

The Tropical Rainfall Measurement Mission (TRMM) (daily; 3B-42; 0.25° by 0.25° grid) is used to generate daily gridded precipitation data (Huffman et al. 2007). TRMM rainfall estimates are produced in four stages: (1) the microwave estimates precipitation are calibrated and combined, (2) infrared precipitation estimates are created using the calibrated microwave precipitation, (3) the microwave and IR estimates are combined, and (4) rescaling to monthly data is applied.

- GPCP

The Global Precipitation Climatology Project (GPCP) (daily; 1DD; 1° grid by 1° grid) daily precipitation is produced at the NASA Goddard Space Flight Center. They used the geo-synchronous-satellite operators to collect histograms of geo-IR brightness temperature that allowed the estimation of the precipitation. To complete

the global coverage, they estimated the precipitation outside of the geo-IR coverage using sounding data from low-earth polar satellites. The different methods employed for the construction of this dataset are detailed in Huffman et al. (2001).

Reanalysis

ECMWF (European Centre for Medium-range Weather Forecasts) – Reanalysis

- ERA-40

A 44-year integration (1958–2001) ERA-40 product (daily, 1.12° by 1.12° grid) has been developed by the ECMWF. This dataset is obtained through a global spectral model with T159L60 truncation. ERA data are freely distributed to the scientific community, but after being downgraded to a lower resolution corresponding to a T95 truncation (2.5° resolution). Analysis involves comprehensive use of satellite data, starting 1972 and later including Cloud Motion Winds will be used from 1979 onwards. More details can be found in Uppala et al. (2005).

- ERA-Interim

The ERA-Interim (daily, 1.5° by 1.5° grid) archive is more extensive than that for ERA-40. The number of pressure levels is increased from ERA-40's 23 to 37 levels, main advances are done in the data assimilation and the sets of observations acquired for ERA-40 are supplemented by data for later years from ECMWF's operational archive. Several of the problems experienced in ERA-40 have been significantly reduced in ERA-Interim such as the too-strong tropical oceanic precipitation beginning in the 1990s (Uppala et al. 2008).

NCEP (National Center for Environmental Prediction) / NCAR (National Center for Atmospheric Research – Reanalysis)

- NCEP-1

This data archive is issued by NCEP/NCAR center, covering the period from 1948 to present. NCEP-1 reanalysis (daily; 2.5° by 2.5° grid) was provided by a global spectral model with T62 truncation and 28 vertical levels (T62L28; Kalnay et al., 1996).

- NCEP-2

NCEP-2 (daily; 1.875° by 1.875° grid) is an improved version of the NCEP Reanalysis I model that fixes errors and updates parameterizations of physical processes. For a detailed explanation of the improvements see Kanamitsu et al. (2002).

2.1.2 Tracking Methodology

The NOAA National Climatic Data Center (NCDC) created a new global tropical cyclone 6-hourly best track dataset. The International Best Track Archive for

Climate Stewardship, IBTrACS is a global best track compilation dataset which contains information on all documented tropical cyclones which have been compiled and archived by many agencies from around the world. The methods used to combine the disparate datasets into a centralized repository of global TC best track data are detailed in Kruk et al. (2009) and Knapp et al. (2009).

2.2 TCs Rainfall

To assemble the mean daily TCs rainfall data, observations and reanalysis of TCs rain rates are used. Only the rain rates that are observed within a 10°×10° box around the center of TCs are sampled. This TC rain-rate sampling area is chosen to encompass the majority of the rainfall that is contributed by TCs. The radius of a TC, defined by the location and area of threshold speed, varies widely (radii between 100 and 1,100 km have been observed) and is not necessarily proportional to TC intensity. Most of the time, the precipitation shield is found to be asymmetric, but for an objective procedure we supposed that the TCs rainfall were symmetric around the center. The radius of 5° around the center has already been tested by Englehart and Douglas (2001) who showed that the distance between the center of a TC and an outer edge of its cloud shield is between 550 and 600 km for 90% of the cases. Larson (2004) also did some sensitivity tests between 2.5° and 7.5° radius and found that radii smaller than 5° necessarily exclude much of the TCs-rainfall. Centers of the sampled tropical cyclones for the time of the observations and the reanalyses comes from IBTrACS data.

The precipitation associated with TCs is seen in Fig. 1 for TRMM (left panel) and GPCP (right panel) for 1998 to 2006, in the NATL ocean. Figure 1 shows that a TCs rainfall maximum is located in the Caribbean Sea and in the South-eastern part of the Gulf of Mexico, for both datasets. TRMM shows higher values (310 mm/year) in comparison with GPCP (240 mm/year). We can see that in the Honduras Bay, GPCP clearly underestimates the local maxima detected by TRMM. TRMM and GPCP also detect three rainfall maxima in the center of the Atlantic Ocean. They

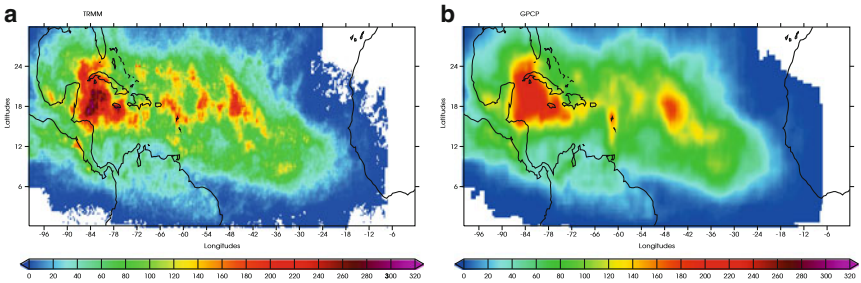

Fig. 1 A plan view showing the TRMM (**a**) and the GPCP interpoled on the TRMM grid (**b**) North Atlantic TCs rainfall (mm/year) averaged over the time period 1998–2006

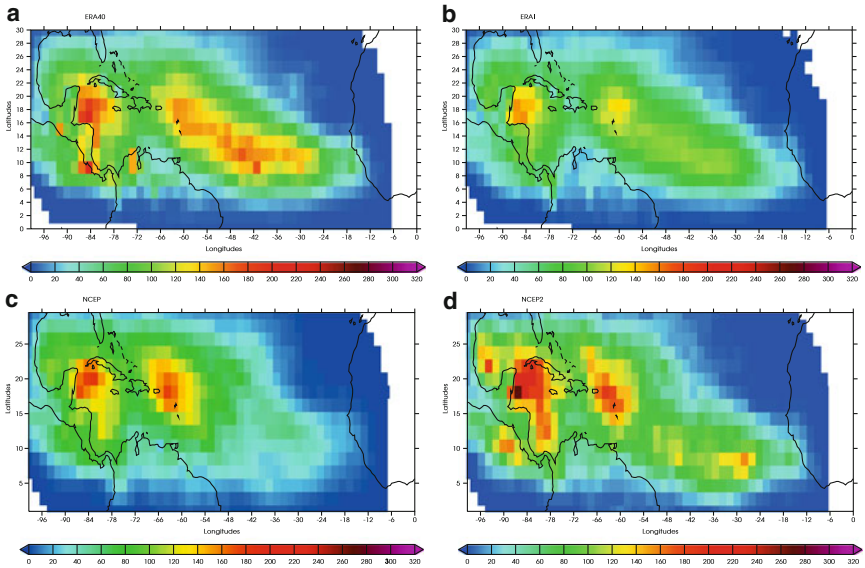

Fig. 2 A plan view showing the ERA-40 (**a**), ERA-Interim (**b**), NCEP-1 (**c**) and NCEP-2 (**d**) North Atlantic tropical cyclones precipitation (mm/year) averaged over the time period 1989–2001

are located around the latitude 18°N: on the French Antilles (64°W), at the longitudes 55°W and 46°W; attaining values between 160 and 220 mm/year. The highest values of TCs rainfall are obtained by TRMM. Differences in range of value between TRMM and GPCP must partly be due to the higher spatial resolution of the TRMM experiment.

Figure 2 presents the TCs rainfall calculated in the reanalysis from the ECMWF and NCEP/NCAR centres in the NATL Ocean. On the top left panel, we find ERA-40 and on the top right panel ERA-Interim for 1989–2001. A comparison of these two figures shows that ERA-40 TCs rainfall is globally higher than ERA-Interim, especially in the Carribean Sea and the center of the NATL basin. A reason for this difference is explained in (Uppala et al. 2008). ERA-40 has a problem in term of humidity from the 1990s. Strong discrepancies have been detected over the oceanic domains, where values are more likely influenced by the physics of the atmospheric model and the method used for the extrapolation of unmonitored locations. Few values of RH850 are lower than 0%, but numerous are higher than 100%. The maxima encountered in Fig. 1 for the satellite observations, in the Caribbean Sea, the Gulf of Mexico and the French Antilles are also detected by ERAs datasets, but with a lower range of value, around 150 mm/year for ERA-40 (Fig. 2a) and 175 mm/year for ERA-Interim (Fig. 2b). Theses differences in range of value must partly be due to the change of time period between Figs. 1 and 2 from 1998–2006 to 1989–2001 respectively. However, it still remains an underestimate of TCs rainfall from the reanalysis. The lower resolution could also impact local maxima in the center of the NATL Ocean (18°N, 55°W) obtained by TRMM and GPCP (Fig. 1) because

they are not detected by the ECMWF reanalysis. Except the eastern maxima (Fig. 1, 18°N, 46°W) not detected by TRMM, GPCP and ERAs datasets which comes from the time period from 2002 to 2006. Figure 2 also shows the TCs rainfall calculated in two datasets of the NCAR/NCEP center in the NATL Ocean. Bottom left panel shows NCEP-1 and the bottom right panel NCEP-2 for 1989–2001. The maximum encountered in Figs. 1 and 2a, b on the Caribbean Sea, the Gulf of Mexico and the French Antilles are also detected by the NCEP datasets. NCEP-1 obtains a lower range of value in comparison with TRMM and GPCP, around 175 mm/year (Fig. 2c) and NCEP-2 (Fig. 2d) attains values in between the satellite observations with 270 mm/year. Both NCEP datasets miss the local maxima situated at 18°N, 55°W. It should also be noticed that a maximum appears for NCEP-1 and especially NCEP-2 in the Bay in front of Panama and Costa Rica that is not detected by ERAs reanalysis, it could be an artifact of the NCEPs reanalysis.

Uppala et al. (2008) allows us to identify ERA interim as the more reliable dataset in comparison with ERA-40. The results from the Figs. 1 and 2 pointed out NCEP-2 with regard to NCEP-1. NCEP-2 is even closer than ERA-Interim to the results obtained by our reference TRMM in terms of amplitude and localization of TCs precipitation maxima. The differences between ERA-Interim and NCEP-2 come partly from the way of assimilating the satellite observations. NCEP-2 directly assimilates the rain rates from the instruments on the satellite TRMM, the TRMM Microwave Imager (TMI) and the Special Sensor Microwave Imager (SSM/I). On the other hand, ERA-interim only uses the data from the SSM/I instruments and they do not assimilate the rain rate but the humidity profiles obtained with the variance.

Figure 3 presents the TCs rainfall of ERA-Interim (Fig. 3a) and NCEP-2 (Fig. 3b) on the common time period from 1998 to 2006. Figure 3 confirms the good agreement between TRMM and NCEP-2 in amplitude and localization of the maxima of TCs rainfall. The amplitudes of the maxima from NCEP-2 in the North of the Caribbean Sea and the French Antilles islands is nearly the same as those obtained by TRMM (Fig. 1a). However, we should also notice that the maximum in the South of the Caribbean Sea detected by NCEP-2 and discussed in the precedent section seems to be an artifact of this dataset as we are now on the same time period, and

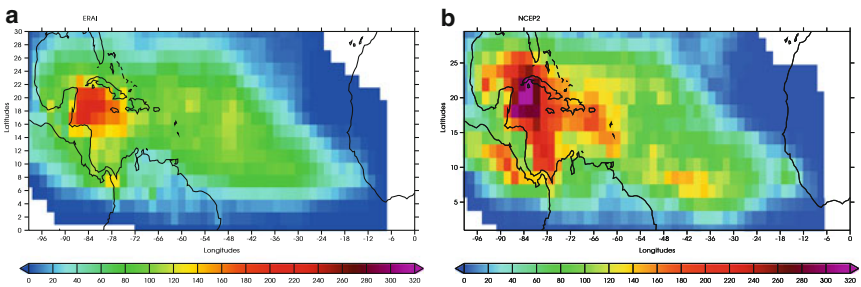

Fig. 3 A plan view showing the ERA-Interim (**a**) and NCEP-2 (**b**) North Atlantic tropical cyclones precipitation (mm/year) averaged over the time period 1998–2006

Table 1 TCs rainfall averaged over the four regions defined in Fig. 4 for the satellite observations TRMM and GPCP, and the reanalysis ERAI and NCEP2

TCs rainfall (mm/year)	NW-NATL	NE-NATL	SW-NATL	SE-NATL
TRMM	68.43	18.73	81.53	55.17
GPCP	40.51	11.76	49.02	39.85
ERAI	54.99	15.90	85.79	53.90
NCEP2	89.79	16.81	128.24	62.67

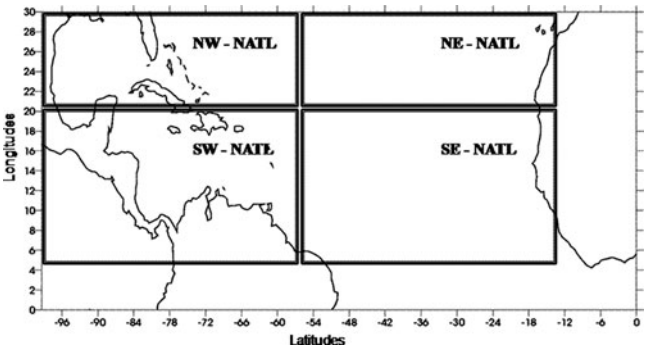

Fig. 4 A plan view showing the map of the NATL basin with *four boxes* presenting the areas of studies: NW-NATL, NE-NATL, SW-NATL and SE-NATL

this maximum is not appearing in TRMM. In order to obtain a more objective vision of the performance of GPCP, ERA-interim and NCEP-2 in comparison with TRMM, we derived the mean TCs rainfall in different regions of the NATL basin presented in Table 1. The NATL basin has been divided in four areas as presented in Fig. 4. The coordinates of the regions are

- NW (North-Western) – NATL = 96–56°W and 22–30°N
- NE (North-Eastern) – NATL = 55–15°W and 22–30°N
- SW (South-Western) – NATL = 96–56°W and 5–21°N
- SE (South-Eastern) – NATL = 55–15°W and 5–21°N

Table 1 allows us to see that for the TCs rainfall in average, ERA-Interim seems to be closer to TRMM than GPCP and NCEP-2 in the four areas of study. The bias encountered for NCEP-2 in the Caribbean Sea is visible in the Table 1 as the value of TCs rainfall in the SW-NATL zone is the highest for NCEP-2. With Figs. 1 and 3, we noticed that in term of amplitude of maxima NCEP-2 offers the closest results to TRMM, but the Table 1 showed that in term of average, ERA-Interim seems to be closer.

As we have seen with the study of the Figs. 1 to 3, GPCP, ERA-Interim and NCEP-2 underestimate, miss or create some of the TCs rainfall maxima when comparing with TRMM. We hypothesized that these biases could be related to the higher spatial resolution of TRMM. The lower resolution of GPCP and the reanalysis datasets could have an effect on the winds and on the representativeness of the

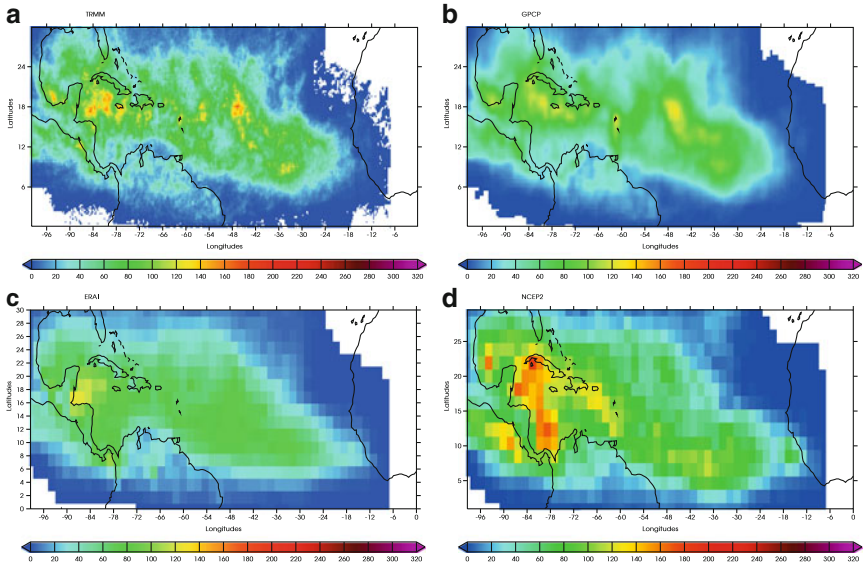

Fig. 5 A plan view showing the TRMM (**a**), GPCP (**b**), ERAI (**c**) and NCEP-2 (**d**) North Atlantic tropical cyclones precipitation (mm/year) averaged over the time period 1998–2006 for the systems from Tropical Storm to Category 2 on the Saffir–Simpson scale

different categories of TCs. Figure 5 presents the TCs rainfall associated with systems from Tropical Storms (TSs) to Category 2 of TCs for the satellite observations TRMM (Fig. 5a), GPCP (Fig. 5b), the reanalysis ERA-Interim (Fig. 5c) and NCEP-2 (Fig. 5d) for the time period 1998–2006 on the NATL basin. TRMM (Fig. 5a) shows the same maximum encountered in Fig. 1a, on the Caribbean Sea and local maximum in the center of the NATL basin (55°W and 46°W) but they attain lower values and are less spread. GPCP (Fig. 5b) presents the same maximum with an underestimate in comparison with TRMM, which is coherent with the results of Fig. 1b for the total TCs rainfall. ERA-Interim misses all the maximum obtained by TRMM and overestimates the TCs rainfall in the Honduras Bay. NCEP-2 (Fig. 5d) overestimates the maximum on the North of the Caribbean Sea and does not show those in the center of the NATL basin. NCEP-2 presents a maximum in the South of the Caribbean Sea assumed as an artifact, as it is present neither in TRMM, nor in GPCP. NCEP-2 also represents fairly well the maximum in the Main Development Region (MDR) except that it is located too West.

Figure 6 presents the precipitation from intense TCs (Category 3 to 5) for TRMM (Fig. 6a), GPCP (Fig. 6b), ERA-Interim (Fig. 6c) and NCEP-2 (Fig. 6d) from 1998 to 2006 in the NATL basin. TRMM presents a maximum of precipitation for intense TCs in the North of the Caribbean Sea with the maximum cumulated value equal to what is obtained at the same place for weak TCs (TS to Category 2). GPCP, ERA-Interim and NCEP-2 find the same maxima with nearly the same rain rate as TRMM for NCEP-2, but GPCP and ERA-Interim present an underestimate. The maxima on

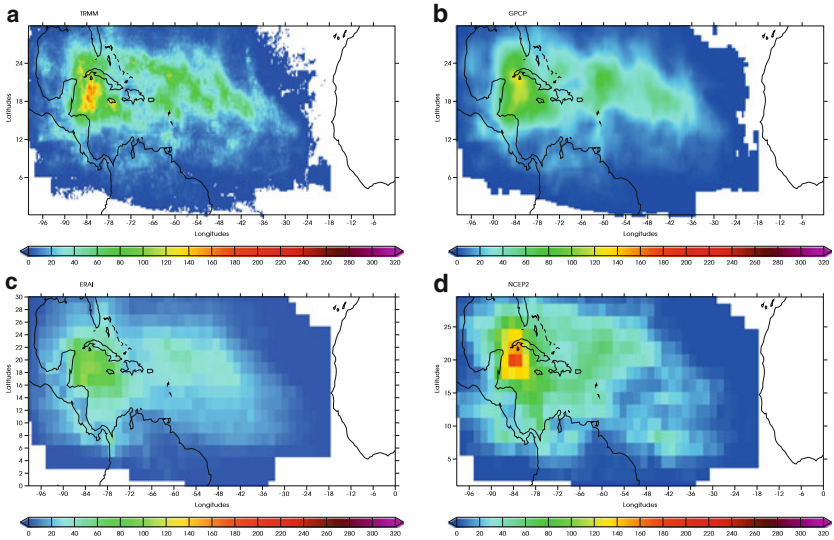

Fig. 6 A plan view showing the TRMM (**a**), GPCP (**b**), ERAI (**c**) and NCEP-2 (**d**) North Atlantic tropical cyclones precipitation (mm/year) averaged over the time period 1998–2006 for the systems from Catergory 3 to 5 on the Saffir–Simpson scale

the center of the NATL basin are nearly the same for GPCP in comparison with TRMM, however NCEP-2 and ERA-Interim missed it, except the one on the French Antilles.

Figures 1 to 6 present the tropical cyclonic precipitation in satellite observation and reanalysis. They suggest that the tropical cyclone rainfall maxima are concentrated in the subtropical latitudes from the middle NATL basin, toward the Gulf of Mexico. No TC rainfall is found off the west coast of Spain and Africa and equartorward of 5°N latitude. The regional area with the greatest tropical cyclone rainfall occurs in the Caribbean Sea and the Gulf of Mexico. Many weak and intense TCs are born and intensify in this region. Local maximum are also found in the center of the NATL Ocean. For example around the French Antilles, which is a region where many TCs recurve and momentarily intensify. We also noticed that the values of the maxima of TCs rainfall are higher for the satellite observations in comparison with the reanalysis; this is especially true for TRMM. The dissimilarities between the datasets are partly due to a difference of spatial resolution which create discrepancies in the representation of weak and intense TCs.

2.3 Fraction of TCs Rainfall

The fraction of TCs rainfall is defined as the ratio of tropical cyclone rainfall to total rainfall multiplied by one hundred. Figure 7 presents the geographical distribution of the percentage of rainfall contribution by TCs over the NATL basin for 1998–2006 for the satellite observations TRMM (Fig. 7a) and GPCP (Fig. 7b), ERA-Interim

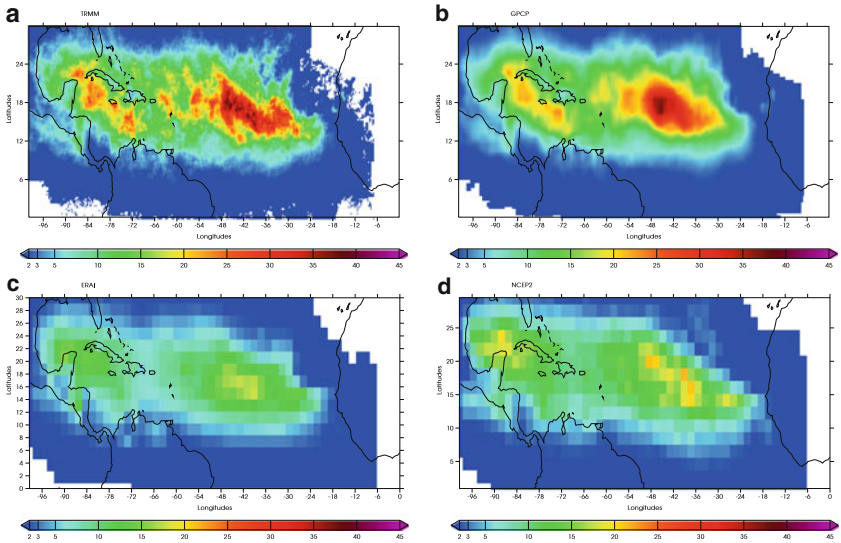

Fig. 7 Fraction of TCs rainfall (%) in the NATL basin for 1998–2006 for: TRMM (**a**), the GPCP interpoled on the TRMM grid (**b**), ERA-Interim (**c**) and NCEP2 (**d**)

(Fig. 7c) and the reanalysis NCEP-2 (Fig. 7d). In the eastern NATL Ocean (12–20°N; 56–30°W), there is a broad region where the contribution of TCs rainfall is high for TRMM (Fig. 7a), GPCP (Fig. 7b), ERA-Interim (Fig. 7c) and NCEP-2 (Fig. 7d). The satellite observations obtain values between 30% and 40%, the reanalysis between 20% and 25%. This result shows that the area where contribution of TCs rainfall is the highest (eastern NATL) is not necessarily the region of highest TCs rainfall rates (cf. Fig. 1, western NATL). In the western NATL Ocean, the contribution of TCs rainfall is not negligible as it reaches around 30% for TRMM, 20% for GPCP and NCEP-2, and 10% for ERA-Interim. The fraction is lower as others mecanims such Mesoscale Convective Systems (MCSs, Houze, 1988) contribute to the total rainfall. It should also be noticed that a large area (green in the figures) for the four datasets presents no negligible values of fraction, as it attains values around 10% of the total rainfall.

Table 2 presents the averaged fraction of TCs rainfall for the observations and the reanalysis on the four areas of study defined in Section 2.2. In average for the four regions, all the datasets underestimate the fraction of TCs rainfall from TRMM. The closer results on the four regions are obtained by NCEP-2 in comparison with TRMM even if it is underestimated; GPCP and ERA-Interim are both under NCEP-2. These results put in evidence the good results of NCEP-2 in terms of maximum and average for the fraction of TCs rainfall, that is maybe due to the way of assimilating the precipitation. Table 2 also shows that GPCP and the two reanalysis datasets obtain a too low contribution of TCs rainfall to total rainfall.

Table 2 Fraction of TCs rainfall (%) averaged over the four regions defined in Fig. 4 for the satellite observations TRMM and GPCP, and the reanalysis ERAI and NCEP-2

Fraction (%)	NW-NATL	NE-NATL	SW-NATL	SE-NATL
TRMM	7.5	3.48	8.47	10.11
GPCP	4.83	2.17	5.64	7.38
ERAI	5.07	2.04	5.81	6.60
NCEP2	6.71	2.13	6.88	7.75

2.4 Tropical Cyclonic Precipitation Efficiency – TCPE

We defined the TCs precipitation efficiency (TCPE) as the mean precipitation per day of TCs. TCPE is equal to the precipitation associated with TCs, divided by the number of days of TCs activity over each grid point in a 10° × 10° box of precipitation. The unit of this variable is mm/ TC day. Figure 8 presents the TCPE over the NATL basin averaged over the time period 1998–2006 for TRMM (Fig. 8a), GPCP (Fig. 8b), ERA-Interim (Fig. 8c) and NCEP-2 (Fig. 8d). A maximum over the Southern Gulf of Mexico and the Caribbean Sea is detected by TRMM (30 mm/TC day), GPCP (35 mm/TC day) and NCEP-2 (30 mm/TC day). TRMM also detects a maximum of TCPE in front of the West African coast (20 mm/TC day). In this area GPCP (30 mm/TC day) and NCEP-2 (36 mm/TC day) also find a maximum but they overestimate it, as it is higher and further spread. Globally, GPCP is overestimating the TCPE. NCEP-2 has a maximum in the South of the Caribbean Sea, but as we have seen with the TCs rainfall Figs. 1a and 3b, it is an artifact of the reanalysis. In the Western NATL basin, all the datasets obtain a maximum off the West African coast, but NCEP-2 (Fig. 8d) overestimates it.

Table 3 presents the TCPE for the four regions of the NATL basin described in Section 2.2 for the satellite observations and the reanalysis for the time period 1998–2006. ERA-Interim is closer to TRMM but still underestimates the Northern region and overestimates the Southern region. These results show a better agreement between ERA-Interim and TRMM than from GPCP and NCEP-2 with TRMM for the average of TCPE.

The results obtained in Figs. 1 to 8 show that in the Gulf of Mexico and the Caribbean Sea, we have a maximum of tropical cyclonic precipitation (Fig. 1 to 6) certainly due to the high efficiency of the TCs in this region (Fig. 8). However the contribution of TCs rainfall to total rainfall is not the highest in the western NATL basin (Fig. 7) even if it is not negligible as it varies between 10% and 25%. Nevertheless in this area other mechanisms are highly contributing to the total rainfall. It should be noticed that, the regions where the fraction is over 10% and the TCPE is over 10 mm/TC day are inhabited area such as the South of Florida, Cuba and the French Antilles. In the eastern part of the NATL basin, we do not find such high values of TCs rainfall (Fig. 1 to 6) and TCPE (Fig. 8) but the fraction is really elevated (Fig. 7) due to the type of precipitation in this area. The rainfall in this region

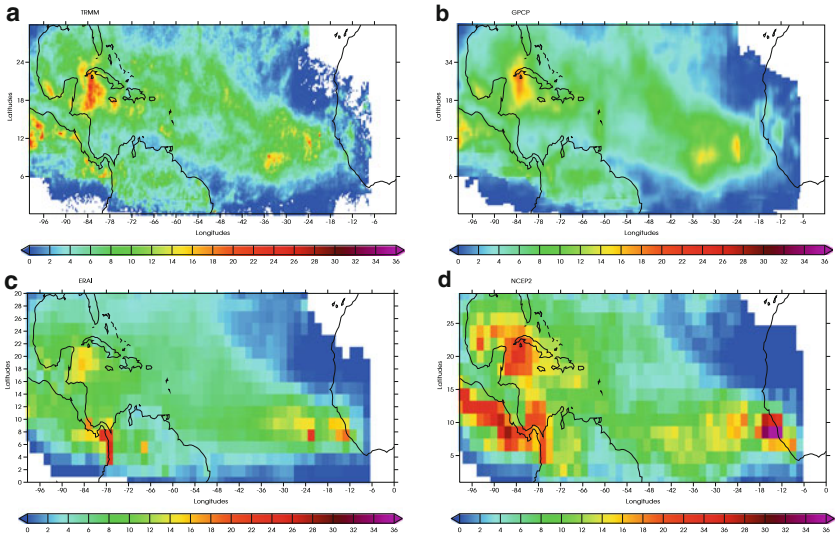

Fig. 8 Tropical cyclonic precipitation efficiency (TCPE, mm/TC day) in the NATL basin for 1998–2006 for: TRMM (**a**), the GPCP interpoled on the TRMM grid (**b**), ERA-Interim (**c**) and NCEP-2 (**d**)

Table 3 TCPE averaged over the four regions defined in Fig. 4 for the satellite observations TRMM and GPCP, and the reanalysis ERAI and NCEP2

TCPE (mm/TC day)	NW-NATL	NE-NATL	SW-NATL	SE-NATL
TRMM	6.16	12.16	5.2	8.4
GPCP	2.32	5.76	1.88	2.08
ERAI	7.48	10	8.4	12.28
NCEP2	5.6	9.52	6.04	7.52

comes in majority from the tracks of the just born TCs from the West African continent. The fraction and the TCPE have allowed us to indicate the areas where TCs are the most dangerous in term of precipitation and through the possible spot of floods. These two variables have also permitted us to test the different datasets of satellite observations and reanalysis. This characteristic can also be used to test the capability of the models to represent the tropical cyclonic precipitation.

3 Global Climate Model ARPEGE

3.1 Model Description and Tracking Methodology

3.1.1 Model Description and Experiment Design

The ARPEGE-Climate model originates from the ARPEGE/IFS (Integrated Forecast System) numerical weather prediction model developed jointly by

Meteo-France and ECMWF. It is a spectral atmospheric model with a hybrid - pressure vertical coordinate. Since the first release of the ARPEGE-Climate model (Deque et al. 1994), many developments have been included, both dynamical and physical. Here we use the third generation ARPEGE-Climat model (Deque 1999). The main difference compared to former versions is the use of a time-level semi-lagrangian numerical integration scheme with a 30 min time-step. The physical package includes the turbulence-scheme of Louis et al. (1981), the statistical cloud scheme of Ricard and Royer (1993) and the mass-flux convective scheme with Kuo-type closure of Bougeault (1985). The radiative scheme is derived from Morcrette (1990) and is activated every 3 hours. More details about the physics of the model can be found in Geleyn et al. (1995).

A rotated-stretched twentieth–twenty-first century experiment was performed using the ARP-EGE-Climat GCM (Courtier and Geleyn 1988), to represent Atlantic hurricane activity. The grid stretching technique permits distortion of the initial globally uniform grid in such a way that a maximum concentration of grid points will cover the region of interest at the expense of antipode. Once the region of interest is chosen, the grid is rotated so as to bring the pole over the center of the domain. This method has been used and validated for a long time in operational meteorological forecast (Courtier et al. 1991) and in climate modeling studies (Deque and Piedelievre 1995; Lorant and Royer 2001; Moustaoui et al. 2002). It has also been validated by Chauvin et al. (2006) for the ARPEGE integrations used in this paper. In addition, they showed that, for a spatial resolution high enough, ARPEGE is able to represent TCs structures. The stretching coefficient is 2.5 in our simulations, and the pole of the grid is located 60°W, 20°N in the Western Atlantic. Simulations for present and future climates are 30 years long with year-to-year variation of SSTs, reproducing the interannual variability of 1960–1989 observed patterns. The equivalent resolution is of approximately 50 km over the Atlantic basin and decreases linearly when going far away from the pole to reach approximately 310 km at the opposite. Another experiment was performed in the stretched configuration for the twenty-first century scenario. For the future climate, an anomaly was added to the 1960–1989 climatology. SST anomaly was taken from a Hadley Centre coupled simulation and following a SRES-A2 IPCC scenario for the GHGs (Johns et al. 2001) for 2070–2099.

3.1.2 Tracking Methodology

In order to track the tropical storms, Chauvin et al. (2006) used and updated the method developed at Mto-France by Ayrault and Joly (2000) to track mid-latitude lows for the Atlantic tropical cyclones. For the construction of the tracks, criteria from Bengtsson et al. (1995) have been introduced and the following criteria were retained:

- Mean sea level pressure (MSLP) is a local minimum (considered therefore as the center of the system)
- 850 hPa vorticity $\succ$ VT (a vorticity threshold)

- 850 hPa wind intensity ≻ WT (a wind threshold)
- Mean 700–300 hPa temperature anomaly ≻ TT (a temperature threshold)
- 300 hPa temperature anomaly ≻ 850 hPa temperature anomaly
- 850 hPa tangential wind ≻ 300 hPa tangential wind

Anomalies are defined as the difference between the system and its environment. For each criterion, a threshold is fixed and a grid point, at a given time step, must meet all conditions to be selected for a track. Choice of the thresholds was made subjectively, partly in agreement with literature and partly to compare favourably with the real world. The threshold combinations adopted, for this case, are the followings

$$\mathrm{VT} = 14.10\text{–}5\ 1/\mathrm{s},\ \mathrm{WT} = 15\ \mathrm{m/s}\ \text{and}\ \mathrm{TT} = 3°\mathrm{K}$$

The entire description of the tracking method is given in Chauvin et al. (2006).

3.2 *Present Integration*

3.2.1 TCs Rainfall

Figure 9 presents the tropical cyclonic precipitation in the NATL basin in the present integration of ARPEGE for the three decades: 1960–1969 (Fig. 9a), 1970–1979 (Fig. 9b) and 1980–1989 (Fig. 9c). The first decade (Fig. 9a) presents a maximum of TCs rainfall in the Caribbean Sea (850 mm/year) and from the South of the Gulf of Mexico (500 mm/year) to the eastern Florida peninsula. We also have some traces of

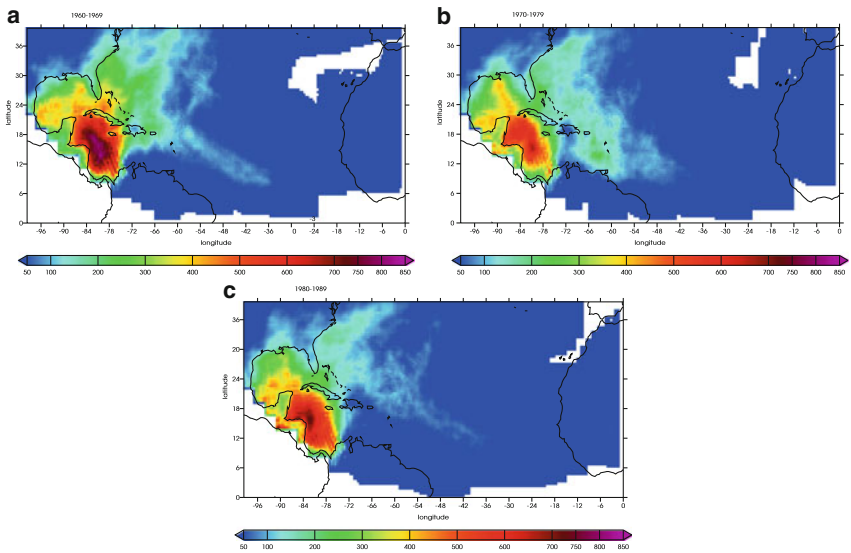

Fig. 9 TCs rainfall (mm/year) in the NATL basin in the present ARPEGE integration for the time periods:1960–1969 (**a**), 1970–1979 (**b**) and 1980–1989 (**c**)

tracks in the center of the NATL basin coming from the West African coast, but the signal is really lower (100 mm/year). The second decade (Fig. 9b) presents the same position of maximum but with a lower range of value than the first decade except for the south of the Gulf of Mexico. The maximum on the Caribbean Sea attains 600 mm/year, the eastern Florida 250 mm/year. The trace of TCs from the West African coast is less visible in this decade. For the last decade, the maximum on the Caribbean Sea obtains values between the two other decades (∼700 mm/year). In the Gulf of Mexico, the TCs rainfall give the same range of value as the two other decades. The TCs rainfall in the eastern Florida and the center of the NATL basin, as the second decade, are lower than the first decade. The results from Fig. 9 put in evidence the sensitivity of the simulated TCs rainfall to the period of study. The amplitude of the maxima in all the areas vary in function of the time period, except the Gulf of Mexico. We could also notice that the decades where ARPEGE simulates a lower activity are the real time period known for lower TCs rainfall. If we compare the results of ARPEGE, to those obtains by TRMM in Fig. 1, taking account that it is not the same period of study, we can still see that ARPEGE is highly overestimating the TCs rainfall. However the bias of the TCs rainfall of ARPEGE must also be due to the errors in the tracking of the TCs. We surely have too many tracks on the west side of the NATL basin and not enough in the east side explaining why we have so low precipitation in the center of the NATL basin.

3.2.2 Fraction of TCs Rainfall

Figure 10 presents the fraction of TCs rainfall simulated by ARPEGE in the North Atlantic Basin for the three decades: 1960–1969 (Fig. 10a), 1970–1979 (Fig. 10b) and 1980–1989 (Fig. 10c). The first decade (Fig. 10a) presents maxima over the Gulf of Mexico, the Caribbean Sea with equivalent values (∼25%) and close to the West African coast with a higher amplitude (60%). The next decades (Fig. 10b, c) show nearly the same results for the Gulf of Mexico and the Caribbean Sea. However the maxima on the West African coast nearly disappears in the second decade (1970–1979) and comes back in 1980–1989. When comparing the results of the simulation with those of TRMM, we can see that the maximum in the west of the NATL basin is broader and northern for ARPEGE. The difference on the localization can come from the sensitivity to the time period. On the eastern part of the NATL basin ARPEGE finds a maximum on two decades which is, in the satellite observation, more in the center of the ocean and broader. This maximum is highly overestimated by the model. Like in the TCs rainfall, we can assume that some of the differences between the model and the observation come from the tracking in the simulations.

3.2.3 Tropical Cyclonic Precipitation Efficiency – TCPE

Figure 11 presents the TCPE simulated by ARPEGE in the North Atlantic Basin for the three decades: 1960–1969 (Fig. 11a), 1970–1979 (Fig. 11b) and 1980–1989 (Fig. 11c). In the three panels, we nearly obtain the same amplitude (25–40 mm/TC

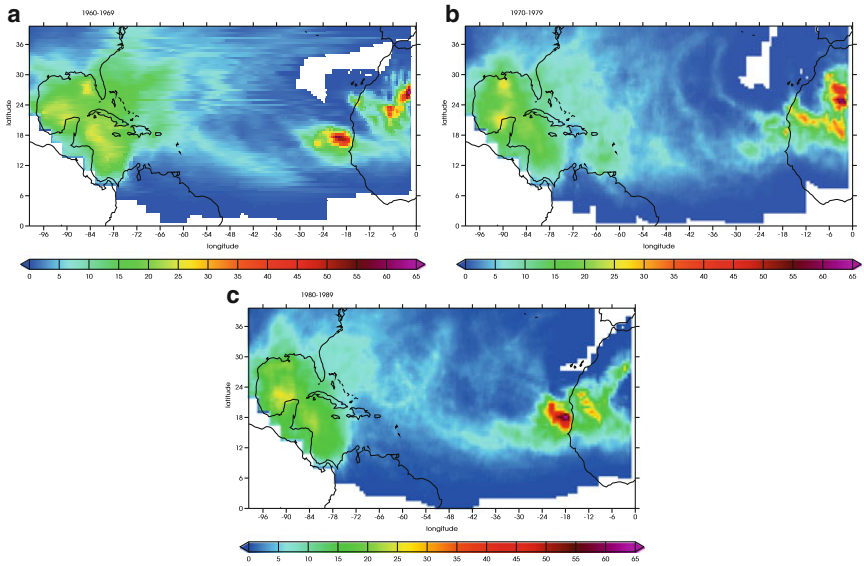

Fig. 10 Fraction (%) in the NATL basin in a present ARPEGE integration for the time periods:1960–1969 (**a**), 1970–1979 (**b**) and 1980–1989 (**c**)

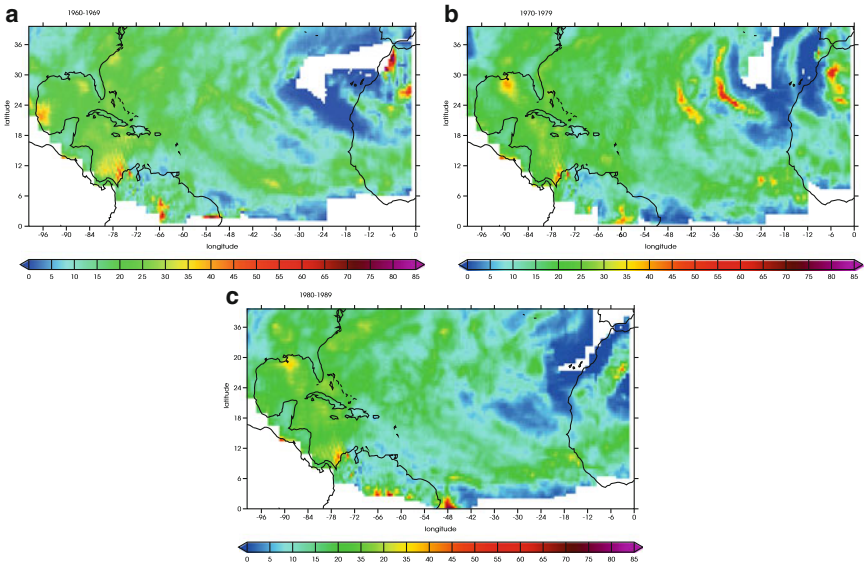

Fig. 11 TCPE (mm/TC day) in the NATL basin in a present ARPEGE integration for the time periods:1960–1969 (**a**), 1970–1979 (**b**) and 1980–1989 (**c**)

day) in the Gulf of Mexico and the Caribbean Sea. We can also notice the trace of efficient TCs in the New Orleans and Guatemala coast, regions vulnerable to TCs. For the TCPE, the sensitivity to the time period is visible especially off the West African coast. The amplitude is nearly the same in the center and the east of the NATL basin and is really close to what obtained TRMM in Fig. 1.

3.3 Future Integration

3.3.1 Fraction of TCs Rainfall

Figure 12 presents the fraction of TCs rainfall from the future integration (2060–2089) minus the present integration (1960–1989) over the NATL basin. The blue values indicate a decrease of fraction of TCs rainfall and the red, an increase. This figure shows that for this configuration of ARPEGE, the contribution of TCs rainfall is decreasing in the future in comparison with the present. But as the fraction is a ratio this decrease means a decrease of TCs rainfall or an increase in total rainfall.

3.3.2 Tropical Cyclonic Precipitation Efficiency – TCPE

Figure 13 presents the TCPE from the future integration (2060–2089) minus the present integration (1960–1989) over the NATL basin. The blue values indicate a decrease of TCPE and the red, an increase. It seems that the efficiency is slightly increasing in the future, in comparison with the present, as the red value indicate a positive difference between the two integrations.

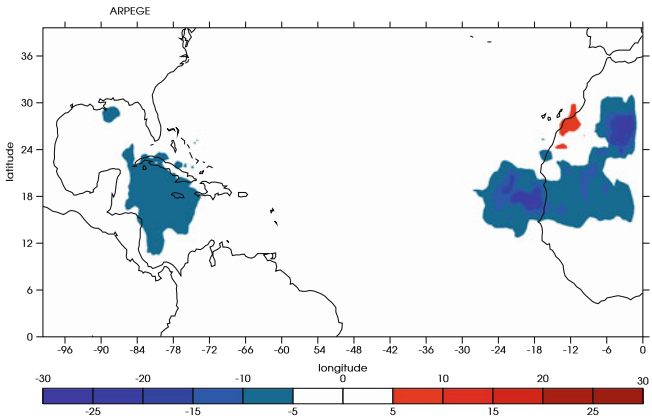

Fig. 12 Difference in fraction of TCs rainfall (%) between the future (2060–2089) and present (1960–1989) ARPEGE integration in the NATL basin

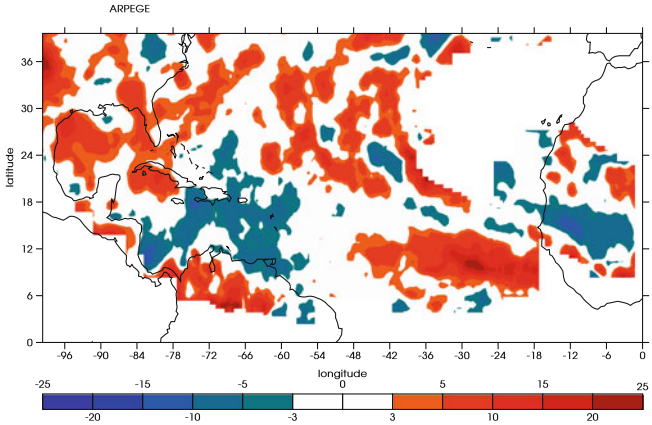

Fig. 13 Difference in TCPE (mm/TC day) between the future (2060–2089) and present (1960–1989) ARPEGE integration in the NATL basin

4 Conclusion and Discussions

The impacts of the TCs rainfall on geographical variability of the total rainfall over the NATL basin is investigated in a first part, in daily satellite observations and reanalysis. We studied TRMM and GPCP for the satellite observations, ERA-40, ERA-Interim, NCEP-1 and NCEP-2 for the reanalysis. The patterns of TRMM TCs rainfall are similar to GPCP features, but GPCP presents an underestimates in amplitude and misses some local maxima in the center of the NATL basin surely due to the lower spatial resolution of the latter. Then, we studied the ability of GPCP and the reanalysis to represent the tropical cyclonic precipitation in comparison with TRMM. It may be surprising to study the TCs rainfall from the reanalysis as we said before that the spatial resolution seems to be important for the TCs rainfall. However the time period covered by the reanalysis is not offered by the satellite observations and for the study of climate integrations, we need a longer time period, that is why we tried to validate the reanalysis. In this aim, we used a variety of metrics such as the fraction of TCs rainfall and the TCPE. We noticed the improvement with the new versions of the reanalysis from ECMWF and NCEP/NCAR centers (ERA-Interim and NCEP-2). We especially note the good representation of the TCs rainfall for NCEP-2 in comparison with TRMM, that is surely due to the way that NCEP-2 assimilates the precipitation. The maximum of cyclonic precipitation is located in the Caribbean Sea and the Gulf of Mexico, for the observation and the reanalysis. GPCP and ERA-Interim underestimate the TCs rainfall in comparison with TRMM due to an underestimate of intense TCs. TCs contribute to a maximum of precipitation (between 15° and 25°N) over the Southern Gulf of Mexico, the Caribbean sea and the West Atlantic ocean for the observation and the reanalysis.The most efficient TCs are located in the Gulf of Mexico, the Caribbean Sea and the West Atlantic Ocean for the observations and the reanalysis.

In a second part, we studied the ability of ARPEGE to simulate the TCs rainfall in present simulation. ARPEGE is able to detect the maxima of TCs rainfall, fraction of TCs rainfall and TCs efficiency obtained in the observation and reanalysis however it overestimates them in term of amplitude. The decomposition of the 30 years of integrations in decades has permitted to show the sensitivity of the model to the time period. It is interesting to notice that the two last decades present lower TCs rainfall which is consistent with the real TCs activity. This study has also allowed to see the problems in the localization of the tracks. The tracking produces too much TCs in the western NATL basin and not enough off the West African coast. Finally, we run a future simulation to see the possible evolution of the fraction of TCs rainfall and the TCPE. The difference between the future and present simulations shows an decreasing contribution of TCs rainfall to total rainfall and an increasing efficiency of TCs.

References

Ayrault F, Joly A (2000) Une nouvelle topologie des depressions meterologiques: classification des phases de maturation. compte-rendus l'acadmie des sciences, sciences de la terre et des planetes. Earth Planet Sci 330:167–172

Bengtsson L, Botzet M, Esch M (1995) Simulation of hurricane-type vortices in a general circulation model. Tellus 47A:175–196

Bougeault P (1985) A simple parameterization of the large-scale effects of cumulus convection. Mon Weather Rev 113:2108–2121

Chauvin F, Royer JF, Deque M (2006) Response of hurricane-type vortices to global warming as simulated by the arpege-climat at high resolution. Clim Dynam 27:377–399

Courtier F, Freydier C, Geleyn JF, Rochas M (1991) The arpege project at meteo-france. ECMWF seminar proceedings, reading, 9–13 Sept 1991, Volume II pp 193–221

Courtier P, Geleyn J (1988) A global numerical weather prediction model with variable resolution: application to a shallow water equation. Quart J R Meteor Soc 114:1321–1346

Deque M (1999) Documentation arpege-climat. Tech Report Centre National de Recherches Meteorologiques, Meteo-France, Toulouse, France

Deque M, Piedelievre J (1995) High resolution climate simulation over europe. Clim Dynam 11:321–339

Deque M, Dreveton C, Braun A, Cariolle D (1994) 1994. Clim Dynam 10:249–266

Englehart P, Douglas A (2001) The role of eastern north pacific tropical storms in the rainfall climatology of western mexico. Int J Clim 21:1357–1370

Fitzpatrick PJ (2006) Hurricanes, 2nd edition. ABC-CLIO

Geleyn JF, Bazile E, Bougeault P, Deque M, Ivanovici V, Joly A, Labbe L, Piedelievre J, Piriou J, Royer J (1995) Atmospheric parameterization schemes in meteo-france's arpege nwp model. Proceedings of the ECMWF seminar pareterization of sub-grid scale physical processes, 5–9 Sept 1994. ECMWF Reading, pp 385–402

Hasegawa A, Emori S (2005) Tropical cyclones and associated precipitation over the western north pacific: T106 atmospheric gcm simulation for present-day and doubled co2 climates. SOLA 1:145–148

Houze RAJ (1988) Convective and stratiform precipitation in the tropics. In: Theon JS, Fugono N (eds) Tropical rainfall measurements, A. Deepak Publishing, ISBN 0-937194-14-4, pp 27–35

Huffman G, Adler R, Morrissey M, Bolvin D, Curtis S, Joyce R, McGavock B, Susskind J (2001) Global precipitation at one-degree daily resolution from multi-satellite observations. J Hydrometeor 2:36–50

Huffman G, Adler R, Bolvin D, Gu G, Nelkin E, Bowman K, Hong Y, Stocker E, Wolff D (2007) The trmm multisatellite precipitation analysis (tmpa): quasi-global, multiyear, combined-sensor precipitation estimates at fine scales. J Hydrometeor 8:38–55

Inoue M, Handoh IC, Bigg GR (2008) Bimodal distribution of tropical cyclogenesis in teh carribean: characteristics and environment factors. J Climate 15:2897–2905

IPCC (2007) Climate change 2007: the physical science basis. In: Solomon S, Qin D, Manning M, Chen Z, Marquis M, Averyt KB, Tignor M, Miller HL (eds) Contribution of working Group I to the fourth assessment report of the intergovernmental panel on climate change. Cambridge University Press, Cambridge, United Kingdom and New York, NY, USA, pp 996

Jiang H, Zipser EJ (2009) Contribution of tropical cyclones to the global precipitation from 8 seasons of trmm data: regional, seasonal and interannual variations. J Climate. doi:10.1175/2009JCLI3303.1

Johns T, Gregory J, Ingram W, Johnson C, Jones A, Mitchell J, Roberts D, Sexton D, Stevenson D, Tett S, Woodage M (2001) Anthropogenic climate change for 1860 to 2100 simulated with the hadcm3 model under updated emission scenarios. Technical Note 22, Hadley Center p 22

Kalnay E, Kanamitsu M, Kistler R, Collins W, et al. (1996) Ncep/ncar 40 years reanalysis project. Bull Am Meteorol Soc 77:437–471

Kanamitsu M, Ebisuzaki W, Woolen J, Yang JK, Hnilo J, Fiorino M, Potter GL (2002) Ncep-doe amip-ii reanalysis (r-2). Bull Am Meteorol Soc 83:1631–1643

Knapp KR, Kruk M, Levinson DH, Gibney E (2009) Archive compiles new resource for global tropical cyclone research eos. AGU 90. doi:10.1029/2009EO060,002

Knight D, Davis R (2009) Contribution of tropical cyclones to extreme rainfall in the southeastern united states. J Geophys Res 14:D23,102. doi:10.1029/2009JD012,511

Kruk MC, Knapp K, Levinson D, Diamond H, Kossin J (2009) An overview of the international best track archive for climate stewardship (ibtracs). Twenty-first conference on climate variability and change, Phoenix, AZ, AMS

Kubota H (2009) How much do tropical cyclones affect seasonal and interannual rainfall variability over the western north pacific. J Climate 22:5495–5510

Larson J (2004) Characteristics of landfalling tropical cyclones in the united states and mexico: climatology and interannual variability. J Climate 18:1247–1262

Lau KM, Zhou Y, Wu HT (2008) Have tropical cyclones been feeding more extreme rainfall? J Geophys Res 113. doi:10.1029/2008JD009,963

Lorant V, Royer J (2001) Seensitivity of equatorial convection to horizontal resolution in aqua-planet simulations with a variable-resolution gcm. Mon Weather Rev 129:2730–2745

Louis J, Tiedtke M, Geleyn J (1981) A short history of the operational pbl-parameterization at ecmwf. In: ECMWF workshop planetary boundary layer parameterization, Nov 1981, ECMWF, Reading, UK, pp 25–27

Molinari J, Knight D, Dickinson D, Vollaro D, Skubis S (1997) Potential vorticity, easterly waves and tropical cyclogenesis. Mont Weather Rev 127:520–534

Morcrette J (1990) Impact of changes to the radiation transfer parameterizations plus cloud optical properties in the ecmwf model. Mon Weather Rev 118:847–873

Moustaoui M, Royer JF, Chauvin F (2002) African easterly wave activity in a variable resolution gcm. Clim Dynam 25:289–301

Neumann CJ, Jarvinen BR, McAdie CJ, Hammer GR (1999) Tropical cyclones of the north atlantic ocean. National Climatic Data Center, NCDC in Asheville, NC, USA, p 206

Rappaport E (2000) Loss of life in the united states associated with recent atlantic tropical cyclones. Bull Am Meteorol Soc 81:2065–2073

Ren F, Wu G, Dong W, Wang X, Wang Y, Ai W, Li W (2006) Changes in tropical cyclone precipitation over china. Geophys Res Lett 33. doi: 10.1029/2006GL027,951

Ricard J, Royer J (1993) A statistical cloud scheme for use in an agcm. Ann Geophys 11: 1095–1115

Rodgers EB, Adler F (1999) Contribution of tropical cyclones to the north pacific climatological rainfall as observed from satellites. J Appl Meteorol 39:1658–1678

Rodgers EB, Adler F (2001) Contribution of tropical cyclones to the north atlantic climatological rainfall as observed from satellites. J Appl Meteorol 40(10):1785–1800

Sheperd JM, Grundstein A, Mote TL (2007) Quantifying the contribution of tropical cyclones to extreme rainfall along coastal southeastern united states. Geophys Res Lett 34. doi: 10.1029/2007GL031,694

Uppala S, Dee D, Kobayashi S, Simmons A (2008) Evolution of reanalysis at ecmwf. In: Proceedings WCRP, Proceedings of the 3rd International Conference on Reanalysis, 28 Jan – 2 Feb 2007

Uppala SM, Kallberg PW, Simmons U A Jand Andrae, Bechtold VD, Fiorino M, Gibson JK, Haseler J, Hernandez A, Kelly GA, Li X, Onogi K, Saarinen S, Sokka N, Allan RP, Andersson E, Arpe K, Balmaseda MA, Beljaars ACM, Van De Berg L, Bidlot J, Bormann N, Caires S, Chevallier F, Dethof A, Dragosavac M, Fisher M, Fuentes M, Hagemann S, Holm E, Hoskins BJ, Isaksen L, Janssen PAEM, Jenne R, McNally AP, Mahfouf JF, Morcrette JJ, Rayner NA, Saunders RW, Simon P, Sterl A, Trenberth KE, Untch A, Vasiljevic D, Viterbo P, Woollen J (2005) The era-40 re-analysis. Q J Roy Meteorol Soc 131:2961–3012

Wu Y, Wu S, Zhai P (2007) The impact of tropical cyclones on hainan island's extreme and total precipitation. Intl J Climatol 27:1059–1064

Chapter 5
Tropical Cyclones as a Critical Phenomenon

Álvaro Corral

Abstract It has been proposed that the number of tropical cyclones as a function of the energy they release is a decreasing power-law function, up to a characteristic energy cutoff determined by the spatial size of the ocean basin in which the storm occurs. This means that no characteristic scale exists for the energy of tropical cyclones, except for the finite-size effects induced by the boundaries of the basins. This has important implications for the physics of tropical cyclones. In this chapter, we discuss up to what point tropical cyclones are related to critical phenomena (in the same way as earthquakes, rainfall, etc.), providing a consistent picture of the energy balance in the system. Moreover, this perspective allows one to visualize more clearly the effects of global warming on tropical-cyclone occurrence.

Keywords Power laws · Scaling · Self-organized criticality · Power dissipation index · Hurricanes

1 Introduction

A fundamental way to characterize a physical phenomenon is by analyzing the fluctuations of the energy it releases over successive occurrences. Of course, in most of the cases this is not a simple issue. For tropical cyclones, Bister and Emanuel (1998) have found that the dissipated energy E can be estimated by integrating the cube of the surface velocity field over space and time, by means of the formula

$$E \simeq \int \rho C_D |v(\mathbf{r}, t)|^3 d^2 r \, dt, \tag{1}$$

with ρ the surface air density, C_D the surface drag coefficient, and $v(\mathbf{r}, t)$ the surface wind velocity at position $\mathbf{r}$ and time t. It is implicit in the formula that the main contribution to dissipation comes from the atmospheric surface layer.

Á. Corral (✉)
Centre de Recerca Matemàtica, Edifici Cc, Campus Bellaterra, E-08193 Barcelona, Spain
e-mail: Acorral@crm.cat

J.B. Elsner et al. (eds.), *Hurricanes and Climate Change: Volume 2*,
DOI 10.1007/978-90-481-9510-7_5, © Springer Science+Business Media B.V. 2010

In order to obtain the distribution of energy then, one only needs to apply the previous formula to as many tropical cyclones as possible (without any selection bias) and perform the corresponding statistics. However, in practice, the available records do not allow such a detailed calculation: instead of providing a nearly instantaneous velocity field, best-track data consist of a single value of the velocity reported every 6 h (the maximum sustained surface wind velocity).

Emanuel has envisaged a way to reconcile the calculation of the energy with the limitation of the data (Emanuel 2005b). First, ρ and C_D can be approximated as constants in Eq. 1. Second, one can apply the similarity between radial profiles of velocities for different tropical cyclones to write $v(\mathbf{r}, t) = v_m(t) f(\mathbf{r}/R(t))$, where $R(t)$ is the radius of storm at time t (no matter how it is defined), $v_m(t)$ is the maximum of the velocity field for all $\mathbf{r}$ at t, and f is the function that describes the shape of the velocity profile (the same for all storms, the scale given by v_m and R). This yields a scaling between the integral over space on the one side and the maximum velocity and the radius on the other (with the same constant of proportionality), and then,

$$E \propto \int |v_m(t)|^3 R^2(t) dt,$$

where the symbol $\propto$ indicates proportionality. An additional approximation is that the radius of the storm is nearly uncorrelated with the velocity, and therefore assigning a common radius to all storms leads only to random errors in the evaluation of the energy. Finally, enlarging the integration time step up to $\Delta t = 6$ h gives

$$E \propto PDI \equiv \sum_t v_t^3 \Delta t,$$

with *PDI* defining the so-called power dissipation index, which is then a proxy for the total energy dissipated by a tropical cyclone during all its life. The symbol v_t denotes the maximum sustained surface wind velocity.

A similar definition is that of the so-called accumulated cyclone energy (*ACE*) (Bell et al. 2000; Gray et al 1992), which integrates kinetic energy over time,

$$ACE \equiv \sum_t v_t^2 \Delta t,$$

where the essential difference with the *PDI* is the replacement of the cube of the velocity by a square. Note that the time integral of the kinetic energy is not an energy, unless some proportionality factors are introduced in the formula, in the same way as in Eq. 1. In any case, in this work we will study the distribution of energy dissipated by tropical cyclones using both *PDI* and *ACE* as proxies for the energy, evaluated over the complete lifetime of the storms.

2 Power-Law Distribution of the Energy of Tropical Cyclones

In order to describe probability distributions we use the probability density function. For the case of power dissipation index this is defined as the probability that the value of this variable lies in a narrow interval of size *dPDI* around a concrete PDI, divided by $dPDI$ to make the result independent on *dPDI*, i.e.,

$$D(PDI) \equiv \frac{\text{Prob}[\, PDI - dPDI/2 \leq \text{value} < PDI + dPDI/2\,]}{dPDI},$$

where Prob denotes probability, which is evaluated as the number of events that fulfill the condition divided by the total number of events. This definition ensures normalization, $\int_0^\infty D(PDI)dPDI = 1$. Note also that the units of the density are the reciprocal of the units of the variable, so, for $D(PDI)$ these are $\mathrm{s}^2/\mathrm{m}^3$ (if the *PDI* is measured in $\mathrm{m}^3/\mathrm{s}^2$). An analogous definition applies to the probability density of the *ACE*, $D(ACE)$, or of any other variable.

Recently, we have shown that the distribution of *PDI* in different tropical-cyclone basins follows a power law,

$$D(PDI) \propto 1/PDI^{\alpha},$$

except for the largest and smallest values of *PDI*. The exponent α turns out to be close to 1 (between 1 and 1.2, roughly) (Ossó et al. 2009). Note that an exponent equal to one implies that all decades contribute in the same proportion to the total number of events, in other words, any interval of *PDI* values in which the extremes keep the same proportion contains the same probability.

The calculation of $D(PDI)$ is not direct, though. The quantity of interest, the *PDI*, varies across a broad range in the basins studied, from less than 10^9 $\mathrm{m}^3/\mathrm{s}^2$ to more that 10^{11} $\mathrm{m}^3/\mathrm{s}^2$, being necessary to plot the distribution in logarithmic scale in order to represent the different scales. Moreover, this has the advantage that on a log-log plot a power law appears as a straight line (note that this is not the case for the cumulative distribution function if the power law has an upper cutoff (Hergarten 2002).

On the other hand, the broad range of variation also makes it inappropriate to use a constant interval size *dPDI*. Essentially, *dPDI* should be large enough to contain enough statistics but small enough to provide a complete sampling of the range of variation of $D(PDI)$. Logarithmic binning is a solution to this problem (Hergarten 2002), where the size of the bins appears as constant in the logarithmic scale used. (An equivalent, simpler solution, is to work with the distribution of $\ell \equiv \ln PDI$, calculating its probability density $D(\ell)$ using standard linear binning and then obtaining the *PDI* density by means of the change of variable $D(PDI) = D(\ell)d\ell/dPDI = D(\ell)/PDI$; of course, $D(PDI)$ and $D(\ell)$ have different functional forms, despite the ambiguous notation.) Naturally, similar considerations hold for the distribution of *ACE*.

Turning back to the results of Ossó et al. (2009), it is shown that the *PDI* distribution is well described by a decreasing power law in the North Atlantic (NAtl), the Northeastern and Northwestern Pacific (EPac and WPac), and the Southern Hemisphere (SHem) basins, with an exponent α ranging from 0.98 ± 0.03 in the WPac to 1.19 ± 0.07 in the NAtl, where the uncertainty refers to one standard deviation of the maximum-likelihood-estimator mean value. The power law holds from a range of a bit more than one decade (for the NAtl and the EPac) up to two decades (for the WPac). The data used were the best tracks from NOAA's National Hurricane Center for NAtl and EPac (Jarvinen et al. 1988; National Hurricane Center 2010) and from US Navy's Joint Typhoon Warning Center for WPac and SHem (Chu et al. 2002; Joint Typhoon Warning Center 2010). Here we will use the same data sets.

As an illustration, we show in Fig. 1a the *PDI* distribution for the Northern Hemisphere (excluding the Indian Ocean, i.e., only NAtl+EPac+WPac) for the years 1986 to 2007. Tropical depressions (storms whose maximum sustained surface wind velocity does not exceed 34 knots), not included in the NAtl and EPac records, have been eliminated from our analysis of the WPac, for consistency. Of course, the results are in agreement with Ossó et al. (2009), with an exponent $\alpha = 1.07 \pm 0.06$.

If instead of the *PDI* we use the *ACE* the results do not change in essence, yielding $\alpha = 1.10 \pm 0.05$, as displayed in Fig. 1b. The reason for the coincidence of results between both variables is due to the fact that they are highly (though non-linearly) correlated. Figure 2 shows a scatter plot for the values of the *PDI* versus the *ACE*, using the same data as above. A linear regression applied to $\ln PDI$ versus $\ln ACE$ yields $PDI \propto ACE^{\gamma}$, with $\gamma \simeq 1.36$ and a correlation coefficient $\rho = 0.994$. If we write our probability distributions as $D(PDI) \propto 1/PDI^{1+\beta_p}$ and $D(ACE) \propto 1/ACE^{1+\beta_a}$, and introduce $PDI \propto ACE^{\gamma}$ in the identity relation $D(PDI) = D(ACE)dACE/dPDI$, one gets $\beta_a = \gamma\beta_p$, which implies that a power law with exponent $\alpha = 1$ (i.e., $\beta = 0$) is invariant under power-law changes of variables. These results are in good concordance with our numerical findings.

An important issue is the deviation of the distribution from the power-law behavior for small and large energies. In the first case, the deviation is due to the scarcity of data referring to small storms. The best tracks of the National Hurricane Center (for NAtl and EPac) do not contain tropical depressions, so the data are truncated including only hurricanes (of category 1 at least) and tropical storms (maximum sustained surface wind velocity larger than 34 knots but below hurricane category). In the case of the best tracks of the Joint Typhoon Warning Center some tropical depressions are included, but these are very few, only those ones which are consider "significant". This artificial truncation of the data obviously makes the distribution depart from the power-law behavior for small values of the energy. The paths of the tropical cyclones of a small part of the record, just for the 5 year period 2003–2007, are shown in Fig. 3, separated in distinct *PDI* ranges; the top panel shows how the set of storms with $PDI < 10^9\ \mathrm{m}^3/\mathrm{s}^2$ seems certainly incomplete.

More fundamental is a decay faster than power law for large values of the energy. We suggest in Ossó et al. (2009) that this is due to a finite size effect: the spatial size of the basin is not big enough to sustain tropical cyclones with larger *PDI* values (remember that the *PDI* integrates v_t^3 over time, and time can be considered equivalent

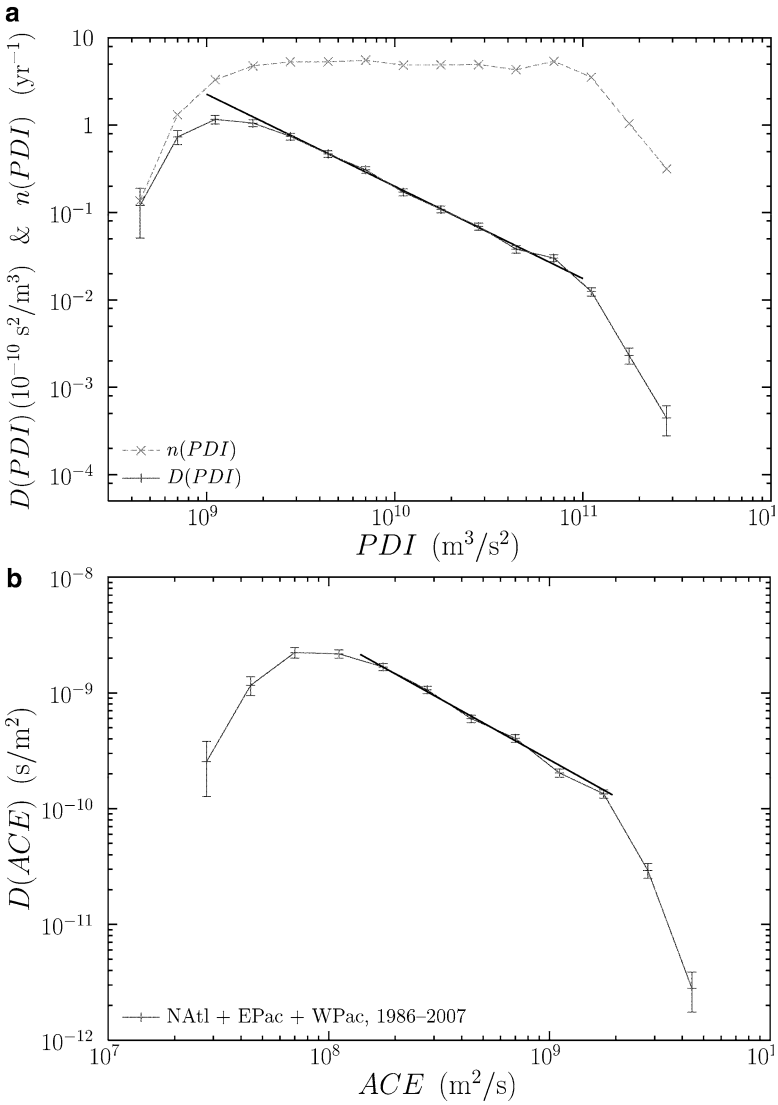

Fig. 1 Probability density of tropical-cyclone dissipated energy, for the NAtl, EPac, and WPac basins, during 1986–2007, compressing 1,212 storms. (**a**) *PDI* probability density, $D(PDI)$, together with the number of tropical cyclones in each bin per year $n(PDI)$. A maximum-likelihood fit of the distribution between the values $3.2 \cdot 10^9$ and $4.0 \cdot 10^{10}$ $\mathrm{m}^3/\mathrm{s}^2$ yields $\alpha = 1.07 \pm 0.06$ with a $p-$value $= 99 \pm 0.3\%$ (calculated generalizing the method of Clauset et al. (2009), with a resolution in the optimization of 10 points per decade). (**b**) *ACE* probability density. A maximum-likelihood fit between the values $1.6 \cdot 10^8$ and $2.0 \cdot 10^9$ m^2/s yields $\alpha = 1.10 \pm 0.05$ with a p-value $= 59 \pm 1.6\%$

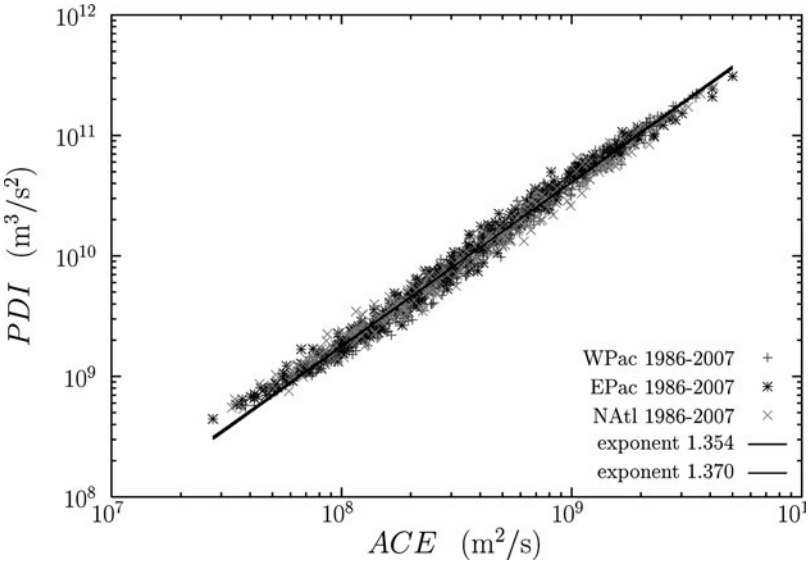

Fig. 2 Non-linear correlation between *PDI* and *ACE*. The former variable is plotted versus the latter for all hurricanes, typhoons, and tropical storms occurring in the NAtl, EPac, and WPac for the period 1986–2007. A power-law correlation $PDI \propto ACE^{1.36}$ shows up, with a corresponding linear correlation coefficient (for the logarithm of the variables) $\rho = 0.994$. The two regression lines are included, although they overlap

to space). Indeed, when a tropical cyclone in any of the basins considered reaches a *PDI* of about 10^{11} m^3/s^2 it is very likely that its evolution is affected by the boundaries of the basin, which are constituted essentially either by continental land or by a colder environment; this deprives the tropical cyclone from its source of energy in the form of warm water and provokes its attenuation and eventual death, see Fig. 3, bottom panel. Under the name "colder environment" we can compress both a low sea surface temperature (as it happens in high latitudes or with the cold California Current) or the presence of extratropical weather systems. In any case, this makes the boundaries of the basin be not fully "rigid" in contrast to condensed matter physics (even for the case of continental boundaries, there have been hurricanes that have jumped from the NAtl to the EPac).

Another relevant issue to take into account is up to what point the power law is the right distribution to fit the *PDI* and *ACE* distributions. We have shown in Ossó et al. (2009) that the power law provides indeed a good fit, but this does not exclude that other distributions can fit the data equally well, or even better. In fact, any power law in a finite domain (let us say, with the variable x in between m_1 and m_2) can be fit also by a lognormal distribution, with a σ-parameter (the standard deviation of the underlying normal distribution) which tends to infinity. Indeed, the lognormal probability density,

$$D(x) \propto \frac{1}{x} \exp\left(-\frac{(\ln x - \mu)^2}{2\sigma^2}\right),$$

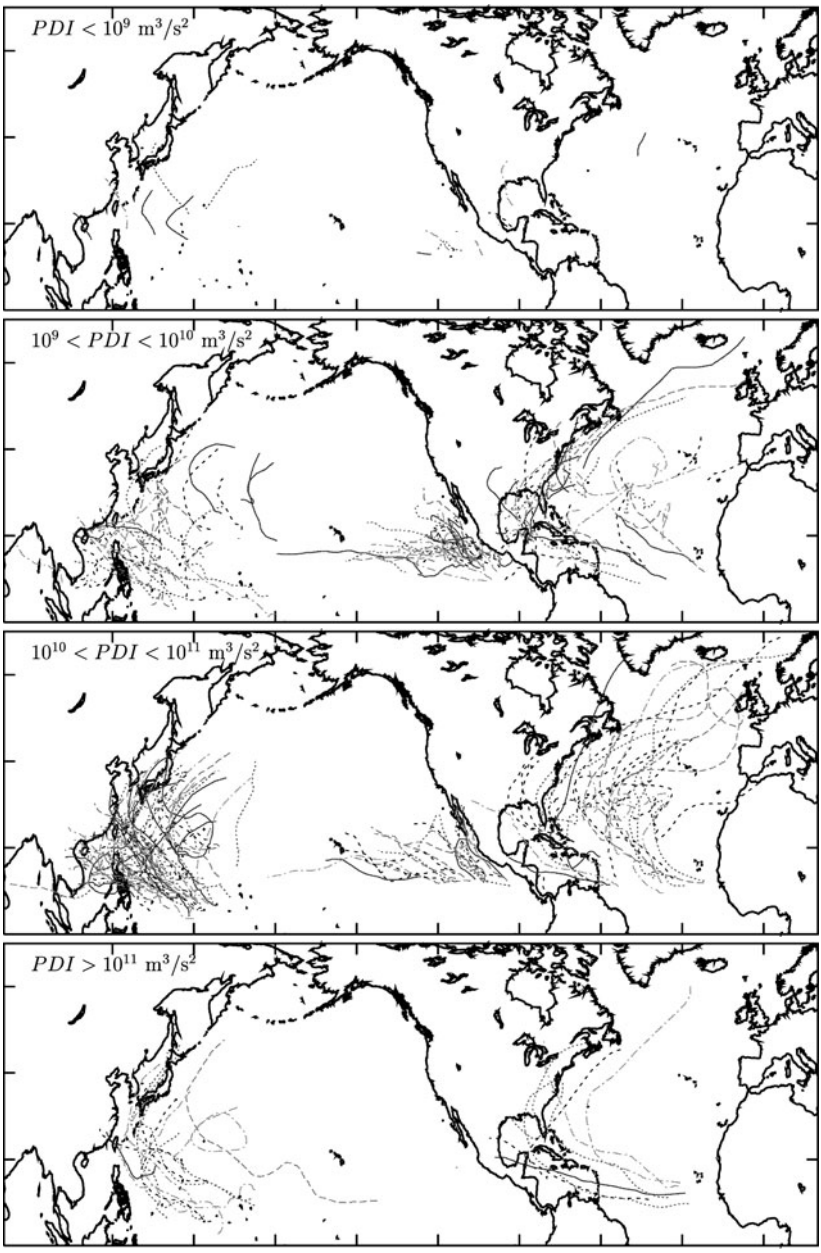

Fig. 3 Trajectories of hurricanes, typhoons, and tropical storms (i.e., excluding tropical depressions) in the WPac, EPac, and NAtl, separated for different values of the *PDI*. Different line styles correspond to different years, from 2003 to 2007. The *top panel* points to the incompleteness of the record for the smallest *PDI* values, whereas the *bottom panel* shows that the tropical cyclones with the largest *PDI* values tend to travel through the whole basin

can be written as

$$D(x) \propto \left(\frac{e^{\mu}}{x}\right)^{1+(\ln x-\mu)/(2\sigma^2)}.$$

This is a kind of pseudo-power-law, with a pseudo-exponent $1 + (\ln x - \mu)/(2\sigma^2)$ that changes very slowly with x if σ is big enough. Taking $m_1 \equiv e^{\mu+2\sigma^2\varepsilon_1}$ and $m_2 \equiv e^{\mu+2\sigma^2\varepsilon_2}$, the pseudo-exponent changes from $1 + \varepsilon_1$ for $x = m_1$ to $1 + \varepsilon_2$ for $x = m_2$, and the extreme values m_1 and m_2 can be as large as desired if σ is big enough. Note, anyhow, that the lognormal distribution has two parameters (μ and σ), whereas the power law has just one (α). A similar argument can be presented for other long-tailed distributions. In conclusion, the choice of the right fit is a problem that cannot be solved only by means of the statistical analysis, and the physical knowledge provides a criterion to select the most appropriate distribution. The rest of this work will justify the preferability of the power law as a physical model of tropical-cyclone dissipation distribution.

3 Power-Law Distribution of Earthquake Energies

The power-law distribution of energy dissipation in tropical cyclones is analogous to the well known Gutenberg–Richter law of earthquakes. This law states that, for a given spatial region and over a certain period of time, the number of earthquakes with magnitude larger than M is about 10 times greater than the number of earthquakes with magnitude larger than $M + 1$, which in its turn is 10 times greater than the number of earthquakes larger than $M + 2$ and so on (Kanamori and Brodsky 2004). In mathematical terms, the number of earthquakes above M, denoted by $N(M)$, is a decreasing exponential function,

$$N(M) \propto 10^{-bM}$$

where the b-value is a parameter close to 1.

The cumulative distribution function of magnitudes, defined as $S(M) \equiv$ Prob[magnitude value $\geq$M] is estimated directly from $N(M)$ as $S(M) = N(M)/\mathcal{N}$, where $\mathcal{N}$ is the total number of earthquakes considered, of any magnitude. It is obvious that the cumulative distribution is exponential, and therefore the density, given as $D(M) = -dS(M)/dM$, is an exponential too, with the same $b-$value. (This allows that, when working with magnitude distributions, one does not need to specify if one is measuring the density or the cumulative distribution. Of course, this is only acceptable for exponential distributions).

However, magnitude is not a physical variable, as it is a unitless variable. It is believed, at least as a first approximation, that the energy E radiated in an earthquake is an exponential function of the magnitude, $E \propto 10^{3M/2}$ (with a proportionality factor between 10^3 and 10^5 J) (Kanamori and Brodsky 2004). Therefore, the energy probability density will be a power law,

$$D(E) = D(M)dM/dE \propto D(M)/E \propto 1/E^{1+2b/3}.$$

Note that, as in the case of tropical cyclones, we have used the same symbol for the density of energies and for the density of the logarithm, although the functional form of each one is not the same (power law versus exponential, respectively).

Summarizing, although the Gutenberg–Richter law implies an exponential distribution of the magnitudes of earthquakes, in terms of the radiated energy the Gutenberg–Richter law is given by a power law. Then the fundamental difference in the structure of energy release between earthquakes and tropical cyclones is only quantitative and not qualitative, as both phenomena follow power-law distributions of energy with $\alpha \simeq 1.7$ in the first case and $\alpha \simeq 1.1$ for tropical cyclones. Another difference is the deviation from the power-law behavior at the largest values of the energy in tropical cyclones; in the case of earthquakes the existence or not of this boundary effect is not clear (Kagan 2006; Main et al. 2008).

In fact, many other complex phenomena in the geosciences yield power-law distributions of energies, or, broadly speaking, "sizes". These phenomena include, in addition to earthquakes and tropical cyclones: rainfall (Peters et al. 2002), landslides and rock avalanches (Malamud 2004; Frette et al. 1996), forest fires (Malamud et al. 1998), volcanic eruptions (Lahaie and Grasso 1998), solar flares (Arcangelis et al. 2006; Baiesi et al. 2006), the activity of the magnetosphere (Wanliss and Weygand 2007), tsunamis (Burroughs and Tebbens 2005), and perhaps meteorite impacts (Chapman and Morrison 1989). Nevertheless, the power laws are not totally ubiquitous, see for instance Corral et al. (2008).

4 Relevance and Mechanisms for Power-Law Distributions

What are the implications of having a power-law distribution, as it happens for the released energy of tropical cyclones, earthquakes and other phenomena just mentioned? In general, power-law distributions denote the presence of three main characteristics:

- Divergence of the mean value of the variable
- Absence of a characteristic scale
- Possible connection with criticality

Here we explain each one.

4.1 Divergence of the Mean Value

Regarding the first issue, it is obvious that, if we consider the mean energy value, this fulfills $\langle E \rangle \equiv \int_m^\infty ED(E)dE = \infty$, if the power law exponent α is smaller than 2 (but larger than 1 for normalization), with m the minimum value of the energy. Note

that this is a property which is neither a characteristic of all power laws nor exclusive of some power laws (there are many other distributions which show this divergence, for instance, $D(E) \propto E^{-\alpha} \cos^2 E$).

Obviously, from a physical point of view, the mean energy dissipated by a phenomenon as earthquakes or hurricanes cannot be infinite (the Earth has a finite energy content) and therefore the power-law behavior cannot be extrapolated to infinity. But if we do not know up to which maximum energy value the power law holds (which seems to be the case of earthquakes, but not that of tropical cyclones), the mean value of the energy is not defined and its calculation from any data set does not converge. What happens is that the scarce extreme events dominate the calculation of the average, as when they occur their contribution to the mean value is large enough to alter significantly this mean value. So, the fluctuations are the most significant trend of the energy, and not the mean value. In the case of tropical cyclones, we can only say that if it were not for the finite-size effects imposed by the boundaries of the basins, the mean released energy could not be calculated.

4.2 Lack of Characteristic Scale

In contrast to the first one, the second property, the absence of any characteristic scale for the energy release, is an exclusive property of power laws (Christensen and Moloney 2005). It is possible to show that a power-law function $g(x) \propto 1/x^\alpha$ (with $-\infty < \alpha < \infty$) is the only solution to the scale-invariance condition: $g(x) = c g(x/a)$, $\forall x, \forall a$, where it turns out then that c has to be related to a by $c = 1/a^\alpha$ (alternatively, fixing the relation between a and c determines the value of the exponent α). This condition means that it does not matter in which scale we look at the variable x, we will see the same shape for the function $g(x)$. For example, let us take $a = 1,000$, then, when we write x/a we are looking at x at a scale that is three orders of magnitude smaller than the original one (we go from the scale of kilo-Joules to Joules, let us say). If we take $c = 0.01$, which means that we are performing another linear transformation in the $y-$axis, we find that the corresponding scale-invariant function is $g(x) \propto 1/\sqrt[3]{x^2}$, indeed, $\alpha = -\log c/\log a = 2/3$. Another example is given in Fig. 4.

Nevertheless, there is a "little" problem regarding scale invariance of probability distributions: a function of the kind $g(x) \propto 1/x^\alpha$ cannot be a probability density for all x, even for just $x > 0$, as $\int_0^\infty g(x)dx = \infty$, for all α. In practice, it is necessary a small-energy cutoff m if $\alpha \geq 1$ or a large-energy cutoff if $\alpha \leq 1$, so, the scale invariance only can exist for a range of x and a, and not for all of them.

4.3 Criticality

One has to recognize that scale invariance is a rather strange property. How can it be that the relative proportion of the value of a physical observable at two different values of its variable, $g(x)/g(x/a)$, is the same $(=c)$ at the milli-scale and at the

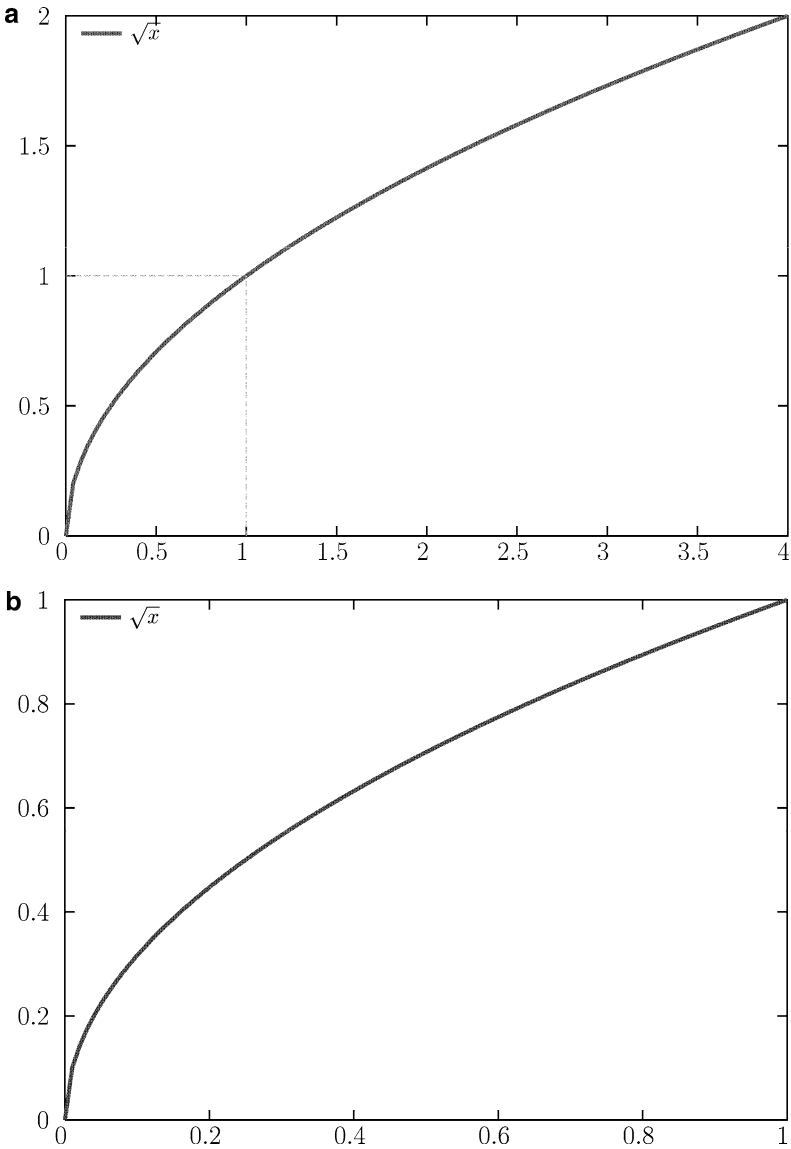

Fig. 4 Illustration of the scale invariance of power laws. A power-law function with $\alpha = -0.5$ looks exactly the same at two different scales. The *box* in the *top panel* (**a**) is enlarged in the bottom one (**b**), the scale factors of the scale transformation are $a = 4$ and $c = 1/a^{\alpha} = 2$

Mega-scale (i.e., independent on x) if the values x and x/a take a constant proportion (a)? This means that the study of the function g does not allow us to distinguish the scale of observation (in order words, g cannot be used as an x-meter). It seems obvious that the same physics has to operate at very different scales.

In order to elucidate how scale invariance in energy distributions is achieved we need a model of the energy release. Once again we use earthquakes as an example. Earthquake energy is released in tectonic faults in an avalanche-like process. The picture can be summarized as follows: stress in the Earth crust displays very small changes. At some point the static friction cannot sustain a small variation in stress and a slip takes place. This local slip increases the stress in the neighboring area, where more slip can be induced in this way, and so on.

A very simple model of this process is given by a chain of dominoes. The slip at a fault patch is represented by the toppling of one piece. A sequence of topplings until the end of the activity constitutes an avalanche that represents an earthquake (or other phenomenon). The energy released in the process will be proportional to the number of topplings, which is called the avalanche size. In the usual game, the toppling of one piece induces the toppling of the next and so on. This is the so-called *domino effect* and yields toppling events (avalanches) whose size is equal to the size of the system (the number of topplings equals the total number pieces). We arrive then to the so-called characteristic-earthquake model. But this is not what the data tells us, as the Gutenberg–Richter law shows that there should be avalanches of all sizes, with no characteristic scale.

We need to modify the domino model. Instead of having that one toppling always induces just one toppling, let us consider that one toppling induces one toppling, or none, or may be two, or three, etc. That is, we have a random number of topplings, with the probability of the number of induced topplings given by the same probability distribution for all pieces. For this purpose it is convenient to imagine not a one-dimensional domino chain but an array of pieces. Mathematically, this is just an image of a simple *branching process*, introduced in science to describe in the first place the growth and extinction of populations.

The outcome of a branching process depends on the so-called branching ratio B, which is the average number of topplings induced directly by a single toppling (from one time step to the next) (Harris 1989; Sornette 2004). It is clear that if $B > 1$ the process will have a tendency to grow exponentially, giving rise to a system-spanning avalanche (although there is also a finite probability that the chain of topplings dies spontaneously). In contrast, if $B < 1$, the activity attenuates fast, on average, and the size of the avalanches is small. However, if B is precisely equal to one (with a standard deviation different than zero) these two tendencies compensate, and then we loose any characteristic scale in the size of the avalanches: they are power-law distributed, the concrete shape of the density being $D(s) \propto 1/s^{3/2}$, with s the size of the avalanche (proportional to the energy). This case is called a *critical branching process*.

So, in principle, we have arrived at a reasonable model to generate power-law distributions by adjusting the branching ratio to be equal to one. The next question in order to give an explanation of these phenomena is of course how the fine tuning of the branching ratio is achieved in nature. An answer is given by the idea of *self-organized criticality* proposed by Bak et al. in the 80s (Bak 1996; Jensen 1998). The basic idea is the existence of a feedback mechanism that keeps the branching ratio close to one. If it is larger than one this produces large avalanches and in this case

the branching ratio is reduced (the distance between the domino pieces is increased somehow); if the branching ratio is small, the avalanches are small, and then the branching ratio is increased (Zapperi et al. 1995).

The idea is better illustrated substituting the toppling of domino pieces by the toppling of grains in a sandpile (Bak et al. 1987; Christensen et al. 1996). The advantage of the sandpile is that after a large avalanche (which usually happens for high B), many grains leave the pile through its open boundaries (the pile is built over a finite support) and this decreases the average slope of the pile, making more difficult the toppling of the remaining grains and reducing then the branching ratio. On the contrary, when small avalanches predominate (low B) the grains do not reach the boundaries of the pile, and a subsequent slow addition of more grains increases the slope and also the branching ratio (as the toppling of the grains is facilitated by a steeper pile).

The ideal sandpile is a particular realization of one kind of system called *slowly driven, interaction-dominated threshold systems* (Jensen 1998). The three main ingredients are, as the name denotes: a slow energy input, an intermediate energy storage caused by local thresholds, and sudden bursty energy releases that spread through the system (Peters and Christensen 2006). The energy input comes from the slow addition of grains and the energy storage is in the form of potential energy of the metastable configurations of the grains, which are possible thanks to the thresholds built by the static friction between grains. When the input of grains causes one of the thresholds to be overpassed, some grains start to move. This helps other grains to overpass their thresholds, giving rise (or not) to an energy release in the form of an avalanche.

Earthquakes also fulfill this picture. In this case the slow energy input comes from the relative motion of the tectonic plates. This energy is stored in the form of stress in the faults, due again to the thresholds provided by static friction. When an increase in stress cannot be sustained by friction, energy is released and redistributed in the system, triggering an avalanche of slips, i.e, an earthquake.

Among the geophysical phenomena mentioned at the end of Section 3 as displaying power-law statistics in their energy release, most of them (rainfall, landslides, rock avalanches, forest fires, volcanic eruptions, magnetosphere activity, and solar flares) can be understood as self-organized critical systems (see Table 1). Perhaps, the only exceptions are tsunamis, which are not slowly driven (but driven by earthquakes, landslides, etc.), and maybe meteorites. In the next section we will discuss if the evolution of tropical cyclones can be understood in these terms.

5 Criticality of Tropical Cyclones

Previously we have shown that the energy dissipated by tropical cyclones follows a power-law distribution. As other catastrophic phenomena also show this behavior, and as some of these other complex phenomena can be accommodated to the

Table 1 Self-organized critical characteristics of diverse phenomena. All systems receive a slow driving of energy which is stored thanks to local thresholds; eventually, a sudden release of energy spreads through the system

	Sandpile	Earthquakes	Rainfall	Tropical cyclones
Driving	Addition of grains	Motion of tectonic plates	Solar radiation	Solar radiation
Storage of energy	Gravitational potential energy	Elastic potential energy	Water in atmosphere	Heat of the sea
Threshold	Friction	Friction	Saturation	Sea surface temperature[a]
Spread of energy	Toppling of grains	Release of stress	Nucleation of drops	Wind

[a]Plus an external trigger.

perspective of self-organized criticality, it is natural to investigate the possible connections between self-organized criticality and tropical cyclones.

In principle, we can guarantee that the broad requirements of self-organized criticality are fulfilled in tropical cyclones. Indeed, the tropical sea surface stores enormous quantities of energy in the form of warm water. Naturally, this energy is slowly supplied to the sea by solar radiation. Moreover, a certain amount of stored energy is necessary previous to its release by a tropical cyclone, as if the sea surface temperature is below about 26°C these storms cannot develop (Gray 2000). However, when the tropical cyclone is at work, the release of energy is very rapid (even more rapid compared with the slow heating of the sea by the sun). This release is facilitated by the strong winds, which increase the evaporation of water from the sea and then also the release of energy, which in turn increase the strength of the winds. This is in some sense analogous to the chain-reaction nature of avalanches, in which part of the released energy is invested in facilitating further release. It is important to stress that tropical cyclones liberate vast amounts of heat from the tropical oceans; Emanuel estimates that quantity in more than 10^{22} Joules every year (Emanuel 2008). Table 1 illustrates the energy flow of tropical cyclones comparing it with that of some well-known self-organized critical phenomena.

Nevertheless, there are also differences between tropical cyclones and earthquakes or sandpiles. In the latter cases, the release of energy spreads through the system in all possible directions, in principle. In contrast, a tropical cyclone attains a characteristic radius and moves in an irregular but close to one-dimensional path, carried by the predominant large-scale winds. Another difference is that favorable conditions, i.e., more than enough energy content in the sea, is not a sufficient condition for these storms to develop. As the experts know, some kind of perturbation is needed to trigger the genesis process, by means of easterly waves for example (Emanuel 2005a). So, some kind of overheating or supercriticality seems to be present in the process. Curiously, recent research seems to indicate that most earthquakes do not occur "spontaneously" by the slow increase of the tectonic stress, rather, they are triggered by the passing of seismic waves (Elst and Brodsky 2010).

6 Tropical Cyclone Energy and Climate Change

The relationship between global warming and tropical cyclones constitutes a very complex issue. In recent years, many works have investigated the response of tropical cyclones to increased sea surface temperature and other changing climate indicators (Emanuel 2005b; Goldenberg et al. 2001; Trenberth 2005; Landsea 2005; Webster et al. 2005; Chan 2006; Klotzbach 2006; Shepherd and Knutson 2007; Kossin et al. 2007; Elsner et al. 2008; Gray 2006; Landsea et al. 2006; Landsea 2007; Aberson 2009; Elsner and Jagger 2009). Most of these studies use measures that involve the change in the annual number of tropical cyclones, as for instance the *PDI* defined originally by Emanuel (2005b). In contrast, the individual-cyclone *PDI* probability distribution (introduced in the previous sections) is independent on the number of cyclones, and allows the comparison of the characteristics of single events in different years (Ossó et al. 2009). This has the advantage of avoiding the frequency of storms, which is underestimated in old records.

But what can one expect from the response of a self-organized critical system under a change in external conditions? This kind of system is supposed to show a robust behavior. After all, the critical point is an attractor of the dynamics, which means that perturbations in the parameters that define the system are usually not relevant. So the power-law behavior should hold independently of the changing of climatic conditions.

That was indeed the result of Ossó et al. (2009), where it was shown that $D(PDI) \propto 1/PDI^{\alpha}$, both for periods of high or low tropical-cyclone activity or for periods of high or low sea surface temperature (in the NAtl and EPac). Does this mean that changing climate does not alter the distribution of the energy released by tropical cyclones? Not at all: although the power-law exponent α does not change (under the statistical uncertainties) the high$-PDI$ tail of the distribution does change. Let us approximate the distribution by means of the following formula,

$$D(PDI) \propto \frac{\exp(-PDI/a)}{PDI^{\alpha}},$$

which covers both the power-law behavior for $PDI \ll a$ and the faster high$-PDI$ decrease, modeled here by an exponential, for $PDI \gg a$. The parameter a, called the cutoff, separates then both behaviors. A normalization constant, hidden under the proportionality symbol, also depends on a, but this dependence is not important in our argument.

The effect of an increase in sea surface temperature is just an increase in the value of a, so,the transition from power-law behavior to exponential decay occurs at a larger *PDI* value (given by a). In other words, the *PDI* values are shifted by a scale factor equal to the ratio of increase of a. As a denotes the value of the *PDI* for which tropical cyclones are affected by the boundaries of the basin, we can understand the increase in a as an enlargement of the effective size of the basin. This is not surprising, as higher sea surface temperature implies that the part of the ocean over which tropical cyclones can develop is larger.

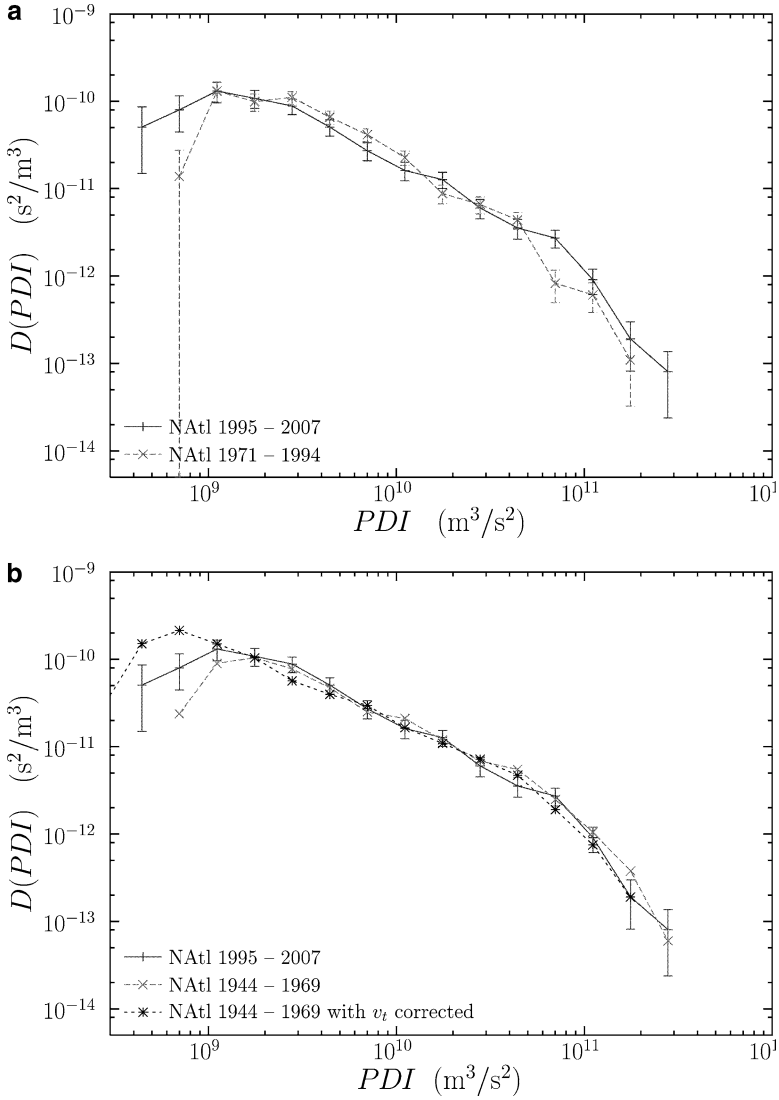

Fig. 5 Probability density of tropical-cyclone *PDI* for time periods with different levels of activity. (**a**) The comparison between 1971–1994 and 1995–2007 shows that in the latter period larger PDI values are possible. (**b**) In contrast, the period 1944–1969 shows no significant differences with 1995–2007. Even, a correction of the velocities of the former period (subtracting 4 m/s (Landsea 1993) does not change noticeably the results

Figure 5a shows the *PDI* distributions in the North Atlantic for the years 1971–1994 and 1995–2007. The first period corresponds predominantly to relatively low sea surface temperatures, whereas in the second period the temperatures are higher. We clearly see how the scale that delimits the boundary effects increases.

In summary, the last years of the North Atlantic are characterized by larger hurricanes, in terms of dissipation of energy, in comparison with the period 1971–1994.

Nevertheless, going back beyond 1970 yields a different tendency, as then the hurricanes show a distribution very similar to that of recent years. In fact, Fig. 5b compares the *PDI* distribution for the period 1944–1969 with the one corresponding to 1995–2007, showing no significant differences. Even a correction of old values of the velocities inspired in the work of Landsea (1993, 2005), in which they are decreased by an amount of 4 m/s, does not alter significantly the results.

7 Discussion

The criticality of tropical cyclones offers a new perspective for the understanding this complex phenomenon. Naturally, many questions arise, and much more research will be necessary to answer them. First, we wonder how this criticality relates to the results of Peters and Neelin (2006), who have recently proposed the criticality of the atmosphere for the transition to rainfall occurrence (i.e., the transition from no precipitation to precipitation). After all, tropical cyclones show, in addition to strong winds, enormous quantities of rainfall, and so they contribute to the precipitation data analyzed by Peters and Neelin. These authors showed that the state of the atmosphere, represented by its water-vapor content, is usually close to the onset of precipitation (this onset marks the critical point of the transition). However, tropical cyclones clearly surpass this onset of precipitation (O. Peters, private communication) and then it is not clear why they still retain critical characteristics.

A subsequent question is how the idea of criticality affects our vision of atmospheric processes, and, in particular, the concept of a chaotic weather (Lorenz 1993). It is true that both behaviors, chaos and criticality, share some characteristics, among them an inherent unpredictability. But there are also fundamental differences. First, chaos usually appears in low-dimensional systems, i.e., systems described by a few non-linear differential equations, for instance, whereas criticality is the hallmark of a high number of strongly interacting degrees of freedom. And second, the unpredictability in chaos is described by the exponential separation of close trajectories (positive maximum Lyapunov exponent), whereas in a critical system this divergence should be a power law (with a zero maximum Lyapunov exponent, if one likes). This suggests that a reconsideration of the limits of predictability of the weather could give interesting outcomes (Orrell 2002).

Acknowledgements The author was benefited by previous interaction with A. Ossó, made possible thanks to J. E. Llebot. Feedback from K. Emanuel, E. Fukada, J. Kossin, O. Peters, G. B. Raga, R. Romero, and A. Turiel was very valuable. Table 1 is based on a previous one by O. Peters and K. Christensen. Research projects 2009SGR-164, FIS2009-09508, and specially FIS2007-29088-E, from the EXPLORA - Ingenio 2010 program, have contributed in one form or another to the execution of the research.

References

Aberson SD (2009) Regimes or cycles in tropical cyclone activity in the North Atlantic. Bull Am Met Soc 90(1):39–43

Arcangelis LD, Godano C, Lippiello E, Nicodemi M (2006) Universality in solar flare and earthquake occurrence. Phys Rev Lett 96:051,102

Baiesi M, Paczuski M, Stella AL (2006) Intensity thresholds and the statistics of the temporal occurrence of solar flares. Phys Rev Lett 96:051,103

Bak P (1996) How nature works: the science of self-organized criticality. Copernicus, New York

Bak P, Tang C, Wiesenfeld K (1987) Self-organized criticality: an explanation of $1/f$ noise. Phys Rev Lett 59:381–384

Bell GD, Halpert MS, Schnell RC, Higgins RW, Lawrimore J, Kousky VE, Tinker R, Thiaw W, Chelliah M, Artusa A (2000) Climate assessment for 1999. Bull Am Met Soc 81(6):S1–S50

Bister M, Emanuel KA (1998) Dissipative heating and hurricane intensity. Meteorol Atmos Phys 65:233–240

Burroughs SM, Tebbens SF (2005) Power-law scaling and probabilistic forecasting of tsunami runup heights. Pure Appl Geophys 162:331–342

Chan JCL (2006) Comment on "Changes in tropical cyclone number, duration, and intensity in a warming environment". Science 311:1713b

Chapman CR, Morrison D (1989) Cosmic catastrophes. Plenum, New York

Christensen K, Moloney NR (2005) Complexity and criticality. Imperial College Press, London

Christensen K, Corral A, Frette V, Feder J, Jøssang T (1996) Tracer dispersion in a self-organized critical system. Phys Rev Lett 77:107–110

Chu JH, Sampson CR, Levine AS, Fukada E (2002) The Joint Typhoon Warning Center tropical cyclone best-tracks, 1945-2000. https://metocph.nmci.navy.mil/jtwc/best_tracks/TC_bt_report.html

Clauset A, Shalizi CR, Newman MEJ (2009) Power-law distributions in empirical data. SIAM Rev 51:661–703

Corral A, Telesca L, Lasaponara R (2008) Scaling and correlations in the dynamics of forest-fire occurrence. Phys Rev E 77:016,101

Elsner JB, Jagger TH (eds) (2009) Hurricanes and climate change. Springer, New York

Elsner JB, Kossin JP, Jagger TH (2008) The increasing intensity of the strongest tropical cyclones. Nature 455:92–95

Elst NJvd, Brodsky EE (2010) Connecting near and farfield earthquake triggering to dynamic strain. J Geophys Res (submitted)

Emanuel K (2005a) Divine wind: the history and science of hurricanes. Oxford University Press, New York

Emanuel K (2005b) Increasing destructiveness of tropical cyclones over the past 30 years. Nature 436:686–688

Emanuel K (2008) The hurricane-climate connection. Bull Am Met Soc (5):ES10–ES20

Frette V, Christensen K, Malthe-Sørenssen A, Feder J, Jøssang T, Meakin P (1996) Avalanche dynamics in a pile of rice. Nature 379:49–52

Goldenberg SB, Landsea CW, Mestas-Nuñez AM, Gray WM (2001) The recent increase in Atlantic hurricane activity: Causes and implications. Science 293:474–479

Gray WM (2000) General characteristics of tropical cyclones. In: Pielke Jr R, Pielke Sr R (eds) Storms. Routledge, London, pp 145–163

Gray WM (2006) Comments on "Increasing destructiveness of tropical cyclones over the past 30 years". arxiv 0601050

Gray WM, Landsea CW, Mielke Jr PW, Berry KJ (1992) Predicting Atlantic seasonal hurricane activity 6–11 months in advance. Wea Forecast 7:440–455

Harris TE (1989) The theory of branching processes. Dover, New York

Hergarten S (2002) Self-organized criticality in earth systems. Springer, Berlin

Jarvinen BR, Neumann CJ, David MAS (1988) A tropical cyclone data tape for the North Atlantic basin, 1886-1983: contents, limitations, and uses. http://www.nhc.noaa.gov/pdf/NWS-NHC-1988-22.pdf

Jensen HJ (1998) Self-organized criticality. Cambridge University Press, Cambridge

Joint Typhoon Warning Center (2010) https://metocph.nmci.navy.mil/jtwc/best_tracks/index.html

Kagan YY (2006) Why does theoretical physics fail to explain and predict earthquake occurrence? In: Bhattacharyya P, Chakrabarti BK (eds) Modelling critical and catastrophic phenomena in geoscience. Springer, Berlin, Lecture Notes in Physics, 705, pp 303–359

Kanamori H, Brodsky EE (2004) The physics of earthquakes. Rep Prog Phys 67:1429–1496

Klotzbach PJ (2006) Trends in global tropical cyclone activity over the past twenty years (1986-2005). Geophys Res Lett 33:L10,805

Kossin JP, Knapp KR, Vimont DJ, Murnane RJ, Harper BA (2007) A globally consistent reanalysis of hurricane variability and trends. Geophys Res Lett 34:L04,815

Lahaie F, Grasso JR (1998) A fluid-rock interaction cellular automaton of volcano mechanics: Application to the Piton de la Fournaise. J Geophys Res 103 B:9637–9650

Landsea CW (1993) A climatology of intense (or major) hurricanes. Mon Weather Rev 121:1703–1713

Landsea CW (2005) Hurricanes and global warming. Nature 438:E11–E12

Landsea CW (2007) Counting Atlantic tropical cyclones back to 1900. Eos 88 (18):197–202

Landsea CW, Harper BA, Hoarau K, Knaff JA (2006) Can we detect trends in extreme tropical cyclones? Science 313:452–454

Lorenz EN (1993) The essence of chaos. University of Washington Press, Washington

Main IG, Li L, McCloskey J, Naylor M (2008) Effect of the Sumatran mega-earthquake on the global magnitude cut-off and event rate. Nature Geosci 1:142

Malamud BD (2004) Tails of natural hazards. Phys World 17 (8):31–35

Malamud BD, Morein G, Turcotte DL (1998) Forest fires: An example of self-organized critical behavior. Science 281:1840–1842

National Hurricane Center (2010) http://www.nhc.noaa.gov/tracks1851to2007_atl_reanal.txt and http://www.nhc.noaa.gov/tracks1949to2007_epa.txt

Orrell D (2002) Role of the metric in forecast error growth: how chaotic is the weather. Tellus 54A:350–362

Ossó A, Corral A, Llebot JE (2009) Scaling of tropical-cyclone dissipation. Accepted in Nature Phys arxiv 0910.0054

Peters O, Christensen K (2006) Rain viewed as relaxational events. J Hidrol 328:46–55

Peters O, Neelin JD (2006) Critical phenomena in atmospheric precipitation. Nature Phys 2:393–396

Peters O, Hertlein C, Christensen K (2002) A complexity view of rainfall. Phys Rev Lett 88:018,701

Shepherd JM, Knutson T (2007) The current debate on the linkage between global warming and hurricanes. Geography Compass 1:1–24

Sornette D (2004) Critical phenomena in natural sciences, 2nd edn. Springer, Berlin

Trenberth K (2005) Uncertainty in hurricanes and global warming. Science 308:1753–1754

Wanliss JA, Weygand JM (2007) Power law burst lifetime distribution of the SYM-H index. Geophys Res Lett 34:L04,107

Webster PJ, Holland GJ, Curry JA, Chang HR (2005) Changes in tropical cyclone number, duration, and intensity in a warming environment. Science 309:1844–1846

Zapperi S, Lauritsen KB, Stanley HE (1995) Self-organized branching processes: Mean-field theory for avalanches. Phys Rev Lett 75:4071–4074

Chapter 6
Environmental Signals in Property Damage Losses from Hurricanes

Thomas H. Jagger, James B. Elsner, and R. King Burch

Abstract In this chapter, we demonstrate the existence of environmental signals in property damage losses from hurricanes affecting the United States. The methodology is based on a random sums model, where the number of damaging hurricane events is modeled separately from the amount of damage per event. It is shown that when the springtime north-south surface pressure gradient over the North Atlantic is weaker than normal, the Atlantic ocean is warmer than normal, there is no El Niño event, and sunspots are few, the probability of at least one loss event increases. However, given at least some losses, the magnitude of the damage per annum is correlated only to ocean temperatures in the Atlantic. The magnitude of damage losses at a return period of 50 years is largest under a scenario featuring a warm Atlantic Ocean, a weak North Atlantic surface pressure gradient, El Niño, and few sunspots.

Keywords Hurricanes · Loss model · Property damage · Climate · Risk

1 Introduction

Hurricanes at landfall generate large financial losses. Hurricane climatologists have developed statistical models to anticipate the level of coastal hurricane activity from independent climate signals. In addition, these models can be used to account for changes in hurricane intensity. Thus we posit that it should be possible to detect environmental signals in historical damages. Our purpose here is to show to what extent environmental patterns that are known to influence the frequency and intensity of hurricanes over the North Atlantic can be detected in long records of damage losses from hurricanes along the U.S. coastline (Gulf and Atlantic).

T.H. Jagger (✉) and J.B. Elsner
Department of Geography, Florida State University, Tallahassee, FL 32306, USA
e-mail: tjagger@fsu.edu; jelsner@fsu.edu

R.K. Burch
3418 Kaimuki Avenue, Honolulu, HI 96816, USA
e-mail: kingburch@aol.com

J.B. Elsner et al. (eds.), *Hurricanes and Climate Change: Volume 2*,
DOI 10.1007/978-90-481-9510-7_6, © Springer Science+Business Media B.V. 2010

Elucidating this connection between ambient environmental conditions and future economic threats from natural hazards is an important new and interesting line of inquiry (Leckebusch et al. 2007). Lane (2008a) writes that insurance markets and capital markets are converging that they are borrowing techniques from each other to access capital and to assess and deal with risk. As the participation of the financial markets becomes more important so does the need to provide investors with sufficient and timely information. Early information is particularly valuable if it aids investors in predicting the number or severity of loss events. For example, Lane (2008b) analyzes investment returns for Insurance Linked Securities (i.e., Catastrophe Bonds) and notes, unsurprisingly, that different loss magnitudes and loss timing patterns are controlled by nature and that this can significantly affect investment results.

Although others have shown environmental signals in damage losses using bivariate relationships including El Niño and wind shear (Katz 2002; Saunders and Lea 2005), this paper is the first to look at the problem from a multivariate perspective. It is based on a recent study that uses pre-season environmental conditions to anticipate insured losses before the start of the hurricane season (Jagger et al. 2008). Here we focus on the set of predictors shown to directly influence U.S. hurricane activity and intensity (Jagger and Elsner 2006). These predictors are the most likely candidates to elucidate the multivariate relationships between the environment and losses from hurricanes. Based on recent research into Atlantic hurricane activity (Elsner et al. 2008) we also introduce the solar cycle as a potentially important covariate in estimating losses.

The strategy is to model annual total economic losses associated with hurricanes as a compound stochastic point process. The process is compound since the number of hurricanes causing damage in a given year is fit using a Poisson distribution, while the amount of damage is fit using a log-normal distribution. Loss totals are thus represented as a random sum, with variations in total losses decomposed into two sources, one attributable to variations in the frequency of events and another to variations in the amount of damage from individual events. We also consider a model for losses over a longer time horizon using a generalized Pareto distribution for the amount of losses coupled with a Poisson distribution for the number of loss events exceeding a threshold amount.

We begin with an examination of the normalized damage loss data and the data associated with climate patterns. We then describe the overall modeling approach and conclude with forecasts of annual and maximum losses for a variety of climate scenarios.

2 Normalized Damage Losses: 1900–2007

We obtain normalized hurricane damage data from the work of Pielke et al. (2008). The normalization attempts to adjust damage amounts to what they would be if the hurricane struck in the year 2005 by accounting for inflation and changes in wealth

and population, plus an additional factor that represents a change in the number of housing units that exceeds population growth between the year of the loss and 2005. The methodology produces a longitudinally consistent estimate of economic damage from past tropical cyclones affecting the U.S. Gulf and Atlantic coasts.

Economic damage is the direct losses associated with the hurricane's impact. It does not include losses due to business interruption or other macroeconomic effects including demand surge and mitigation. Details and caveats for two slightly different normalization procedures are provided in Pielke et al. (2008). Here we focus on the data set from the Collins/Lowe methodology, but note that both data sets are quite similar. Results presented in this study are not sensitive to the choice of data set.

We extend the data by adding the estimated economic damage losses from the three tropical cyclones during 2006 and 2007. The damage estimates are those reported in the *National Hurricane Center* (NHC) storm summaries and derived by the NHC by the *American Insurance Services* and the *Property Claim Services*. This is the same primary data source used in both normalization methods described in Pielke et al. (2008). We did not adjust these losses at this time. There were six tropical cyclones that caused at least some damage in the United Stated during this two-year period, but loss levels were quite small, especially when compared with the losses experienced in 2004 and 2005. In fact loss levels for three of the six tropical storms were below the $25 million reporting threshold (Alberto in 2006, and Barry and Gabrielle in 2007).

Tropical storm Ernesto in 2006 struck southern Florida and North Carolina. Total direct damage losses are estimated at $500 mn (million). We estimate that 4/5ths of those losses occurred in North Carolina where the storm was stronger at landfall. An estimate of the total property damage from tropical storm Erin and hurricane Humberto, both of which hit Texas in 2007, is $35 and $50 mn, respectively. The NHC suggests that the low damage total from Humberto was probably due to its small size and the relatively unpopulated area subjected to Humberto. In addition, the large losses in the same area from Hurricane Rita in 2005 and may have moderated the amount of damage that could have been done by Humberto. We make no attempt to normalize the losses from 2006 and 2007.

Here we assume that multiple landfalls from a single tropical cyclone produce multiple loss events. For example, in 1992 Hurricane Andrew produced a $52 bn (billion) loss in southeast Florida and a separate $2 bn loss in Louisiana. When multiple landfall events are included, the updated data set contains 221 loss events from 210 separate tropical cyclones over the period 1900–2007. Figure 1 shows the distribution and time series of the damages from all loss events. The histogram bars indicate the percentage of events with losses in groups of $10 bn. The distribution is highly skewed with 88% of the events having losses less than or equal to $10 bn and 95% of the events having losses less than $20 bn. The worst loss occurred with the 1926 hurricane that struck southeast Florida creating an estimated damage loss adjusted to $2005 of $129 bn. The Galveston hurricane of 1900 ranks second with an estimated loss of $99 bn and hurricane Katrina of 2005 ranks third with an estimated total loss of $81 bn. Years with more than one loss have more than

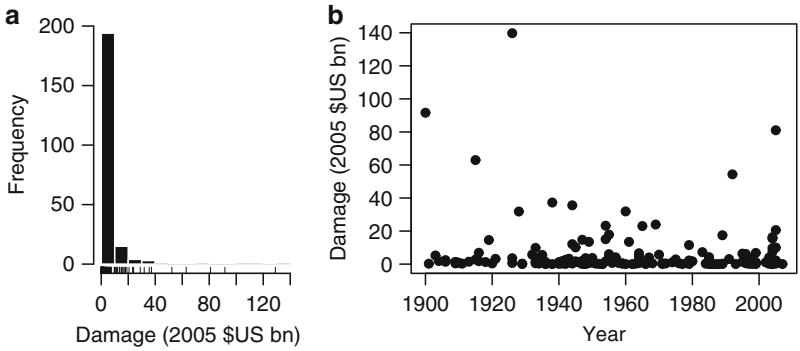

Fig. 1 (**a**) Distribution of per storm damage losses from hurricanes in the United States (excluding Hawaii). The distribution is highly skewed with a few events generating very large damage losses. (**b**) Time series of the damage losses. Individual years may have more than one loss event

Table 1 Damage exceedances ($US adjusted to 2005$). The values are the number of events exceeding various damage loss thresholds from 1900 to 2007 inclusive

Exceedance $US (2005)	Number events (CL)[a]	Number events (PL)[b]
1 million	219	219
10 million	207	207
100 million	169	169
1 billion	98	94
10 billion	28	27
100 billion	1	1

[a]Collins and Lowe data set.
[b]Pielke and Landsea data set.

one dot in the time series plot. There is large year-to-year variability but no obvious long-term trend, although here the data are not disaggregated into loss amount and the number of loss events.

The damage loss exceedances are shown in Table 1. Of the 221 loss events from 1900 to 2007, 169 exceeded $100 mn in losses and 28 of these exceeded $10 bn. The distribution of losses is similar using the Collins/Lowe (CL) method and the Pielke/Landsea (PL) methods, although the Collins/Lowe method tends to result in somewhat larger losses. The two events producing losses less than $1 mn include Gustav in 2002 and Dean in 1995. Another way to examine the data is to look at the total amount of loss for storms exceeding the Saffir–Simpson lower intensity threshold. Table 2 shows losses in billions of U.S. dollars from 1900 to 2007, inclusive. For example, category 0 is for the minimum tropical storm threshold (17 m s^{-1}), and category 1 is for the minimum hurricane threshold (33 m s^{-1}). So from this table, all tropical storms accounted for of $1,103.9 bn 2005 adjusted $US with hurricanes accounting for 1063.1 bn. Here again we see the similarity in the two data sets and that category 4 and 5 hurricanes, although rare, have historically accounted for nearly 50% of all losses.

Table 2 Cumulative losses by Saffir–Simpson scale ($US bn adjusted to 2005)

Category (Saffir/Simp)	Cumulative losses (CL)	Cumulative losses (PL)
0	1,103.9	1,125.1
1	1,063.1	1,084.5
2	1,022.7	1,045.6
3	941.4	964.4
4	533.1	557.3
5	79.4	79.3

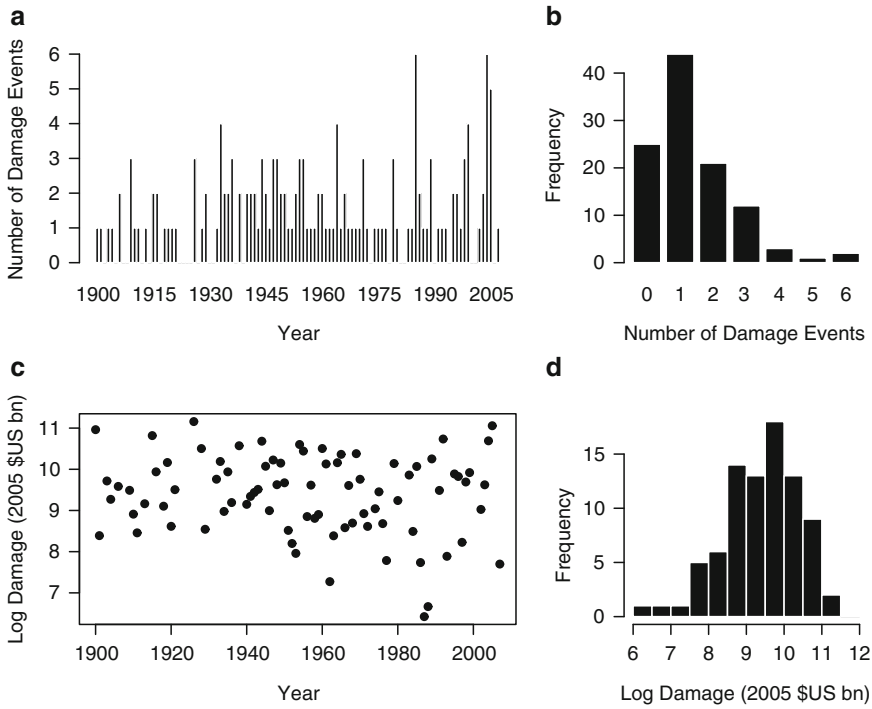

Fig. 2 Annual total damage losses. (**a**) Time series and (**b**) distribution of loss events and the (**c**) time series and (**d**) distribution of the number of the logarithm (base 10) of annual total damage losses

Figure 2 shows the annual number of loss events and their distribution. There are five years with six loss events, the most recent being 2005. The annual rate of loss events is 1.94 events/year with a variance of 2.48 (events/year)^2. There is a distinct upward trend in the number of loss events attributable to some extent to an increase in coastal population. As population increases so do the number of loss events from the weaker tropical cyclones. Indeed, prior to 1950 the number of loss events from tropical storms was 6% of the total number of events. This increases to nearly 38% from 1950 onward. In the present work we focus on the

set of large losses from the stronger tropical cyclones. There is significant positive skewness in per storm damage amounts. If we transform the data using base-10 logarithms then the loss frequency distribution becomes more symmetric.

3 Climate and Solar Factors

Statistical relationships between U.S. hurricane activity and climate are well established (Elsner et al. 2004; Murnane et al. 2000). More importantly for the present work, Jagger et al. (2001) and Jagger and Elsner (2006) model the wind speeds of hurricanes at or near landfall and show that the exceedance probabilities (e.g., wind speeds in excess of 50 m s^{-1}) vary appreciably with the phase of the ENSO, the NAO, and Atlantic sea-surface temperature (SST). Recent work has also shown a linkage between U.S. hurricanes and sunspot numbers (SSN) (Elsner et al. 2008).

The ENSO can be characterized by basin-scale fluctuations in sea-level pressure between Tahiti and Darwin. Although noisier than equatorial Pacific ocean temperatures, pressure values are available back to 1900. The Southern Oscillation Index (SOI) is defined as the normalized sea-level pressure difference between Tahiti and Darwin (in units of standard deviation). Negative values of the SOI indicate an El Niño event. The relationship between ENSO and hurricane activity is strongest during the hurricane season so we use a August–October average of the SOI as a climate factor. The monthly SOI values (Ropelewski and Jones 1997) are obtained from the *Climatic Research Unit* (CRU).

The NAO is characterized by fluctuations in sea level pressure (SLP) differences. Index values for the NAO (NAOI) are calculated as the difference in SLP between Gibraltar and a station over southwest Iceland (in units of standard deviation), and are obtained from the CRU (Jones et al. 1997). The values are averaged over the pre- and early-hurricane season months of May and June (Elsner et al. 2001) as this is when the relationship with hurricane activity is strongest. (Elsner 2006).

The SST values are a blend of modeled and observed data and, to a first order, correlate with the amount of fuel for hurricane development. Unsmoothed and undetrended Monthly North Atlantic arealy averaged SST anomalies from 0 to 70°N (in units of °C) were computed using the base period 1951–2000. Data are obtained from the NOAA-CIRES *Climate Diagnostics Center* back to 1871. For this study we average the North Atlantic SST anomalies over the peak hurricane season months of August through October.

For SSN we use the monthly total sunspot number for September (the peak month of the hurricane season). Sunspots are magnetic disturbances of the sun surface having both dark and brighter regions. The brighter regions (plages and faculae) increase the intensity of the UV emissions. Increased sunspot numbers correspond to more magnetic disturbances. Sunspot numbers produced by the *Solar Influences Data Analysis Center* (SIDC), *World Data Center for the Sunspot Index*, at the *Royal Observatory* of Belgium are obtained from the U.S. *National Oceanic and Atmospheric Administration*.

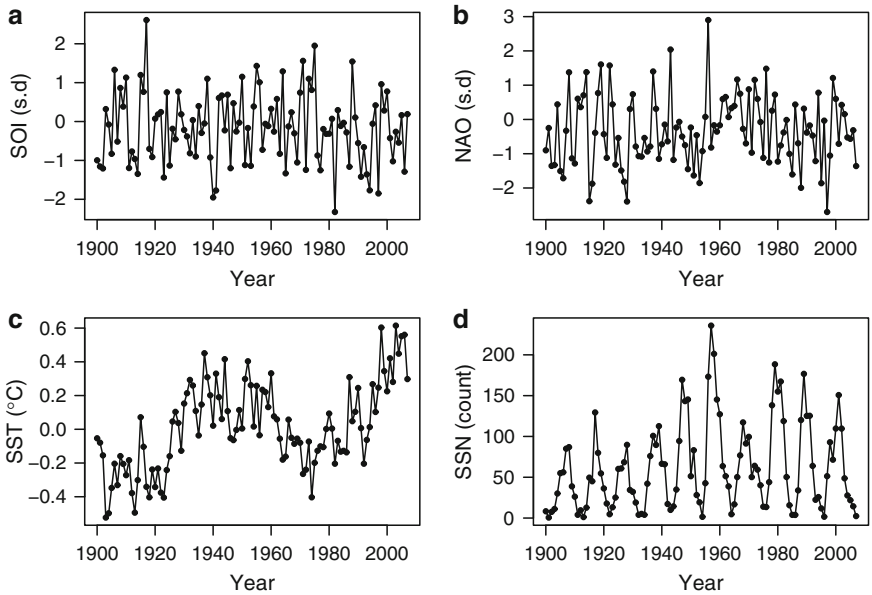

Fig. 3 Time series of the four covariates used to estimate wind damage losses from hurricanes

In summary, normalized historical economic damage losses from hurricane events from the period 1900 to 2007 will be modeled using climate and solar data that represent optimal relationships found in previous studies on U.S. hurricane activity. By "optimal" we mean relative to what is currently understood about how environmental variables influence hurricanes. It does not mean relative to an exhaustive search for correlations across many different variables.

Figure 3 shows the time series of the climate factors that are used in the model. Upper and lower quartile values of the SOI are 0.40 and −0.90 s.d., respectively with a median (mean) value of −0.18 (−0.16) s.d. Years of above (below) normal SOI correspond to La Niña (El Niño) events and thus a higher probability of at least one U.S. hurricane. The upper and lower quartile values of the NAO are 0.40 and −1.09 s.d., respectively with a median (mean) value of −0.39 (−0.33) s.d. Years of below (above) normal values of the NAO correspond to a weak (strong) NAO phase and thus to higher (lower) probability of U.S. hurricanes. The upper and lower quartile values of the Atlantic SST anomalies are 0.22°C and −0.16°C, respectively. Years of above (below) normal values of SST correspond to higher (lower) probability of hurricane activity. The upper and lower quartile values of the September SSN are 91.7 and 17.1, respectively with a median (mean) value of 50.2 (62.0). Years of below (above) normal SSN correspond to a lower (higher) probability of U.S. hurricanes. The largest correlation among the covariates occurs between the SSN and SST at a marginally statistically significant value of 0.18 (p-value = 0.064).

As an initial analysis of the damage data relative to the climate signals, here we compare locations on the distribution of per storm damage losses conditional on the

Table 3 Damage amounts for Hurricanes in billions $US adjusted to 2005 along with conditional damage ratios. The damage ratio is the respective quantile amount of damage per storm during above normal years to the amount during below normal years

	Collins/Lowe		Pielke/Landsea	
	50%	99%	50%	99%
Damage	1.326	86.308	1.216	90.181
SOI	2.460	0.578	2.860	0.560
NAO	0.829	0.354	0.711	0.319
SST	1.027	1.342	1.233	1.289
SSN	0.671	0.493	0.557	0.480

various climate factors. Table 3 lists the damage amounts at the median and upper 99th percentile for both data sets and the damage ratio as the amount of damage during above normal years to the amount during below normal years. During seasons characterized by La Niña conditions (above normal values of SOI) the median losses are greater by a factor of more than two compared with years with El Niño conditions. However, the extreme losses are greater during El Niño conditions. During seasons with below normal springtime NAO conditions, the damages tend to be greater at the median level and even more so at the extremes.

Interestingly, seasons characterized by higher than average SSTs show lower amounts of total damage at the median levels compared with seasons characterized by lower SSTs. There is, however, a modest increase in damage loss amounts during warm years over loss amounts during the cold years at the upper tails of the distribution. During seasons with below normal sunspots, damage losses tend to be greater at the median level and similarly so at the extremes. These results are expected from what we know about how these climate factors influence U.S. hurricane activity (Elsner 2006; Jagger and Elsner 2006). Again, note that the CL and PL damage loss data sets give practically the same results.

4 Large and Small Losses

Figure 4 shows the amount of losses by the Saffir–Simpson category of storm intensity. It is clear that both the category 0 and 1 tropical cyclones are different from the stronger tropical cyclones, in that the range of damage is larger. For instance, at the 80% interval of losses the range is from 6.8 to 9.0 for category 0 storms, and from 7.2 to 9.1 for category 1 storms, this is about 2.2 and 1.9, respectively, or approximately a factor of 100. In comparison, the category 2, 3, 4, and 5 ranges are 1.3, 1.5, 1.4, and 1.1, respectively. Thus it makes sense to model tropical storms (category 0) and category 1 hurricanes separately from category 2 and higher storms. However, there is a practical limitation in that we lose 109 of the 212 storms. Thus for this

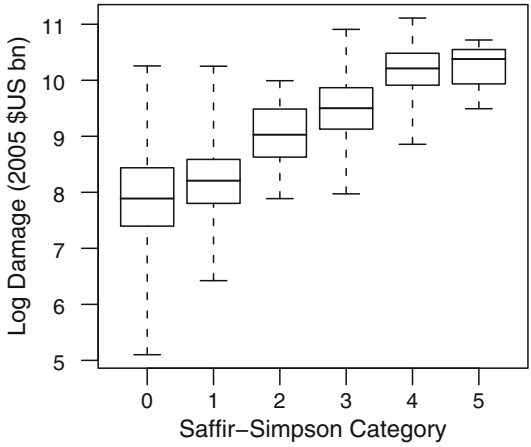

Fig. 4 Common logarithm ($\log_{10}$) of damage losses by Saffir–Simpson hurricane category

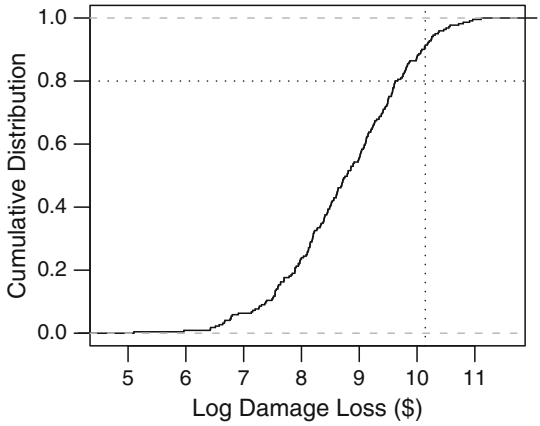

Fig. 5 Empirical cumulative distribution function of per storm damage losses expressed on the common logarithm scale. The values on the ordinate are the fraction of damage events less than or equal to the damage values on the abscissa. The *horizontal dotted line* is the 80th percentile and the *vertical dotted line* is the damage amount of the 20th worst event

paper we restrict our analysis to category 1 and higher tropical cyclones (hurricanes only) as a compromise between removing too much data and keeping too many weaker events.

Moreover, the total damage from the 221 events (1900–2007) calibrated to 2005 is estimated at US $1.1 trillion. The large skewness in damage losses per event and per annum suggests that it might be a good strategy to separate large losses from small losses for the purpose of modeling. It is often noted that 80% of the total damage from tropical cyclones is caused by 20% of the biggest loss events. Figure 5 shows that the distribution of damage data is more skewed than that. In fact, the top 35 loss events (less than 16% of the total number of loss events) account for more than 81% of the total loss amount. The relative infrequency of the largest loss events argues for a split that favors more data for modeling the largest losses. Here we use a cutoff of 1 bn $US and find that 90 of the 160 hurricane events (56.3%) exceed this threshold. The remaining 70 events (43.7%) account for only 15.4% of the total

damages. Thus it might be reasonable to assume that the small loss events are at the "noise" level. In summary, our focus here is on the set of large losses from the stronger tropical cyclones.

5 A Model for Annual Expected Loss

Given a loss event, the logarithm of the amount of loss on an annual basis is modeled using a linear regression with the logarithm of the loss amount modeled as a truncated Normal distribution. The only statistically significant climate signal in the loss amount is the SST. Thus given a loss event, the magnitude of the loss increases with increasing ocean warmth. This is consistent with SST acting as a proxy for upper-ocean heat; a source of energy for hurricanes (Emanuel 1991).

To arrive at an estimate of the annual loss we need to combine this loss amount estimate given an event with the frequency of a loss event. Since we divide loss events into large and small events, we use separate models. Thus, given a mean annual rate of large (small) loss events, the annual number of large (small) loss events follows a Poisson distribution with the natural logarithm of the loss event rate given as a linear function of the climate variables. We find that SST, NAO, SOI, and SSN are all statistically significant indicators of the frequency of large losses, but none of the climate variables are important for the frequency of small losses.

Mathematically we write the model for large losses as:

$$\begin{aligned} \log L &\sim \text{Normal}(\mu, \sigma^2) \\ \mu &= \alpha_0 + \alpha_1 \text{SST} \\ N &\sim \text{Poisson}(\lambda) \\ \lambda &= \exp(\beta_0 + \beta_1 \text{SST} + \beta_2 \text{NAO} + \beta_3 \text{SOI} + \beta_4 \text{SSN}) \end{aligned} \tag{1}$$

where L is the amount of total loss for an event and λ is the yearly hurricane frequency. The symbol $\sim$ refers to a stochastic relationship and indicates that the variable on the left hand side is a random draw (sample) from a distribution specified on the right hand side. The equal sign indicates a logical relationship with the variable on the left hand side algebraically related to variable(s) on the right hand side. As mentioned, the size of the loss is modeled as a truncated Normal distribution with parameters μ and σ^2 indicating the location and scale for the distribution. Unlike the normal distribution the location and scale parameters of the truncated normal distribution are not the same as its mean and variance. In short, the model describes a compound Poisson process with rate λ and logarithm of the jump size distributed as a truncated normal distribution with parameters μ and σ.

Chi-square goodness-of-fit statistics do not show any evidence against adequacy of the rate model. Furthermore, there is no trend in the deviance residuals implying the rate model for large losses conditioned on the climate variables chosen is statistically stationary and the addition of a trend term does not improve the model. This suggests to us that there is no significant historical under reporting of the number of loss events from hurricanes in the United States over the period considered here.

The final model that combines the frequency of loss events with the magnitude of the loss given an event uses a hierarchical Bayesian specification. Bayesian models provide posterior distributions of model parameters, as opposed to a frequentist model using maximum likelihood estimation (MLE) which only provides the parameter estimate and prediction error. For non normal distributions these MLE estimates lead to biased predictions. We chose flat (uniform) model priors for the location and model precision ($1/\sigma^2$) parameters to minimize the influence of prior. The final model is selected from a set of possible models by comparing the Deviance Information Criterion (DIC) for each model and then choosing the model with the smallest DIC. The DIC is the formulated explicitly for model selection in Bayesian models, in the same fashion that the AIC which is used to compare models using maximum likelihood estimation (Spiegelhalter et al. 2002). It is useful in Bayesian model selection where the posterior distributions of the models are obtained by Markov Chain Monte Carlo (MCMC) simulation. The model with the smallest DIC is estimated to be the model that would best predict a replicate data set that has the same structure as the observed one.

Given the hierarchical form of the model, samples of the annual losses are generated using WinBUGS (Windows version of Bayesian inference Using Gibbs Sampling) developed at the *Medical Research Council* in the UK (Gilks et al. 1996; Spiegelhalter et al. 1996). WinBUGS chooses an appropriate MCMC sampling algorithm based on the model structure. In this way annual losses are sampled conditional on the model coefficients and the observed values of the covariates. The cost associated with a Bayesian approach is the requirement to formally specify prior beliefs. Here we take the standard route and assume noninformative priors that provide little information about the parameters of interest.

MCMC, in particular Gibbs sampling, is used to sample the parameters given the data since no closed form solution exists for the posterior distribution of the model parameters in the truncated Normal (or for the generalized Pareto distribution (GPD) used in the next section). Indeed, WinBUGS is useful in that it allows us to sample the parameters from the posteriors created from arbitrary likelihood functions. As far as we are aware, there is no software for finding the maximum likelihood estimates of the regression parameters for a truncated normal distribution.

We check for mixing and convergence by examining successive samples of the parameters. Samples from the posterior distributions of the parameters indicate relatively good mixing and quick settling as two different sets of initial conditions produce sample values that fluctuate around a fixed mean. Based on these diagnostics, we discard the first 10,000 samples and analyze the output from the next 10,000 samples. The utility of the Bayesian approach for modeling the mean number of coastal hurricanes is described in Elsner and Jagger (2004) and for predicting damage losses is described in Jagger et al. (2008).

Figure 6 shows the predictive posterior distributions of annually aggregated losses for six different climate scenarios. The set of scenarios is ordered by generally increasing favorable climate conditions for hurricanes to affect the United States. Each panel shows the probability of no losses and the probability of losses on a logarithm (base 10) scale given at least one loss event. The upper left panel

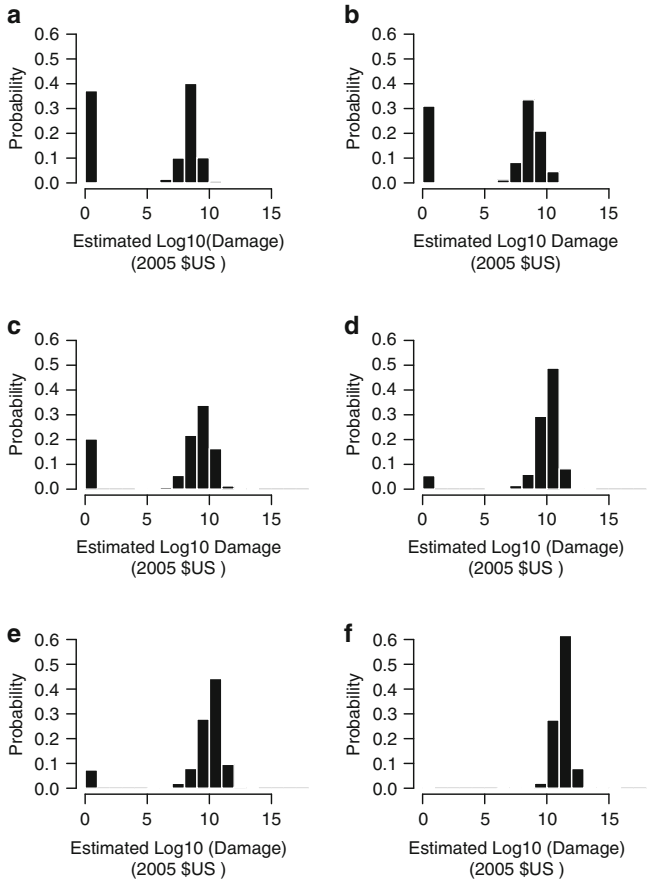

Fig. 6 Simulated annual losses for six different climate scenarios. The histograms show the probability of no losses on the *left* and the distribution of annual amount of loss on a logarithmic scale on the *right*. The panels are ordered toward conditions increasingly favorable for hurricane activity along the U.S. coast. The histograms are created from posterior samples generated from the hierarchical Bayesian model using (**a**) SST = −0.52°C, NAO = +2.9 s.d., SOI = −2.3 s.d., and SSN = 236, (**b**) SST = −0.24°C, NAO = +0.7 s.d., SOI = −1.1 s.d., and SSN = 115, (**c**) SST = +0.01°C, NAO = −0.3 s.d., SOI = −0.2 s.d., and SSN = 62, (**d**) SST = +0.27°C, NAO = −1.4 s.d., SOI = +0.8 s.d., and SSN = 9, (**e**) SST = +0.43°C, NAO = −1.3 s.d., SOI = −0.1 s.d., and SSN = 5, and (**f**) SST = +0.61°C, NAO = −2.7 s.d., SOI = +2.6 s.d., and SSN = 1

shows the posterior probabilities for a year during which the SST is much below normal, the NAO is much above normal, there is a strong El Niño, and the sun is very active (many sunspots). The specific covariate values are listed in the figure caption. The posterior samples indicate a relatively large probability of no damage events (37%) under this scenario. The estimated annual loss taking into account the non-zero probability of no loss events is centered in the range between $0.1 and $1 bn.

As the climate factors change to indicate more favorable conditions for hurricanes, the posterior samples provide a distribution of annual losses that are more

ominous with the probability of no losses decreasing to less than 1% and the expected annual total loss amount exceeding $100 bn. All estimated loss amounts are converted to $2005. The results of the model integration are rather remarkable in showing a distinct climate signal in aggregate property losses in the United States from hurricanes. The annual expected loss increases with warmer Atlantic SSTs, cooler equatorial eastern Pacific SSTs, a negative phase of the NAO, and fewer sunspots.

6 A Model for the Probable Maximum Loss

While the above modeling strategy makes sense for estimating the distribution of likely annual damage associated with variations in environmental conditions from one year to the next, for financial planning it might be of greater importance to know the maximum possible storm loss. In this case, the normal distribution is replaced by an extreme value distribution for the logarithm of losses. For example, the family of Generalized Pareto Distributions (GPD) describes the behavior of individual extreme events.

Consider observations from a collection of random variables in which only those observations that exceed a fixed value are kept. As the magnitude of this value increases, the GPD family represents the limiting behavior of each new collection of random variables. This property makes the family of GPD a good choice for modeling extreme events including large losses from wind storms. The choice of threshold, above which we treat the values as extreme, is a compromise between retaining enough observations to properly estimate the distributional parameters (scale and shape), but few enough that the observations follow a GPD family.

The GPD describes the distribution of losses that exceed a threshold l but not the frequency of losses at that threshold. As we did with the annual loss model, we specify that, given a rate of loss events above the threshold, the number of loss events follows a Poisson distribution. Here there is no need to consider small loss events as we are only interested in the large ones. Combining the GPD for the distribution of large loss amounts with the Poisson distribution for the frequency of loss events above the threshold allows us to obtain return periods for given levels of losses.

Mathematically we are modeling the exceedances, $L - l$, as samples from a family of GPD distributions so that for any threshold l and any event with losses L, the probability that L exceeds some arbitrary level x above l is

$$\Pr(L > x + l | L > l) = \begin{cases} \exp(-\frac{x}{\sigma}) & \xi = 0 \\ \left(1 + \frac{\xi}{\sigma_l} x\right)^{-\frac{1}{\xi}} & \xi \neq 0 \end{cases} \tag{2}$$

$$= \mathrm{GPD}(x | \sigma_l, \xi) \tag{3}$$

where $\sigma_l > 0$, $x \geq 0$, and $\sigma_l + \xi x \geq 0$. If the exceedances above l_0 follow a GPD then the exceedances above $l > l_0$ follow a GPD with the same shape, ξ and scale

that shifts linearly with the threshold:

$$\sigma_l = \sigma_0 + \xi l$$

The parameters σ_l and ξ are the scale and shape parameters respectively. For negative shape parameters the GPD family of distributions has an upper limit of $L_{\max} = l + \sigma_l/|\xi|$. The equation for σ_l specifies that if the values follow a GPD, then for any threshold the distribution of exceedances is GPD with the same value of the shape parameter (ξ) from the original distribution and a scale parameter that changes linearly with the threshold at a rate equal to the shape parameter.

We determine the threshold value at $1 bn U.S. for the set of losses by examining the mean residual life plot. This is a plot of the mean value of the exceedances as a function of the threshold. If the data follow a GPD distribution, this plot is linear. The threshold is chosen as the smallest value where the function is linear for all larger thresholds Coles (2001).

The GPD describes the loss distribution for each wind event whose losses exceed l but not the frequency of events at that magnitude. We assume that the number of loss events in year y that exceed l has a Poisson distribution with mean (or exceedance) rate is λ_l. Thus by combining the exceedance probability and the exceedance rate with our assumption that they are independent we get a Poisson distribution for the number of loss events per year with losses exceeding m (N_m) with a rate given by

$$\lambda_m = \lambda_l \Pr(L > m | L > l). \tag{4}$$

This specification is physically realistic since it allows us to model loss occurrence separately from loss amount. Moreover from a practical perspective, rather than a return rate per loss occurrence, the above specification allows us to obtain an annual return rate on the extreme losses, which is more meaningful for the business of risk and insurance.

Now, the probability that the yearly maximum will be less than m is the probability that $N_m = 0$. Since N_m has a Poisson distribution

$$\Pr(L_{\max} \leq m) = \Pr(N_m = 0) \tag{5}$$

$$= \exp(-\lambda_m) \tag{6}$$

$$= \exp\{-\lambda_l \mathrm{GPD}(m - l | \sigma_l, \xi)\} \tag{7}$$

If we make the substitution for $\xi \neq 0$:

$$\sigma_\mu = \lambda_l^\xi \sigma_l \tag{8}$$

$$\mu = l + \frac{\sigma_\mu - \sigma_l}{\xi} \tag{9}$$

then

$$\Pr(L_{\max} \leq m) = \exp\left\{-\left[1 + \xi\left(\frac{m-\mu}{\sigma_\mu}\right)\right]^{-\frac{1}{\xi}}\right\} \tag{10}$$

has a Generalized Extreme Value (GEV) distribution, which is in canonical form. If $\xi = 0$ then we make the substitutions

$$\begin{aligned}\sigma_\mu &= \sigma_l \\ \mu &= l + \sigma_l \log(\lambda_l)\end{aligned}$$

then

$$\Pr(L_{\max} \leq m) = \exp\left\{-\exp\left[-\left(\frac{m-\mu}{\sigma_\mu}\right)\right]\right\} \tag{11}$$

We convert the peaks-over-threshold parameters λ_l, σ_l, ξ to the GEV canonical parameters μ, σ_μ, ξ, and so compare results obtained with different thresholds. Using the canonical parameters, for example we calculate the yearly (seasonal) return level, $\mathrm{rl}(r)$, corresponding to a given return period, r and GEV parameters μ, σ, ξ by solving for m in $\Pr(L_{\max} \geq m) = \frac{1}{r}$ giving

$$\mathrm{rl}(r) = \begin{array}{ll} \mu + \frac{\sigma}{\xi}\left\{\left[\log\left(\frac{r}{r-1}\right)^{-\xi} - 1\right]\right\} & \xi \neq 0 \\ \mu - \sigma \cdot \log\left\{\log\left(\frac{r}{r-1}\right)\right\} & \xi = 0 \end{array} \tag{12}$$

Additional details are given in (Coles 2001).

As with the annual loss model we use a Bayesian hierarchical specification for the model of extreme losses. MCMC samples are used to generate posterior predictive distributions. Here we are interested in the return level as a function of return period. The annual return level is determined by the return level of individual extreme events and the annual frequency of such events above a threshold rate. The annual number of extreme events follows a Poisson distribution with the natural logarithm of the rate specified as a linear function of the four covariates.

Given values for the scale (σ) and shape (ξ) parameters, the return level of individual extreme events follows a GPD. The logarithm of the scale parameter and the shape parameter are both linear functions of the four covariates.

As before, samples of the return levels are generated using WinBUGS and we use noninformative prior distributions. Samples from the posterior distribution of the model parameters indicate good mixing and good convergence properties. We discard the first 10,000 samples and analyze the output from the next 10,000 samples. Applications of Bayesian extremal analysis are found in Coles and Tawn (1996), Walshaw (2000), Katz et al. 2002, Coles et al. (2003), Hsieh (2004), and Jagger and Elsner (2006). Figure 7 shows the predictive posterior distributions of extreme losses for four different climate scenarios using quantile values. For each return period the 0.025, 0.05, 0.25, 0.5, 0.75, 0.95, and 0.975 quantile values of the maximum storm damage losses are plotted. The first scenario is characterized by covariates in favor of fewer hurricanes, the second scenario represents long-term

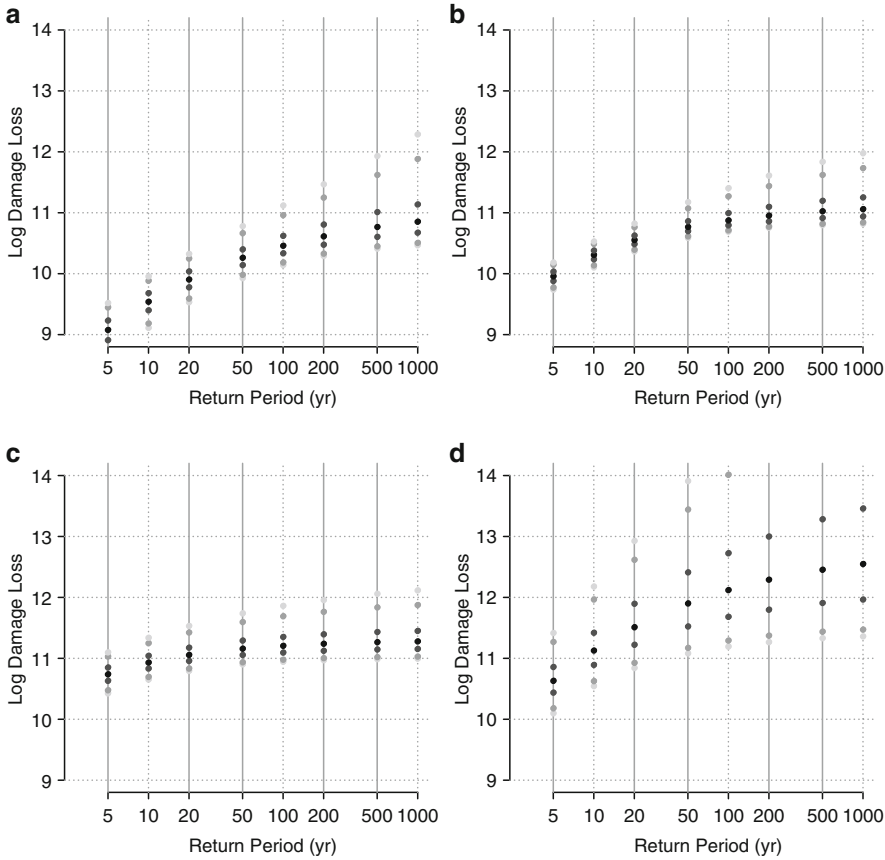

Fig. 7 Simulated extreme losses for four different climate scenarios. The points are the 0.025, 0.05, 0.25, 0.5, 0.75, 0.95, and 0.975 quantiles from the posterior distribution of the loss model. The panels are ordered toward conditions increasingly favorable for large losses. (**a**) SST = −0.243°C, NAO = +0.698 s.d., SOI = −1.087 s.d., and SSN = 115, (**b**) SST = +0.012°C, NAO = −0.331 s.d., SOI = −0.160 s.d., and SSN = 62, (**c**) SST = +0.268°C, NAO = −1.359 s.d., SOI = −0.766 s.d., and SSN = 9, (**d**) SST = +0.268°C, NAO = −1.359 s.d., SOI = −1.087 s.d., and SSN = 9. The *upper quantile values* in panel (**d**) are outside the range of the plot

climatological conditions, the third scenario is characterized by covariates favoring more hurricanes, and the fourth scenario is characterized by covariates favoring stronger hurricanes. The loss distribution changes substantially between the different climate and solar scenarios and in a direction that is consistent with our understanding about the relationship between climate and hurricane activity.

Under the first scenario we find the median return level of a 50-year extreme event at approximately $18 bn, this compares with a median return level of the same 50-year extreme event loss of approximately $793 bn under the fourth scenario. Thus the model can be useful for projecting extreme losses over time horizons longer than a year given values of the covariates. Note that the results are interpreted

as the posterior distributions of the return level for a return period of 50 years of the covariate values as extreme or more extreme than 1 standard deviation. With four independent covariates and an annual probability of about 16% that a particular covariate is more than 1 s.d. from its mean, the chance that all covariates will be this extreme or more in a given year is less than 0.1%.

7 Summary

Coastal hurricanes are capable of generating large financial losses to the insurance industry. Annual loss totals are directly related to the intensity and frequency of hurricanes affecting the coast. Since a measurable amount of skill exists in forecasts of coastal hurricane activity, it makes sense to investigate the potential of modeling losses directly. This paper demonstrates clear climate and solar signals in the historical estimates of property damage losses.

Two separate statistical models are specified using hierarchical Bayesian technology and predictive posterior distributions are generated using MCMC sampling. The first model can be used to estimate the expected annual loss under various environmental scenarios. The annual expected loss increases with warmer Atlantic SSTs, cooler equatorial eastern Pacific SSTs, a negative phase of the NAO, and fewer sunspots. The second model can be used to estimate the distribution of losses over a longer time horizon conditional on the values of the four covariates.

Results are consistent with current understanding of hurricane climate variability. While the models here are developed from aggregate loss data for the entire United States susceptible to Atlantic hurricanes, it would be possible to apply the techniques to model data representing a subset of losses capturing, for example, a particular reinsurance portfolio. Moreover, since the models make use of MCMC sampling they can be easily extended to include measurement error and missing data.

Hazard risk affects the profit and loss of the insurance industry. Some of this risk is transferred to the performance of securities traded in financial markets. This implies that early and reliable information concerning potential hazards will be useful to investors. This paper advances those goals.

Traditional hurricane risk models used by the insurance industry rely on a catalog of storms that represent the historical data in some way or another. While useful for estimating AAL and loss exceedance curves for aggregate and occurrence portfolio losses, these catalogs are not easily suited for anticipating losses based on an ever-changing climate. Specifically, at the core of the catalog is a set of synthetic storms and a way to assign a probability to each. However, it is not obvious how to condition the set of storm characteristics on climate. The approach demonstrated here provides an alternative way to anticipate losses on the seasonal to multi-year time scale.

Concerning the future, increases in ocean temperature will raise a hurricane's potential intensity, all else being equal. However, corresponding increases in atmospheric wind shear – in which winds at different altitudes blow in differ-

ent directions – could tear apart developing hurricanes and could counter this tendency by dispersing the hurricane's heat. However, a recent study based on a set of homogenized satellite-derived wind speeds indicates the strongest hurricanes are getting stronger worldwide (Elsner et al. 2008). This new information can be incorporated in models of the type demonstrated here by placing a discount factor on the older information relative to the more recent events.

Acknowledgements This research is supported by Florida State University's *Catastrophic Storm Risk Management Center*, the *Risk Prediction Initiative* of the Bermuda Institute for Ocean Studies (RPI-08-02-002), and by the U.S. *National Science Foundation* (ATM-0738172). The views expressed within are those of the authors and do not reflect those of the funding agency.

References

Coles S (2001) An introduction to statistical modeling of extreme values. Springer, New York

Coles S, Tawn JA (1996) A Bayesian analysis of extreme rainfall data. Appl Stat 45:463–478

Coles S, Pericchi LR, Sisson S (2003) A fully probabilistic approach to extreme rainfall modeling. J Hydrol 273:35–50

Elsner JB, Jagger TH (2004) A hierarchical Bayesian approach to seasonal hurricane modeling. J Climate 17:2813–2827

Elsner JB, Jagger TH (2006) Prediction models for annual U.S. hurricane counts. J Climate 19:2935–2952

Elsner JB, Jagger TH (2008) United States and Caribbean tropical cyclone activity related to the solar cycle. Geophys Res Lett 35:L18705, doi:10.1029/2008/GL034431

Elsner JB, Bossak BH, Niu X-F (2001) Secular changes to the ENSO-U.S. hurricane relationship. Geophys Res Lett 28:4123–4126

Elsner JB, Niu X-F, Jagger TH (2004) Detecting shifts in hurricane rates using a Markov Chain Monte Carlo approach. J Climate 17:2652–2666

Elsner JB, Kossin JP, Jagger TH (2008) The increasing intensity of the strongest tropical cyclones. Nature 455:92–95

Emanuel KA (1991) The theory of hurricanes. Ann Rev Fluid Mechan 23:179–196

Gilks WR, Richardson S, Spiegelhalter DJ (1996) Markov Chain Monte Carlo in practice. Chapman & Hall/CRC, London

Hsieh PH (2004) A data-analytic method for forecasting next record catastrophe loss. J Risk Insur 71:309–322

Jagger TH, Elsner JB (2006) Climatology models for extreme hurricane winds near the United States. J Climate 19:3220–3236

Jagger TH, Elsner JB, Niu X-F (2001) A dynamic probability model of hurricane winds in coastal counties of the United States. J Appl Meteorol 40:853–863

Jagger TH, Elsner JB, Saunders MA (2008) Forecasting U.S. insured hurricane losses. In: Murnane R, Diaz H (eds) Climate extremes and society. Cambridge University Press, Cambridge

Jones PD, Jónsson T, Wheeler D (1997) Extension to the North Atlantic oscillation using early instrumental pressure observations from Gibraltar and south-west Iceland. Int J Climatol 17:1433–1450

Katz RW (2002) Stochastic modeling of hurricane damage. J Appl Meteorol 41:754–762

Katz RW, Parlange MB, Naveau P (2002) Statistics of extremes in hydrology. Adv Water Resour 25:1287–1304

Lane MN (2008a) Beyond convergence, toward integration. Trade Notes, Lane Financial LLC, August 29, 2008

Lane MN (2008b) The measurement of ILS returns. Trade Notes, Lane Financial LLC, August 29, 2008

Leckebusch GC, Ulbrich U, Fröhlich L, Pinto JG (2007) Property loss potentials for European midlatitude storms in a changing climate. Geophys Res Lett 34:L05703, doi:10.1029/2006GL027663

Murnane RJ, Barton C, Collins E, Donnelly J, Elsner J, Emanuel K, Ginis I, Howard S, Landsea C, Liu K-B, Malmquist D, McKay M, Michaels A, Nelson N, O'Brien J, Scott D, Webb T (2000) Model estimates hurricane wind speed probabilities. Eos Trans Amer Geophys Union 81:433–438

Pielke RA, Gratz J, Landsea CW, Collins D, Saunders MA, Musulin R (2008) Normalized hurricane damage in the United States 1900–2005. Nat Hazards Rev 9(1):29–42

Ropelewski CF, Jones PD (1997) An extension of the Tahiti-Darwin southern oscillation index. Monthly Weather Rev 115:2161–2165

Saunders MA, Lea AS (2005) Seasonal prediction of hurricane activity reaching the coast of the United States. Nature 434:1005–1008

Spiegelhalter DJ, Best NG, Gilks WR, Inskip H (1996) Hepatitis B: a case study in MCMC methods. In: Gilks WR, Richardson S, Spiegelhalter DJ (eds) Markov chain Monte Carlo in practice. Chapman & Hall/CRC, London, pp 21–43

Spiegelhalter DJ, Best NG, Carlin BP, van der Linde A (2002) Bayesian measures of model complexity and fit (with discussion). J Roy Stat Soc Ser B 64, Part q4:583–639

Walshaw D (2000) Modeling extreme wind speeds in regions prone to hurricanes. Appl Stat 49: 51–62

Chapter 7
A Statistical Analysis of the Frequency of United States and Eastern North Pacific Hurricanes Related to Solar Activity

Robert E. Hodges and James B. Elsner

Abstract In this chapter, we examine the statistical relationship between the frequency of United States and eastern North Pacific (ENP) hurricanes and the solar cycle. First, a relationship between the probability of a hurricane and sunspot numbers is shown that is conditional on ocean temperature. For years of above normal ocean temperatures, the probability of three or more hurricanes in the United States decreases from 40% to 20% as sunspot numbers increase. Second, a solar index that tracks intraseasonal variability in sunspot numbers is constructed and correlated with hurricane activity. The index is inversely related to the total sunspot numbers (SSN) and is significantly correlated with the probability of hurricanes and major hurricanes affecting the United States. The chances of at least one U.S. hurricane in the lowest and highest SSN anomaly season are 25% and 64%, respectively. The solar index is then used as a predictor of major hurricane frequency over the ENP where it is found that the chance of at least six major ENP hurricanes increases from about 1% when the solar index lowest to 28% when the index is highest.

Keywords UV radiation · Sunspots · Poisson process · Multivariate regression

1 Introduction

Tropical cyclones are different from their middle-latitude counterparts because of their warm central core. This warm core is generated and sustained by sensible heat realized from water vapor condensation in rising air. A supply of water vapor comes from the flow of air toward low pressures that remains in contact with the warm ocean surface. Indeed, the heat-engine theory of idealized tropical cyclones (Emanuel 1991) stipulates that the tangential wind speed of a tropical cyclone (intensity) is directly proportional to inflow temperature. However, it also stipulates that intensity is inversely related the outflow temperature aloft.

R.E. Hodges (✉) and J.B. Elsner
Department of Geography, The Florida State University, Tallahassee, FL 32306, USA
e-mail: reh3682@fsu.edu; jelsner@fsu.edu

J.B. Elsner et al. (eds.), *Hurricanes and Climate Change: Volume 2*,
DOI 10.1007/978-90-481-9510-7_7, © Springer Science+Business Media B.V. 2010

Exogenous controls on upper atmospheric temperatures include variations in ultraviolet (UV) radiation from the sun related to the presence of ozone. Increased UV radiation warms the upper troposphere and lower stratosphere, possibly decreasing the intensity of tropical cyclones. Elsner and Jagger (2008) (hereafter, EJ08) show an inverse relationship between the probability of a hurricane hitting the United States or the Caribbean and sunspot number (SSN) although a sun–hurricane relationship was postulated as early as the eighteenth century (Meldrum 1872; Poey 1873).

This chapter examines the case for a relationship between solar activity and the probability of ENP tropical cyclones. In Section 2, background information is introduced regarding solar variability and its possible relationship with hurricane activity. In Section 3 the data used in the study are described. In Section 4 we examine the sun–hurricane relationship using data since 1851 for US hurricanes, and data since 1953 for ENP major hurricanes. An index of solar activity is proposed, which articulates the two principal time scales of solar variability as the relate to hurricane intensity. For years with a large solar index there is a statistically significant increase in the probability of US hurricanes and ENP major hurricanes.

2 Background

The purpose of this chapter is to examine the inverse relationship between solar activity and US hurricanes, and whether it exists for hurricanes over the ENP tropical cyclone basin. We begin by considering how solar radiation fluctuates on time scales of days to years, and then we consider how these fluctuations might relate to hurricanes through the heat-engine theory.

Variation in solar radiation is a consequence of disturbances in the sun's magnetic field. These traveling disturbances are slightly cooler than their surroundings, appearing as dark blotches in the photosphere (surface layer of the sun). The sunspots tend to come in pairs on opposite sides of the sun's equator and wax and wane in frequency over 27 days or so. The number of overall sunspots varies directly with the strength of the magnetic field, which waxes and wanes over an 11-year period (Schwabe solar cycle). When the strength of the magnetic field reaches a minimum, the polarity of the field switches beginning a new solar cycle.

The heat-engine theory postulates that in an idealized thermodynamic environment a hurricane's maximum possible intensity (MPI) is proportional to the thermodynamic efficiency between input energy (entropy gain from ocean/atmosphere interaction) and outflow venting (mechanical dissipation) (Miller 1958; Emanuel 1991; Holland 1997; Bister and Emanuel 1998). An increase in ocean temperature as indexed by sea-surface temperature (SST) increases the thermodynamic potential energy available for convection, all else being equal. However, the sun's total solar irradiance varies directly with the number of sunspots (SSN) especially in the UV and extreme UV wavelengths. Upper-tropospheric warming is a known response to increases in UV radiation, especially over the tropics (Pap and Fox 2004; Labitzke 2002; Hood 2003). Subsequently, an active sun (many sunspots) leads to

warmer ocean temperatures over regions where hurricanes form (White et al. 1997), but also to a warmer upper troposphere due to additional UV radiation absorbed by ozone.

EJ08 unmask the solar variability effect on hurricanes over the North Atlantic basin. Over the western half of the basin ocean heat content is nearly always high enough to support tropical cyclogenesis; the limiting thermodynamic factor is upper tropospheric temperatures. There exists a significant negative relationship between daily SSN and hurricane intensity. Because of the region's already warm SSTs the extra energy from an active sun limits intensification via a warmer upper troposphere. Thus, a solar signal is detected in hurricanes by controlling for SST.

In the western North Atlantic, including the Caribbean Sea and Gulf of Mexico, ocean heat content is spatially expansive. Here the limiting thermodynamic factor for a tropical cyclone to reach maximum intensity is the temperature of the atmosphere near the tropopause. Since this covariate is inversely related to MPI, we note that an active sun warms the lower stratosphere, thereby decreasing potential intensity. The correlation between seasonally-averaged SSN and temperatures near the tropopause over the domain is consistently positive based on atmospheric data over the period 1948–2008 (EJ08). In contrast, the daily SSN is positively correlated with daily averaged tropical cyclone intensity for cyclones over the eastern North Atlantic.

One hypothesis for this geographic difference in the sun–hurricane relationship centers on the difference in the limiting factors associated with tropical cyclone intensity. Over the western Atlantic cloud top temperature appears to be the limiting factor, whereas over the eastern and central tropical Atlantic, the limiting factor in the thermodynamic potential for intensity is oceanic heat content. Since there is a direct relationship between SST and potential intensity, an active sun increases the shortwave flux to the ocean, raising the heat content and increasing the potential for tropical cyclone intensification. In fact, an autoregressive time series model of North Atlantic SST contains a component corresponding to the solar cycle (Elsner et al. 2008) with August through October averaged SST values generally higher (lower) during years of high (low) SSN.

Thus, there are two mechanisms at work. On the time scale of months to years, an increase in solar radiation helps warm the ocean leading to a positive correlation between SSN and hurricane frequency. In contrast, on the time scale of days to weeks, an increase in solar radiation helps to warm the upper troposphere leading to a negative correlation between SSN and hurricane frequency. The present work examines the sun–hurricane relationship by constructing an index that accounts for both the low (11-year Schwabe cycle) and high (27-day solar rotation) frequency variability inherent in the solar cycle.

3 Data

The National Hurricane Center (NHC) maintains the North Atlantic-basin hurricane database (HURDAT, or Best Track), containing the date, location, wind speed, and central pressure values for six-hourly observations of tropical cyclones since

1851 (Jarvinen et al. 1984). With refining work begun by Jose Fernandez–Partagàs (Partagás and Diaz 1996), over 5,000 additions and alterations have been approved by the NHC Best Track Change Committee in an effort to improve the accuracy of storm data between 1851–1910 (AOML 2008). Through the 2008 hurricane season, HURDAT identifies 1,362 unique North Atlantic storms ($\geq$17 m s^{-1}) and 819 individual hurricanes ($\geq$33 m s^{-1}), 283 of which struck the U.S. mainland.

For ENP hurricanes, data are obtained from the IBTrACS (Overview of the International Best Track Archive for Climate Stewardship) repository available online from the National Climatic Data Center (Knapp et al. 2009). The data set provides storm dates, locations, wind speeds, and central pressures as available. Information on these hurricanes is available back to 1957.

SSN used for this study are the international sunspot number as made available by the National Geographic Data Center. The data set was originally constructed by Solar Influences Data Analysis Center, World Data Center at the Royal Observatory of Belgium (Van Der Linden 2009). Reliable monthly observations extend back to 1749. Swiss astronomer Johann Rudolph Wolf introduced a daily measurement technique that observes both total spots observed and the quantity of their clusterings. The data set addresses observed error by incorporating a weighted average of cooperating observations.

North Atlantic SST used for this study are departures from the long-term average over the entire North Atlantic basin. The SST data are maintained by the Physical Sciences Division of the Earth System Research Laboratory, NOAA, and is derived from the Kaplan SST dataset (Kaplan et al. 1998). ENP SST data are from the El Niño 3 region of the tropical Pacific bounded between 90°W and 150°W longitudes and between 5°N and 5°S latitudes. Monthly data for this region are available back to 1950 courtesy of NASA's Global Change Master Directory.

Other covariates included in this study are the North Atlantic oscillation (NAO) and the Southern Oscillation index (SOI). The NAO May–June monthly index values are courtesy of the Climatic Research Unit, and are calculated from sea level pressures at Gibraltar and at a station over southwest Iceland (Jones et al. 1997). More information about the NAO as a covariate for U.S. hurricane activity is provided in Elsner and Jagger (2006). The SOI is defined as the normalized sea-level pressure difference between Tahiti and Darwin, and is obtained also from the Climatic Research Unit. The NAO, SST, and SOI are standardized to have a mean of zero and a standard deviation of one.

4 The Sun–Hurricane Relationship

4.1 Seasonal Variability

We begin with a look at the sun–hurricane relationship U.S.-affecting hurricanes. EJ08 assume a Poisson model for U.S. hurricane frequency and the model includes ocean temperature and SSN as covariates. Here we make the same Poisson

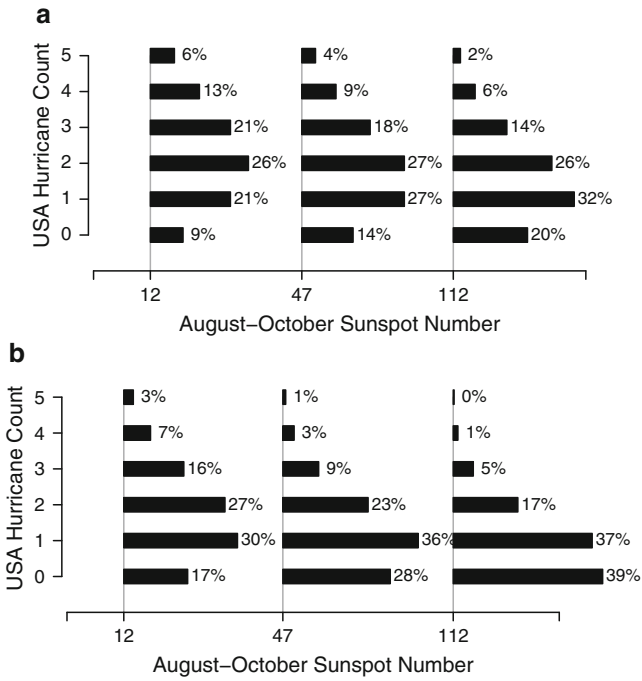

Fig. 1 Probability distribution of U.S. hurricanes. The probability is conditional on upper (**a**) and lower (**b**) tercile years of August–October Atlantic SST anomalies. Sunspot values are displayed as means of their respective terciles. Data spans from 1856 to 2008

assumption and look at the bivariate relationship between hurricanes and the SSN, conditional on the SST being above and below normal.

Figure 1 shows the probability distribution of hurricanes conditioned on values of August–October SSN for seasons of (a) above-normal and (b) below-normal SST, based on upper and lower tercile SST values averaged from June–November, respectively. For each hurricane count the percent bar represents the probability of that many hurricanes given the data and the Poisson rate. For above normal SST values amongst lowest August–October SSN, the probability of no U.S. hurricanes is 9%. This probability increases to 17% for the highest-tercile value of SSN. Conversely, the probability for exactly four hurricanes is 13% and 6% for lowest and highest SSN, respectively. Likewise, the probability of three or more hurricanes occurring dwindles from 40% to 22%.

In years of below normal SST values amongst lowest August–October SSN, the probability of one U.S. hurricanes occurring is 17%. This probability increases to 39% for highest-tercile SSN. Note that these probabilities are greater than those for warm years, but also demonstrate the same inverse relationship for increasing SSN. Conversely, the probability of exactly four hurricanes is 7% and 1% for lowest and highest SSN, respectively. Likewise, the probability of three or more hurricanes

dwindles from 26% to 6%. Note that the higher storm count probabilities are less than for those of the warm years. With hurricane intensity dependent on SST (e.g., Emanuel 1991; Holland 1997; Henderson-Sellers et al. 1998), the decrease in overall U.S. hurricane probabilities from warm SST to cold SST is expected. However, increasing SSN under both regimes support the heat-engine theory, in that warmed upper tropospheric temperatures inhibit hurricane intensification.

Another way to consider the relationship between SSN and hurricanes as modulated by SST is through the conditional correlation. Figure 2 shows the correlation between SSN and hurricane counts (U.S. and ENP) at different percentiles of SST. For U.S. hurricanes the correlation (Pearson product moment) over all years is -0.13 as indicated by the left-most point on the graph. The correlation is based on a sample size of $N = 153$ years. Each storm season is considered independent, and the standard error on the overall correlation estimate is 0.14, providing a 90% confidence interval on the correlation value of $(-0.264, +0.01)$. The confidence

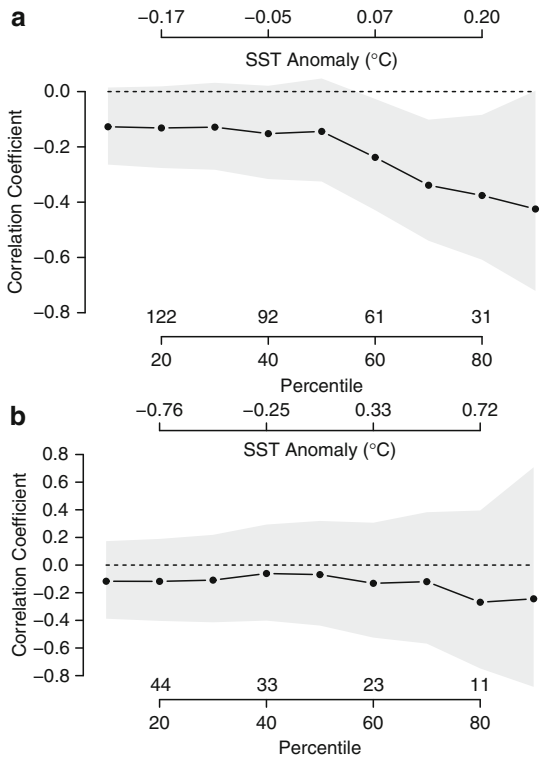

Fig. 2 Correlation between August–October SSN and hurricane counts. (**a**) U.S. hurricanes using data over the period 1856–2008 and (**b**) ENP major hurricanes using data over the period 1953–2008. The correlations are computed at increasing percentiles of SST. The *shaded region* represents the 90% confidence bound at each computed value. The number of seasons on which the correlation is based is shown above the abscissa

interval is shown by the width of the gray band in the figure. The next point on the graph to the immediate right is the correlation between hurricane counts and SSN after removing the coldest 20% (20th percentile) seasons. The 20th percentile SST value constitutes an anomaly of −0.17°C. The correlation changes negligibly, but with reduced sample size the confidence band widens. The sample size is plotted along the horizontal axis. The correlation does not change much for the coldest 50% of seasons. However, when 60% of the coldest seasons are removed, the correlation decreases to −0.24 with a 90% confidence interval of (−0.429, −0.027), based on a sample size of 61 years. The correlation continues to decrease as only the warmest years remain. With sample size decreasing accordingly the confidence bands expand, but the relationship between hurricane counts and August–October SSN remains statistically significant. The strengthening negative correlation indicates that the warmest core-season SSTs display the most suppressive effects from high core-season SSN. Warmer core-season SSTs provide a fertile developing ground for tropical development. As such, suppressed tropical development from high August–October SSN should be most evident at this time. Very similar results are obtained using the Spearman rank correlation. For ENP hurricanes the correlation is also negative but not statistically significant as the sample size is considerably smaller.

4.2 Within Season Variability

As mentioned, EJ08 suggest that the sun–hurricane relationship results from changes in upper-level temperatures due to changes in UV radiation. In short, increased solar activity – associated with sunspots – means more UV radiation reaching the Earth's upper atmosphere. This is corroborated by UV/upper-level temperature studies (Hood 2003) and solar activity/ozone production increases (Angell 1989; Calisesi and Matthes 2007). The extra radiation contributes to warming the air aloft (via the exothermic response from ozone photodissociation), thus decreasing the temperature differential between high and low elevations that would otherwise foster vertical motion and cloud growth. This thermodynamic explanation is in line theoretically with the observed changes in hurricane intensity concurrent with the diurnal cycle and net radiation changes (Hobgood 1986; Gray 1998). However, increased solar activity also contributes to the warming of the oceans (White et al. 1997, 1998), thus complicating the role solar variability plays in modulating hurricane activity.

Solar UV radiation at wavelengths near 200 nm is important for ozone production in the Earth's upper stratosphere. Variation in the amount of this radiation is best measured by the Mg II core-to-wing ratio (Mg II index) (Heath and Schlesinger 1986; Lean et al. 1997; Viereck and Puga 1999; Viereck et al. 2001) and is shown in Fig. 3. The time series reveals the well-known 11-year Schwabe cycle and short-term fluctuations (near 27 days) caused by the asymmetric distribution of active, rotating solar regions (plages and sunspots). The short-term fluctuations are

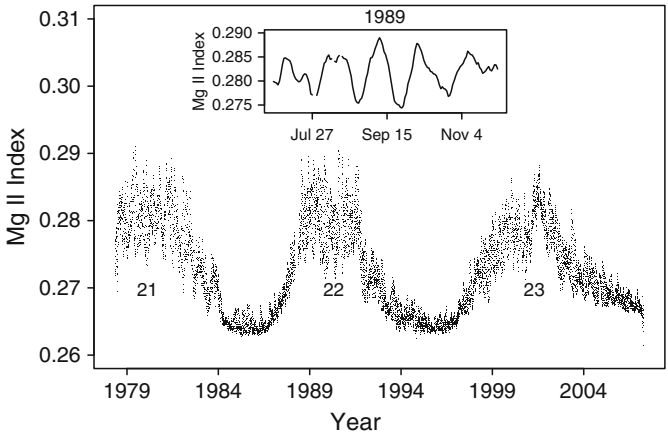

Fig. 3 Time series of daily Mg II core-to-wing ratio values. The series begins on November 7, 1997 and ends on October 14, 2007 (10,578 days). Values are plotted as points. Values below the 11-year peaks indicate the solar cycle number. Horizontal axis is labeled on July 1st of the year. The inset graph shows the Mg II index values as a time series over the hurricane season of 1989. Values are connected as a curve. Breaks in the curve indicate missing values. There are 1,331 missing values (12.6% of the days)

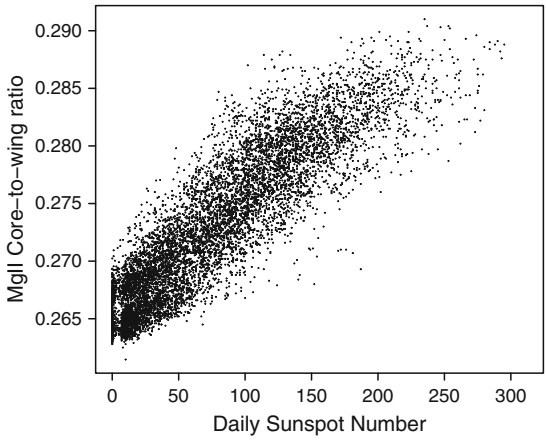

Fig. 4 Scatter plot of daily Mg II core-to-wing ratio values and SSN. The correlation between the two variables is +0.9

especially pronounced near solar maxima (Mg II index values exceeding 0.27). Although accurate estimates of UV radiation are only available since the advent of satellite measurements, the record of sunspots dating back to the eighteenth century is robust. The relationship between daily SSN and Mg II core-to-wing ratio is quite strong as shown in Fig. 4 with a correlation of +0.9, allowing us to use sunspot numbers as a reasonable proxy for UV radiation.

The impact of changes in UV radiation on upper tropospheric temperature is a fast process. Hood (2003) notes that tropical tropopause (~15 km) temperatures

vary in phase with incoming UV at a zero-day lag. As such the UV impact on hurricane is better represented on a short time scale compared with the sun's influence on warming the oceans, which occurs on a monthly to yearly timescale. Thus, if EJ08 are correct, we should be able to detect an immediate solar influence on hurricanes by using changes in UV radiation caused by the 27-day solar rotational period.

We do this by defining solar activity during the hurricane season as anomalous if the August–October SSN is substantially different from the SSN during the months of May–July and November. Formally, let $SSN_{anom} = SSN_{MJJN} - SSN_{ASO}$, where SSN_{MJJN} is the sunspot number averaged over May, June, July, and November, and SSN_{ASO} is the sunspot number averaged over August through October. Negative (positive) anomalies indicate solar activity during the hurricane season is greater (less) than the solar activity during the months prior to and after the season. In general, positive anomalies arise during hurricane seasons when the Schwabe cycle is near a peak but sunspot numbers are relatively low during August, September, or October in response to the phase and intensity of the 27-day solar rotation. Negative anomalies arise during hurricane seasons when the Schwabe cycle is near a trough but sunspot numbers are relatively high during August, September, or October. Thus there is a inverse relationship between total SSN during the hurricane season and the SSN anomaly as defined here.

Hurricane season peripheral month (May, June, July, November) SSN averages reflect the 11-year Schwabe cycle position most directly. It also demonstrates intraseasonal SST variability (Dima et al. 2005), and core month (August, September, October) SSN averages describe the impact of increased upper-level temperatures from increased UV radiation, decreasing a storm's environmental thermodynamic efficiency and, thus, maximum potential intensity (Emanuel 1988; Holland 1997; EJ08). Therefore, hurricane seasons characterized by positive SSN anomalies (higher inflow temperature and colder outflow temperatures) should correspond with greater hurricane activity.

Table 1 lists the top and bottom 10 hurricane seasons according to the value of the SSN anomaly using the years 1851–2008. The list includes the estimated number of U.S. and major U.S. hurricanes by year along with anomaly values of other covariates known to be related to hurricane activity. These covariates include the NAO (averaged over May and June prior to the hurricane season), the SOI (averaged over the hurricane season months of June through November), and North Atlantic SST (averaged over June through November). The NAO is a precursor signal for hurricane steering and the SOI is an indicator of the El Ninõ-Southern Oscillation and therefore wind shear and subsidence over the tropical Atlantic. Data for the SOI is available back only to 1866.

Of the top 10 positive SSN anomaly years, 2 years featured four U.S. hurricanes and 3 years featured three hurricanes. There was at least one hurricane in each of the top 10 anomalous years. In contrast, half of the bottom 10 years had no hurricanes affect the United States and four had only one hurricane. The mean hurricane rate for

Table 1 SSN anomalies and U.S. hurricanes: 1851–2008. The years are listed according to the value of the 10 most positive SSN anomalies (*top*) and 10 most negative anomalies (*bottom*). Corresponding columns include the number of U.S. hurricanes (US), major U.S.hurricanes (MUS), the NAO as a May–June average anomaly, the SOI as a June–November average anomaly, and SST as a June–November average anomaly. The mean values in each column are given in bold

SSN Anomaly	US	MUS	Year	NAO	SOI	SST
+28.7	3	1	1999	+1.21	+0.43	+0.19
+27.9	1	0	1984	−1.01	−0.22	−0.26
+26.6	2	1	1938	+0.31	+1.19	+0.29
+25.3	4	1	1906	−1.72	+0.99	−0.05
+21.7	4	2	1916	−1.88	+1.06	−0.06
+20.8	1	1	1885	+0.96	−1.23	+0.01
+20.1	2	1	1894	+0.70	−0.29	−0.27
+19.0	2	1	1929	+0.31	+0.30	−0.12
+18.3	3	1	1871	−1.94	+0.23	+0.01
+17.9	3	2	1950	−0.24	+1.59	+0.01
+22.6	**2.5**	**1.1**	**1927**	**−0.33**	**+0.4**	**−0.03**
−37.9	0	0	1981	−0.76	0.41	−0.07
−27.4	0	0	1990	−0.39	−0.31	+0.07
−26.9	6	0	1858	+0.15	−	−0.17
−26.4	1	0	1909	+1.38	+0.58	−0.06
−25.0	1	1	1957	−0.82	−0.60	+0.14
−24.8	4	1	1880	−0.67	+0.75	+0.13
−22.8	0	0	2001	−0.71	−0.18	+0.25
−21.7	1	1	1958	−0.17	−0.14	+0.21
−20.6	0	0	1978	+0.26	+0.01	−0.19
−20.1	1	0	1956	+2.9	+0.93	−0.09
−25.4	**1.4**	**0.3**	**1947**	**+0.12**	**+0.16**	**+0.02**

positive SSN anomaly years is 37% higher than the overall mean rate (1.8 hur/year). For negative SSN anomalies the mean rate is 56% lower. The mean major U.S. hurricane rates is 72% above the average rate (0.6 hur/year) during high SSN anomaly years and 53% below during low SSN anomaly years. Mean values of the SST and SOI over these two contrasting periods indicate that these variables are clearly not able to explain the difference in hurricane rates, however the NAO might be a confounding variable. This is examined later in the context of a multivariate regression model.

Table 2 lists the top and bottom 10 major hurricane seasons according to the value of the SSN anomaly for the years 1953–2008. The list includes the estimated number of major (1) East Pacific and (2) U.S. hurricanes and the corresponding year of occurrence. Interestingly enough, the mean major U.S. hurricane rate is the same as that of those listed in Table 1. Over the entirety of this period, mean East Pacific major hurricane rate is 3.3 storms. For the most positive anomaly seasons, the mean

Table 2 SSN anomalies and major ENP and U.S. hurricanes: 1953–2008. The years are listed according to the value of the 10 most positive SSN anomalies (*top*) and 10 most negative anomalies (*bottom*). Corresponding columns include the number of major ENP (MEP) and the number of major U.S. (MUS) hurricanes. The mean values in each column are given in bold

SSN Anomaly	MEP	MUS	Year
+28.7	2	1	1999
+27.9	9	0	1984
+17.7	2	0	2000
+17.5	1	1	1970
+17.2	9	1	1983
+13.5	8	2	1985
+12.7	2	4	2005
+10.8	9	1	1993
+9.1	0	1	1969
+8.4	6	0	1971
+16.3	**4.8**	**1.1**	**1985.9**
−37.9	1	0	1981
−27.4	6	0	1990
−25.0	1	1	1957
−22.8	2	0	2001
−21.7	0	1	1958
−20.6	6	0	1978
−20.1	0	0	1956
−18.7	3	0	1988
−15.6	4	1	1979
−13.6	4	0	1987
−22.3	**2.7**	**0.3**	**1977.5**

rate of 4.8 major hurricanes represents a 45% increase over the mean rate. For the most negative anomaly seasons, the mean rate of 2.7 major hurricanes represents an 18% decrease over the mean rate.

The results suggest that indeed variations in solar activity appear to influence seasonal hurricane activity; not only the probability of a U.S. hurricane but also the probability of a major hurricane over the ENP. Since other factors are known to affect hurricane probability for the United States next we consider the sun–hurricane relationship using a multivariate model.

4.3 Multivariate Models of Seasonal Hurricane Frequency

To examine the SSN anomaly as a predictor for hurricanes we need a multivariate setting. This is best achieved through the use of a statistical regression model. Separate models are developed for hurricanes and major hurricanes that make landfall in the United States. The model of choice is the generalized linear model with a logarithmic link function (see EJ08). This is the same as a Poisson regression model. The model covariates include May–June NAO (as an indicator of steering flow), the SOI (as an indicator of Atlantic basin shear), SST (as an indicator of ocean heat content), and the SSN anomaly (as an indicator of thermodynamic potential).

The NAO is the atmospheric pressure difference between the permanent Icelandic Low and semi-permanent Azores High, and has been shown to be statistically significant in prediction models of U.S. hurricane landfall probability (Elsner and Kocher 2000; Elsner and Jagger 2006). When the NAO values are below normal the subtropical high pressure region tends to be located farther south and west of its normal position. With this setup hurricanes that form over the central Atlantic and eastern Caribbean tend to track westward toward the Greater Antilles, the Bahamas, and the United States. The SOI is also an atmospheric pressure difference, but between Tahiti and Darwin, Australia that is positively related to North Atlantic hurricane activity (Gray 1984). When the SOI is negative the tropical Pacific is experiencing El Niño conditions, which tends to inhibit hurricanes over the North Atlantic due to wind shear. SST as a proxy for ocean heat content is positively related to hurricane activity (Holland 1997).

We create three separate Poisson regression models, one for U.S. hurricanes, one for major U.S. hurricanes, and another for major ENP hurricanes. Table 3 lists the parameters and the output of an analysis of deviance for the U.S. and major U.S. hurricane models. The data for the model are from the period 1866–2008, inclusive. The coefficient on the SSN anomaly term indicates a positive relationship with hurricane frequency, consistent with the relationship proposed from the analysis of Table 1. Model covariates are added sequentially to the model. Model parameters and analysis of deviance for the first three covariates were originally shown to be statistically significant in EJ08. The SSN anomaly is determined to be the second most important variable (based on the magnitude of deviance) toward explaining the U.S. hurricanes. The model for major USA hurricanes is similar, but here the SSN anomaly term is the most important variable. Model adequacy is checked by examining the residual deviance after all terms are included. For the hurricane model

Table 3 Poisson regression model of U.S. (*top*) and major U.S. (*bottom*) hurricanes. The columns include the parameter estimate, the deviance, the residual degrees of freedom (dof), the residual deviance and the p-value. All p-values are less than 0.1 indicating the importance of the term to the model after accounting for the terms already in the model

Term	Estimate	Deviance	Residual dof	Residual Deviance	p-Value
U.S. hurricanes					
NULL	0.498		142	180.756	
NAO	−0.176	12.166	141	168.589	0.005
SOI	+0.157	6.254	140	162.336	0.022
SST	+0.665	4.186	139	158.150	0.034
SSN_{anom}	+0.028	6.447	138	151.703	0.011
Major U.S. hurricanes					
NULL	−0.604		142	152.929	
NAO	−0.190	5.654	141	147.275	0.073
SOI	+0.256	5.936	140	141.338	0.022
SST	+1.144	4.424	139	136.914	0.030
SSN_{anom}	+0.047	6.624	138	130.290	0.010

Table 4 Same as Table 3 except for major ENP hurricanes

Term	Estimate	Deviance	Residual dof	Residual Deviance	p-Value
Major ENP hurricanes					
NULL	1.089		52	168.003	
SOI	−0.295	10.313	51	157.690	<0.001
SSN_{anom}	+0.015	6.026	50	151.633	0.014

the residual deviance is 151.7 with 138 degrees of freedom (dof). The p-value as evidence in favor of model adequacy from a χ^2 distribution with this quantile value and this dof is 0.2 indicating no strong evidence against model adequacy. The p-value on the residual deviance of the major hurricane model is 0.7 again providing no evidence against model adequacy.

Table 4 lists the parameters and the output of an analysis of deviance for the major ENP hurricane model. The data for the model are from the period 1953–2008. As mentioned earlier, the relationship between solar activity and all ENP hurricanes is negligible. However, a statistical significant relationship exists for major ENP hurricanes. The coefficient on the SSN anomaly term again indicates a positive relationship with major hurricane frequency, consistent with the findings for U.S. hurricanes. SST from June–November for the region were originally included as an additional covariate in the model, but were determined to be insignificant and, thus, removed. SOI values (June–November averaged) were demonstrated as best explaining the changes in the major hurricane occurrence based on the overall decrease in model deviance, buttressing what is already known about ENP hurricanes and El Niño (Chu 2004). However, SSN anomalies also demonstrate a significant role in describing strong hurricanes over this part of the world.

The models can be used for predicting the probability of a hurricane given values for the covariates. Here we contrast the probability predictions when the SSN anomaly are highest and lowest. Figure 5 illustrates how the probability of a U.S. hurricane and a major ENP hurricane changes given the two models and holding the other covariates in the model at their mean values. For the U.S. hurricane model the probability of no hurricanes during the season is twice as likely during the lowest SSN anomaly season compared with the probability during the highest SSN anomaly season. In fact, the lowest SSN anomaly season has 3:1 odds of no hurricanes striking the United States. In contrast the chances of at least one hurricane affecting the U.S. in the lowest and highest SSN anomaly season are 25% and 64%, respectively.

For the major ENP hurricane model the difference in annual probability between extremes of the SSN anomalies is even more dramatic. Assuming the SOI value is zero, the model predicts a 16% chance of no major hurricanes when the SSN anomalies are their lowest compared with only a 1% of not seeing a major hurricane when the anomalies are their largest. Conversely, the predicted probability of six or more major hurricanes is 28% in the very highest SSN anomaly season compared with only 1% in the very lowest SSN anomaly season. The results are compelling in showing a strong solar signal in major ENP hurricanes. This finding is new.

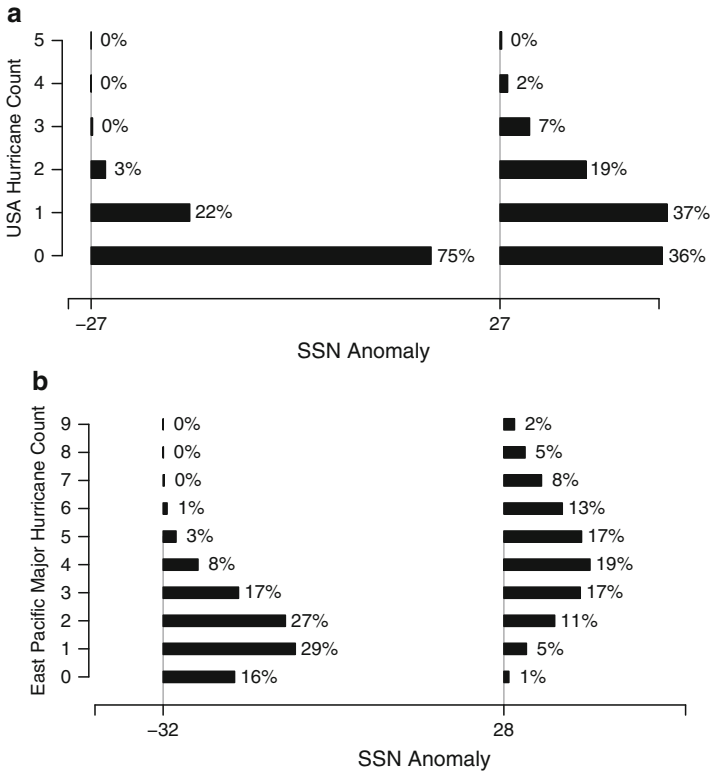

Fig. 5 Predicted probability distributions. The models include (**a**) U.S. hurricanes and (**b**) ENP major hurricanes. Predictions are made using a generalized linear regression model (Poisson) for values of SSN anomalies corresponding to the 1st and 99th percentiles keeping the other covariates at neutral values. The quantile SSN anomalies are different because of differing number of years

5 Summary and Conclusions

Here we examined the evidence for a sun–hurricane relationship that was identified recently by EJ08. We first looked at seasonal activity and noted a consistent inverse relationship between U.S. hurricane probabilities and SSN. The relationship occurs for both warm and cold years as defined by Atlantic SSTs. Since it has been suggested that the sun–hurricane relationship arises due to changes in upper tropospheric temperature (UTT) associated with variations in the ultra-violet (UV) radiation, next we show the strong correlation between sunspot numbers and a core-to-wing ratio as a satellite-derived measure of the UV flux. While the findings were not statistically significant, the negative correlation between SSN and ENP major hurricanes was consistent with North Atlantic findings.

Since the ocean temperatures respond on a slower timescale to changes in total solar irradiance we derive a SSN anomaly that captures a portion of the

intra-hurricane season variability in solar activity by subtracting the SSN averaged over August through October from the SSN averaged over May, June, July, and November. The SSN anomaly is used to divide the hurricane record from 1851 to 2008 into top and bottom years with respect to their anomaly values. As expected, years with positive SSN anomalies featuring high peripheral month sunspot numbers but low in-season numbers have, on average, significantly more (68%) U.S. hurricanes. This relationship is checked over all years by controlling for SST, El Niño, and the NAO in a statistical regression model. The SSN anomaly is statistically significant in models for U.S. hurricanes, major U.S. hurricanes, and major ENP hurricanes.

The study has extended our understanding of the sun–hurricane relationship by developing an SSN anomaly index and by considering hurricanes over the ENP. More work is needed to better understand this relationship and a next step will be to consider whether there is a solar signal in global tropical cyclone activity.

Acknowledgements The authors thank Thomas H. Jagger for his help with some of the statistics. Thanks are extended to the SIDC for the sunspot data and to the NHC for HURDAT. All statistical modeling was done using R (R Development Core Team 2009). The work is supported by the USA National Science Foundation (ATM-0738172) and the Risk Predicition Initiative (RPI-08-02-002) of the Bermuda Institute for Ocean Sciences. Interpretations and opinions expressed here are those of the authors and do not necessarily reflect those of the funding agencies.

References

Angell J (1989) On the relation between atmospheric ozone and sunspot number. J Clim 2: 1404–1416

Atlantic Oceanic and Meteorological Laboratory — National Oceanic and Atmospheric Administration (2008) HURDAT Re-analysis. Retrieved on 2008-03-21. Web site: http://www.aoml.noaa.gov/hrd/hurdat/

Bister M, Emanuel K (1998) Dissipative heating and hurricane intensity. Meteor Atmos Phys 50:233–240

Calisesi Y, Matthes K (2007) The middle atmospheric ozone response to the 11-year solar cycle. Space Sci Rev 125(1–4):273

Chu P (2004) ENSO and tropical cyclone activity. In: J Murnane, Liu K (eds) Hurricanes and typhoons: past, present, and future. Columbia University Press, New York, pp 297

Dima M, Lohmann G, Dima I (2005) Solar-induced internal climate variability at decadal time series. Int J Climatol 25:713–733

Elsner J, Jagger T (2006) Prediction models for annual U.S. hurricane counts. J Clim 19: 2935–2952

Elsner J, Jagger T (2008) United States and Caribbean tropical cyclone activity related to the solar cycle. Geophys Res Lett 35:L18705

Elsner J, Kocher B (2000) Global tropical activity: a link to the North Atlantic oscillation. Geophys Res Lett 27:129–232

Emanuel K (1988) The maximum potential intensity of hurricanes. J Atmos Sci 45:1143–1155

Emanuel K (1991) The theory of hurricanes. Annu Rev Fluid Mech 23:179–196

Fernańdez-Partagaś J, Diaz HF (1996) Atlantic hurricanes in the second half of the nineteenth century. Bull Amer Meteor Soc 77:2899–2906

Gray W (1984) Atlantic seasonal hurricane frequency Part I: El Nino and 30 mb quasi-biennial oscillation influences. Mon Wea Rev 112:1649–1668

Gray W (1998) The formation of tropical cyclones. Meterol Atmos Phys 67:37–69

Heath D, Schlesinger B (1986) The Mg 280 nm doublet as a monitor for changes in solar ultraviolet irradiance. J Geophys Res 91:8672–8688

Henderson-Sellers A, Zhang H, Berz G, Emanuel K, Gray W, Landsea C, Holland G, Lighthill J, Shieh S, Webster P, McGuffie K (1998) Tropical cyclones and global climate change: a post-IPCC assessment. Bull Amer Meteor Soc 79:19–38

Hobgood J (1986) A possible mechanism for the diurnal oscillations of tropical cyclones. J Atmos Sci 43(23):2901–2922

Holland G (1997) The maximum potential intensity of tropical cyclones. J Atmos Sci 54:2519–2541

Hood L (2003) Thermal response of the tropical tropopause region to solar ultraviolet variations. J Geophys Res 30(23):2215

Jarvinen B, Neumann C, Davis M (1984) A tropical cyclone data tape for the North Atlantic Basin, 1886–1983: Contents, limitations, and uses. NOAA Tech Memo, NWS NHC-22, pp 21, National Oceanic & Atmospheric Administration, Washington, D.C.

Jones PD, Jónsson T, Wheeler D (1997) Extension to the North Atlantic Oscillation using early instrumental pressure observations from Gibraltar and South-West Iceland. Int J Climatol 17:1433–1450

Kaplan A, Cane MA, Kushnir Y, Clement AC, Blumenthal MB, Rajagopalan B (1998) Analyses of Global Sea Surface Temperature 1856–1991. Geophys Res 103:18567–18589

Knapp K, Kruk M, Levinson D, Gibney E (2009) Archive compiles new resource for global tropical cyclone research. Eos Transactions AGU 90(46), doi:10.1029/2009EO060002

Labitzke K (2002) The global signal of the 11-year solar cycle in the stratosphere: observations and models. J Atmos Sol-Terr Phy 64(2):203–210

Lean JL, Rottman GJ, Kyle HL, Woods TN, Hickey JR, Puga LC (1997) Detection and parameterization of variations in solar mid- and near-ultraviolet radiation (200-400 nm). J Geophys Res 102:29,939–29,956

Meldrum C (1872) On a periodicity in the frequency of cyclones in the Indian Ocean south of the equator. Nature 6:357–358

Miller B (1958) On the maximum intensity of hurricanes. J Meteor 15:184–195

Pap J, Fox P (2004) Solar variability and its effects on climate. AGU Press, Washington, pp 366

Poey A (1873) Sur les rapports entre les taches solaires et les ourages des Antilles de l'Atlantique-nord et de l'Ocean Indien sud. Compt Rend 77:1223–1226

R Development Core Team (2009) R: a language and environment for statistical computing and graphics. R Found for Stat Comput Vienna Austria. Available at http://www.R- project.org

Van der Linden R, the SIDC team (2009) Online catalogue of the sunspot index. Retrieved on 02-01-2009 Web site: http://sidc.oma.be/html/sunspot.html

Viereck RA, Puga LC (1999) The NOAA Mg II core-to-wing solar index: Construction of a 20-year time series of chromospheric variability from multiple satellites. J Geophys Res 104:9995–10,005

Viereck R, Puga L, McMullin D, Judge D, Weber M, Tobiska WK (2001) The Mg II index: A proxy for solar EUV. Geophys Res Lett 28:1343–1346

White W, Lean J, Cayan D, Dettinger M (1997) Response of global upper ocean temperature to changing solar irradiance. J Geo Res 102:3255–3266

White WB, Cayan DR, Lean J (1998) Global upper ocean heat storage response to radiative forcing from changing solar irradiance and increasing greenhouse gas/aerosol concentrations. J Geo Res 103:21355–21366

Chapter 8
Regional Typhoon Activity as Revealed by Track Patterns and Climate Change

Pao-Shin Chu, Xin Zhao, and Joo-Hong Kim

Abstract In this chapter the Joint Typhoon Warning Center (JTWC) best-track records of western North Pacific tropical cyclones (TC) are classified by track type using the expectation-maximization (EM) algorithm. The first three types are labeled as straight movers (A, B, and C), followed by four recurved types (D, E, F, and G), and one mixed straight-recurved type (H). For each type, a log-linear regression model is then applied to detect abrupt shifts in the time series of TC attributes including frequency, lifespan, intensity, and accumulated cyclone energy (ACE). In this chapter, results indicate that the major climate shift in 1976/1977 may have affected storm's counts for two track patterns (types F and H). All eight types exhibit at least one abrupt shift in their duration since 1945, with three types (A, C, and H) showing a common shift in 1972. For a majority of the eight types, the storms' mean lifetime became longer after the shift. TC intensity shows a prevalence of abrupt shifts in the 1970s. For type D, its intensity has undergone several changes (1972, 1988, and 1998) with stronger intensity since the last shift. Because of its proximity to the East Asian landmasses and its abundance in numbers, the increasing intensity of type D since 1998 is a concern for Taiwan, the east China coast, the Philippines, Japan, and Korea. For ACE, the signal is mixed. To draw more definitive conclusions, a consistency check with another best-track record is called for.

Keywords Typhoon track clusters · Regional typhoon activity · Climate change

P.-S. Chu (✉)
Department of Meteorology, 2525 Correa Road, University of Hawaii, Honolulu, HI 96822, USA
e-mail: chu@hawaii.edu

X. Zhao
Department of Meteorology, School of Ocean and Earth Science and Technology, University of Hawaii, Honolulu, HI 96822, USA
e-mail: xzhao@sanjole.com

J.-H. Kim
Department of Atmospheric Sciences, National Taiwan University, Taipei, Taiwan
e-mail: jhkim004@gmail.com

J.B. Elsner et al. (eds.), *Hurricanes and Climate Change: Volume 2*,
DOI 10.1007/978-90-481-9510-7_8, © Springer Science+Business Media B.V. 2010

1 Introduction

There is a growing interest in knowing the impact of climate change on tropical cyclone (TC) activity. This interest stems from the fact that tropical storms are among the most destructive of natural disasters. As the world becomes warmer, it is conceivable that the intensity, frequency, tracks, and location of occurrences of tropical storms will be altered from the present-day climate. Using the Joint Typhoon Warning Center (JTWC) best-track records or satellite data, Emanuel (2005), Webster et al. (2005), and more recently Elsner et al. (2008) demonstrated that historical storm intensity has increased dramatically in the western North Pacific (WNP) as well as the North Atlantic. In particular, Webster et al. (2005) noted a large increase in the frequency for the strongest TC categories (4 and 5) in the WNP over the last 30 years: 25 such storms were found in the first 15 years (1975–1989) but the 41 strongest storms occurred during the second 15 years (1990–2004). However, this large trend has been questioned due to large interdecadal variations in the number of intense TCs (Chan 2006) or possible measurement errors in the dataset (Knaff and Zehr 2007). In addition, based on the best-track records over a more recent 20-year (1986–2006), Klotzbach (2006) found small or no trends using alternative analysis methods. Besides the variation in intensity, TC induced rainfall in the WNP also appears to have undergone long-term variations with decadal signatures (Kim et al. 2006; Lau et al. 2008).

Given this dramatic increase over the entire basin as noted by Webster et al. (2005), it is of interest to examine whether there is any change in TC activity at the regional level within the WNP as this is a huge basin and TCs have preferred tracks. Some of them form over the Philippine Sea and track westward to the South China Sea, southern China, and/or Vietnam. Others form over the tropical Pacific and move northwestward toward Taiwan and/or China's coast or recurve toward Japan and Korea (Tu et al. 2009). This study examines the temporal changes in regional typhoon activity over the WNP during the past 60 years using the 6-h best track data from the JTWC. A mixture Gaussian model is built for WNP typhoon tracks based on which historical typhoon tracks are categorized using a clustering algorithm. Eight track patterns are identified and the TC frequency, intensity, lifespan, and ACE of these eight patterns are individually examined for temporal changes over the last 60 years.

2 Methods

2.1 Clustering Methodology

Our TC track clustering method is based on the mixture Gaussian model. A key feature of the mixture Gaussian model is its ability to model multimodal densities while adopting a small set of basic component densities. Finite mixture models

have been widely used for clustering data in a variety of areas such as large-scale atmospheric circulation (Camargo et al. 2007). In this study, we assume that there are a few distinct path track types characterizing TC tracks in the WNP. For each TC track path, we model it as a second-order polynomial function of the lifetime of this TC. The basic assumption we impose here is that for each specific track type, the set of coefficient of this polynomial function is jointly Gaussian distributed. Each TC track type has its unique distribution parameter. Therefore, the space spanned by the parameters of this track type model is a linear combination of a set of Gaussian distribution, or a mixture Gaussian distribution model.

We assume there are n observed track records at 6-h intervals for a given TC. For each record, there will be three features reported – latitude, longitude, and the time. We will denote the path record of a TC by

$$\mathbf{z} = [\mathbf{z}_{lat}, \mathbf{z}_{long}] = \begin{bmatrix} z_{1,lat} & z_{1,long} \\ \dots & \dots \\ z_{n,lat} & z_{n,long} \end{bmatrix} \tag{1a}$$

where $z_{i,lat}$ and $z_{i,long}$ for $i = 1, \dots, n$ represent the ith latitude and longitude record, respectively. We then denote the relative observed time vector for the second order polynomial function by

$$\mathbf{T} = \begin{bmatrix} 1 & t_1 & t_1^2 \\ \dots & \dots & \dots \\ 1 & t_n & t_n^2 \end{bmatrix} \tag{1b}$$

where t_i for $i = 1, \dots, n$ represents the time for the ith records of this TC relative to the first record. We further assume that there are K distinct TC track types in the WNP, where K is assumed to be a constant throughout this study. With definitions (1a) and (1b), provided that this TC is categorized as type k, $1 \le k \le K$, the linkage between the passage and relative time is governed by the following formula

$$\mathbf{z} = \mathbf{T}\boldsymbol{\beta}^{\mathbf{k}} + \boldsymbol{\varepsilon}, \text{ where } \boldsymbol{\beta}^{\mathbf{k}} = \begin{bmatrix} \beta^k_{0,lat} & \beta^k_{0,long} \\ \beta^k_{1,lat} & \beta^k_{1,long} \\ \beta^k_{2,lat} & \beta^k_{2,long} \end{bmatrix} \text{ and } \boldsymbol{\varepsilon} \sim N(\mathbf{0}, \boldsymbol{\Sigma}^{\mathbf{k}}). \tag{1c}$$

In (1c), the parameter set $\boldsymbol{\beta}^{\mathbf{k}}$ is distinct from other TC types. With the model given in (1) for type k, intuitively we can see that the zero-order coefficient dual provides the mean genesis location of this type; the first-order term features the characteristic direction of this path type; the second-order type will determine the recurving shape of the typical path of this type; and the covariance matrix (Σ) in (1c) determines the spread of a particular type. The noise term in (1), $\boldsymbol{\varepsilon}_i$, is multivariate Gaussian with zero mean and a 2 by 2 covariance matrix, $\boldsymbol{\Sigma}_k$. The covariance matrix $\boldsymbol{\Sigma}_k$ contains diagonal elements $\sigma^2_{0.k}$ and $\sigma^2_{1.k}$, which are the noise variances for each latitude and longitude observation, respectively, in the cluster k. For simplicity the cross covariance of $\boldsymbol{\Sigma}_k$ is set to 0.

The conditional density for the ith cyclone, conditioned on membership in the cluster k, is thus defined as

$$P(\mathbf{z}_i|\mathbf{T}_i, \boldsymbol{\theta}_k) = (2\pi)^{-n_i} |\boldsymbol{\Sigma}_k|^{-n_i/2} \exp\left\{-\mathrm{tr}[(\mathbf{z}_i - \mathbf{T}_i\boldsymbol{\beta}_k)\boldsymbol{\Sigma}_k^{-1}(\mathbf{z}_i - \mathbf{T}_i\boldsymbol{\beta}_k)']/2\right\} \tag{2}$$

In (2), we adopt the notation $\boldsymbol{\theta}_k = \{\boldsymbol{\beta}_k, \boldsymbol{\Sigma}_k\}$. This distribution leads to the marginal regression mixture model with $K = 8$ clusters,

$$P(\mathbf{z}_i|\mathbf{T}_i) = \sum_{k=1}^{K} \alpha_k P(\mathbf{z}_i|\mathbf{T}_i, \boldsymbol{\theta}_k). \tag{3}$$

In (3), α_k is the probability of cluster k, and $\sum_{k=1}^{K} \alpha_k = 1$. If we let $\mathbf{Z}' = [\mathbf{z}_1', \mathbf{z}_2', \ldots, \mathbf{z}_N']$ be the complete set of all observed TC trajectories and $\mathbf{T}' = [\mathbf{T}_1', \mathbf{T}_2', \ldots, \mathbf{T}_N']$ be the associated measurement times, then the full probability density of $\mathbf{Z}$ given $\mathbf{T}$, which is also known as the conditional likelihood, is

$$P(\mathbf{Z}|\mathbf{T}) = \prod_{i=1}^{N} \sum_{k=1}^{K} \alpha_k P(\mathbf{z}_i|\mathbf{T}_i, \boldsymbol{\theta}_k). \tag{4}$$

Given a set of a total N TC records, $\{\mathbf{z}_i, \mathbf{T}_i | i = 1, \ldots, N\}$, to derive the maximum likelihood estimation of all model parameters and class type, we resort to the Expectation-Maximization (EM) algorithm. In the E-step, we calculate the membership probability of each type for each TC as follows

$$w_{i,k} = \frac{\alpha_k f(\mathbf{z}_i|\mathbf{T}_i\boldsymbol{\beta}^{\mathbf{k}}, \boldsymbol{\Sigma}^{\mathbf{k}})}{\sum_{j=1}^{K} \alpha_j f(\mathbf{z}_i|\mathbf{T}_i\boldsymbol{\beta}^{\mathbf{j}}, \boldsymbol{\Sigma}^{\mathbf{j}})}, \ i = 1, \ldots, N \tag{5}$$

where $\alpha_k = f(\mathrm{k})$ is the prior probability of type k. Apparently, the membership probability of a TC in (5) is virtually the Bayes' posterior probability of each track type given all model parameter sets. If $\mathbf{w}_{i,k} = w_{i,k}\mathbf{1}_{n_i}$, where n_i denotes the record length of the ith TC and $\mathbf{1}_{n_i}$ represents the n_i vector of ones, we define a new diagonal matrix $\mathbf{W}^{\mathbf{k}} = \mathrm{diag}([\mathbf{w}_{1,k}', \mathbf{w}_{2,k}', \ldots, \mathbf{w}_{N,k}'])$ for each track type k. In the M-step, we then calculate the following estimation for the model parameter set of each type.

$$\hat{\boldsymbol{\beta}}^{\mathbf{k}} = (\mathbf{T}'\mathbf{W}^{\mathbf{k}}\mathbf{T})^{-1}\mathbf{T}'\mathbf{W}^{\mathbf{k}}\mathbf{Z} \tag{6a}$$

$$\hat{\alpha}_k = \frac{1}{S}\sum_{i=1}^{N} n_i w_{i,k} \tag{6b}$$

$$\mathbf{\Sigma}^{\mathbf{k}} = \frac{1}{S}\frac{(\mathbf{Z} - \mathbf{T}\boldsymbol{\beta}^{\mathbf{k}})'\mathbf{W}^{\mathbf{k}}(\mathbf{Z} - \mathbf{T}\boldsymbol{\beta}^{\mathbf{k}})}{\hat{\alpha}_k} \tag{6c}$$

In (6), $\mathbf{Z}' = [\mathbf{z}_1, \mathbf{z}_2, \ldots, \mathbf{z}_N]'$, $\mathbf{T}' = [\mathbf{T}_1, \mathbf{T}_2, \ldots, \mathbf{T}_N]'$, where $\mathbf{z}$, $\mathbf{T}$ are defined in (1) and the subscript represents the index of a TC; and $S = \sum_{i=1}^{N} n_i$ is the total number of observations.

If the number of clusters, K, is provided, given an initial setting of the model parameters and with multiple iterations of (5) and (6), the proposed EM algorithm will converge to a fixed set of parameter estimation. These convergence values are not necessarily the global best estimation and are determined by the initial starting values. Therefore, we apply multiple different initial values and choose the set of estimation with the maximum likelihood. It is also noteworthy that the cluster problem presented hereby is essentially a missing value problem in which the indicators of class identification are not available.

2.2 Change-Point Analysis

In this study we analyze the time series of annual TC counts, average life spans, average ACE, and average intensity to determine any abrupt shifts. All these series are positive numbers and can be approximated by a gamma distribution. On the other hand, it is well known that a logarithm of a gamma distribution can be well approximated by a Gaussian distribution. In view of this fact, we adopt a (generalized) log linear regression model to determine abrupt shifts (or change-points) of the aforementioned time series (Elsner et al. 2000; Chu 2002). More elaborately, change-point analysis can be cast in the Bayesian framework to explicitly provide the posterior probabilities of the change points as a function of time (e.g., Chu and Zhao 2004; Zhao and Chu 2006). Assuming that a time series is denoted by X_i, $i = 1, \ldots, n$, we calculate the latent set $Y_i = \log(1 + X_i)$. We then define the following function

$$S_i(l) = \begin{cases} 0 & i < l \\ 1 & i \geq l \end{cases}, \qquad \text{for } 1 < l < n. \tag{7a}$$

We thereby adopt the following linear regression model

$$Y_i = c_0(l) + c_1(l)S_i(l) + \varepsilon_i(l). \tag{7b}$$

For each l, we use a Least Square Error (LSE) algorithm to compute the intercept $c_0(l)$ and slope $c_1(l)$. Subsequently we define t-ratio as follows.

$$t(l) = \hat{c}_1(l)/se(\hat{c}_1(l)) \tag{7c}$$

In (7c), $\hat{c}_1(l)$ is the estimated slope term and $se(\hat{c}_1(l))$ the estimated standard error of this term. If $t(m) = \max\{t(l), l = 2, \ldots, n-1\}$ is larger than a critical value, we set index m as a change-point. The critical value is obtained from a t-distribution. For example, this critical value is set as 2.65 for a 99% confidence level. After finding the first change-point$m$, the process (7) is repeated with a new response series $Y_i^* = Y_i - c_1(m)S_i(m)$, which yields the second change-point if there is any. We repeat this iterative process until no more change-points are found.

3 Data

The TC data over the WNP come from the US JTWC in Honolulu. The data cover the period 1945–2007. The data sets contain measurements of TC center location in latitude, longitude, 1-min sustained maximum wind speed, and central pressure at 6-h intervals for all TCs in the WNP. Here TC refers to tropical storms and typhoons. Tropical storms are defined as maximum sustained surface wind speeds between 17.5 and 33 m s^{-1}, and typhoons are defined as wind speeds at least 33 m s^{-1}. The ACE of a year is defined by summing the squares of the estimated maximum sustained velocity of every tropical storm or typhoon at 6-h intervals during the lifetime of a storm through the course of a year. This summed value is then divided by the number of TCs in that year to get the ACE per storm for each year. Because the original numbers are large, they are divided by 10,000 to make them more manageable. ACE is related to storm kinetic energy.

4 Results

The methods presented in Section 2 are applied to the data outlined in Section 3. Using an empirical argument, Camargo et al. (2007) suggested that the optimum number of track patterns in the WNP varies from six to eight. Based on our own simulation results with longer data sets, it seems that eight clusters offer the best explanation for the data.

Figure 1 shows eight major track patterns over the WNP and the South China Sea, with three straight movers (types A, B and C), four recurved ones (types D, E, F, and G), and one mixed pattern of both straight moving and recurved (type H). The type A and B clusters are similar in nature in that they both move more or less straight across Philippines to the South China Sea and/or Hong Kong, Hainan, and Vietnam. The major difference is that type B storms tend to form farther eastward and southward than type A storms. As a result, the mean track for type B storms is longer than that of Type A. Type C cyclones form in the South China Sea and are landlocked by the Indochina peninsula and southern China's coast, with very short paths. Similar to types A and B, type D and E systems form in the Philippine Sea but they follow a northward path and many of them made landfall on Taiwan, the

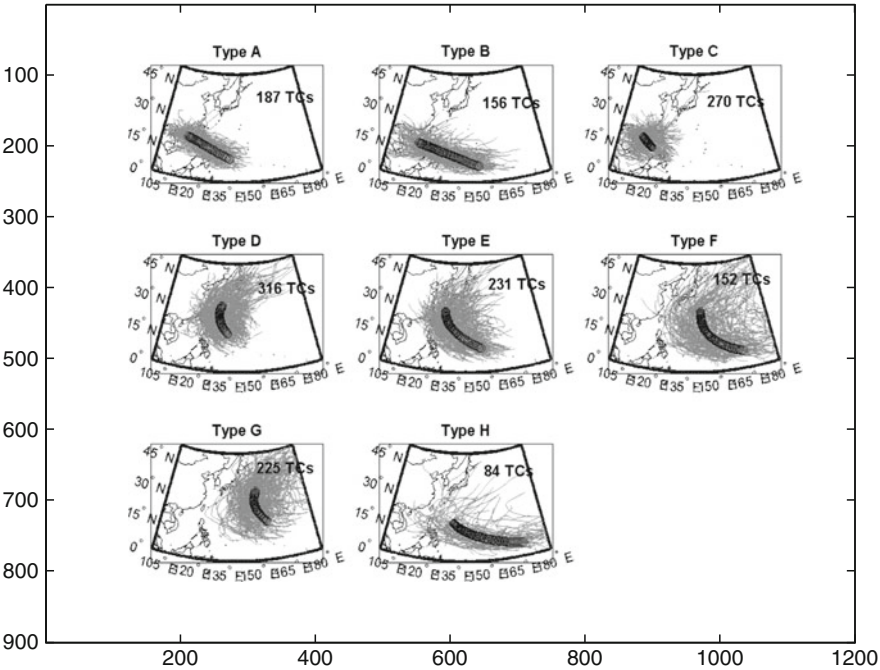

Fig. 1 Eight TC track types identified by the mixture Gaussian model. The number in each panel indicates the number of cases in each type. Black circles denote the mean track for each type

eastern China coast, Japan, and Korea. Type F storms tend to form in low-latitudes and away from Asia. Type G storms also form far away from the Asian continent but at higher latitudes (~15°N). They move northwestward and then northward to the east of Japan over the open ocean. Storms associated with type H are generally formed near the equator and to the east of 165°E, and have a long trajectory over the water. In terms of the frequency of occurrence, Type D has the highest number (316 out of a total of 1,621 cases). This is followed by type C (270), E (231), and G (225). Type H has the least number of occurrences (84) among eight types.

For each pattern, temporal variations of typhoon related attributes such as frequency, intensity, lifetime, and energy (ACE) are examined. A change-point analysis is applied to detect abrupt shifts in the time series of such attributes. For TC frequency (Fig. 2), five out of eight types (B, D, F, G, and H) show at least one step-like change since 1945. For types F and H, the abrupt shift occurs in 1976, at a time when major climate regime underwent a phase shift (e.g., Trenberth 1990). After 1976, TCs became more active for both types F and H. For type D storms, which are the leading pattern among all eight groups, typhoon activity has very likely undergone a decadal variation with two abrupt shifts occurring around 1987 and 1998 with three epochs characterized by the active 1945–1986 epoch, the inactive 1987–1997 epoch, and the active 1998–2007 epoch. The reincreasing activity

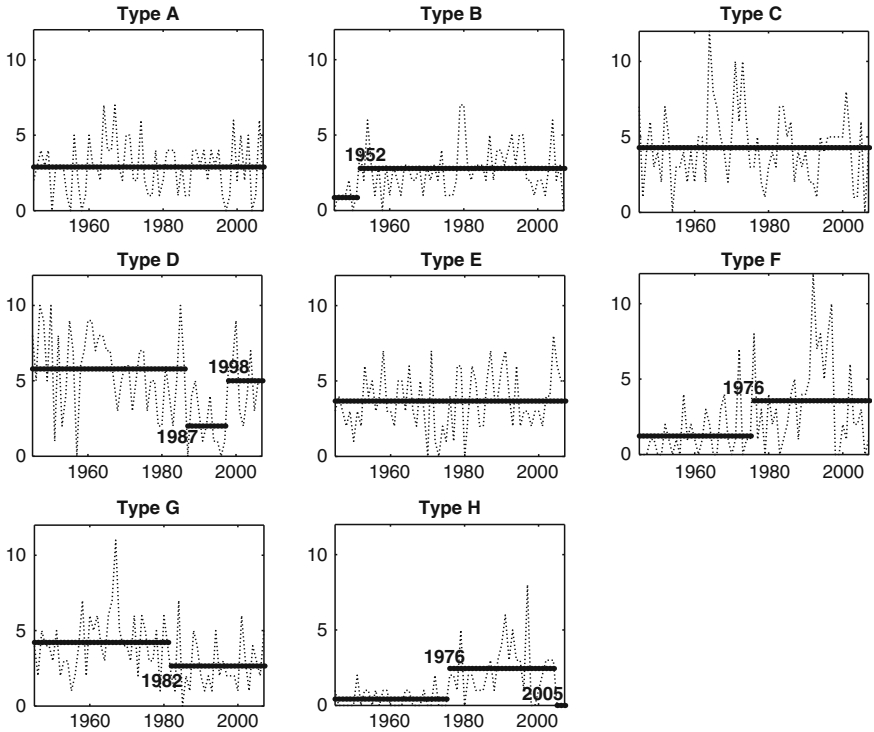

Fig. 2 Time series of annual tropical cyclone counts in the western North Pacific for eight track types. Years in each panel indicate possible change-points or abrupt shifts. Dotted lines are time-mean for each sub-period. The y-axis is the tropical cyclone number

for type D since 1998 is a concern because storms associated with this type are formed near the eastern Asian landmass and their preferred tracks are likely to cause damage to Taiwan, east China coast, Japan, and Korea.

In Fig. 3, six of the track types (A, B, C, D, F, and H) exhibit one abrupt shift over the last 60 years with the exception of type B, which experienced two shifts. Interestingly, after the shift all five types (A, C, D, F, and H) show an increasing level of storm days, indicative of longer mean storm days after the identified shifts. It is possible that steering flows over the WNP become weaker, making storms traverse more slowly and increasing the lifetime of the storms. This possibility will be examined in future research. Also noteworthy in Fig. 3 is the phase shift in 1972, which occurs in types A, C and H.

The change in TC intensity is also quite interesting (Fig. 4), although this quantity from the JTWC is subject to larger uncertainty. Over the last 60 years, seven (A, B, C, D, E, F, and G) out of the eight types exhibit abrupt shifts in the 1970s. For types B, C, D and G, the shift occurs in 1971–1973 and for types E and F in 1974. For type D, which is not only the leading cluster but also bears threats to Taiwan, east China, Japan, and Korea, a step-like change also occurred recently

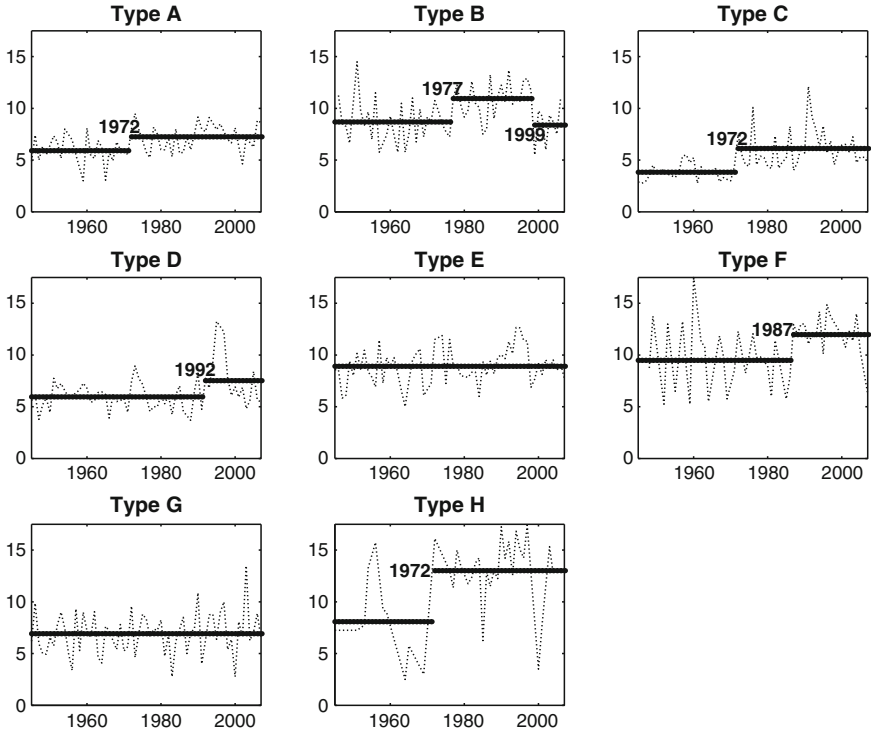

Fig. 3 Same as Fig. 2 but for tropical cyclone lifespan. The y-axis is number of days

(1998) with higher intensities, signifying stronger TC intensities in the last few years. This increase in intensity, together with the concurrent increase in frequency (Fig. 2), deserves further investigation.

For ACE (Fig. 5), types C, E, and F do not show any apparent change in the past 60 years. The lifetime, intensity, and number of tropical cyclones all contribute to the magnitude of ACE. During El Niño and La Niña years, Camargo and Sobel (2005) found that the lifetime effect appears to be more important than the other two factors to ACE variations in the WNP. This may be reflected by a shift in type H in the 1972 El Niño (Figs. 3 and 5), but not on other types (e.g., A and C). Emanuel (2005) noted a substantial increase in the power dissipation index (PDI) for the WNP since 1970s. The PDI is similar to ACE, except that maximum wind speed is cubed over the storm's lifetime. Emanuel (2005) attributed this increase to the longer lifetime of the storm and greater storm intensities. In our case, only five types show an increase in their lifetimes (Types A, C, D, F, and H) and there is a lack of general intensity increase. These results are different from Emanuel which is based on the basin-wide values.

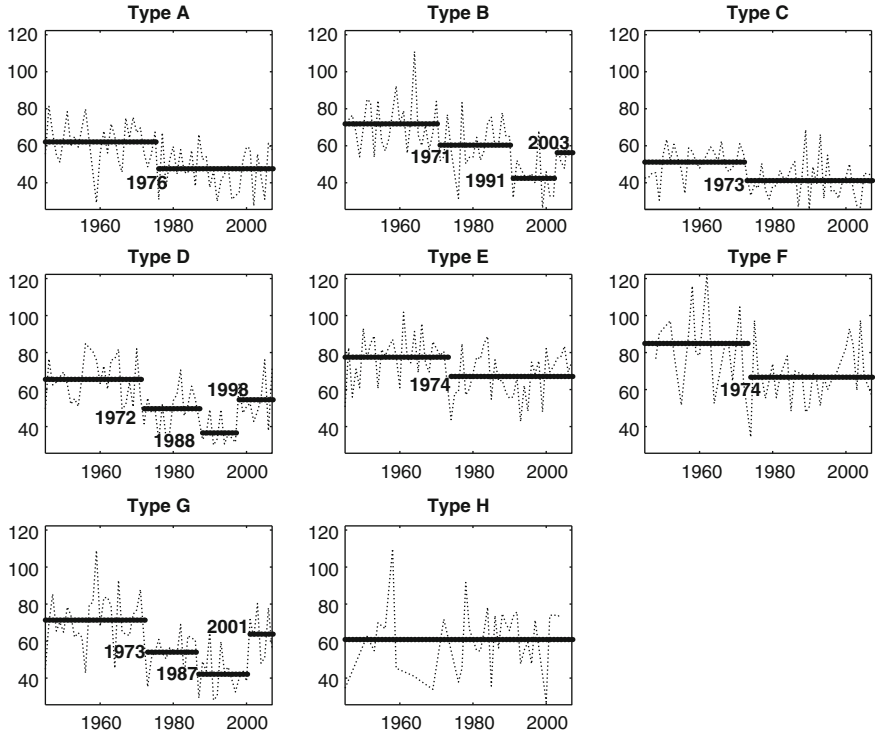

Fig. 4 Same as Fig. 2 but for tropical cyclone intensity. The y-axis is knots

5 A Suggestion for Future Research

It should be noted that the results presented in this study are based on the JTWC best-track dataset. The veracity of JTWC data during the period prior to satellite observation (before 1970) is called into question (Knaff and Zehr 2007; Lowry et al. 2009). While the track patterns, TC counts, and lifetime are probably reliable, TC intensity estimates and ACE may be subject to uncertainty. Therefore, extreme caution must be exercised in the intensity and ACE analysis and interpretations. In the future, we plan to apply the same methodology outlined in foregoing section to other best-track data to check for consistency.

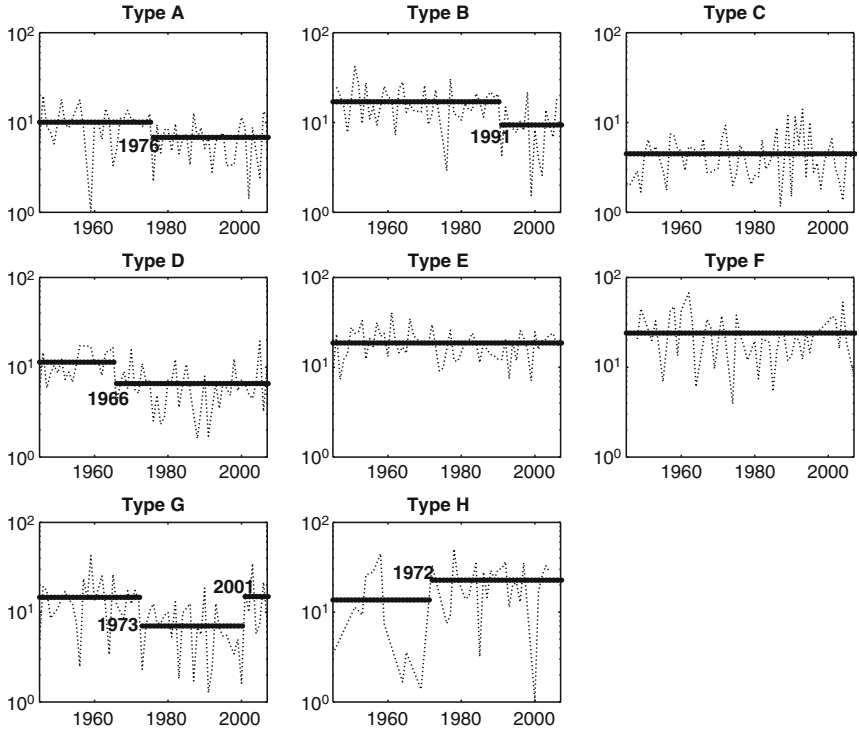

Fig. 5 Same as Fig. 2 but for the average ACE per storm (10^4 kt^2)

Acknowledgments This study was partially funded by the Pacific Disaster Center on Maui, Hawaii, the Central Weather Bureau in Taiwan, and the Korean Ocean Research Development Institute. P.-S. Chu also benefited from discussions with Mr. M. Lowry.

References

Camargo SJ, Sobel AH (2005) Western North Pacific tropical cyclone intensities and ENSO. J Clim 18:2996–3006

Camargo SJ, Robertson AW, Gaffney SJ, Smyth P, Ghil M (2007) Cluster analysis of typhoon tracks. Part I: General properties. J Clim 20:3635–3653

Chan JCL (2006) Comment on "changes in tropical cyclone number, duration, and intensity in a warming environment". Science 311:1713. doi:10.1126/science.1121522

Chu P-S (2002) Large-scale circulation features associated with decadal variations of tropical cyclone activity over the central North Pacific. J Clim 15:2678–2689

Chu P-S, Zhao X (2004) Bayesian change-point analysis of tropical cyclone activity: The central North Pacific case. J Clim 17:4893–4901

Elsner JB, Jagger TH, Niu X-F (2000) Changes in the rates of North Atlantic major hurricane activity during the 20th century. Geophys Res Lett 27:1743–1746

Elsner JB, Kossin JP, Jagger TH (2008) The increasing intensity of the strongest tropical cyclones. Nature 455:92–95. doi:10.1038/nature07234

Emanuel K (2005) Increasing destructiveness of tropical cyclones over the past 30 years. Nature 436:686–688. doi:10.1038/nature03906

Kim J-H, Ho C-H, Lee M-H, Jeong J-H, Chen D (2006) Large increase in heavy rainfall associated with tropical cyclone landfalls in Korea after the late 1970s. Geophys Res Lett 33:L18706. doi:10.1029/2006GL027430

Klotzbach PJ (2006) Trends in global tropical cyclone activity over the past twenty years (1986–2005). Geophys Res Lett 33:L10805. doi:10.1019/2006GL025881

Knaff JA, Zehr RM (2007) Reexamination of tropical cyclone wind-pressure relationships. Wea Forecast 22:71–88

Lau KM, Zhou YP, Wu HT (2008) Have tropical cyclones been feeding more extreme rainfall? J Geophys Res 113:D23113. doi:10.1029/2008JD009963

Lowry MR, O'Brien JJ, Griffin ML (2009) The role of observational changes on empirical trends in tropical cyclone intensity across the western North Pacific. *2nd International Summit on Hurricanes and Climate Change*, Aegean Conference Series, Vol. 41, May 31–June 5, Corfu, Greece, p. 56

Trenberth K (1990) Recent observed interdecadal climate changes in the Northern Hemisphere. Bull Am Meteor Soc 71:988–992

Tu JY, Chou C, Chu P-S (2009) The abrupt shift of typhoon activity in the vicinity of Taiwan and its association with Western North Pacific-East Asian climate change. J Clim 22:3617–3628

Webster PJ, Holland GJ, Curry JA, Chang H-R (2005) Changes in tropical cyclone number, duration, and intensity in warming environment. Science 309:1844–1846

Zhao X, Chu P-S (2006) Bayesian multiple change-point analysis of hurricane activity in the eastern North Pacific: A Markov chain Monte Carlo approach. J Clim 19: 564–578

Chapter 9
Climatic Features and Their Relationship with Tropical Cyclones Over the Intra-Americas Seas

Jorge A. Amador, Eric J. Alfaro, Erick R. Rivera, and Blanca Calderón

Abstract In this chapter, indexes of the Intra-Americas or Caribbean Low-Level Jet (IALLJ or CLLJ, respectively), Niño 3, Tropical North Atlantic (NATL), Atlantic Multidecadal Oscillation (AMO), and Outgoing Long Wave Radiation (OLR) are quantified for the period 1950–2007, to study their relationship with tropical cyclone (TC) frequency for summer–autumn of the Northern Hemisphere. A remarkable inverse relationship is found between both, the strength of the wind speed at 925 hPa and the vertical wind shear at low levels, and the monthly relative frequency of TCs for two selected areas in the Caribbean. The July peak in wind speed and low-level vertical wind shear are associated with a minimum in the monthly relative frequency of TCs. On the contrary, a decrease in the wind speed and vertical shears are associated with a maximum value of the relative frequency of TCs. Stronger (weaker) than normal IALLJ summer winds (July–August) during warm (cold) ENSO events imply a stronger (weaker) than normal vertical wind shear at low-levels in the Caribbean. This condition may inhibit (allow) deep convection, disfavoring (favoring) TC development during these months. Correlation values of the monthly mean CLLJ core winds and the monthly normalized values of NATL – Niño 3 index for 1950–2007 showed statistical significance greater than 99% during July–August. During El Niño years, low-level wind increases at the jet core strengthening the low level convergence near Central America at the jet exit and the low-level divergence in the central Caribbean at the jet entrance. The descending motion associated with the latter acts as an inhibiting factor for convection and TC development. TC activity in the Caribbean is not only sensitive to ENSO influences, but to the strength of the CLLJ vertical wind shear, to barotropic energy conversions induced by the lateral wind shear, to the intensity of the regional scale descending motion associated with the jet entrance, and to the SST cooling generated by the CLLJ at

J.A. Amador (✉) and E.J. Alfaro
School of Physics, University of Costa Rica, San Pedro 11501, Costa Rica
and
Center for Geophysical Research, University of Costa Rica, San Pedro 11501, Costa Rica
e-mail: jorge.amador@ucr.ac.cr; erick.alfaro@ucr.ac.cr

E.R. Rivera and B. Calderón
Center for Geophysical Research, University of Costa Rica, San Pedro 11501, Costa Rica
e-mail: erick.rivera@ucr.ac.cr; blanca.calderon@ucr.ac.cr

J.B. Elsner et al. (eds.), *Hurricanes and Climate Change: Volume 2*,
DOI 10.1007/978-90-481-9510-7_9, © Springer Science+Business Media B.V. 2010

the sea surface. Climatology of a group of General Circulation Models used in the 2007 report of the IPCC were tested to study their ability to capture the low-level wind annual cycle over the Caribbean and the known CLLJ structure. Some models do not capture basic characteristics of the jet. A discussion of cyclone potential over the Caribbean, based on the relationships developed using the models climatology, is presented for the period 2010–2050. As a study case, the findings were contrasted with the observed 2008 climate over the IAS region. Rainy season for 2008 in Central America evolved in a way consistent with the presence of La Niña event and the meridional migration of the ITCZ. Wind anomalies associated with the IALLJ were larger (smaller) than normal during February (July) 2008, in agreement with earlier findings in regards to the relationship of the IALLJ and ENSO phases. The year of 2008 was very active for tropical storm formation in the Caribbean basin (10–22.5°N, 60–82.5°W). From 16 named storms observed in the Atlantic, 10 entered the Caribbean basin. Eight (five) Atlantic cyclones were hurricanes (strong hurricanes) and from the five hurricanes crossing the Caribbean basin, four were strong.

Keywords Intra-Americas (Caribbean) Low-Level Jet · Mid-Summer Drought · Tropical cyclone frequency · El Niño-Southern Oscillation (ENSO) · Tropical North Atlantic (NATL)

1 Introduction

Climate monitoring, the development of conceptual models and the understanding of interactions between elements of the climate system, are the basis for planning activities focused on the reduction of societal impacts caused by climate variability and climate change. Different regions of the world, however, are generally affected by different predominant meteorological and climate features with associated particular challenges for societal protection. For example, the western Africa is known for the predominance of tropical waves (Burpee 1972), the Panama Bight and the western Caribbean for severe and frequent presence of convective systems (Mapes et al. 2003; Amador 1998, 2008), and some tropical basins for the seasonal generation of tropical cyclones (TC; Gray 1993; Goldenberg et al. 2001; Wang and Chan 2002; Frank and Young 2007; Kuleshov et al. 2008). This chapter will investigate, in particular, some of the links between climate features for different space and time scales (from regional to global and from intraseasonal to interannual modes, respectively), and variations in the intensity and frequency of tropical storms (TS) in the Intra-Americas Seas (IAS). The IAS region is defined here as consisting of the Gulf of Mexico, Southern Mexico, Central America, the eastern tropical Pacific, the Caribbean, and northern South America, and is one of the most active regions in the world, as far as TC formation is concerned.

Gray (1993) was among the first to study the El Niño-Southern Oscillation (ENSO) relationship with seasonal TC activity for different worldwide regions. He reported that TC activity in the North Atlantic is more sensitive to El Niño (warm phase of ENSO) influences than that in any other ocean basin. His study indicates

that in the North Atlantic region, moderate to strong El Niño conditions are generally associated with a substantial decrement in the number of cyclones (especially at low latitudes); a 60% reduction in numbers of hurricane days; and an overall decrease in the cyclonic system intensity. In the Eastern North Pacific basin, there is a strong ENSO signal in hurricane activity, as there is a tendency for an increased frequency of hurricane systems during El Niño years. Statistical analysis of the records for 40 years of TC in the Indian Ocean indicates no obvious consistent, ENSO related response on seasonal TC frequency, location or intensity in the North and South Indian Oceans. For the Australian region Gray determined that differences in sea surface temperatures and surface pressure seemed to provide the primary physical linkage. In this region, El Nino events were usually associated with cool sea surface temperature anomalies, high barometric pressure, and a diminished frequency of Australian Coral Sea area cyclones.

In terms of the variability of cyclonic activity, Goldenberg et al. (2001) reported that years 1995–2000 experienced the highest level of North Atlantic hurricane activity occurrences in the reliable 1971–2000 record. Compared with the generally low activity of the previous 24 years (1971–1994), the latter years showed a doubling of overall frequency activity for the whole basin, a 2.5-fold increase in the intensity of the maximum wind-speed of major hurricanes ($\geq$50 m/s), and a fivefold increase in hurricanes affecting the Caribbean. These authors showed that greater activity results from simultaneous increases in North Atlantic sea-surface temperatures along with decreases in vertical wind shear (a common condition observed during La Niña events). Because these changes exhibit a multidecadal time scale, the present high level of hurricane activity is likely to persist for an additional period of 10–40 years, approximately.

Wang and Chan (2002) found impacts of strong (but not moderate) El Niño and La Niña events on TS activity over the western North Pacific (WNP). Although the total number of TS formed in the entire WNP does not vary significantly from year to year, during El Niño summer and fall seasons, the frequency of TS formation increases remarkably in the southeast quadrant (0–17°N, 140–180°E) and decreases in the northwest quadrant (17–30°N, 120–140°E). After the El Niño (La Niña), the early season (January–July) TS formation in the entire WNP is suppressed (enhanced). In strong warm (cold) ENSO years, the mean TS life span is about 7 (4) days, and the mean number of days of TS occurrence is 159 (84) days. Wang and Chan (2002) also reported during the fall of strong warm ENSO years, the number of TS curving northward across 35°N, is 2.5 times greater than during strong cold ENSO years. This implies that El Niño substantially enhances poleward transport of heat–moisture and impacts high latitudes through changing TS formation and tracks. The enhanced TS formation in the southeast quadrant during El Nino events is attributed to the increase of the low-level shear vorticity generated by El Niño–induced equatorial westerlies, while the suppressed TS generation over the northwest quadrant is ascribed to upper-level convergence induced by the deepening of the east Asian trough and strengthening of the WNP subtropical high. The WNP TS activity in July–December is noticeably predictable using preceding winter–spring Niño-3.4 sea surface temperature (SST) anomalies, while the TS formation in March– July is exceedingly predictable using preceding October–December Niño-

3.4 SST anomalies. The physical basis for the former is the phase lock of ENSO evolution to the annual cycle, while for the latter it is the persistence of Philippine Sea wind anomalies that are excited by ENSO forcing but maintained by local atmosphere–ocean interaction.

Frank and Young (2007) examined the interannual variability of TCs in each of the earth's cyclone basins using data from 1985 to 2003. Interbasin correlations and factor analysis of patterns of TC activity revealed that there are several significant modes of variability. The largest three factors explain together about 70% of the variance, and each of these factors shows significant correlation with ENSO, the North Atlantic Oscillation (NAO), or both, with ENSO producing the largest effects. Their results suggest that patterns of TC variability are strongly affected by large-scale modes of interannual variability. The temporal and spatial variations in storm activity are quite different for weaker TCs (tropical storm through category 2 strength) than for major storms (categories 3–5). The most intense storms tend to show the stronger interbasin correlations and stronger relationships with ENSO and the NAO than do the weaker storms. This suggests that factors controlling TC formation differ in important ways from those that ultimately determine storm intensity.

Kuleshov et al. (2008) developed a collective list of historical El Niño and La Niña events, based on an examination of different indexes describing ENSO phenomenon. Based on this list, TC data from a newly created TC archive for the Southern Hemisphere (SH) have been stratified accordingly and significant changes in TC occurrences depending on warm or cold phases of ENSO have been identified. TC trends in the SH (area south of the equator, 30°E–120°W) were examined. For the 1981/82 to 2005/06 TC seasons, there are no apparent trends in the total number of TCs and cyclone days, nor in the numbers and number of cyclone days of severe TCs with minimum central pressure of 970 hPa or lower. However, significant positive trends in occurrences and cyclone days of severe TCs with minimum central pressure of 945 hPa or lower were identified.

As discussed above, atmospheric and oceanic factors influencing TC formation, frequency and intensity range over a large variety of time and space modes. This problem is approached here, by selecting the dominant meteorological and climate features of the IAS region in order to quantify atmospheric and oceanic indexes that are then linked to TC formation and characteristics. The IAS region is characterized by unique climate features, such as the Mid-Summer Drought (MSD) or "veranillo", a phenomenon rarely observed in the tropics (Magaña et al. 1999); the Caribbean low-level jet during summer (Amador 1998) and its winter counterpart (Amador et al. 2006; Amador 2008), the only mostly zonal marine low-level jet in the Americas; the Caribbean and eastern tropical Pacific warm pools and associated cyclogenetic regions (Gray 1979; Wang and Enfield 2001, 2003); and the strong convective activity of the Intertropical Convergence Zone (ITCZ). The importance of studying these phenomena and its relationship with TC response is that they all heavily imprint the economy and human well-being of the inhabitants of the IAS region.

The IAS low-level jet (IALLJ), also known as the Caribbean Low-Level Jet (CLLJ), is a relevant climate feature that dominates the IAS circulation, both in

summer and winter (Amador 2008). Its relationship with TC formation, another prominent climate characteristic of the Caribbean Sea, is not well understood despite CLLJ's known influence over the lower troposphere vertical wind shear (Amador and Magaña 1999) and in the reduction of sea surface temperature over the Caribbean Sea (Amador 2008). Over the Pacific slope of Central America and southern Mexico, there is a climatological relative minimum in July–August precipitation known as the MSD (Magaña et al. 1999). This phenomenon strongly affects the agriculture sector over that region, especially when the MSD extends into the climatological wet season (June and September) or when TC activity is intense during the summer months. The MSD, a component of the annual cycle of precipitation (Magaña et al. 1999), has a remarkable interannual variability (Amador 2008) that is not known to be associated with any regional or global signals such as the CLLJ, ENSO, Pacific Decadal Oscillation (PDO), or North Atlantic Index (NATL), among others.

The relevance of improving the scientific knowledge about the IAS climatic features lies on the fact that their variations are associated with very important socioeconomic losses caused by floods, droughts, landslides, wind damage, and extreme precipitation events. This paper focuses its attention in the quantification of a set of indexes, associated with some of these relevant climate features of the Caribbean and eastern tropical Pacific basins (the IAS), and their relationship with TC activity.

Since there still is a scientific debate about the potential increase (decrease) in hurricane occurrences and their intensities under specific climate change scenarios in the Atlantic (see, Gutowski, Jr. et al. (2008) who presented results opposite to those of Bender et al. (2010), Knutson et al. (2008), and Bengtsson et al. (2007), who reported a reduction in the occurrences of the Atlantic hurricanes under the same warming scenario), this work also studies the internal statistical structure of TC activity under potential climate change scenarios. To do this, the same set of climate indexes, as quantified from historical data, is estimated from climate projections based on global model output used by the Intergovernmental Panel on Climate Change (IPCC 2007) for the period 2010–2050.

The key climate features of the IAS region used for the quantification of the indexes, are briefly reviewed in the next section, especially in regards to atmospheric and oceanic conditions for TC development. Section 3 presents the data and the methods used to carry out the estimates of the climate indexes and the procedures for the statistical analysis. The results for both periods analyzed, 1950–2007, and 2010–2050 are presented in Section 4, along with a discussion and interpretation of these results on the basis of some climate change scenarios generated by selected general circulation models. The lessons learned from the indexes and their associated statistical interactions are used to understand the role of the physical mechanisms involved and their potential prediction skill in a case study; the 2008 climate of the IAS (Section 5). Final remarks and conclusions are found in Section 6.

2 Brief Review of the Intra-Americas Seas Climate Features

Central America is characterized by a relatively high mountain range crossing the region from northwest highlands in Guatemala to southeast summits near the Costa Rica–Panama border. Topography across Central America determines climate distribution, especially that part relative to the precipitation and surface temperature distributions.

The climate of the IAS is determined by a wide range of atmospheric signals, however, some of them are particularly important and are observed to dominate the regional circulations. As it is known, SST variations are associated with the origin and structure of many climate systems at low latitudes and their association with convective activity and rainfall distribution. Regarding the start and end of the rainy season, several studies have shown that the SST anomalies of the tropical Atlantic and Pacific Oceans are related to variations in the duration and timing of the rainy season in Central America (Enfield and Alfaro 1999). Central America and the Caribbean islands are embedded in oceanic "warm pools" (Wang and Enfield 2001, 2003), one in the eastern tropical north Pacific, where the ITCZ forms and rainfall is a maximum, and the other one over the Caribbean Sea, where precipitation is relatively scarce.

In Central America, the prevailing trade wind regime interacting with topographic barriers imprints unique characteristics to the spatial and temporal distribution of precipitation. The annual distribution of rainfall in Central America exhibits two contrasting regimes, one in the Caribbean side and the other one on the Pacific slope (Magaña et al. 1999; Taylor and Alfaro 2005; Amador 2008). The latter pattern exhibits a bimodal distribution, with two maxima, one in June and the other one in September–October, and a relative minimum during July–August (MSD). The existence of such a fluctuation in the annual distribution of precipitation has been shown to be part of the seasonal cycle of precipitation in the region (Magaña et al. 1999), and it partially relates to changes in the intensity of convective activity over the northeastern Pacific "warm pool". These authors proposed that the intensity of the ITCZ over the eastern Pacific produces a dynamical response in the low level circulation that controls the MSD intensity. A weak ITCZ allows the intensification of the MSD along the Pacific side of Central America.

The most interesting dynamical feature over the IAS is, however, the CLLJ, known also as the IASLLJ, that appears during June, reaches a maximum in July and weakens in September (Amador 1998), with another maximum in February (Amador et al. 2006; Amador 2008). The flow is relatively weak during the rest of the annual cycle. According to Wang and Lee (2007) the semi-annual feature of the CLLJ results from the semi-annual variation of sea level pressure in the Caribbean region associated with the east-west excursion of the North Atlantic Subtropical High. The warm pools impact is to weaken the summertime component of the subtropical high, especially at its southwestern edge and thus weaken the easterly CLLJ. The weakening of the easterly CLLJ, in conjunction with the warm pools induced change of upper-level wind, reduces the tropospheric vertical wind shear thus favoring hurricane formation and intensification during August–October.

The presence of this strong low level easterly jet constitutes the most important factor in determining the distribution of regional precipitation during summer, and partially during winter through interactions with regional topographical features and cold fronts reaching low latitudes. The intense convergence that forms at the exit of the low level jet is associated with a maximum in convective activity over the western Caribbean (Amador 1998, 2008).

3 Data and Methods

Several indexes were estimated to quantify the relationship between atmospheric and oceanic physical mechanisms and TC activity in the Caribbean. The indexes are based on values of the low-level wind shear, SST anomalies, outgoing long wave radiation (OLR) averaged over selected areas, on the MSD intensity (Amador 2008) for selected precipitation stations and on Niño 3, NATL, and Atlantic Multidecadal Oscillation (AMO) familiar indexes. The wind shear is known to be a relevant factor in the development of TCs (Gray 1979). Monthly estimates of vertical wind shear (VWS) for 925 hPa to surface, and for 700–925 hPa, for regions comprising the CLLJ core (12.5–17.5°N, 75–80°W), the whole basin (10–22.5°N, 60–82.5°W), and eastern tropical Pacific (5–12.5°N, 87.5–105°W) were calculated using National Center for Environmental Prediction (NCEP) and the National Center for Atmospheric Research (NCAR) data (Kalnay et al. 1996). The areas selected are shown in Fig. 1. Also, monthly values of SST (Smith et al. 2008) and surface wind (SW) from NCEP/NCAR for the same two regions above were computed. Values of OLR (Liebmann and Smith 1996) were calculated for the same

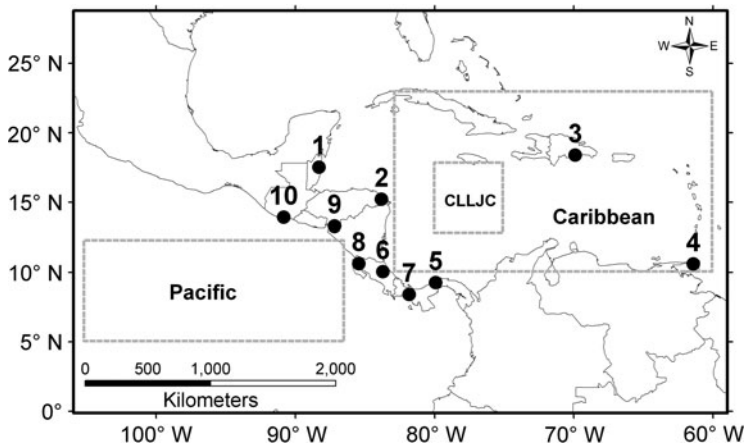

Fig. 1 Stations and areas used in this study to estimate the analyzed indexes. Station information is in Table 1 and the areas are located in the eastern tropical Pacific (Pacific), the Caribbean Low-Level Jet core (CLLJ core), and the whole Caribbean basin (Caribbean). See text for other details

areas above over the Caribbean and the eastern tropical Pacific. The standard Pearson correlation function was used to compute the statistical relationship among variables (Wilks 1995). Monthly climatologies (1950–1999) and indexes (2010–2050) from a group of General Circulation Models (GCMs) used in the 2007 report of the IPCC (2007) were also calculated to study their ability to capture some known physical features, such as the low-level wind annual cycle over the Caribbean, the known CLLJ structure and its relationship with TC activity in the region. Models used are: ECHAM5 [T63] (Roeckner et al. 2003; Marsland et al. 2003), HadCM3 [2.75° latitude by 3.75° longitude] (Gordon et al. 2000), CGCM3 [T63] (Kim et al. 2002, 2003), and Mk3.5 [T63] (Gordon et al. 2002). Twentieth Century simulations and SRES A1B data for all models were obtained from the World Climate Research Programme's (WCRP's) Coupled Model Intercomparison Project phase 3 (CMIP3) multi-model dataset (http://cmip-pcmdi.llnl.gov/).

The variability of some atmospheric variables in Central America and its association with fluctuations in the NATL and that of ENSO related SST, was studied by following the method discussed by Wilks (1995). Accordingly, monthly SST indexes for the NATL and Niño 3 regions (available at the Climate Prediction Center database, http://www.cpc.ncep.noaa.gov/data/indices) were used. The difference of the normalized indexes indicated above was also calculated. Observed categories for the AMO from the Climate Diagnostics Center (http://www.cdc.noaa.gov/Timeseries/AMO/) were included in the analysis as well.

To study the 2008 climate of the IAS region, daily mean temperature and pentad precipitation data from the ten selected stations described in Table 1 (see also Fig. 1) were used in order to compare their climatology for 1971–2000, with corresponding values for that particular year. A seven-point moving average was applied to temperature occurrence time-series to reduce high frequency oscillations in the

Table 1 Station characteristics, elevation in meters above sea level (masl); latitude (lat); longitude (lon); missing data in %; temperature T in °C, and precipitation p in mm, climatology "clim" 1971–2000; T and p for 2008

Station, country [altitude, m]	Lat (°N) Lon (°W)	Missing data (%) T(clim, 2008) p[clim, 2008]	p (mm) clim [2008]
P. G., Belize [50]	17.53 88.30	(38.1, 4.9) [39.7, 6.6]	1988 [1171]
S. J., Guatemala [20]	13.92 90.82	(21.0, 1.9) [38.9, 9.9]	1334 [1326]
P. L., Honduras [130]	15.22 83.80	(34.6, 3.3) [39.4, 3.3]	2247 [1945]
C., Honduras [480]	13.30 87.18	(36.0, 2.7) [39.2, 5.2]	2204 [1628]
P. L., Costa Rica [30]	10.00 83.05	(30.0, 1.7) [37.0, 10.1]	3372 [1511]
L., Costa Rica [800]	10.62 85.43	(12.9, 0.8) [54.9, 8.0]	1603 [2165]
D., Panamá [260]	08.40 82.42	(12.9,12.8) [29.0, 17.8]	2213 [2116]
G., Panama [30]	9.27 79.92	(0.0[a], 0.0) [0.0, 0.0]	2740 [2828]
S.D., Dominican Rep. [14]	18.40 69.90	(32.1, 4.6) [34.1, 11.2]	1519 [1694]
P., Trinidad and Tobago [12]	10.60 61.40	(8.2, 0.5) [11.2, 0.8]	2157 [1584]

[a]Data for temperature climatology only available for 1985–2000. Station Name: P.G. (Phillip Goldson), S.J. (San Jose), P. L. (Puerto Lempira), C. (Choluteca), P. L. (Puerto Limon), L. (Liberia), D. (David), G. (Gatun), S.D. (Santo Domingo), P. (Piarco)

data. The accumulated daily rainfall for 2008 was also calculated at each station to analyze the MSD characteristics. Meteorological data for all stations come from the National Climatic Data Center archives (NCDC, http://www.ncdc.noaa.gov), except data for Gatun, Panama, provided by the Panama Canal Authority. Gridded data from the NCEP/NCAR Reanalysis Project (Kalnay et al. 1996) was used to obtain wind anomalies over the IAS (12.5–17.5°N, 75.0–80.0°W) at 925 hPa from corresponding long term mean (1958–1999) during the 2008 cold ENSO event (La Niña) for February and July. Definition of a warm, cold and neutral ENSO conditions was based on criteria by Mora and Amador (2000).

4 Results

4.1 Annual Cycle

Figure 2 presents the mean annual cycle of wind speed (m/s) at 925 hPa for the Caribbean region (dashed line), and the CLLJ core region (dashed-circled line), the mean vertical wind shear (m/s) between 925 hPa and surface for the Caribbean region (solid line), and for the CLLJ core region (solid-squared line), and the monthly relative frequency (%) of TCs (bars) for the period 1950–2007. A remarkable inverse relationship is observed between both the strength of the wind speed at 925 hPa and the vertical wind shear, and the monthly relative frequency of TCs for the two selected areas. The July peak in wind speed and vertical shears with values of more than 12 and about 3 m/s, respectively, are associated with a minimum in the

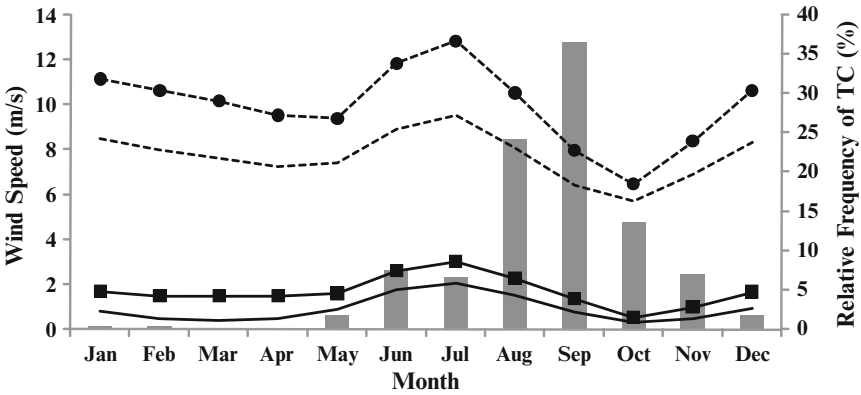

Fig. 2 Mean annual cycle of wind speed (m/s) at 925 hPa for the Caribbean region (10–22.5° N, 60–82.5° W, *dashed line*), and the CLLJ core region (12.5–17.5° N,75–80° W, *dashed-circled line*), mean vertical wind shear (m/s) between 925 hPa and surface for the Caribbean region (*solid line*), and the CLLJ core region (*solid-squared line*) (925 hPa – surface), and monthly relative frequency (%) of tropical cyclones (*bars*) for the period 1950–2007

monthly relative frequency of TCs. On the contrary, a decrease in the wind speed and vertical shears are associated with a maximum value of the relative frequency of TCs.

In order to analyze the relationship between the strength of the easterly flow at 925 hPa and the number of TCs for the summer months of July and August, when the CLLJ attains maximum values, wind anomalies were estimated at that level. The anomalies were calculated in a standard way, in other words, as the difference between the wind speed at a particular month minus the mean monthly wind, both at 925 hPa. Figure 3 shows the number of TCs (bars) and the wind speed anomalies (m/s) at 925 hPa for the Caribbean region for July (Fig. 3a), and August (Fig. 3b). Squared (circled) marks denote anomalies for warm (cold) ENSO events, and crossed marks denote anomalies for non-ENSO (neutral) events (Mora and Amador 2000). The most active July years (1966, 1970, 1979, 1996, and 2005, Fig. 3a) are associated with either neutral or cold ENSO conditions, however, this relationship does not hold for all years. In this context, it is widely known that ENSO is not the only variability mode for TC activity. Also from this figure, it is seen that most warm ENSO events (squares) are characterized by practically no July TC activity in the Caribbean. Many negative (eastward) wind anomalies (stronger than normal July winds) are observed during neutral ENSO conditions, whereas

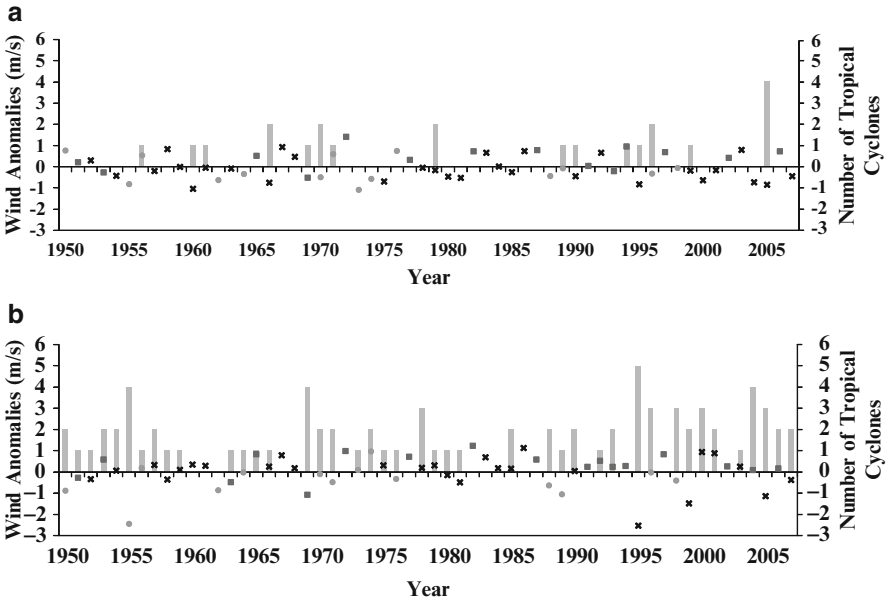

Fig. 3 Number of tropical cyclones (*bars*), and wind speed anomalies (m/s) at 925 hPa for the Caribbean region (see Fig. 1) for (**a**) July, and (**b**) August. Squared (*circled*) marks denote anomalies for warm (cold) ENSO events, and crossed marks denote anomalies for non-ENSO (neutral) events, according to the criteria of Mora and Amador (2000)

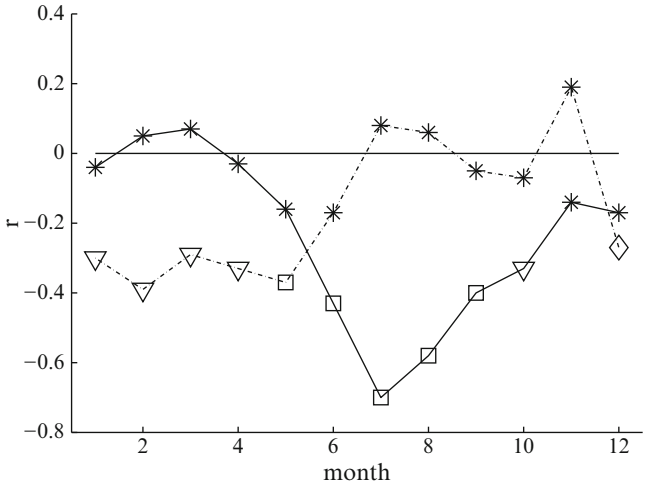

Fig. 4 Correlation values of the CLLJ core monthly wind averages and the monthly normalized values of (NATL + Niño 3, dashed line; and (NATL – Niño 3) indexes, solid line, for 1950–2007. Asterisks are values with statistical significance smaller than 90%, diamonds are between 90% and 95%, triangles are between 95% and 99% and squares are greater than 99%

positive (westward) wind anomalies (weaker than normal July winds) are mostly associated with no TC activity. Comparing Fig. 3a with b, it is observed that August is more active, in regards to TC formation, than July. Figure 3b also shows that some of the most active August years with at least 3 TCs (1955, 1978, 1995, 1996, 1998, 2000, and 2005, except 1969 and 2004) correspond to neutral conditions or La Niña events with some of them with relatively large negative (less than –1 m/s) wind speed anomalies (1995, 1995, and 2005).

Figure 4 shows the correlation values of the CLLJ core monthly wind averages and the monthly normalized values of (NATL + Niño 3), dashed line; and (NATL – Niño 3) indexes, solid line, for 1950–2007. Asterisks are values with statistical significance smaller than 90%, diamonds are between 90% and 95%, triangles are between 95% and 99% and squares are greater than 99%. This figure indicates that during winter and spring when anomalies in both, NATL and Niño 3 regions have the same sign, the time series associated with the CLLJ tends to covariate in the opposite direction, for example, NATL and Niño 3 warm (cold) anomalies, coincident in both ocean basins during winter-spring, are associated with negative (positive) anomalies in the CLLJ index (notice that during these months NATL – Niño 3_CLLJ correlations are non significant). For the rest of the year (summer–early autumn), the NATL + Niño 3 index has a non significant correlation value with the CLLJ index, meanwhile the NATL – Niño 3 index has a significant value. During those months that index has negative covariance with the CLLJ. It means that when NATL tends to be warm (cold) when it is compared with Niño 3, the CLLJ tends to present negative (positive) anomalies. This figure suggests that CLLJ strength is mainly controlled by

tropical mid-latitude contrast during winter-spring and by the contrast between the anomalies in the two ocean basins that surrounds Central America during summer-early autumn, suggesting a more local control during this period.

4.2 Climate Indexes for 1950–2007

The Pearson correlation coefficients for some indexes are shown in Table 2 (treated here as an inter-correlation matrix in the usual sense). The elements [1, 1], [1, 3], [2, 2], and [3, 3] of the correlation matrix imply that the VWS below the CLLJ maximum at 925 hPa covariates negatively with its counterpart above this level. Note the relatively high positive correlation values (99% significance level) between the VWS at the jet core and the whole basin, below (0.92) and above (0.87) 925 hPa, clearly indicating the importance of the jet in determining mean atmospheric flow conditions for this TC active region. At the jet core, the correlation is positive with Niño 3 below 925 hPa, in other words, the greater the VWS in this layer, the TC frequency is smaller, being the opposite true above 925 hPa (see elements [3, 4] and [4, 4], respectively). The above results are consistent for the whole Caribbean (elements [1, 4], and [2, 4]). Other elements of this matrix [2, 5] and [4, 5] indicate that the VWS below 925 hPa behaves in an opposite way to that above this level. During a warm ENSO phase the low level VWS is stronger, so the TC frequency diminishes. The opposite is true for La Niña decreases in low level VWS and increases in TC numbers ([5,5] = –0.42 at a significance level of 99%). Though the correlation values of Table 2 indicate that there is no straightforward relationship among the indexes, perhaps the most important one, explaining about 40% of the variance of TC formation is the CLLJ VWS at the jet core below 925 hPa. This result also applies to the whole basin (see elements [1,1], and [1,5]).

Table 2 Pearson correlation function for the yearly indexes of the June to November means used in this study. All series have a record from January 1950 to December 2007 (italics and boldface indicate significance level = 0.01; boldface indicates = 0.5, and italics indicates = 0.10, calculated as in Davis, 1976)

Index	Caribbean VWS (700–925)	CLLJ core VWS (925-Sfc)	CLLJ core VWS (700–925)	Niño 3	TC
Caribbean VWS (925-Sfc)	***–0.56***	***0.92***	***–0.74***	**0.39**	***–0.55***
Caribbean VWS (700–925)	–	***–0.62***	***0.87***	***–0.40***	***0.46***
CLLJ core VWS (925-Sfc)	–	–	***–0.78***	***0.43***	***–0.61***
CLLJ core VWS (700–925)	–	–	–	***–0.53***	***0.52***
Niño 3	–	–	–	–	***–0.42***

Table 3 Same as Table 2, except for indexes for the July–August means (1950–2007)

Index	CLLJ core SW	Caribbean SST	CLLJ core SST	Pacific SST	Niño 3
Caribbean SW	***0.88***	***–0.48***	***–0.50***	*0.31*	***0.44***
CLLJ core SW	–	***–0.46***	***–0.50***	*0.30*	***0.53***
Caribbean SST	–	–	***0.97***	**0.38**	***–0.04***
CLLJ core SST	–	–	–	**0.33**	–0.11
Pacific SST	–	–	–	–	***0.77***

The SST distribution is a very important factor for cyclone development, so in this part of the paper, the SST at the jet core and the Caribbean are analyzed in terms of the CLLJ intensity at the sea surface. Table 3 shows the matrix correlation elements of the SST, Niño 3 and SW. As in the case of the VWS, the SW and SST at the CLLJ core are highly correlated with the SW and SST for the whole basin, respectively. This relationship is observed in the elements [1,1] and [3,3]. The correlation between the Niño 3 and Pacific SST is, as also expected, positive ([5,5] = 0.77, at a confidence level of 99%). A very interesting result is found between SW and SST for both the jet core and the whole Caribbean (see elements [1,2], [2,2], [1,3], and [2,3] of Table 3). The covariance for all these indexes is indicative of negative SST anomalies in the presence of greater than normal surface winds. Under warm (cold) ENSO phases, SW is stronger (weaker) than normal decreasing (not decreasing) the SST in the Caribbean Sea, the VWS is stronger (weaker) than normal below 925 hPa inhibiting (allowing) convective activity and associated moisture transfer, both conditions being not favorable (favorable) for TC formation. No significant relationship was found between the MSD and ENSO (not shown).

4.3 Climate Indexes for 2010–2050

As in the previous section, the Pearson correlation function was obtained for all indexes from projections made by four GCMs (ECHAM5, HadCM3, CGCM3 and Mk3.5) for 2010–2050 (Table 4). Only all correlation matrix elements from ECHAM5 and HadCM3 (suffixes "a" and "b", respectively) are consistent with those obtained for 1950–2007 (see Table 2). CGCM3 (suffix "c") presents the most notorious discrepancies. The first two models as well as Mk3.5 (suffix "d") show that the VWS below 925 hPa at the CLLJ core region is negatively correlated (significance level of 99%) with the VWS above this level (elements [1, 1abd], [1, 3abd], [2, 2abd], and [3, 3abd]). The positive correlations with significance levels of 99% in elements [1,2abcd], and [2, 3abcd] indicate that these models capture the basic dynamics of the regional circulation that determine the atmospheric conditions in the Caribbean basin (compare with Table 3). The CLLJ core indexes below (above) 925 hPa for ECHAM5 and HadCM3 covariate positively (negatively) with Niño 3 (elements [3,4ab], and [4,4ab]), which is in agreement with results from

Table 4 Pearson correlation function for the yearly indexes of the projected June to November means used in this study. All series have a record from January 2010 to December 2050 (italics and boldface indicate significance level = 0.01; boldface indicates = 0.5, and italics indicates = 0.10, calculated as in Davis, 1976). Rows in the cells correspond vertically to correlation values for (a) ECHAM5, (b) HadCM3, (c) CGCM3, and (d) Mk3.5

Index	Caribbean VWS (700–925)	CLLJ core VWS (925-Sfc)	CLLJ core VWS (700–925)	Niño 3
Caribbean VWS	***−0.73***	***0.97***	***−0.51***	***0.54***
(925-Sfc)	***−0.54***	***0.95***	***−0.77***	***0.57***
	0.15	***0.91***	−0.21	*0.33*
	−0.53	***0.95***	***−0.63***	0.10
Caribbean VWS		***−0.72***	***0.53***	***−0.78***
(700–925)	–	***−0.51***	***0.86***	***−0.74***
		0.24	***0.78***	0.07
		−0.48	***0.93***	***−0.62***
CLLJ core VWS			***−0.53***	***0.58***
(925-Sfc)	–	–	***−0.82***	***0.55***
			−0.15	*0.32*
			−0.60	0.13
CLLJ core VWS				**−0.34**
(700–925)	–	–	–	***−0.77***
				0.03
				−0.65

Section 4.2. Same relationship occurs for the Caribbean region (elements [1, 4ab], and [2, 4ab]). Mk3.5 only exhibits consistent negative correlations between the VWS above 925 hPa and Niño 3 for both the jet core and the whole basin. No significant correlations are found between the VWS at any level and Niño 3 for the CGCM3.

The correlation matrix for modeled SST, Niño 3 and SW for July and August is presented in Table 5. At first, it is important to note that none of the models completely captures the correlation patterns featured in Table 3; however, some agreements are obtained. SW and SST values for all GCMs in the CLLJ core region have positive correlations with those in the Caribbean basin (elements [1, 1abcd], and [3, 3abcd]). Positive covariances (at a significance level greater or equal to 95%) between Pacific SST and Niño 3 are present for all models. HadCM3 and Mk3.5 show that negative (positive) anomalies of SST in the jet core are related to greater (lesser) SW in the same region (elements [2, 2bd]). Caribbean SW and SST are not significantly correlated, except for Mk3.5 (element [1, 2d]). HadCM3 also captures the positive correlation pattern found in Table 3 between Niño 3 and SW in the CLLJ core (elements [1, 5b], and [2, 5b]), indicating that in presence of warm (cold) Niño 3 SST, the SW is stronger (weaker), and thus decreases (not decreases) the SST for that particular area.

Figure 5 presents the mean annual cycle of wind speed (m/s) at 925 hPa for the CLLJ core region (12.5–17.5°N, 75–80°W) from NCEP/NCAR (solid black

Table 5 Same as Table 4, except for indexes for the July–August means (2010–2050)

Index	CLLJ core SW	Caribbean SST	CLLJ core SST	Pacific SST	Niño3
Caribbean	***0.94***	–0.11	–0.27	**0.53**	**0.44**
SW	***0.95***	–0.28	*–0.33*	***0.75***	***0.55***
	0.89	–0.26	–0.19	0.04	0.18
	0.93	**–0.37**	**–0.41**	0.25	0.24
CLLJ core		–0.11	–0.30	**0.54**	***0.53***
SW	–	**–0.41**	**–0.45**	***0.73***	***0.50***
		–0.22	–0.16	0.13	0.25
		–0.40	***–0.49***	*0.32*	*0.35*
Caribbean			***0.96***	**0.60**	0.22
SST	–	–	***0.95***	0.05	0.03
			0.97	0.71	0.60
			0.97	**0.60**	0.34
CLLJ core				*0.40*	0.05
SST	–	–	–	–0.11	–0.11
				0.69	*0.61*
				0.48	0.23
Pacific					***0.72***
SST	–	–	–	–	***0.78***
					0.82
					0.79

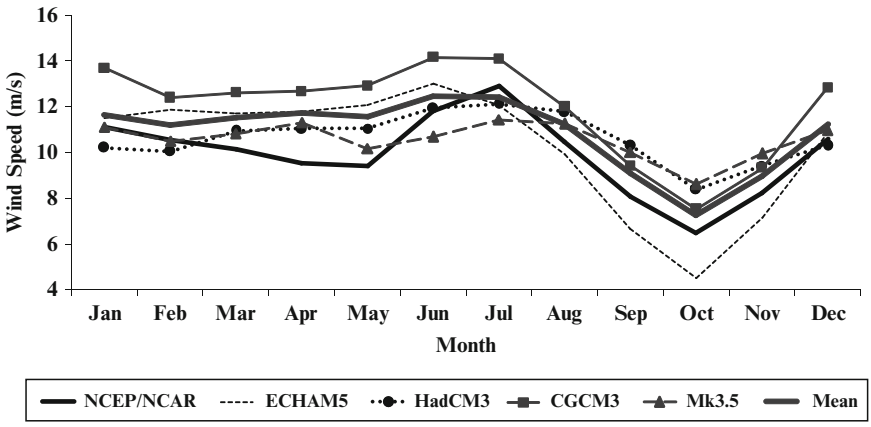

Fig. 5 Mean annual cycle of wind speed (m/s) at 925 hPa for the CLLJ core region (12.5–17.5° N, 75–80° W) from NCEP/NCAR (*solid black line*), and for 20c3m simulations for ECHAM5 (*dashed line*), HadCM3 (*dashed-circled*), CGCM3 (*gray line-squared*), Mk3.5 (*gray line-triangles*), and the ensemble mean (*solid gray line*)

line), and for Twentieth Century simulations (1950–1999) for ECHAM5 (dashed line), HadCM3 (dashed-circled), CGCM3 (gray line-squared), Mk3.5 (gray line-triangles), and the ensemble mean (solid gray line). The NCEP/NCAR data clearly

shows the two known maxima of the CLLJ in summer and winter and an absolute minimum in October. Most models used in this work resemble the NCEP/NCAR analysis, however, when look carefully major discrepancies are found. The CGCM3 overestimates the monthly values for 2–3 m/s all year round and does not show the maximum peak in July. During the first semester, the ECHAM5 presents little wind speed variations with a marked overestimation of the wind speed during these months and a peak in June, 1 month earlier than observed. The HadCM3 also shows a small gradual increase in wind speed from January to June–July and overestimates the October minimum by nearly 5 m/s. The Mk3.5 shows the lesser skill in determining the wind annual cycle presenting two maxima one in April and the other in August. As it has been shown by Amador (2008), the models ensemble mean does not necessarily capture, as it is the case here, the mean annual cycle of the IALLJ. To study the CLLJ time variability, a very important factor for future climate projections, Fig. 6 is presented. A very simple measure of variability of the wind at 925 hPa, its standard deviation, is used to show that there is great dispersion in this parameter among all analyzed models. Values range from 1.69 m/s in the ensemble mean to 1.72, 2.22, 2.22, and 3.35 m/s in the Mk3.5, CGCM3, HadCM3, and ECHAM5, respectively, for the period 2010–2050. The "observed" NCEP/NCAR data estimates of the standard deviation are 2.24 and 2.29 m/s, for the 1950–2007 and 1967–2007 periods, respectively. From Figs. 5 and 6, and the results shown before with the indexes correlation functions (Tables 2, 3, 4, and 5), it is easy to recognize severe limitations of the general circulation models used to represent adequately one of the most important features of the IAS regional climate, the IALLJ. This, of course, has important implications on the future climate and the IPCC scenarios of 2007, especially if some indexes and characteristics of the models are to be used to estimate future TC activity and societal impacts.

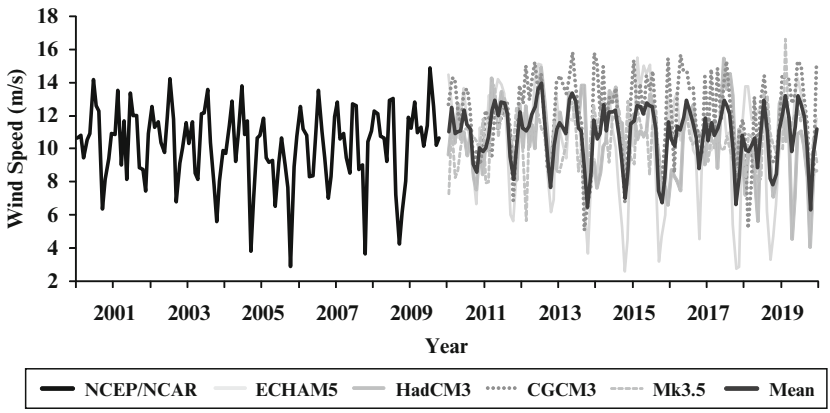

Fig. 6 CLLJ variability at the jet core in NCEP/NCAR data (2000–2009) and models used in this study for the period 2010–2020 (see Fig. 5 and text for details of models used)

5 The 2008 Regional Climate

5.1 Sea Surface Temperature

According to Enfield and Alfaro (1999), the variability in the NATL and the ENSO related SST is also associated with the variability of several atmospheric variables in Central America. Table 6 results follow basically the method discussed by Wilks (1995). This table shows the categories observed in the SST indexes associated with the NATL, Niño 3 regions (http://www.cpc.ncep.noaa.gov/data/indices/), and the difference and addition of the normalized indexes indicated above. This table also includes the different observed categories for the AMO (http://www.cdc.noaa.gov/Timeseries/AMO/). According to Enfield et al. (2001), AMO should be considered as a variability source in the IAS region. Some implications of the results shown in Table 6 are discussed below.

5.2 Surface Temperature

To illustrate the behavior of the 2008 surface temperature in the context of its long-term mean, four stations were analyzed for the Pacific and four for the Caribbean slopes along the region, as well as two for the Caribbean islands. Figure 1 shows the location of the ten stations selected (see also Table 1). Results for the surface temperature are presented in Fig. 7a. As observed in this figure, all four

Table 6 Monthly 2008 categories observed in the SST indexes associated with the NATL, Niño 3 regions (http://www.cpc.ncep.noaa.gov/data/indices/), and the difference of the normalized two indexes indicated above. Also includes is the different observed categories for the Atlantic Multidecadal Oscillation, AMO (http://www.cdc.noaa.gov/Timeseries/AMO/). Categories where defined for 1950–2007, in which VBN, very below normal (<P20), BN, below normal (>P20 & <P40), N, normal (>P40 & <P60), AN, above normal (>P60 & <P80), VAN, very above normal (>P80). Pnn means percentile nn

Index	NATL	Niño 3	NATL-Niño 3	AMO	AMO-Niño 3
Jan	AN	VBN	VAN	AN	VAN
Feb	N	VBN	VAN	VAN	VAN
Mar	N	VBN	AN	VAN	VAN
Apr	N	N	N	AN	AN
May	N	AN	N	VAN	AN
June	AN	AN	N	VAN	AN
July	VAN	VAN	N	AN	N
Aug	AN	VAN	AN	AN	N
Sept	VAN	AN	VAN	VAN	AN
Oct	VAN	AN	VAN	AN	AN
Nov	VAN	N	VAN	AN	N
Dec	VAN	N	VAN	AN	AN

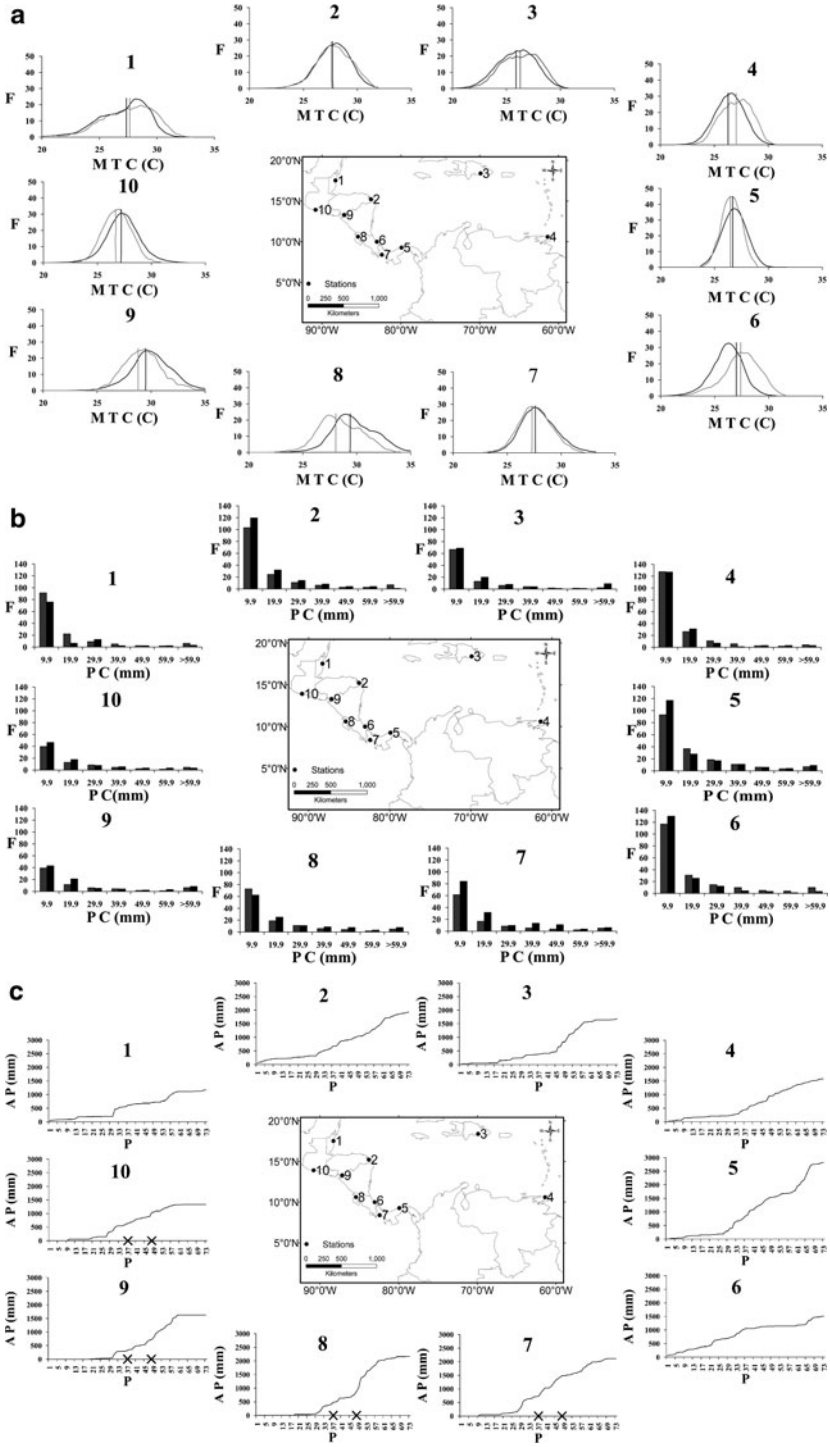
a
b
c
F
M T C (C)
P C (mm)
A P (mm)
P
Stations
Kilometers
0 250 500 1,000
20°0'N
15°0'N
10°0'N
5°0'N
90°0'W
80°0'W
70°0'W
60°0'W

stations located in the Pacific side, show a consistent decrease in the 2008 mean temperature with respect to climate. This feature is seen as a shift to the left in the 2008 frequency distribution when compared with the corresponding climatology. Liberia in northwestern Costa Rica has a shift of about 2°C, the largest of them all. On the contrary, two stations in the Caribbean side (those located in Belize and Costa Rica) and Santo Domingo and Piarco present an increase in surface temperature with respect to normal conditions; the other ones do not exhibit any significant shift. Maximum increment of less than 1°C is found in Limon, Costa Rica. The bias toward positive temperature anomalies in the Caribbean slope is in agreement with the observed values in the NATL SST in Table 6 (an above normal condition in most 2008 months). Negative shifts of temperature in the Pacific slope stations are consistent with the relatively cool SST values associated with ENSO during the first 2008 quarter, in which Niño 3 index showed in general Very Below Normal temperatures (Table 6).

5.3 Precipitation

The stations in the Caribbean slope of Central America (Fig. 7b) present a decrease in precipitation for 2008 with respect the climate. Note that in most cases missing data to estimate climatology was relatively high (Table 1). In most of the region, precipitation showers were concentrated in categories smaller than 20 mm approximately with very few extreme events in excess of 40–50 mm. Following the methodology described by Enfield and Alfaro (1999), the Start Date (SD) and End Date (ED) of the rainy season were only calculated for the Pacific slope gauge stations. Stations in the Caribbean slope show practically just one rainy season (see Fig. 7c). Using the technique developed by Alfaro (2002), the SD observed during 2008 is near normal, it is slightly late for David (Panama) and Choluteca (Honduras). ED of the Central America rainy season was about normal.

5.4 The Mid Summer Drought

The behavior of the 2008 MSD is investigated by means of the cumulative precipitation pentad distribution at the ten selected sites in Central America and the Caribbean (Fig. 7c). Pentads 37–48, approximately, correspond to the period where the "veranillo" has been observed. In an accumulated precipitation graph, a rainy

Fig. 7 A comparison at some selected stations in Central America of (**a**) frequency distribution of surface temperature (°C) for climatology (*black lines*) and 2008 (*gray lines*), and (**b**) frequency distribution of precipitation (mm) at 10 mm intervals except for dry days for climatology (*gray bars*) and 2008 (*black bars*). Accumulated pentad precipitation (mm) for all analyzed stations (**c**)

period would have a positive slope, whereas a period with no-rain would show as a horizontal line, so a change in the slope would mean a change in the temporal precipitation distribution. All Pacific stations present a rainy season onset, near pentad 29 or so (end of May), except David that shows an earlier start with respect to the analyzed sites. In regards to the ED (Fig. 7c), the Pacific slope stations to the north (San Jose and Choluteca) had an earlier end than Liberia and David, the latter showing the end near 2 weeks after Liberia. This behavior is fairly consistent with the results presented in Table 6 and with the idea of the meridional migration of the ITCZ. The reduction in precipitation corresponding to the MSD is clearly observed in all stations, especially in Choluteca and Liberia. The Caribbean stations (Fig. 7c) behaved, as expected, differently from those in the Pacific, showing a more continuous rainfall distribution throughout the year with practically very few dry spells (see Puerto Lempira and Limon). The Belize and Piarco stations presented a relatively dry year respect to their climatology.

5.5 The Intra-Americas (Caribbean) Low-Level Jet

Figure 8 shows the wind anomalies over the IAS at 925 hPa, from corresponding long-term mean (1958–1999), during the 2008 cold ENSO event (La Niña) for February and July (Figs. 8a, and b, respectively). As can be observed, wind anomalies were larger (smaller) than normal during February (July) 2008, consistent with the findings of Amador et al. (2003), Amador et al. (2006), and Amador (2008) in regards to the relationship of the IALLJ and ENSO phases. The IALLJ 2008 February and July mean values lay between percentile 60 and 80 (P60 and P80, respectively) when compared with the last 58 years (1950–2007). The trades for the period January–July 2008, except May, were stronger than normal (between P60 and P80). May, October and November were near normal (between P40 and P60), while August was weaker than normal (between P20 and P40), and September was very weak (below P20). December on the other hand, was observed to be very strong (above P80). Following these findings, some questions arise. Is the IALLJ summer component shorter in duration than normal over the Caribbean, for a La Niña event? Is the opposite true for winter?

5.6 Cyclone Activity

Median values of the number of TS and TCs in the Caribbean expected during the year are four named storms, two hurricanes and one strong hurricane. The Caribbean basin was very active during 2008 in regard to tropical storm fomation with 10 named storms, out of which, 4 were strong hurricanes. Additionally, some cyclones landed or were observed near the Central American Caribbean coast: Arthur (May 30–June 6), Dolly (July 20–25), Marco (October 6–8), Tropical

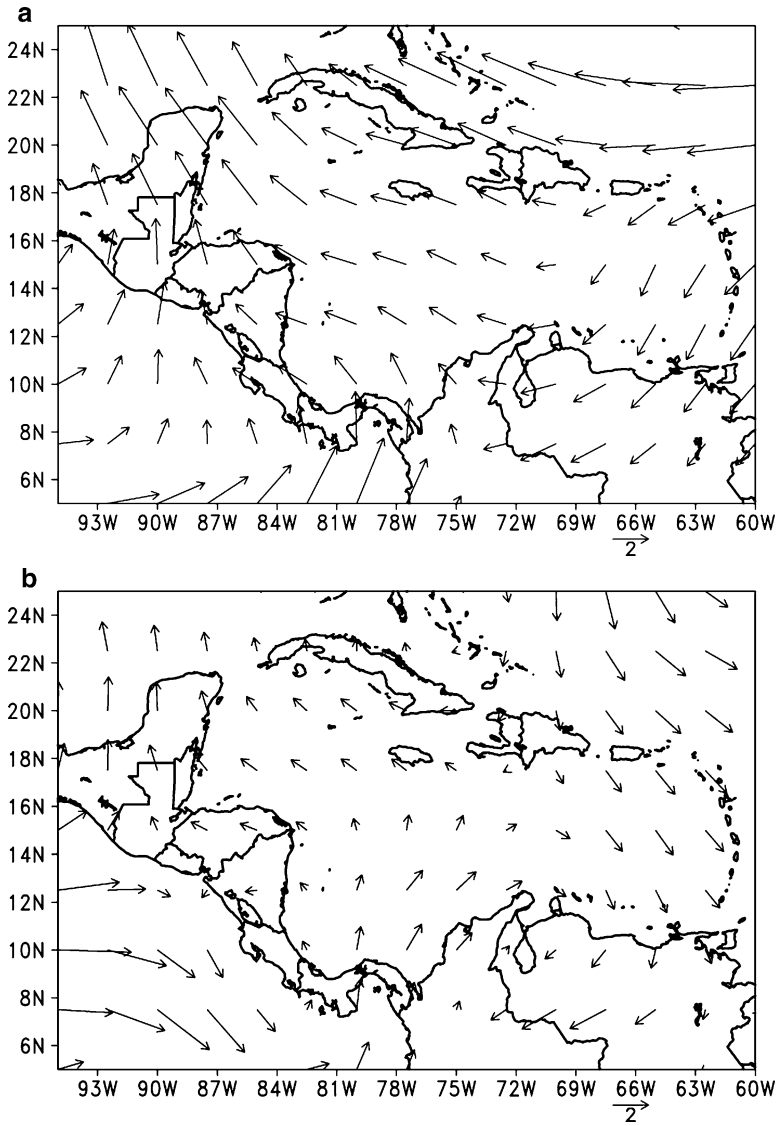

Fig. 8 Wind anomalies over the Intra-Americas Seas (IAS) at 925 hPa from corresponding long-term mean (1958–1999), during the 2008 cold El Niño-Southern Oscillation (ENSO) event (La Niña) for (**a**) February and (**b**) July

Depression 16 (October 14–16) and Paloma (November 5–10). Important impacts associated with hurricanes Fay, Gustav, Hanna and Ike during August–September 2008 were reported in Costa Rica. The Costa Rica National Meteorological Institute reported 36 easterly waves between May and October. In spite that Pacific

hurricanes affect in very rare occasions the Central American isthmus, the first hurricane of the 2008 season, Alma (May 28–30), landed in Leon, Nicaragua, producing important economic and social damage.

6 Concluding Remarks

The analysis of some atmospheric and oceanic indexes and their statistical relationship has provided important clues about the complex processes that determine TC activity in the Caribbean basin. On the one hand, locally controlled mechanisms by the CLLJ, the most important regional climate feature on the annual scale (Amador 2008), and on the other, the influence of remote atmospheric and oceanic signals, determine to a great extent tropical storm formation in this region. The CLLJ, also known as the IALLJ, has a marked annual cycle with two peaks, one in July (the absolute maximum) and the other one in February with an absolute minimum on October. During summer the development of the jet makes the Caribbean atmosphere barotropically unstable (Amador 1998), a condition that allows kinetic energy exchanges between atmospheric perturbations and the mean flow. The IALLJ vertical wind shear plays an important role controlling convective activity and cyclone formation whereas, the low-level divergence and descending motion associated with the jet entrance in the central Caribbean, act as an inhibiting factor for the organization of TCs. The July peak in wind speed and low-level vertical wind shear (with values of more than 12 and about 3 m/s, respectively), are associated with a minimum in the monthly relative frequency of TCs. On the contrary, a decrease in the wind speed and vertical shears are associated with a maximum value of the relative frequency of TCs. A remarkable inverse relationship was found between both, the strength of the wind speed at 925 hPa and the vertical wind shear at low levels, and the monthly relative frequency of TCs for two selected areas in the Caribbean (the IALLJ core and the whole basin). The surface wind below the jet core induces negative SST anomalies, minimizing the chances of systems to form in that region. Non-regional atmospheric and oceanic signals, such as NATL, AMO, and ENSO influence the IALLJ, changing its characteristics on seasonal scales. Stronger (weaker) than normal IALLJ summer winds (July–August), during warm (cold) ENSO events imply a stronger (weaker) than normal vertical wind shear at low-levels in the Caribbean. This condition may inhibit (allow) deep convection, disfavoring (favoring) TC development during these months. Correlation values of the monthly mean CLLJ core winds and the monthly normalized values of NATL + Niño 3, and NATL – Niño 3 indexes for 1950–2007 showed statistical significance greater than 99% during July–August. During El Niño years, low-level wind increases at the jet core strengthening the low level convergence and upward motion near Central America at the jet exit and the low-level divergence and descending motion in the central Caribbean at the jet entrance.

Climatologies of a group of General Circulation Models used in the IPCC (2007) report were studied to test the ability of the models to capture the low-level wind annual cycle over the Caribbean and the known CLLJ structure. Some models do

not capture the basic characteristics of the jet, such as its annual cycle, which has a lot of implications, especially for future climate change scenarios in this region and its associated societal impacts.

As a study case, the findings of this work were contrasted with the observed 2008 climate over the IAS region. Rainy season for 2008 in Central America evolved in a way consistent with the presence of La Niña event and the meridional migration of the ITCZ. Wind anomalies associated with the IALLJ were larger (smaller) than normal during February (July) 2008, consistent with this work and earlier findings in regards to the relationship of the IALLJ and ENSO phases (Amador 2008). The year of 2008 was very active for tropical storm formation in the Caribbean basin (10–22.5°N, 60–82.5°W). From 16 named storms observed in the Atlantic, 10 entered the Caribbean basin. Eight (five) Atlantic cyclones were hurricanes (strong hurricanes) and from the five hurricanes crossing the Caribbean basin, four were strong.

A major scientific problem that needs to be addressed, in the context of the IAS climate features and TC formation, is the observed precipitation distribution and its relationship with the moisture sources in or outside the region. In order to better understand some of the physical processes that explain precipitation variability in the region and its sources it is necessary to rely on numerical models. Rauscher et al. (2008) report that a comparison of the climate of the Twentieth Century simulations with observations over the period 1961–1990 shows that nearly all numerical models underestimate precipitation over Central America, due in part to an underestimation of sea surface temperatures over the tropical North Atlantic and an excessively smooth representation of regional topographical features. In regards to this problem, many questions arise. Do the models capture the moisture sources identified by Durán-Quesada et al. (2010)? Are the moisture sources the same for the wet season day-to-day precipitation and those during cyclone development? What is the mean contribution of precipitation from TC activity to that of the annual cycle? What is the interannual variability of this contribution? Are the strong and weak TC activity variations driven by the same factors in the IAS?

Acknowledgements The authors would like to recognize the partial support of the following projects during the course of this research, IAI-CRN-2050, UCR-VI 805-A7–002/805-A7–755/805-A8–401/805-A8–606/805-A9-532/808-A9–070/808-A9–180. The authors also wish to acknowledge Hugo Hidalgo from the School of Physics and CIGEFI for his valuable comments and suggestions. An anonymous reviewer helped to clarify the manuscript. Jorge Espinosa from the Panama Canal Authority kindly provided meteorological data for the Gatun station. Adolfo Quesada assisted in the preparation of the Central America map and some data analysis. Ingrid Rivera, Natalie Mora, Mariam Briceño and Andre Stahl helped in the digital preparation of the manuscript.

References

Alfaro E (2002) Some characteristics of the annual precipitation cycle in Central America and their relationships with its surrounding tropical oceans. Top Meteorol Oceanogr 9(2):88–103 Available at the Instituto Meteorológico Nacional (http://www.imn.ac.cr/publicaciones/index.html), San José, Costa Rica

Amador J (1998) A climatic feature of tropical Americas: The trade wind easterly jet. Top Meteorol Oceanogr 5(2):91–102 Available at the Instituto Meteorológico Nacional (http://www.imn.ac.cr/publicaciones/index.html) San José, Costa Rica

Amador J (2008) The Intra-Americas Seas Low-Level Jet (IALLJ): Overview and future research. In: Gimeno L, Garcia R, Trigo R (eds) Trends and directions in climate research. Ann NY Acad Sci 1146(1):153–188

Amador J, Magaña V (1999) Dynamics of the low level jet over the Caribbean Sea. Preprints 20th Conference in Tropical Meteorology. 10–15 January 1999 Dallas, Texas. Am Met Soc:401–402

Amador J, Chacón R, Laporte S (2003) Climate and climate variability in the Arenal Basin of Costa Rica. In: Diaz HF, Morehouse B (eds) Climate and water: transboundary challenges in the Americas. Kluwer Academic Publishers, Holland, pp 317–350

Amador J, Alfaro E, Lizano O, Magaña V (2006) Atmospheric forcing of the eastern tropical Pacific. A review. Prog Oceanogr 6(2–4):101–142

Bender M, Knutson T, Tuleya R, Sirutis J, Vecchi G, Barner S, Held I (2010) Modeled impact of anthropogenic warning on the frequency of intense Atlantic hurricanes. Science 327:454–458

Bengtsson L, Hodges K, Esch M, Keenlyside N, Kornblueh L, Luo J, Yamagata T (2007) How may tropical cyclones change in a warmer climate? Tellus 59A:539–561

Burpee R (1972) The origin and structure of easterly waves in the lower troposphere of North Africa. J Atmos Sci 29:77–90

Durán-Quesada A, Gimeno L, Amador J, Nieto R (2010) Moisture sources for Central America: Part I. Identification of moisture sources using a Lagrangian analysis technique. J Geophys Res doi:10.1029/2009JD012455

Enfield D, Alfaro E (1999) The dependence of Caribbean rainfall on the interaction of the tropical Atlantic and Pacific Oceans. J Clim 12:2093–2103

Enfield D, Mestas-Nuñez A, Trimble P (2001) The Atlantic multidecadal oscillation and its relation to rainfall and river flows in the continental U.S. Geophys Res Lett 28(10):2077–2080

Frank W, Young G (2007) The interannual variability of tropical cyclones. Mon Wea Rev 135:3587–3598

Goldenberg S, Landsea C, Mestas-Nunez A, Gray W (2001) The recent increase in Atlantic hurricane activity: Causes and Implications. Science 293:474–479

Gordon C, Cooper C, Senior C, Banks H, Gregory J, Johns T, Mitchell J, Wood R (2000) The simulation of SST, sea ice extents and ocean heat transports in a version of the Hadley Centre coupled model without flux adjustments. Clim Dyn 16:147–168

Gordon H, Rotstayn L, McGregor J, Dix M, Kowalczyk E, O'Farrell S, Waterman L, Hirst A, Wilson S, Collier M, Watterson I, Elliott T (2002) The CSIRO Mk3 climate system model CSIRO atmospheric research technical paper No 60:130

Gray W (1979) Hurricanes: Their formation, structure and likely role in the tropical circulation. In: Shaw D (ed) Meteorology over tropical oceans. Royal Meteorological Society, James Glaisher House, Grenville Place, Bracknell, Berkshire RG12 1BX:155–218

Gray W (1993) Chapter 5, seasonal forecasting, section 5.2, ENSO relationships with seasonal tropical cyclone activity. Global guide to tropical cyclone forecasting. World Meteorological Organization Technical Document WMO/TD No 560 Tropical Cyclone Programme Report No TCP-31

Gutowski W, Hegerl G, Holland G, Knutson T, Mearns L, Stouffer R, Webster P, Wehner M, Zwiers F (2008) Causes of observed changes in extremes and projections of future changes (Chapter 3). In Weather and climate extremes in a changing climate regions of focus: North America, Hawaii, Caribbean, and U.S. Pacific Islands. The US Climate Change Science Program: 81–116

IPCC (2007) Climate change (2007) The physical science basis. In: Solomon S, Qin D, Manning M, Chen Z, Marquis M, Averyt K, Tignor M and Miller H (eds) Contribution of Working Group I to the fourth assessment report of the intergovernmental panel on climate change. Cambridge University Press, Cambridge/New York

Kalnay E, Kanamitsu M, Kistler R, Collins W, Deaven D, Gandin L, Iredell M, Saha S, White G, Woollen J, Zhu Y, Chelliah M, Ebisuzaki W, Higgins W, Janowiak J, Mo K, Ropelewski

C, Wang J, Leetmaa A, Reynolds R, Jenne R, Joseph D (1996) The NCEP/NCAR Reanalysis 40-year Project. Bull Am Meteorol Soc 77:437–471

Kim S, Flato G, Boer G, McFarlane N (2002) A coupled climate model simulation of the Last Glacial Maximum, Part 1: transient multi-decadal response. Clim Dyn 19:515–537

Kim S, Flato G, Boer G (2003) A coupled climate model simulation of the Last Glacial Maximum, Part 2: Approach to equilibrium. Clim Dyn 20:635–661

Knutson T, Sirutis J, Garner S, Vecchi G, Held I (2008) Simulated reduction in Atlantic hurricane frequency under twenty-first-century warming conditions. Nature Geosci 1:359–364

Kuleshov Y, Qi L, Fawcett R, Jones D (2008) On tropical cyclone activity in the Southern Hemisphere: Trends and the ENSO connection. Geophys Res Lett 35:L14S08

Liebmann B, Smith C (1996) Description of a complete (interpolated) outgoing longwave radiation dataset. Bull Am Meteorol Soc 77:1275–1277

Magaña V, Amador J, Medina S (1999) The Mid-Summer Drought over Mexico and Central America. J Clim 12:1577–1588

Mapes B, Warner T, Xu M, Negri A (2003) Diurnal patterns of rainfall in northwestern South American. Part I: Observations and context. Mon Wea Rev 131:799–812

Marsland S, Haak H, Jungclaus J, Latif M, Röske F (2003) The Max Planck Institute global ocean/sea-ice model with orthogonal curvilinear coordinates. Ocean Modell 5:91–127

Mora I, Amador J (2000) EL ENOS, el IOS y la Corriente en Chorro de Bajo Nivel en el Oeste del Caribe. Top Meteorol Oceanog 7(1):1–20. Available at the Instituto Meteorológico Nacional (http://www.imn.ac.cr/publicaciones/index.html) San José, Costa Rica

Rauscher S, Giorgi F, Diffenbaugh N, Seth A (2008) Extension and intesification of the Meso-American mid-summer drought in the twenty-first century. Clim Dyn 31:551–571. doi:10.1007/s00382–007–0359–1

Roeckner E, Bäuml G, Bonaventura L, Brokopf R, Esch M, Giorgetta M, Hagemann S, Kirchner I, Kornblueh L, Manzini E, Rhodin A, Schlese U, Schulzweida U, Tompkins A (2003) The atmospheric general circulation model ECHAM5. Part I: Model description. Max Planck Institute for Meteorology Report No 349:127 pp

Smith T, Reynolds R, Peterson T, Lawrimore J (2008) Improvements to NOAA's historical merged land-ocean surface temperature analysis (1880–2006). J Clim 21:2283–2293

Taylor M, Alfaro E (2005) Climate of Central America and the Caribbean. In: Oliver J (ed) Encyclopedia of world climatology. Springer, The Netherlands, pp 183–189

Wang B, Chan J (2002) How strong ENSO events affect tropical storm activity over the Western North Pacific. J Clim 15:1643–1658

Wang C, Enfield D (2001) The tropical western hemisphere warm pool. Geophys Res Lett 28(8):1635–1638

Wang C, Enfield D (2003) A further study of the tropical western hemisphere warm pool. J Clim 16:1476–1493

Wang C, Lee S (2007) Atlantic warm pool, Caribbean low-level jet, and their potential impact on Atlantic hurricanes. Geophys Res Lett 34:L02703. doi:10.1029/2006GL028579

Wilks D (1995) Statistical methods in the atmospheric sciences. Cambridge University Press, San Diego, California, USA, 465 pp

Chapter 10
On the Increasing Intensity of the Strongest Atlantic Hurricanes

James B. Elsner and Thomas H. Jagger

Abstract The past three decades have seen a significant upward trend in the intensity of the strongest hurricanes worldwide that is most pronounced over the North Atlantic. Questions remain about this trend especially its relevance to coastal communities in the United States and elsewhere. This chapter focuses on observed changes in the intensity of the strongest hurricanes over the North Atlantic basin and on the geographic pattern of these changes. Results show that the upward trend is significantly related to rising sea-surface temperature (SST) after accounting for El Niño. The trend peaks at 16 m s^{-1} per °C at the 75th percentile with a 90% confidence interval of between 7 and 20 m s^{-1} per °C. The consequences of increasing intensity of the strongest hurricanes is not confined to the open ocean as nearly 70% of all hurricanes that occur over the basin reach a lifetime maximum intensity west of 60°W longitude. The largest intensity increases are occurring over the Gulf of Mexico and the Caribbean Sea, where ocean temperatures are warmest and hurricanes are strongest. Decreases in intensity are noted along most of the United States coastline consistent with a hypothesis that continental aerosols act to decrease hurricane intensity. This might help explain why, despite the increasing intensity of basin-wide hurricanes, there is no detectable upward tend in damage costs in the United States.

Keywords Hurricanes · Trends · Strongest · Geographic pattern · Sea surface temperature · Percentile · Quantile · Gulf of Mexico · Caribbean Sea · United States · El Nino · Aerosols

1 Introduction

Hurricanes are getting stronger on average with a recent trend that is related to an increase in ocean temperatures over the Atlantic and elsewhere (Emanuel 2005; Webster et al. 2005). Indeed our paper entitled "The increasing intensity of the

J.B. Elsner (✉) and T.H. Jagger
Department of Geography, Florida State University, Tallahassee, FL 32306, USA
e-mail: jelsner@fsu.edu; tjagger@blarg.net

J.B. Elsner et al. (eds.), *Hurricanes and Climate Change: Volume 2*,
DOI 10.1007/978-90-481-9510-7_10, © Springer Science+Business Media B.V. 2010

strongest tropical cyclones" published in September of 2008 (Elsner et al. 2008) generated considerable attention in the hurricane research community. The purpose of this chapter is to examine the evidence for trends in the strongest Atlantic hurricanes in more detail and to provide rejoinders to some of concerns that were raised about our methods and findings on blogs and especially on the *tropical storms mailing list*.

In particular here we show three new aspects of our original result. (1) The strongest hurricanes are getting stronger and the increase is related to an increase in sea-surface temperature (SST) after statistically controlling for the El Niño cycle. (2) Hurricanes often have a lifetime maximum intensity relatively near the coast of the United States. (3) The largest increase in the intensity of the strongest hurricanes is occurring over the Caribbean Sea and Gulf of Mexico where ocean temperatures are the warmest in the basin and where hurricanes tend to be the strongest.

At present hurricanes cannot be fully resolved in climate models, and the complex relationships between climate and hurricane frequency, intensity, and location are not well understood. Moreover, hurricanes and climate processes extend over a broad range of spatial and temporal scales making it difficult to model the potential relationships with a low-order numerical model. Thus in order to shed light on questions concerning the relationships between hurricanes and climate it is necessary to rely on the available historical data while keeping in mind data limitations and what we might expect to see in the data from theory.

As an example, there is no empirical evidence, modeling result, or theoretical argument that indicates the number of hurricanes will increase in a warmer world. On the other hand, relying on the notion of *ceteris paribus*, we can say from theory that warmer oceans should lead to stronger hurricanes. To detect this signal in historical records, it is necessary to separate hurricane frequency from hurricane intensity. Our approach is to use quantiles of lifetime maximum hurricane intensity and to quantify trends and examine statistical significance of quantile intensities using quantile regression.

This chapter is outlined as follows. A brief description of the hurricane and climate data is provided in Section 2. Here we use the HURDAT data hourly interpolated over the period 1943–2008, inclusive. In Section 3 a short introduction to quantiles is given followed in Section 4 by the results of a quantile regression of hurricane intensity on SST and El Niño. Results from the regression model verify that the strongest hurricanes are getting stronger as SST increases after statistically controlling for El Niño. The geographic distribution of lifetime maximum intensities are considered in Section 5. Areas near the Gulf coast and Florida are relatively more frequently visited by hurricanes near the time of their lifetime maximum than areas farther east over the open ocean. In Section 6 changes over time in the geographic distribution of maximum intensity of hurricanes are examined. The Gulf of Mexico and the Caribbean Sea are regions where some of the strongest Atlantic hurricanes occur and where the trend toward stronger hurricanes is most notable. The summary and conclusions are given in Section 7. The chapter ends with replies to comments made about our earlier research on this topic.

2 Data

As is customary in this kind of research, tropical cyclone wind speed estimates are obtained from the HURricane DATa base (HURDAT or best-track) maintained by the US *National Ocean and Atmospheric Administration* (NOAA) *National Hurricane Center* (NHC). HURDAT is the official record of tropical cyclone information for the Atlantic Ocean, Gulf of Mexico and Caribbean Sea, including those that have made landfall in the United States. HURDAT consists of the 6-h position and intensity estimates for tropical cyclones back to 1851 (Jarvinen et al. 1984; Neumann et al. 1999). Here a natural spline interpolation is used to obtain positions and wind speeds at 1-h intervals from the 6-h values based on the work of Jagger and Elsner (2006), Elsner et al. (2008).

For the present study we consider only tropical cyclones at hurricane intensity or above ($\geq$33 m s^{-1}) over the period 1943–2008, inclusive. The period is long enough to examine temporal changes but not too long that it includes data from the pre-aircraft reconnaissance era (prior to 1943). There are $N = 409$ hurricanes over the 66-year period. The raw wind speed values are given in 5 kt (2.5 m s^{-1}) increments. Although knots (kt) are the operational unit used for reporting tropical cyclone intensity to the public in the United States, here we use the MKS units of m s^{-1}. Throughout this chapter we use the term "intensity" as shorthand for "maximum wind speed," where maximum wind speed refers to the estimated fastest wind velocity somewhere in the core of the hurricane. Lifetime maximum refers to the highest maximum wind speed throughout the lifetime of the hurricane.

On the seasonal time scale and to a first order a warm ocean and a calm atmosphere (low wind shear) allows hurricanes to intensify. Some of the wind shear is related to the El Niño-Southern Oscillation (ENSO) cycle. Here we include data on the Southern Oscillation Index (SOI) as an indicator of ENSO and data on Atlantic SST as an indicator of ocean warmth. ENSO is characterized by basin-scale fluctuations in sea-level pressure between Tahiti and Darwin. The SOI is defined as the normalized sea-level pressure difference between Tahiti and Darwin. The SOI is strongly anti-correlated with equatorial Pacific SST so that an El Niño warming event is associated with negative values of the SOI. Units on the SOI values are given in standard deviations indicating they are standardized by the long-term mean and standard deviation. The relationship between ENSO and hurricane activity is strongest during the hurricane season, so we use an August–October average of the SOI as our covariate (explanatory variable). The monthly SOI values (Ropelewski and Jones 1997) are obtained from the Climatic Research Unit (CRU).

The United Kingdom Hadley model SST and U.S. NOAA optimal interpolated SST datasets were used to compute Atlantic SST anomalies in °C north of the equator. Anomalies are computed by month using the base period 1951–2000. Data are obtained from the NOAA-CIRES Climate Diagnostics Center back to 1871. For this study we average the SST anomalies over the peak hurricane season months of August through October. Monthly global temperature anomalies (1961–1990 base period) from the Intergovernmental Panel on Climate Change (IPCC) values are obtained from the CRU (Folland 2001).

3 Quantiles and Hurricane Intensity

Quantile regression, introduced by Koenker and Bassett (1978), extends the ordinary least-squares regression model to conditional quantiles of the response variable. It is used in Elsner et al. (2008) and Jagger and Elsner (2008) to examine trends in the intensity of tropical cyclones. Before considering our application of quantile regression using hurricane intensity we say a few words about quantiles and hurricane intensity.

Quantiles are points taken at regular intervals from the cumulative distribution function of a random variable. The quantiles mark a set of ordered data into equal-sized data subsets. For example, of the 409 hurricane intensity values in our North Atlantic data set, 25% of them are less than 39 m s^{-1}, while 50% are less than 47 m s^{-1}. Thus there is an equal number of hurricanes with intensities between 33 and 39 m s^{-1} as there is between 39 and 47 m s^{-1}. When we say that the median maximum hurricane intensity is 47 m s^{-1}, we mean that half of all hurricanes have intensities less than this value and half have intensities greater than this value. Similarly, the quartiles (deciles) divide the sample of hurricane intensities into four (ten) groups with equal proportions of the sample in each group. The quantiles, or percentiles, refer to the general case of dividing the intensities into any number of groups.

Quantile values of hurricane intensity are not directly tied to the frequency of hurricanes. This is important to understand before examining how the quantiles might be changing over time. Suppose for instance that in some earlier year there occur four hurricanes with lifetime maximum wind speeds of 33, 38, 48, and 53 m s^{-1}, and that in some later year there occur three hurricanes with lifetime maximum wind speeds of 33, 43 and 61 m s^{-1}. Then using only these 2 years we can see that there is a decrease in the frequency of hurricanes yet there is no change in the mean intensity (46 m s^{-1}) nor is there a change in the median intensity (43 m s^{-1}). However, there is an increase in the quantile values of wind speed above the median. For instance, the 75th percentile increases from 49 to 52 m s^{-1} and the 90th percentile increases from 52 to 57 m s^{-1} over this period.

Others have argued that the percentage of strong hurricanes to total number of hurricanes is the important index for detecting change in hurricane activity (Webster et al. 2005). Consider another example, where in the earlier year there are only three hurricanes with maximum speeds of 33, 40 and 50 m s^{-1} and where the later year is the same as before. Then the ratio of major hurricanes ($\geq$50 m s^{-1}) remains the same yet the strongest hurricane is stronger. Thus we argue that the intensity of the strongest hurricanes as indicated by the change in the upper quantile values of lifetime maximum wind speed is the variable most relevant to the debate on hurricane intensity in a changing climate.

Moreover, the concern that if the total number of hurricanes is not changing and the number of strong hurricanes is increasing, then the number of weak hurricanes must decrease proportionally is misplaced. The rate of strong hurricanes is much smaller than the rate of weak hurricanes. As the ocean warms the stronger hurricanes

can effectively "borrow" a few hurricanes from below a specified threshold intensity that may result in a significant increase in the rate of stronger hurricanes while not significantly reducing the rate of weaker hurricanes.

4 Increases in Hurricane Intensity with Increasing SST Accounting for ENSO

The value of a simple trend analysis (involving only one variable – usually time) is limited by the fact that other explanatory variables also might be trending. In the context of hurricane intensity, it is well known that the ENSO cycle can significantly alter the frequency and intensity of hurricane activity on the seasonal time scale. A trend over time in hurricane intensity could simply reflect a change in this cycle. Thus it is important to look at the trend after controlling for this important factor. Here we go beyond what was done in Elsner et al. (2008) and show the trend as a function of Atlantic SST after controlling for the ENSO cycle. Thus we answer the question of whether the data support the contention that the increasing trend in the intensity of the strongest hurricanes is related to an increase in ocean warmth conditional on ENSO.

Figure 1 shows the results of a quantile regression model using North Atlantic lifetime maximum intensity as the response variable and Atlantic SST and Pacific SOI as the explanatory variables. Other variables including the North Atlantic oscillation (NAO) and sunspots were found not to be statistically significant. The trend values are plotted for percentile values of wind speed between 5% and 95% in intervals of 5%.

Trend values for Atlantic SST range from near zero for the weaker hurricanes (lowest quantiles) to between 10 and 15 m s^{-1} per °C. The trends are statistically significant for hurricanes above the 60th percentile (on average, above 52 m s^{-1}) as can be seen by the 90% confidence band sitting entirely above the zero trend line. The trend peaks at 16 m s^{-1} per °C at the 75th percentile with a 90% confidence interval of between 7 and 20 m s^{-1} per °C. The mean regression line indicates a trend of about 5 m s^{-1} per °C which is statistically significant above the zero trend line as indicated by the dashed lines (90% confidence intervals).

Trend values for the SOI range from about 1 m s^{-1} per standard deviation for the weakest hurricanes to near 3 m s^{-1} per standard deviation for hurricanes above the median intensity (on average 49 m s^{-1}). The trends are mostly statistically significant and the mean regression line indicates a statistically significant trend of 2 m s^{-1} per standard deviation. The results indicate that the rising trend of the most intense hurricanes as the ocean temperatures rise is statistically significant after accounting for the ENSO cycle. Thus the ENSO cycle, although also significant as expected in modulating hurricane intensity, cannot explain the increasing intensity of the strongest Atlantic hurricanes as ocean temperature rises.

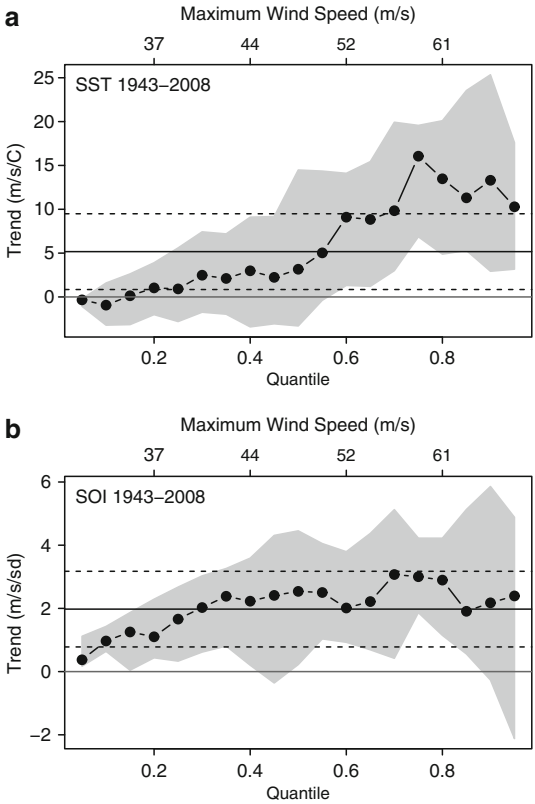

Fig. 1 Basin-wide trends in North Atlantic hurricane intensity. (**a**) Quantile trends with respect to Atlantic SST controlling for ENSO. For an increase in SST there are increases in hurricane intensity with increases generally larger (above 10 m s^{-1} per °C) at higher hurricane intensities. Statistically significant trends are noted for quantile values above the median hurricane intensity. The plot looks similar when using data starting with 1965 (satellite era). (**b**) Quantile trends with respect to ENSO controlling for SST. For a 1 standard deviation increase in the SOI (toward La Niña conditions) there is an increase of around 2 m s^{-1} in hurricane intensity. The *gray area* defines the 90% confidence intervals about the trend estimates. The mean regression line is about 5 m s^{-1} per °C for SST and about 2 m s^{-1} per s.d. for SOI and both are statistically significant above zero as shown by the dashed lines (90% confidence intervals)

5 Geographic Distribution of Lifetime Maximum Intensity

Even though the strongest hurricanes are getting stronger over the period 1943–2008, it does not necessarily imply that hurricanes approaching land or those over land are getting stronger. In fact it has been mentioned that our results might not be particularly relevant to decision makers if most hurricanes reach their maximum intensity far from land. Here we examine the geographic distribution of lifetime maximum intensity and find what might, at first, seem a bit surprising.

We do this by dividing the North Atlantic basin into nearly-equal area hexagon bins and counting the number of times the location of a hurricane's lifetime maximum intensity occurs within each bin. Hexagon bins are used instead of the more common rectangular bins because a hexagon represents the best compromise between overlap and spatial uniformity (Brettschneider 2008). As with the rectangles, hexagons provide a tiling of the two dimensional plane. That is they can be fit together with no gaps. Moreover since all interior angles are congruent and all sides are of equal length, the hexagon is the shape with the most angles that still tiles the plane and that best approximates the circle.

For each hurricane we determine where the hurricane *first* reached its lifetime maximum intensity. Figure 2 shows the results of this counting procedure along with the maximum value over all lifetime maximum intensities for hurricanes within each bin. The "bee hive" plot shows the geographic distribution of the frequency and intensity of the lifetime maximum intensity. Only locations with at least one lifetime maximum intensity value have a hexagon bin and the bin width is approximately 5° of longitude.

Perhaps somewhat surprising is that the U.S. coast (especially along the Gulf and southeast) are more threatened by hurricanes near their lifetime maximum compared with areas farther to the east and south over the open ocean. In fact, 69% of all 409 hurricanes over the period 1943–2008 have a lifetime maxima in a hexagon bin that is centered to the west of 60°W longitude.

Upon deeper reflection, near-coastal locations might be expected to have a greater number of hurricanes at lifetime maximum since an intensifying hurricane

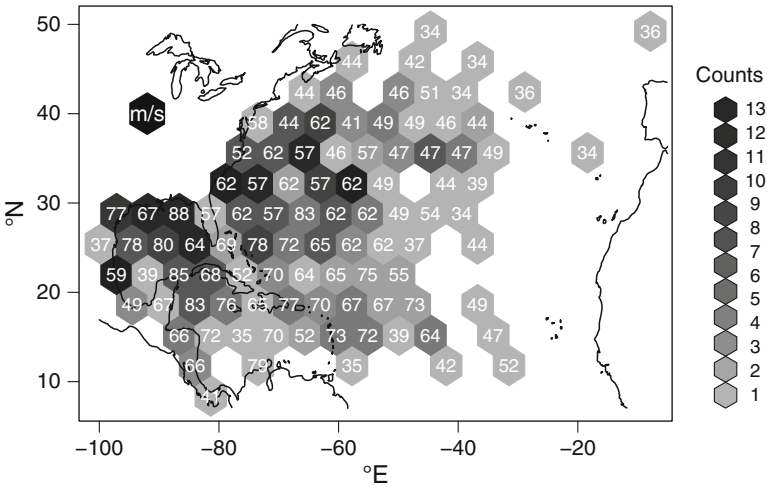

Fig. 2 Frequency and maximum intensity of Atlantic hurricanes at lifetime maximum intensity. The *gray scale* shows the number of times a hurricane reached its lifetime maximum intensity (first time only) within the hexagon bin using hurricanes over the period 1943–2008. The value inside the hexagon is the maximum intensity (m s^{-1}) of all lifetime maxima in the bin

will decay after making landfall thereby capping intensity at or near the coast. Interestingly though, these regions tend also to be where the intensities of the lifetime maxima are large. This is not entirely surprising as these bins contain a larger collection of maxima. In fact the correlation between the number of times a hurricane reaches its lifetime maximum in the bin and the maximum intensity over all lifetime maxima is 0.5 [0.33, 0.63] (95% confidence interval) over the 98 bins.

Hurricanes typically originate over the waters of the wide expanse of the tropical oceans. They intensify over these warm waters then decay as they move over cooler waters or over land. Thus over the western part of the North Atlantic hurricane basin and especially near the Gulf coast the hexagon bins contain a mixture of hurricanes that are close to their theoretical maximum potential intensity as well as hurricanes that were intensifying prior to landfall, but still conceivably far from their theoretical maximum potential intensity. It is this mixture of hurricane intensities that might help explain why a climate change signal is not apparent in the set of hurricane intensities at landfall as it is for the larger set of hurricanes basin wide.

6 Geographic Distribution of Changes in Maximum Intensity

As noted previously, using only the lifetime maximum intensity limits the data set to 409 hurricanes over the period 1943–2008. Examining the geographic distribution of these lifetime maxima as was done in the previous section limits the number of cases to a median of about three hurricanes per bin. This is too few cases to examine the geographic distribution of changes in maximum intensity over time.

Therefore in this section we consider the intensity of hurricanes along their entire path at hourly intervals. The hourly intensities are based on a spline interpolation of the 6-h estimates as mentioned in Section 2. The hourly hurricane intensities are binned using hexagons as before and the maximum intensity value for each bin is obtained. This maximum intensity reflects the strongest estimated wind speed over all hourly observations and over all hurricanes passing through the bin.

Figure 3 shows the geographic distribution of hurricane frequency and maximum intensities using hexagon bins. The regions of higher frequency corresponds to the preferred pathway of hurricanes across the basin. The most notable pathway being the parabolic sweep from the low latitudes of the central Atlantic northwestward to the Bahamas and then northward and northeastward towards higher latitudes. The main focal region for hurricane activity is the area near and just to the north of the Bahamas.

The correlation between the spatial density of hourly hurricane observations and maximum intensity is 0.73 indicating, as expected, a tight spatial relationship between factors that control hurricane frequency and factors that control intensity. However, the strongest of the strong hurricanes occur over the western Caribbean Sea and into the Gulf of Mexico. Next we consider the geographic variation in the change of maximum intensity over time. To do this we divide the 66-year record into

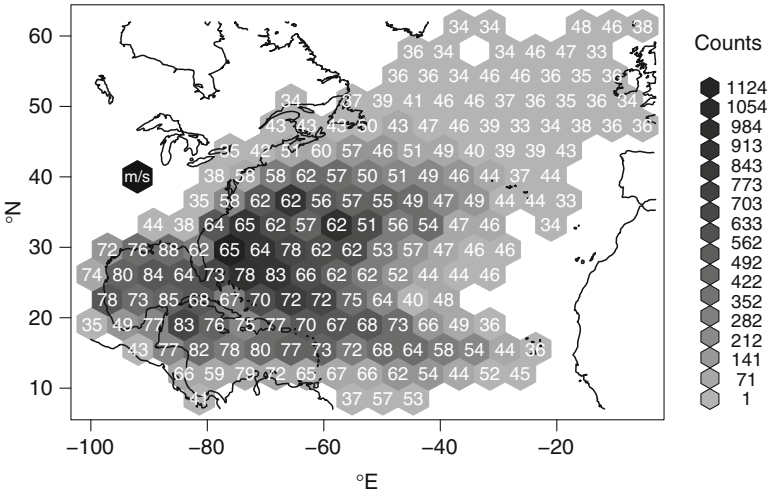

Fig. 3 Frequency and maximum intensity of hourly hurricane observations. The *gray shade* indicates the frequency of hourly observations in the hexagon bin and the number inside the bin is the maximum intensity over all hourly observations in the bin

two parts and create similar bee hives of hurricane intensity and frequency. We then plot the differences using the same bee hive plot. The division is based on separating the years into two equal groups.

The frequency and maximum intensity of hurricanes over two consecutive non-overlapping time periods are displayed in Fig. 4. The top panels show the number of hourly observations and the bottom panels show the maximum intensity value over all the observations. The left panels show the data from the period 1943–1975 and the right panels show the data from the period 1976–2008.

Overall there are 9% fewer hourly observations over the later years compared with the earlier years. But over the Caribbean and Gulf of Mexico the difference is in favor of the earlier period. That is, there are 25% more hourly hurricane observations in the 20 hexagon bins comprising the Gulf of Mexico and the Caribbean during the 33-year period 1943–1975 as there are in the same 20 bins over the later 33-year period 1976–2008. There are also notably more hurricane observations during the earlier period over the Bahamas extending into the western North Atlantic.

One explanation for the fewer hourly hurricane observations is the faster forward speeds in the later period. Although the average forward speed of hurricanes over the entire basin during the earlier period is 6.5 m s^{-1}, which compares with 6.3 m s^{-1} over the later period. Over the region bounded by 100° and 60°W and 10° and 30°N, the average forward speed is 4.9 m s^{-1} over the earlier period compared with 5.2 m s^{-1} over the later period. Thus over the region including the Caribbean Sea, Gulf of Mexico, and the Bahamas, hurricanes moved on average about 6% faster during the most recent 33-year period compared with the earlier period. This difference in forward speed accounts for a 5.6% reduction in counts on average. With fewer hurricane observations we might expect the maximum intensities to be lower.

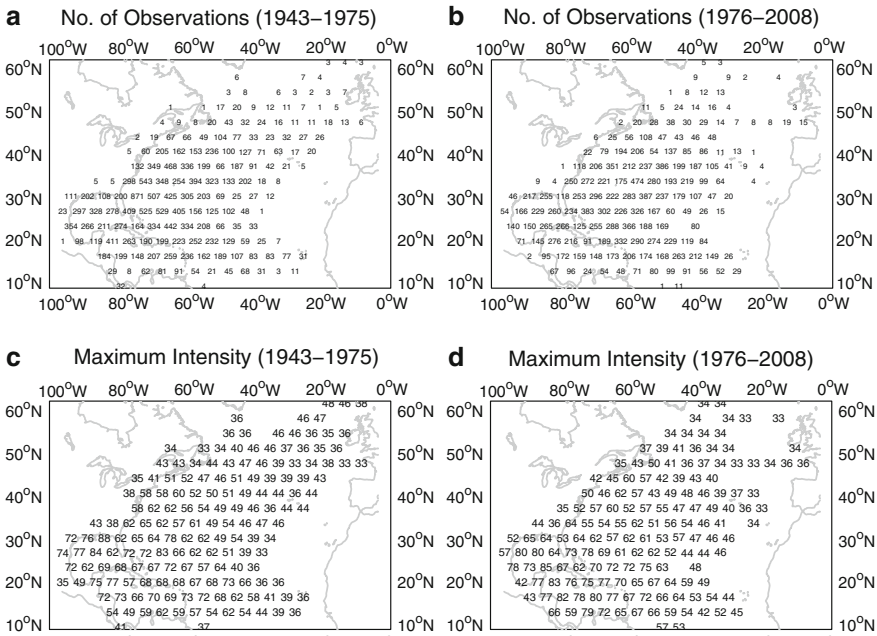

Fig. 4 Number of hurricane hourly values and maximum hurricane intensity by region and period. The regions are the hexagon bins used in Fig. 3. The number of hourly values is based on a spline interpolation of the 6-h HURDAT estimates. The maximum intensity in m s^{-1} is based on all hourly values in the bin. The two periods include the intervals before and after 1975. The number of observations (**a**) 1943–1975 and (**b**) 1976–2008 are shown in the top panels and the maximum intensities (**c**) 1943–1975 and (**d**) 1976–2008 are shown in the bottom panels

Indeed with fewer hurricanes more recently you would expect to see lower maximum intensities as is noted over the western North Atlantic. Interestingly, however, over the Gulf of Mexico and Caribbean Sea, where there are also fewer hurricane observations during the later half of the record, the maximum intensities tend to be larger. In fact the average maximum intensity over the 20 hexagon bins is 68 m s^{-1} during the early period compared with 74 m s^{-1} during the later period, an increase of about 10%. Thus over the Gulf of Mexico and Caribbean the strongest hurricanes are getting stronger. And this is also where hurricanes are generally strongest fueled by the largest ocean heat capacity of anywhere across the basin. In fact, 6 of the 20 hexagon bins over the Gulf and Caribbean have maximum intensities at 80 m s^{-1} or higher compared during the later period compared with only 1 during the earlier period.

The differences in the number of observations (expressed as a percentage) and the differences in maximum hurricane intensities between the two periods is illustrated in Fig. 5. The positive (negative) percentages indicate more (fewer) hurricane observations over the later period. The positive (negative) values indicate higher (lower)

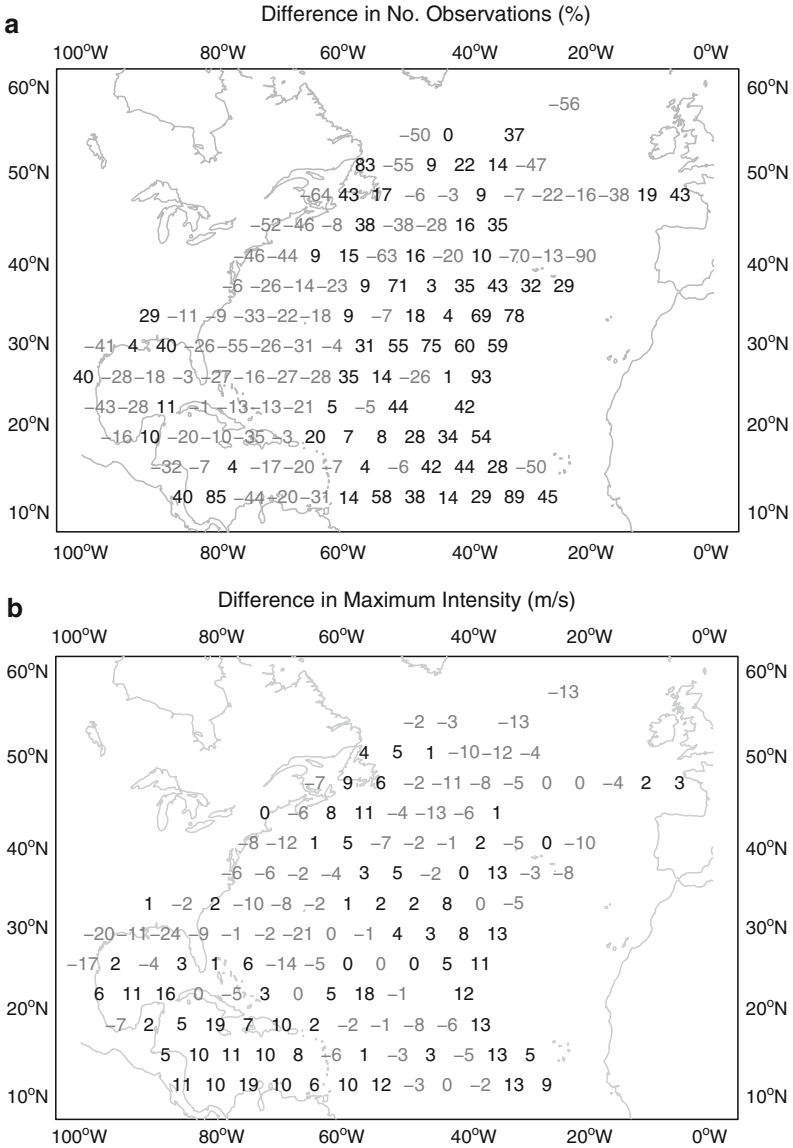

Fig. 5 Differences in the number of observations and maximum hurricane intensities. The differences are based on the periods 1943–1975 and 1976–2008, where the number of observations and maximum hurricane intensity in the bin during the earlier period are subtracted from the number of observations and maximum hurricane intensity in the bin during the later period. (**a**) *Positive (negative) values* indicate more (fewer) hurricane observations over the later period. (**b**) *Positive (negative) values* indicate an increase (a decrease) in the intensity of the strongest hurricanes. Note there are fewer but stronger hurricanes across much of the Gulf of Mexico and the Caribbean Sea during the more recent period

maximum intensities over the later period. Increases as large as 10–19 m s^{-1} are noted over the Gulf of Mexico and the Caribbean Sea. Decreases are noted over the western North Atlantic to the northeast of the Bahamas. Decreases are also noted along most of the United States coastline. This is an interesting finding that is consistent with the hypothesis that continental aerosols can act to decrease hurricane intensity (Khain et al. 2010) and that might help explain why, despite the increasing intensity of basin-wide hurricanes, there is no upward trend in normalized insured losses (Jagger et al. 2008; Pielke et al. 2008). Because of the spatial correlation, the number of comparisons, and the arbitrary division of years, we make no attempt to estimate the statistical significance of these results, only noting that they are largely consistent with our admittedly limited theoretical understanding of hurricanes on a climate scale.

7 Summary and Conclusions

Hurricanes are not well resolved in current climate models thus we must rely on the available historical data to get a glimpse of what might happen in the future. In a recent paper (Elsner et al. 2008) we showed that the strongest hurricanes have been getting stronger with a 26-year trend that is related to an increase in ocean temperature over the Atlantic and elsewhere. In this chapter evidence for this claim is examined in more detail. In particular, quantile trends with respect to SST are estimated after statistically controlling for ENSO. Moreover the geographic variability of lifetime maximum intensities and their changes over time are examined by dividing the North Atlantic hurricane basin into hexagon bins. Hexagon bins provide a tiling of the area of interest while best approximating the ideal shape of a circle.

It is found that the strongest Atlantic hurricanes are getting stronger and the increase is related to an increase in SST after controlling for changes in the ENSO. The trend peaks at 16 m s^{-1} per °C at the 75th percentile with a 90% confidence interval of between 7 and 20 m s^{-1} per °C. The increasing intensity of the strongest hurricanes is not confined to the open ocean as nearly 70% of all hurricanes reach their lifetime maximum intensity west of 60°W longitude. The largest increase in the intensity of the strongest hurricanes is occurring over the Gulf of Mexico and the Caribbean Sea where ocean temperatures are warmest. Interestingly, these regions where the strongest hurricanes are getting stronger correspond to areas with fewer observations. We also note a tendency for decreases in maximum intensities for hurricanes along the U.S. coastline.

In summary, the heat-engine theory of tropical cyclone intensity (Emanuel 1991) is not about more intense hurricanes rather it is about a hurricane becoming more intense. There is an important difference. The first is about a collection of hurricanes so more intense hurricanes could result from simply having more hurricanes. But even under a scenario of constant (or decreasing) hurricane rate, the strongest hurricanes are getting stronger. If we consider near-coastal hurricanes as a subset

of all hurricanes, then we do not necessarily expect to see the signal, since we are capturing hurricanes at a somewhat random part of their lifecycle. This mixing of intensity distributions might help explain why a climate change signal is not apparent in the set of landfall hurricane intensities. Moreover, increasing aerosol concentrations from the increasing built environments could be dampening the intensity of the strongest hurricanes as they approach the coast. More work on this interesting and important topic is needed.

8 Replies to Comments on Elsner et al. (2008)

Our paper entitled "The increasing intensity of the strongest tropical cyclones" published in the September 4th, 2008 issue of *Nature* garnered considerable attention in the scientific community. Here we present comments, listed as bullets, that were received on this work. The comments came from various sources including the *tropical storms mailing list* and we reproduce them here as is. Our replies to the comments follow in the gray boxes.

- **Comment** Intuitively the number of tropical cyclones exceeding the mean rate plus two times the standard deviation as was shown in previous studies (e.g., Kossin et al. 2010) should be equivalent to number of tropical cyclones exceeding some upper quantile level as shown in Elsner et al. (2008).

Reply The number of cyclones exceeding plus two times the standard deviation is positively correlated to the rate of cyclones. A basin with a lower rate of tropical cyclones will have fewer cyclones exceeding plus two times the standard deviation compared with a basin with a higher rate, while the number of cyclones exceeding the 90th percentile is not necessarily dependent on the rate. Thus it is not appropriate to compare, in this way, the differences between Kossin et al. (2007) and Elsner et al. 2008.

- **Comment** I've regressed the most intense tropical cyclones per season on year and my results do not match those presented in Elsner et al. (2008).

Reply A regression of the most intense tropical cyclones per season is not the same as quantile regression on year as was done in Elsner et al. (2008) for the following two reasons. (a) Quantile regression minimizes a linear absolute deviation statistic rather than a quadratic statistic, and (b) quantile regression treats each intensity value equally; no wind speed contributes more to the model fit.

- **Comment** Your results are only marginally significant and there are many factors contributing to hurricane intensification.

Reply That is correct, but all else being equal, a warming of the tropical oceans where tropical cyclones form should increase their intensity. Since the strongest tropical cyclones are, on average, closest to their theoretical maximum potential intensity it stands to reason that if there is a warming signal it should be most apparent in the tendency of the strongest cyclones. Moreover, statistical inference is concerned with drawing conclusions based on data together with prior assumptions. Arguments that include the basic physics of the role ocean heat plays in tropical cyclone intensity have more weight before the data are examined.

- **Comment** The authors claim that the increasing trend is consistent with theory, yet numerical modeling studies suggest a different sensitivity of tropical cyclone intensity to warming.

Reply Numerical models are not theory. They are based on theory, but require ad hoc empirical arguments that place them into the realm of "scenario generators." The theory we have in mind is the 2nd law of thermodynamics. If the future is one with greater wind shear across the warming North Atlantic, then there may indeed be fewer hurricanes.

- **Comment** I'm surprised that the relationship between intensity and sea-surface temperature is not stronger.

Reply The physics of cyclone intensification works against the correlative relationship. An active year of tropical cyclones will effectively remove warmth from the ocean so that a seasonal average temperature will not correlate as strongly with tropical cyclone activity as one might expect even though the physical causality is strong.

- **Comment** Yet when you look at scatter plots of these SST series versus number of intense TCs [tropical cyclones] there is no relationship in the warmer SST, more intense TCs direction.

Reply We did not look at the number of TCs; we looked at the intensity. There is no theory for TC formation. However, given a TC, there is a nice theory for the efficiency of intensification. So, we focused on intensity rather

than on frequency. Given a TC in a nearly optimal dynamic environment, we should expect to see it reach a higher intensity with warmer SST. If on average 10% of the storms get within 5% of their maximum potential intensity (MPI) and the MPI increases then we would see the strongest storms getting stronger, assuming all else stays the same.

- **Comment** Here's a hypothetical, what if the predictor had been another quantity that also shows a significant trend over the period 1981–2006, I don't know. . .my weight, perhaps. . .would one be discussing what the physical meaning of a non-significant correlation between the two was?

Reply This hypothetical has little to do with the relationship of hurricanes to warming seas since in the latter there is a theory linking the two, whereas with your weight and hurricanes there is none. In science this makes a big difference.

Acknowledgements The work was supported by the U.S. National Science Foundation (ATM-0738172) and by the Florida Catastrophic Storm Risk Management Center. Views expressed within do not necessarily reflect the opinions of the funding agencies. Statistical analysis and modeling is performed using the software environment R (http://www.r-project.org) and the quantile regression package quantreg (R package version 4.36; http://www.r-project.org) with special thanks to Roger Koenker.

References

Brettschneider B (2008) Climatological hurricane landfall probability for the United States. J Appl Meteorol Climatol 47:704–716

Elsner JB, Kossin JP, Jagger TH (2008) The increasing intensity of the strongest tropical cyclones. Nature 455:92–95

Emanuel KA (1991) The theory of hurricanes. Ann Rev Fluid Mechan 23:179–196

Emanuel KA (2005) Increasing destructiveness of tropical cyclones over the past 30 years. Nature 436:686–688

Folland C et al. (2001) Global temperature change and its uncertainties since1861. Geophys Res Lett 28:2621–2624

Jagger TH, Elsner JB (2006) Climatology models for extreme hurricane winds near the United States. J Climate 19:3220–3226

Jagger TH, Elsner JB (2008) Modeling tropical cyclone intensity with quantile regression. Int J Climatol, doi:10.1002/joc.1804

Jagger TH, Elsner JB, Saunders MA (2008) Forecasting US insured hurricane losses. In: Diaz HF, Murnane RJ (eds) Climate extremes and society. Cambridge University Press, New York

Jarvinen BR, Neumann CJ, Davis MAS (1984) A tropical cyclone data tape for the North Atlantic Basin, 1886–1983: contents, limitations, and uses. NOAA Tech Memo NWS NHC-22, Coral Gables

Khain A, Lynn B, Dudhia J (2010) Aerosol effects on intensity of landfalling hurricanes as seen from simulations with WRF model with spectral bin microphysics. J Atmos Sci 67:365–384

Koenker R, Bassett G(1978) Regression quantiles. Econometrica 46:33–50

Kossin JP, Knapp KR, Vimont DJ, Murnane RJ, Harper BA (2007) A globally consistent reanalysis of hurricane variability and trends. Geophys Res Lett 34:L04815

Neumann CJ, Jarvinen BR, McAdie CJ, Hammer GR (1999) Tropical cyclones of the North Atlantic Ocean, 1871–1998 National Oceanic and Atmospheric Administration

Pielke, RA Jr, Gratz J, Landsea CW, Collins D, Saunders MA, Musulin RA (2008) Normalized hurricane damage in the United States: 1900–2005. Nat Hazards Rev 9:29–42

Ropelewski CF, Jones PD (1997) An extension of the Tahiti-Darwin southern oscillation index. Monthly Weather Rev 115:2161–2165

Webster PJ, Holland GJ, Curry JA, Chang HR (2005) Changes in tropical cyclone number, duration, and intensity in a warming environment. Science 309:1844–1846

Chapter 11
Frequency and Intensity of Hurricanes Within Florida's Threat Zone

Jill C. Malmstadt, James B. Elsner, and Thomas H. Jagger

Abstract This chapter examines historical hurricanes within Florida's threat zone; a 1,000 km radius around 26°N latitude and 82°W longitude. The area is visited by hurricanes from May through December with a peak in September. Threats come from hurricanes originating or passing over the Gulf of Mexico, Caribbean Sea, and the Bahamas. On average, three hurricanes every 2 years and one major hurricane every other year occur in the threat zone. Hurricane Wilma in 2005 is the strongest hurricane in the record with a peak intensity of 78.4 m s^{-1}. This is approximately a one-in-20 year event for the threat zone as a whole. The region can expect hurricane wind intensities of 60.8 m s^{-1} (58.3–63.3) (90% CI), on average, once every 2 years. There appears to be no upward or downward trend in the frequency of hurricanes within the region, but the intensity of hurricanes is on the rise. The rise could be related to recent (since 1980) warming ocean temperatures in the Caribbean, but a simple linear regression model finds no statistically significant signal. Hurricanes over and around Florida are intensifying and decaying more rapidly than in the past. Explanations for these changes are lacking but they suggest a bias in risk models that assume a stationary hurricane climate over and around Florida.

Keywords Florida · Hurricane · Threat · Return period · Intensity

1 Introduction

The United States' Gulf and Atlantic coasts are threatened by hurricanes each year. The coastal stretch from Louisiana to Florida to the northern shores of South Carolina have experienced numerous catastrophic hurricane events, with some very recent in memory. In particular, hurricanes affecting the state of Florida come from Bahamas, the western Caribbean, and the Gulf of Mexico. The region within a 1,000-km radius of 26°N latitude and 82°W longitude off the southwest coast of

J.C. Malmstadt (✉), J.B. Elsner, and T.H. Jagger
Department of Geography, Florida State University (FIPS Code 12), Tallahassee, FL, USA
e-mail: jmalmstadt@fsu.edu; jelsner@fsu.edu; tjagger@blarg.net

J.B. Elsner et al. (eds.), *Hurricanes and Climate Change: Volume 2*,
DOI 10.1007/978-90-481-9510-7_11, © Springer Science+Business Media B.V. 2010

Florida is the area described by Hamid et al. (2008) in an attempt to identify storms that could conceivably impact Florida. The Florida Commission on Hurricane Loss Projection Methodology (FCHLPM), created during the 1995 Florida Legislative session to evaluate hurricane risk models, advises modelers to consider hurricanes in this area as a potential threat to Florida (Florida threat zone). This is done for the purposes of comparing different risk models used by the insurance industry (Hamid et al. 2008; Jagger and Elsner 2009) using a common set of hurricanes. The threat zone includes the region from Baton Rouge, LA to Myrtle Beach, SC. It also includes most of Cuba, portions of the Yucatan Peninsula, and the Bahamas. A hurricane within the Florida threat zone does not imply it will directly affect the state.

This chapter examines hurricanes in the Florida threat zone including a look at the return periods of the strongest hurricanes and changes in the occurrence rate and intensities over time. According to Blake et al. (2007), 40% of all U.S. hurricanes and major hurricanes hit Florida. The analysis conducted here provides insight into the climatology of hurricanes that have affected Florida and the surrounding threat zone. First, descriptive statistics about the observed frequency and intensity of hurricanes in the zone are provided. Next, using a statistical method developed in Jagger and Elsner (2006), and since employed in Elsner et al. (2008b) and Malmstadt et al. (2010), return levels for the most extreme hurricane winds are estimated, as a way to assess hurricane risk in the threat zone. The analysis concludes with an examination of trends in hurricane intensity and intensification rates using the method of quantile regression. The relationship between changes in wind speed and observed changes in sea surface temperature (SST) over the Gulf and Caribbean is also briefly examined.

2 Data

The wind speed estimates and their locales are derived from the National Hurricane Center's Hurricane Database (HURDAT; or best track). This is the official record of tropical cyclones for the Atlantic Ocean, Gulf of Mexico, and Caribbean Sea, including those that have passed through Florida's threat zone. This record consists of the six-hourly cyclone location and intensity for individual storms back to 1851. The intensities represent an estimate of the maximum wind speed somewhere in the hurricane sustained for 1 min as indexed at a 10-m height above sea level. Estimates are more reliable for data since the time of aircraft observations (middle 1940s) and especially since the time of satellite observations (early 1970s).

This study examines hurricanes in the vicinity of Florida going back to 1899 as this is the start year used by the FCLPM. The FCLPM uses this time period for evaluating historical hurricanes as a common benchmark to compare proprietary hurricane loss models used by the insurance industry. The hurricane data collected are combined with the one-hourly interpolated hurricane positions and intensity values available from the spline interpolation technique provided in Jagger and Elsner (2006). The interpolation scheme provides a nonlinear interpolation of values for each hour.

The Caribbean SST data used in the analysis serve as evidence for climate change over the western Caribbean and Gulf of Mexico. These data can be found at http://www.esrl.noaa.gov/psd/data/correlation/CAR.data. The data include monthly SST anomalies from the Caribbean Index from 1951 to 2006. Here we use the average August–October anomaly for each year. This is done to highlight the SST anomalies during the most active part of the hurricane season for this part of the basin (Landsea et al. 1999). The Caribbean SST data are an area average that includes the entire Caribbean Sea, the Florida Straits and the seas surrounding the Bahamas, as well as the majority of the Gulf of Mexico. More specifically, the spatial coordinates of the averaging region includes 27°N to 9°S latitude and 60°E to 100°W longitude (NOAA Earth Systems Research Laboratory 2009).

3 Hurricanes in the Vicinity of Florida

The analysis of hurricanes in Florida's threat zone begins with some descriptive statistics about the observed hurricane events since 1899. The region, shown with a black outline in Fig. 1, is a 1,000-km radius surrounding 26°N latitude and 82°W longitude; just off the southwest coast of Florida. The area captures hurricanes that may affect the panhandle, west, and northeast coasts of Florida, as well as hurricanes that approach south Florida from the vicinity of Cuba and the Bahamas. Again it is important to remember that not all hurricanes that visit the threat zone actually affect Florida.

Using data from 1899 to 2008, the location of the maximum wind speed per hurricane is plotted based on the Saffir–Simpson category of wind speeds. Different symbols denote different categories on this scale. The maximum wind speed

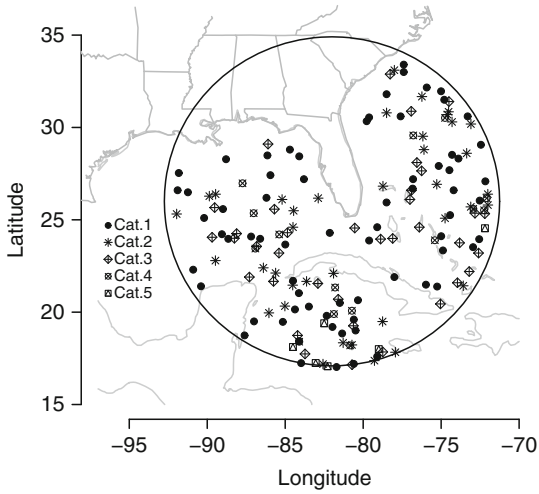

Fig. 1 Florida threat zone and locations of the strongest wind speed of each hurricane that entered the area. The symbol type denotes intensity categories according to the Saffir–Simpson scale

location refers to the strongest wind speed for a hurricane inside the region. A hurricane that reaches this maximum more than once is counted only once and is located at the time of first maxima.

The Florida threat zone experienced 165 hurricanes and 59 major hurricanes (category 3 or higher on the Saffir–Simpson scale) over the 110-year period. As hurricane wind speeds slacken over land the points are generally over water. Two broad clusters of points are noted; one over the western Caribbean Sea extending northwest into the Gulf of Mexico and the other over the Bahamas and areas to the north. Between these two clusters a band of lower point densities is noted over the Greater Antilles. The distribution of category one hurricanes appears more spatially uniform in comparison to the distribution of the stronger categories of hurricanes although no formal tests of clustering are carried out here.

Table 1 lists the top ten highest wind speeds from hurricanes experienced in the threat zone during this time period. Four of these extreme hurricanes occurred since 2004; Hurricane Ivan in 2004, Hurricanes Wilma and Katrina in 2005, and Hurricane Dean in 2007. The other six storms occurred during earlier portions of the record. The highest wind speed experienced in this threat zone came from Hurricane Wilma, with a maximum sustained wind speed of 78.4 m s^{-1}.

Figure 2 shows the monthly occurrence of the hurricanes that have passed through Florida's threat zone. Hurricanes have occurred in this region in all months from May through December. September is the peak month of hurricane threats to Florida followed by August and October. Just over 85% of all hurricanes in this part of the world occur in the 3 months from August through October. The seasonality of hurricanes in the threat zone is similar to the seasonality of hurricanes over the Atlantic basin as a whole, although October is relatively more active over and around Florida.

Figure 3 shows a time series of the observed hurricane counts in the threat zone. All hurricanes are shown with gray lines, and major hurricanes are indicated with black lines. For example, in 1899 there were two hurricanes, one of which was a major hurricane. Most years have at least one hurricane but there are 64 years without a major hurricane in the region. There were six hurricanes in the region in

Table 1 Top ten highest hurricane wind speeds experienced in the Florida threat zone over the period 1899–2008. The year of the hurricane and the hurricane name are provided. Where a hurricane name is not given, the season sequence number is shown

Year	Hurricane	Wind speed (m s^{-1})
2005	Wilma	78.4
2004	Ivan	74.6
1955	Janet	73.1
2007	Dean	72.5
1938	Storm 4	72.2
1988	Gilbert	72.0
1928	Storm 4	69.4
2005	Katrina	68.6
1961	Hattie	66.9
1947	Storm 4	66.8

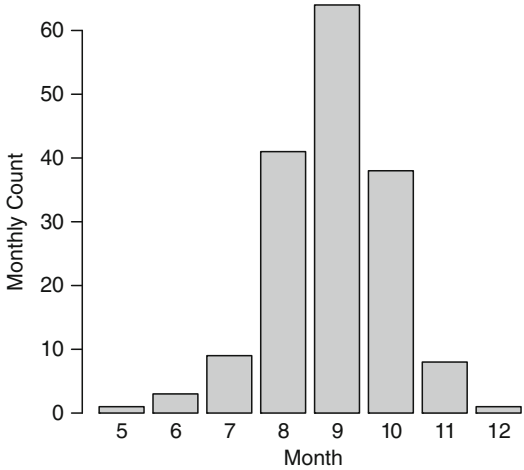

Fig. 2 Monthly occurrence of hurricanes passing through Florida's threat zone. The *bar* indicates the number of hurricanes by month

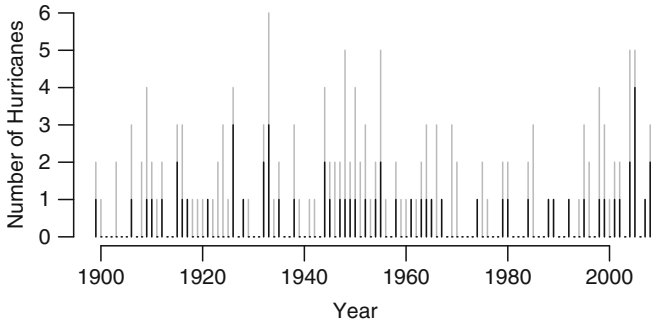

Fig. 3 Time series of hurricanes and major hurricanes. All hurricanes are shown with *gray lines*, and major hurricanes are shown with *black lines*. There does not appear to be any upward or downward trend in these counts

1933 and three of them were major hurricanes. This is the maximum single year occurrence rate over all years in the record. The consecutive years of 2004 and 2005 each featured five hurricanes. The average annual number of hurricanes (major hurricanes) is 1.5 hurricanes/year (0.5 hurricanes/year). In other words, on average, Florida gets threatened by three hurricanes every 2 years and one major hurricane every other year. There does not appear to be any significant upward or downward trend in the frequency of hurricanes in the vicinity of Florida.

Figure 4 shows a time series of the maximum wind speed (m s^{-1}) for each hurricane. The maximum refers to the fastest wind speed in the threat zone. Years with more than one hurricane have more than one value. Hurricanes that reached a maximum intensity over water are shown with circles. Here there appears to be an upward trend in the intensity over time especially for the strongest hurricanes. The average maximum intensity is 47 m s^{-1} with a standard deviation of 10.2 m s^{-1}.

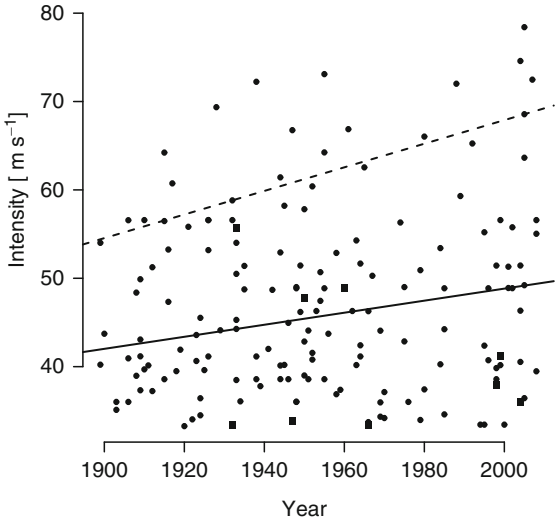

Fig. 4 Maximum sustained wind speeds for hurricanes in the Florida threat zone as a function of time with *trend lines* shown for the 0.5 and 0.9 quantiles. Maximum winds over sea are shown with *circles*, and maximum winds over land are denoted with *squares*

4 Hurricane Return Levels

To assess the risk of hurricane occurrence in the threat zone, a statistical model based on extreme value theory is employed. The risk of a hurricane represents the probability of a region experiencing winds of hurricane force or greater within a specified period. Thus, regional risk is determined by the size and location of the region. Risk is an unobserved and changing quantity that is estimated using a statistical model.

Here the statistical model provides an estimate of the exceedence wind speed (return level) as a function of return period (inverse of the annual probability). Following Jagger and Elsner (2006), the exceedences $W - u$ are modeled as samples from a family of generalized Pareto distributions (GPD), so that for an individual hurricane with maximum wind W,

$$\begin{aligned}\Pr(W > v | W > u) &= \left(1 + \frac{\xi}{\sigma}[v - u]\right)^{-1/\xi} \\ &= \mathrm{GPD}(v - u | \sigma, \xi) \qquad (1)\end{aligned}$$

where $\sigma > 0$ and $\sigma + \xi(v - u) \geq 0$. For negative values of the shape parameter (ξ) the GPD family of distributions has an upper limit of $W_{\max} = u + \sigma_u/|\xi|$.

The frequency of storms with intensity of at least u follows a Poisson distribution with a rate, λ_u, the threshold crossing rate. Thus the number of hurricanes per year with winds exceeding v is a thinned Poisson process with mean $\lambda_v = \lambda_u \Pr(W > v | W > u)$, where v is an arbitrary wind speed above threshold u. This is called the peaks over threshold (POT) method and the resulting model is completely characterized for a given threshold u by σ, ξ, λ_u; the GPD parameters and the threshold crossing rate, respectively.

Since the number of storms exceeding any wind speed v is a Poisson process, the return period for any v has an exponential distribution, with mean $r(v) = 1/\lambda_v$. By substituting for λ_v in terms of both λ_u and the GPD parameters then solving for v as a function of r we can find the corresponding return level for a given return period as

$$\mathrm{rl}(r) = u + \frac{\sigma}{\xi}\left[(r \cdot \lambda_u)^{\xi} - 1\right]. \tag{2}$$

For a more complete description of the statistical theory supporting this model refer to Jagger and Elsner (2006).

Figure 5 shows the return level curve for the Florida threat zone based on the model. The u and σ parameters used to estimate this curve are 35 and 24 m s^{-1}, respectively. The return levels (hurricane intensities) increase with increasing return period in an exponential manner. Specifically, Florida can expect to be threatened by a hurricane with wind speeds of 60.8 m s^{-1} (58.3–63.3) (90% CI), on average, once every 2 years. It also shows that this threat zone can expect a hurricane with wind speeds of 70.6 m s^{-1} (68.2–73.0), on average, once every 5 years.

Table 2 lists return levels for selected return periods, along with the 90% confidence intervals. A confidence interval (CI) for the mean return level at the radial distance of interest is obtained by first, calculating the return levels for a given return period, and then assuming the estimate is asymptotically normal from a knowledge of the limiting variance of the estimator (delta method). The model indicates that Hurricane Wilma with its 78.4 m s^{-1} wind speeds is about a 20-year event for the threat zone as a whole.

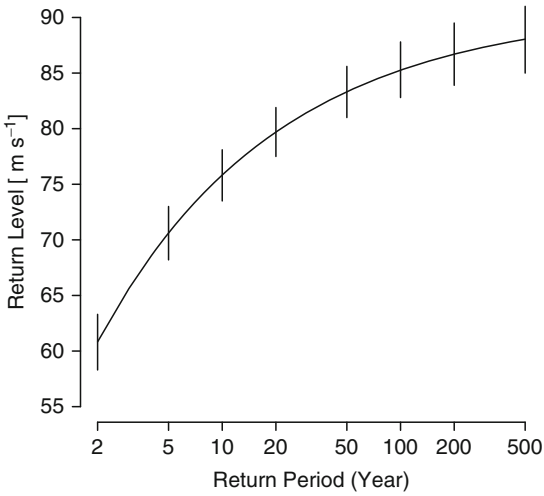

Fig. 5 Return levels as a function of return period. The return levels are based on the statistical model presented above and include data over the period 1899–2008. The return period refers to the expected time between hurricanes of this intensity occurring somewhere within the threat zone. The *vertical lines* represent the 90% confidence intervals on the return levels for selected return periods

Table 2 Return period for selected wind speed exceedance values. The return levels are based on the statistical model presented above and include data over the period 1899–2008. The 90% confidence intervals are also listed

Return period (year)	Wind speed (m s^{-1})
10	75.8 (73.5–78.1)
20	79.7 (77.5–81.9)
50	83.3 (81.0–85.6)
100	85.3 (82.8–87.8)
500	88.0 (85.0–91.0)

5 Trends in Hurricane Intensity

In the previous section we showed that the occurrence of hurricanes threatening Florida is not changing over time but there appears to be an upward trend in hurricane intensity. To quantify the trend we employ quantile regression. Quantile regression is an extension of ordinary regression applied to quantiles of the response variable. A quantile is a point taken from the inverse cumulative distribution function so that the 0.5 quantile is the value such that 50% of the values are less than the value. For instance, the 0.9 quantile (90th percentile) value of hurricane wind speeds near Florida is 61 m s^{-1}. The response variable is the hurricane intensity and the explanatory variable is time (year).

Two trend lines are shown in Fig. 4. The 50th-percentile trend is shown with a solid black line and the 90th-percentile trend is shown with a dashed line. Both trends are upward with the 90th-percentile trend greater than the 50th-percentile trend. The upward trends indicate that hurricanes in the vicinity of Florida are getting stronger over time with the greatest increases noted for the strongest hurricanes. The trend values and their standard errors and p-values are given in Table 3. Although the trend at the 50th percentile is not statistically significant, the trend at the 90th percentile is as indicated by the trend value more than twice its standard error. This result is consistent with those presented in Elsner et al. (2008a) for global and basin-wide tropical cyclone activity.

Increasing SST, with an assumed upward trend in ocean heat content, is one explanation for the observed rise in intensity of the strongest hurricanes. Figure 6 shows the August through October Caribbean SST anomalies as a function of year, and a scatter plot of wind speed maxima and these same SST values. As noted previously, the Caribbean SST data are the August–October averaged SST anomaly over the period 1951–2006. There is a nonlinear change in the SST values over time with a rising trend since about 1980. The upward trend since then is rather large. The nonlinear trend line is based on fitting the data to second-order polynomial. A weak positive relationship between SST and wind speeds exists, but the trend coefficient is not statistically different from zero. The SST trend is consistent with

Table 3 Hurricane wind intensity trend statistics are shown with the associated standard errors and p-values for the 0.5, 0.75, and 0.9 quantiles

	Quantile		
Statistic	0.5	0.75	0.9
W (m s^{-1})	44.6	53.4	61.4
Trend (m s^{-1} $year^{-1}$)	+0.07	+0.04	+0.13
s.e. (m s^{-1} $year^{-1}$)	0.04	0.05	0.06
p-Value	0.06	0.38	0.02

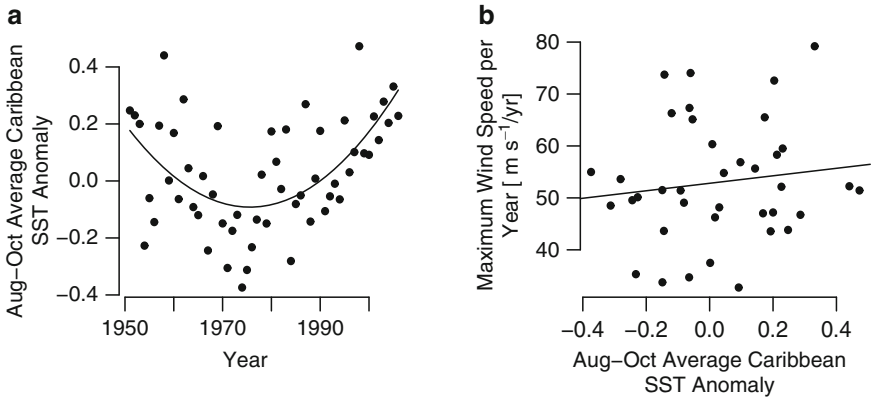

Fig. 6 Caribbean SST anomalies and hurricane wind speeds. (**a**) Time series of the average August–October Caribbean SST anomalies. (**b**) Scatter plot of maximum hurricane wind speed versus Caribbean SST. The regression lines are shown on the plots

the increasing trend in local hurricane intensities. It is also possible that changes in other (local) environmental parameters, such as vertical wind shear, are the reason local hurricane intensities have increased in this region over time.

6 Changes in Intensification and Decay Rates

While increasing ocean heat content may play a role in the increasing intensity of hurricanes in the vicinity of Florida, it is likely not the entire story. Another consideration is hurricane intensification within the threat zone and how it might be changing over time. The intensification is the time change of the maximum hurricane wind speed. We use a Savitzky–Golay filter to compute the time derivative as it has better accuracy than the simpler finite differencing method (Savitzky and Golay 1964).

We divide the data set into values that are above zero indicating hurricane strengthening and values below zero indicate hurricane weakening. We then take the maximum value of strengthening (intensification) along the track of each hurricane

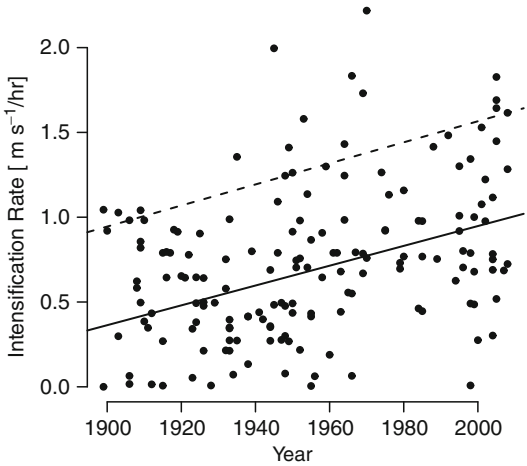

Fig. 7 Hourly hurricane intensification values over time. The values are the maximum intensification rate for a hurricane within the threat zone based on hourly wind speed increases. The 50th- and 90th-percentile trends are plotted with a *dashed* and *solid line*, respectively

within the threat zone to obtain one intensification value per hurricane. We do the same for the maximum value of weakening, or decay (the largest negative value).

The maximum per hurricane intensification in units of m s^{-1} per hour is plotted in Fig. 7. As before, we also plot the 50th- and 90th-percentile trends from a quantile regression of intensification on year. The highest values of intensification exceed 2 m s $^{-1}$ per hour while the lowest are near zero. There is a distinct upward trend in hurricane strengthening rates over time. Hurricanes apparently are intensifying more rapidly in more recent years. The trend values, standard errors, and p-values are given in Table 4. The 50th- and 90th-percentile trends are $+0.6$ m s^{-1}/h/century; both statistically significant from a zero trend.

It is also interesting to consider the maximum decay rates of hurricanes in the vicinity of Florida. The maximum per hurricane decay in units of m s^{-1} per hour is plotted in Fig. 8. Again we plot the 50th- and 90th-percentile trends from a quantile regression of decay on year. The highest decay rates are larger than the highest intensification rates with one hurricane's maximum decay rate exceeding 4 m s^{-1} per hour. As with intensification there is a rather distinct trend in decay over time, with today's hurricanes decaying faster than hurricanes earlier in the twentieth century. This is especially true for the hurricanes with the largest decay rates. The trend statistics for these percentiles, along with their standard errors and p-values, are also shown in Table 4.

In order to recognize spatial patterns in these decay rates, the observations are plotted based on the following criteria: whether the maximum decay rate occurred over land or over sea. If the maximum decay rate occurred over land, the observation is plotted with a square, and if over sea, it is plotted with a circle. Approximately 34% of the hurricanes reached their maximum decay rate over land, and 66% reached it over sea.

Table 4 Hurricane intensification and decay. The intensification rate and decay rate trend statistics are shown with the associated standard errors and *p*-values for the 0.5, 0.75, and 0.9 quantiles based on a quantile regression model

	Quantile		
Statistic	0.5	0.75	0.9
	Intensification rate		
W (m s^{-1} h^{-1})	0.70	0.98	1.34
Trend (m s^{-1} $year^{-1}$)	+0.006	+0.005	+0.006
s.e. (m s^{-1} $year^{-1}$)	0.001	0.002	0.002
p-Value	<0.001	0.006	0.006
	Decay rate		
W (m s^{-1} h^{-1})	−0.83	−0.28	−0.11
Trend (m s^{-1} $year^{-1}$)	−0.01	−0.005	−0.003
s.e. (m s^{-1} $year^{-1}$)	0.003	0.002	0.001
p-Value	0.001	0.02	0.01

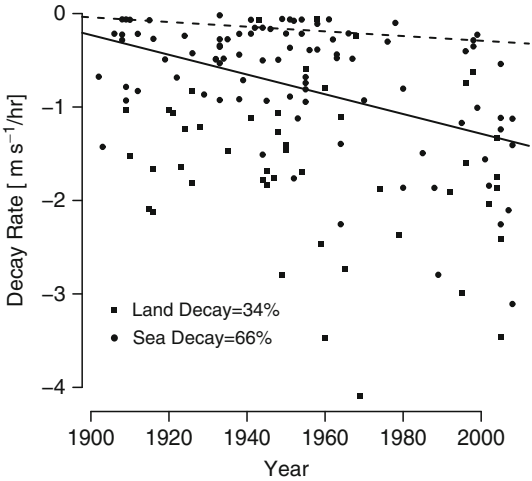

Fig. 8 Hourly hurricane decay rates over time. The values are the maximum decay rate for a hurricane within the threat zone based on hourly wind speed decreases. The 50th- and 90th-percentile trends are plotted with a *dashed* and *solid line*, respectively

7 Summary and Conclusions

Hurricanes head the list of catastrophic and expensive natural phenomena. The state of Florida has experienced well over $450 billion dollars in damages from these deadly events since the early twentieth century (Pielke et al. 2008), and these losses have been increasing through time even after accounting for inflation changes (Malmstadt et al. 2009). This analysis was conducted to provide information for emergency planners and the insurance industry about the characteristics of the hurricanes that pass in the vicinity of Florida.

Since 1899, there have been 165 hurricanes – 59 of them at category 3 or higher on the Saffir–Simpson scale – that have passed within a 1,000-km radius of 26°N

latitude and 82°W longitude off the southwest coast of Florida. Hurricanes occur mainly from June through November with a peak in September. Threats come from hurricanes originating or passing over the Gulf of Mexico, Caribbean Sea, and the Bahamas. On average, the annual number of hurricanes (major hurricanes) threatening Florida is 1.5 hurricanes/year (0.5 hurricanes/year). The frequency of these hurricanes is not changing through time but hurricane intensification rates are.

The strongest hurricane in the record is Hurricane Wilma in 2005, which had a peak intensity of 78.4 m s^{-1}. This is approximately a one-in-20 year event for the threat zone as a whole. The average maximum intensity is 47 m s^{-1} with a standard deviation of 10.2 m s^{-1}. The region can expect hurricane wind intensities of 60.8 m s^{-1} (58.3–63.3) (90% CI), on average, once every 2 years and wind speeds of 70.6 m s^{-1} (68.2–73.0), on average, once every 5 years.

Quantile regression was employed to establish the statistical significance of the upward trend in the intensity of hurricanes, especially at the highest wind speed levels. The rise can be related to warming ocean temperatures in the Caribbean, but the simple linear regression model found no statistically significant signal. Hurricanes are also intensifying more rapidly in the vicinity of Florida today than hurricanes in the past. However, there is also a rather distinct trend in decay rates over time with today's hurricanes decaying faster than hurricanes earlier in the record. This is especially true for the hurricanes with the largest decay rates. Although the explanations for these changes are lacking, the changes suggest models that assume a stationary hurricane climate might be misleading about Florida's future hurricane risk.

Acknowledgements The work was supported by the U.S. National Science Foundation (ATM-0738172) and by the Florida Catastrophic Storm Risk Management Center. Views expressed within do not necessarily reflect the opinions of the funding agencies. Statistical analysis and modeling is performed using the software environment R (http://www.r-project.org) and the quantile regression package quantreg (R package version 4.36; http://www.r-project.org) with special thanks to Roger Koenker.

References

Blake ES, Rappaport EN, Landsea CW (2007) The deadliest, costliest, and most intense United States tropical cyclones from 1851 to 2006 (and other frequently requested hurricane facts). NOAA Tech Memo NWS TPC 5:45

Elsner JB, Kossin JP, Jagger TH (2008a) The increasing intensity of the strongest tropical cyclones. Nat 455:92–95

Elsner JB, Jagger TH, Liu K-B (2008b) Comparison of hurricane return levels using historical and geological records. J Appl Meteor Climatol 47:368–374

Hamid S, Kibria BM, Gulati S, Powell M, Annane B, Cocke S, Pinelli J-P, Chen SC (2008) Public Hurricane Loss Evaluation Models: Predicting Losses of Residential Structures in the State of Florida. In JSM Proceedings, Statistical Computing Section

Jagger TH, Elsner JB (2006) Climatology models for extreme hurricane winds in the United States. J Climate 19:3220–3236

Jagger TH, Elsner JB (2009) Modeling tropical cyclone intensity with quantile regression. Int J Climatol 29:1351–1361

Landsea CW, Pielke RA Jr, Mestas-Nuñez AM, Knaff JA (1999) Atlantic basin hurricanes: indices of climatic changes. Climatic Change 42:89–129

Malmstadt JC, Scheitlin KN, Elsner JB (2009) Florida hurricanes and damage costs. Southeastern Geograph 49:108–131

Malmstadt JC, Elsner JB, Jagger TH (2010) The risk of strong hurricane winds to Florida cities. J Appl Meteor Climatol, in press, doi: 10.1175/2010JAMC2420.1

NOAA Earth Systems Research Laboratory Physical Sciences Division (2009) Monthly Caribbean SST Index (CAR). http://gcmd.nasa.gov/records/GCMD_NOAA_NWS_CPC_CAR.html

Pielke RA Jr, Gratz J, Landsea CW, Collins D, Saunders MA, Musulin R (2008) Normalized hurricane damage in the United States: 1900–2005. Nat Hazards Rev 9:29–42

Savitzky A, Golay MJE (1964) Smoothing and differentiation of data. Anal Chem 36:1627–1639

Chapter 12
Linking Tropical Cyclone Number Over the Western North Pacific with Sea Surface Temperatures

Chongjian Liu, Liping Ma, Ying Liu, Zhexian Luo, Xiaotu Lei, Xiaogang Zhou, Donghai Wang, and Hui Xu

Abstract The analyses based on the observational data show that the tropical cyclone (TC) numbers tend to become decreasing over some oceanic basins during the recent multiple decades despite a rise in their sea surface temperatures (SSTs). A methodology of understanding the mechanism responsible for such seemingly counter intuitive phenomena is suggested in this chapter and thus the causality between the unusually heterogeneous pattern of SSTs in warming environment and TC frequency over, as an example, the western North Pacific (WNP) is explained. This methodology is important in that it provides an insight into the problem why under global warming high SSTs as one of the necessary conditions for TC genesis should unexpectedly contribute to TC number reduction, though locally, and furthermore, in view of that such phenomena have also been observed over the other oceanic basins than the WNP and that the principle of the technique is universal, this procedure of analysis can be expected to apply globally to examine the extreme weather/climate extent frequency trend in the worldwide warning conditions.

Keywords Tropical cyclone · Sea surface temperatures · Climate thermodynamics

C. Liu (✉) and X. Lei
Shanghai Typhoon Institute, China Meteorological Administration, Shanghai 200030, China
e-mail: cliu@cams.cma.gov.cn; leixt@mail.typhoon.gov.cn

C. Liu, L. Ma, Y. Liu, and D. Wang
State Key Laboratory of Severe Weather, Chinese Academy of Meteorological Sciences, Beijing 100081, China
e-mail: maliping@cams.cma.gov.cn; y119@cams.cma.gov.cn; wangdh@cams.cma.gov.cn

Z. Luo
Institute of Remote Sensing, Nanjing University of Information Science and Technology, Nanjing 210044, China
e-mail: luozxma@yeah.net

X. Zhou
Training Centre, China Meteorological Administration, Beijing 100081, China
e-mail: zhouxgang@sina.com

H. Xu
National Meteorological Center, China Meteorological Administration, Beijing 100081, China
e-mail: xuhui@cma.gov.cn

J.B. Elsner et al. (eds.), *Hurricanes and Climate Change: Volume 2*,
DOI 10.1007/978-90-481-9510-7_12, © Springer Science+Business Media B.V. 2010

1 Introduction

A great number of the literatures and the observational data reveal that a variety of devastating weather/climate events happened frequently over the world. Some examples include the most serious drought since 1940 occurred in the central western part of the United States in 1998 with grain drop in production by 38%, the warmest year 1999 experienced in China in the last 100 years, the extraordinarily powerful and deadly Hurricane Katrina happened with the total damage cost of about $81 billion and the total number of fatalities over 1,800 in 2005, and so forth (Easterling et al. 2000; Karl et al. 1991; Manton and Eral 2001; Wang and Gong 2000; Cerveny et al. 2007). However, under the worldwide extreme weather/climate events getting more frequent, a counter intuitive phenomenon that the tropical cyclone (TC) numbers tend to become decreased over some oceanic basins with a rise in their sea surface temperatures (SSTs) has been observed during the recent multiple decades (e.g. Wang et al. 2008; von Storch 2008; McBride and Ramsay 2009). As a result, a scientific question is why, under the background of global warming, higher SSTs with more potential energy supplies implied as one of the necessary conditions for typhoon genesis would lead to decreased TC numbers?

In a recently published monograph (e.g. Elsner and Jagger 2009) it is stated most numerical models indicate an overall decrease in the number of storms attributable to greater atmospheric stability and to a decrease in vertical mass flux. However, the proposed analysis in this chapter for understanding of the observational counter intuitive phenomena is quite different from those described in the previous works. This analysis is based on the fundamental dynamics rather than the numerical experiments whose results are inevitably affected by the numerical model itself. On the other hand, such methodology can be employed to directly address the science behind the fact that the TC numbers are dramatically decreased in some oceanic basins against a background of global warming.

In this chapter the western North Pacific (WNP) over which the TC occurrence frequencies tended to decrease with minor fluctuations from late 1960s (Fig. 1) is taken as an example to discuss the possible mechanism responsible for the causation.

In Fig. 1 the data for TC numbers are from the Tropical Cyclone Annals (CMA 1949–2007) and the relative vorticity (RV) is based on the National Centers for Environmental Prediction/National Center for Atmospheric Research (NCEP/NCAR) $2.5° \times 2.5°$ (latitude–longitude grid) reanalysis data.

In view of the fact that the majority of TCs originate around the intertropical convergence zone (ITCZ) and that the intensity and position of ITCZ can be described reasonably in terms of the RV (see the text below for further details), this chapter is arranged as follows: the main source of TC genesis and ITCZ of monsoon trough type over the WNP are described in the next section; discussions on the ITCZ variabilities and their possible causes are given in Section 3 with focus on SSTs changes and the effect of SSTs pattern on the ITCZ migration; the further discussions and conclusive remarks are presented in Section 4.

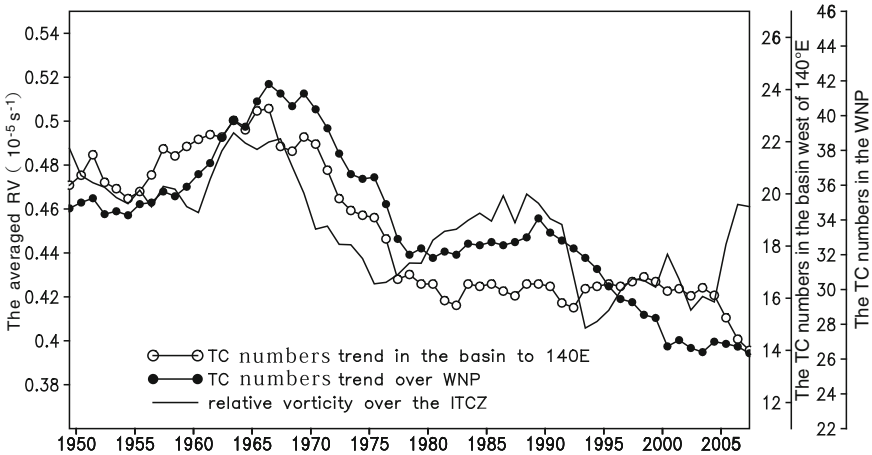

Fig. 1 The long term evolution series for the TC numbers in the WNP and in the basin west of 140°E as well as the averaged RV in 10^{-5} s^{-1} in the ITCZ of monsoon trough type during 1949–2007 (see the text for data source)

2 The Main Source of TC Genesis and the ITCZ

According to previous studies, 80–85% of TCs are originated in the ITCZ or just on its poleward side, and the ITCZ of monsoon trough type located in the basin west of 140°E is the main origin of TCs over the WNP (Gray 1967; Bates 1970; Charney 1971). On the other hand, the necessary conditions of TC genesis and development include higher SSTs, stronger low level vorticity, weaker vertical wind shear, and higher latitudinal position of subtropical anticyclone ridge/ITCZ. These conditions, however, are not equally important. Among them low level vorticity should be the fundamental factor for TC genesis since initial disturbances are the embryo of TCs. In addition, the intensity of the ITCZ as a main system generating TCs can be described in terms of the RV (e.g. use RV at 850 hPa for defining the ITCZ, as is seen in Chan and Evans (2002)). Indeed the TC numbers over the WNP and the basin west of 140°E have a high correlation with the RV around the ITCZ, as is seen in Fig. 1 where these numbers show almost synchronous changes with those of the RV. The corresponding correlation coefficients for the WNP and the basin west of 140°E are 0.6552 and 0.6614 at the 0.001 significance level, respectively. It is noticed, in Ma and Chen (2009), that a 10-year running mean to the annual TC frequency data and NCEP typhoon season mean wind data has been applied to get the long term evolution series of the averaged TC numbers and RV in 10^{-5} s^{-1}, at 925 hPa in the ITCZ of monsoon trough type for the period 1949–2007, and, that July–October (JASO hereafter) is defined as the typhoon season since JASO is the most frequent season of TCs over the WNP. It will therefore be a reasonable way to discuss the causality between the TC frequency trend and warming SSTs over the WNP via the ITCZ variability as the medium.

3 The ITCZ Variabilities and Their Possible Causes

3.1 The ITCZ Variation

The analyses below are based on the NCEP/NCAR 2.5° × 2.5° resolution reanalysis data for horizontal winds from which the ITCZ fields in terms of RV are figured out via the definition of RV at constant pressure

$$\varsigma_p = \left(\frac{\partial v}{\partial x}\right)_p - \left(\frac{\partial u}{\partial y}\right)_p, \tag{1}$$

where ς_p, u and v are the RV, the latitudinal and longitudinal velocities at constant pressure, respectively, and the 2.0° × 2.0° data for the SST fields (Kalnay et al. 1996). All the means are calculated against the period of JASO as mentioned above.

Figure 2 shows the stream fields superimposed by the positive RV at 925 hPa during JASO over the WNP. It is found from near the equator in Fig. 2 that the zones of positive RV in the RV field can simply tell the general position of the convergence zones in the stream fields. This convergence zones should be able to represent the ITCZs due to the fact that the ITCZ is mainly formed by the trade winds converging (e.g., Bjerknes et al. 1969; Holton et al. 1971). In fact, as mentioned in Section 2, the attempt using RV at 850 hPa for defining the ITCZ has been done (e.g. Chan and Evans 2002). However, the RV in terms of 850 hPa is not continuous in some sections of ITCZs over the Pacific owing to its weaker intensity (figures not shown here). Therefore the RV at 925 hPa that is more continuous and smoother than that at 850 hPa is chosen instead in this chapter.

It is noticed from Fig. 2 that the variabilities of the ITCZ of monsoon trough type associated with the reduction in the TC numbers over the WNP under warming SSTs during the last several decades are involved with the following two factors: (1) the intensity of the ITCZ of monsoon trough type as the main origin of TCs over the WNP, in terms of RV at 925 hPa, was weakened and (2) the position of the ITCZ shifted into the latitudes further south (see also Fig. 3), both of which would contribute to the decrease in TC numbers over the WNP.

Next we will specifically discuss these two aspects.

3.2 The Implication of SSTs Variation

Figure 3 shows the 20-year means of SSTs over the WNP for JASO during 1949–2008. It is seen from Fig. 3 that the SSTs over the North Pacific are gradually increased during the recent 60 years, especially, the areas circled with the isotherm of 28°C that is defined as the critical temperature for the warm pool (Ho et al. 1995) extended eastward prominently. This cross-equatorial area of warm pool was limited

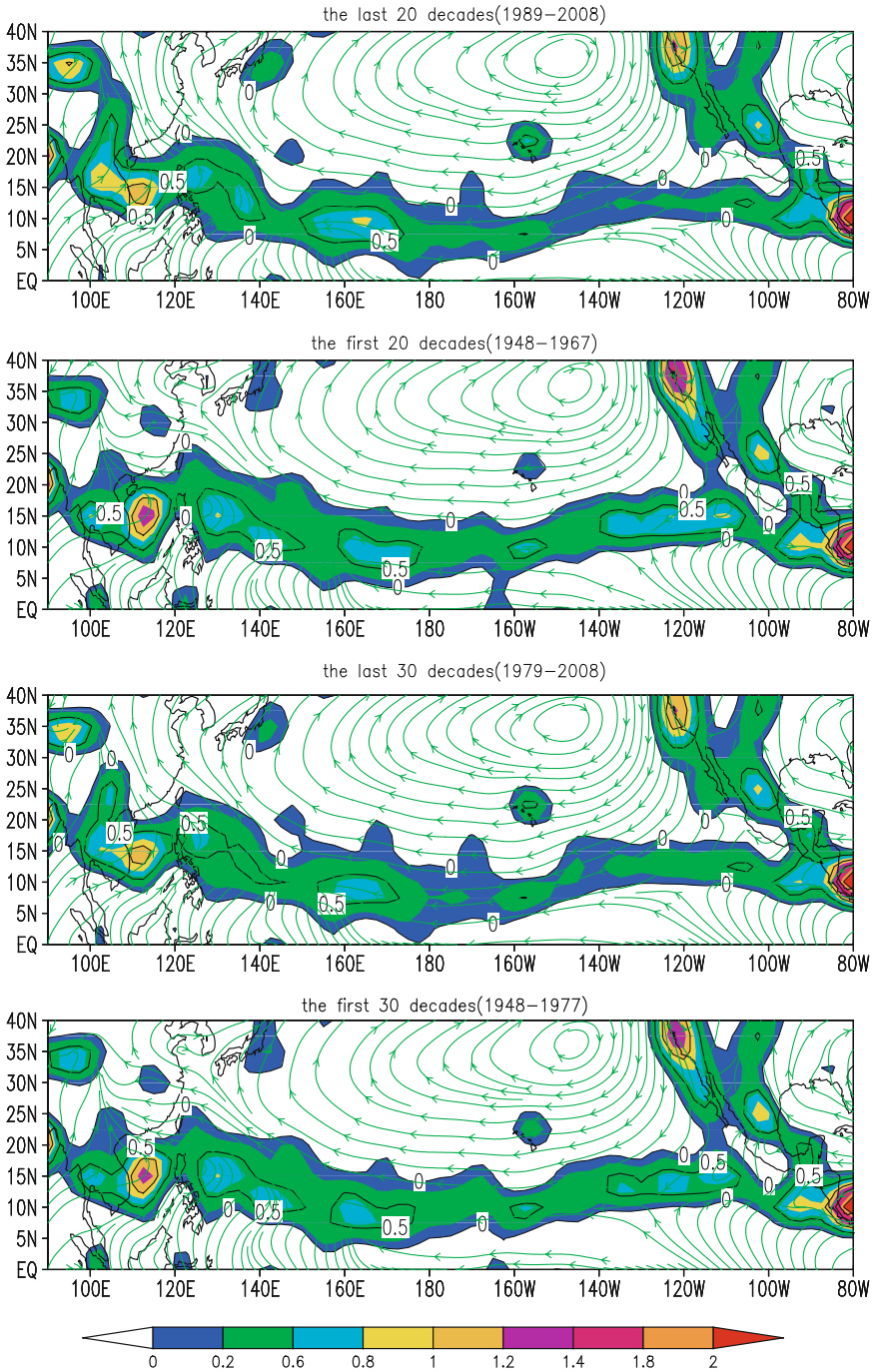

Fig. 2 Comparison of the stream fields superimposed by the positive RV at 925 hPa (isolines are for the positive RV in $10^{-5}\ s^{-1}$) during JASO over the WNP between the first and last 20-year/30-year means (as marked above the respective panel)

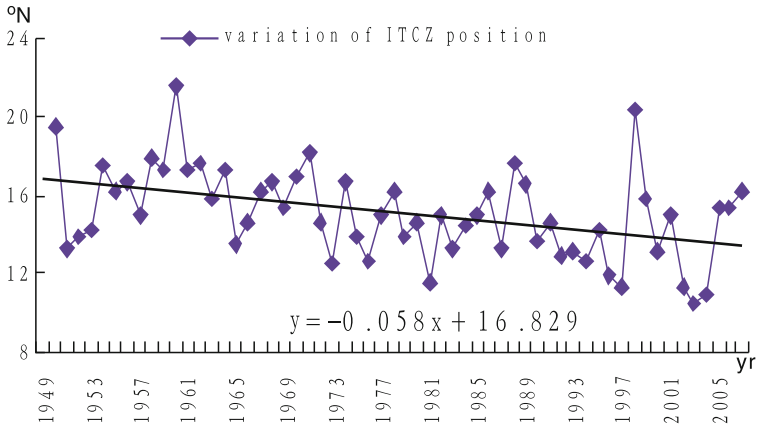

Fig. 3 The illustration of changes in the average position of the ITCZ from 1949 to 2007. Here, the central position of the ITCZ is determined via singling out the points with maximum positive RV along the longitudinal direction within the 100–140°E and then averaging their respective latitudinal position

within the western Pacific initially which has extended straightforwardly till the eastern Pacific, so as to be connected eventually from the western up to eastern Pacific as seen in the panel for the last 20-year period (1989–2008) of Fig. 3. Since there is a close relationship between SSTs and surface wind divergence and convection over the tropical oceans or the ITCZs (Graham and Barnett 1987; Lau et al. 1997; Lindzen and Nigam 1987) the following questions are then raised: how the SSTs or their gradient influence the intensity of the ITCZ, and why the sea surface warming extent reached around the western Pacific covering some part of the warm pool is not as dramatic as those over the central and eastern Pacific. The latter is relevant to the first factor of the ITCZ variabilities mentioned above. A potential clue would be implied by the modern nonlinear non-equilibrium thermodynamics.

For an isolated thermodynamic system, the state function of the system, entropy s per unit mass, will spontaneously increase with time according to the second law of thermodynamics, which can be expressed by the formula (Prigogine 1955; De Groot and Mazur 1962)

$$\frac{ds}{dt} \geq 0, \tag{2}$$

and be usually called the spontaneous entropy increment principle. As a result, an isolated system will spontaneously tend to homogenization. However, for an open system with the diabatic heating rate Q transferred through its boundaries, Eq. (2) should be modified to

$$\frac{ds}{dt} \geq \frac{Q}{T}, \tag{3}$$

where T is the temperature (in Kelvin) of the system. The nature of the second law of thermodynamics shows that, if there exists difference initially, heat (particles) will be spontaneously transferred (diffused) from part with higher T (concentration)

to that with lower T (concentration). Any many-body system like the atmosphere or ocean must be controlled by the second law of thermodynamics and, in fact, the entropy flow properties of the atmospheric systems have been revealed based on this law (Liu and Liu 2005, 2007; Liu et al. 2006; Xu and Liu 2008).

Specifically, if there exists difference of temperature spatially (say, on sea surface), the original part of warmer sea surface will diffuse its thermal energy (the inner energy, proportional positively to temperature via the formula of $e = C_p T$ where e is the inner energy per unit mass, C_p is the specific heat at constant pressure and T is temperature) to its surrounding parts with lower temperature. As a consequence, compared with the surrounding areas the original warmer area (e.g., the area related with the warm pool) will experience a weaker warming under global warming since it will lose a certain amount of heat via the diffusive process at the same time, and vice versa (Fig. 3 showing the case for the North Pacific is only an example in which it is demonstrated that the SSTs around the ITCZ of monsoon trough type have a smaller increment of temperature while those over the adjacent ITCZ sections near the central and eastern equatorial Pacific have larger increments). In view of that the ITCZ is caused, at least in the initial stages, mainly by the thermodynamic forcings such as the gradient in SST that has been regarded as playing more of a role than the absolute SST value with regard to convection and precipitation (Lindzen and Nigam 1987) the ITCZ of monsoon trough type should indeed become weaker in response to more uniform SSTs or weakened SST gradient over there.

3.3 The Effect of SSTs Pattern on the ITCZ Migration

As described above, in the warming environment the higher SSTs area circled with the isotherm of 28°C related to the warm pool has gradually extended eastward and been connected from the western to eastern Pacific eventually during the last 20 years (Fig. 4) so as to form an apparent zone of higher SSTs with a distinct gradient of nearly north–south direction created on the both northern and southern sides of this zone. Such a SST pattern will cause corresponding changes in the average temperature T_m of an immediate air layer above the sea surface. Thus, in some regions to the north of the zone of higher temperature where the semi-geostrophic relation for the Tropics is valid (Lin and Chao 1998) a western wind component at the higher levels (e.g. at 925 hPa) should be superposed, which will cause a positive increment of the latitudinal velocity u with $\Delta u > 0$ (at the higher level), according to the thermal wind relation (Holton 1992):

$$\vec{\mathrm{V}}_{\mathrm{T}} = -\frac{R}{f} \ln \frac{p_1}{p_2} \nabla_p T_m \times \vec{k} \tag{4}$$

where $\vec{\mathrm{V}}_{\mathrm{T}}$ denotes the thermal wind between the constant pressure layers p_1 (e.g. 1,000 hPa that is near the sea surface) and p_2 (e.g. 925 hPa that is used for defining the ITCZ in terms of RV in this chapter); $\nabla_p T_m$ is the average temperature gradient

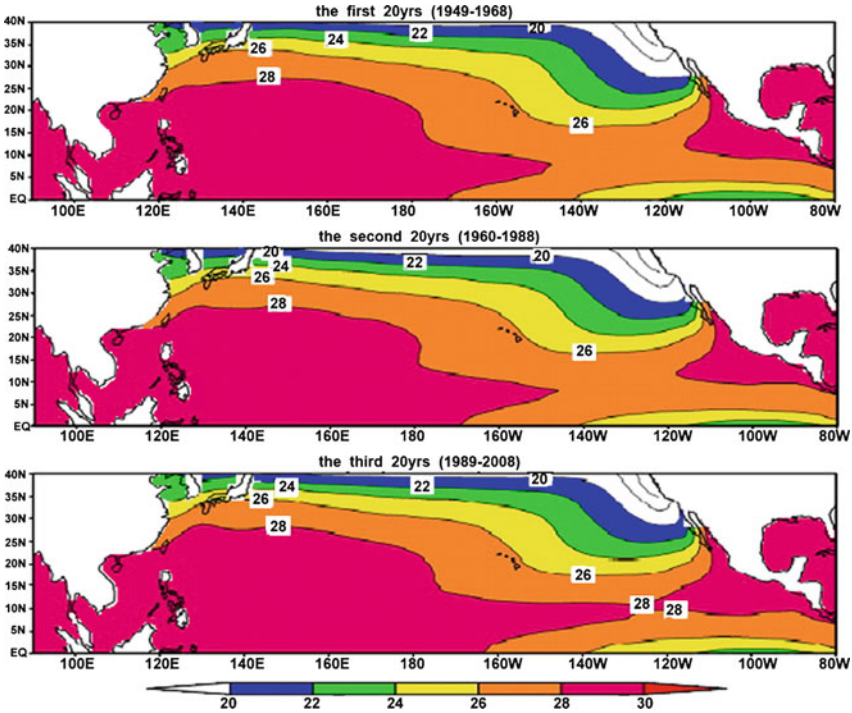

Fig. 4 The every 20-year-averaged SST fields (in degree Celsius) for the North Pacific south of 40°N during the period from 1949 to 2008

with T_m *is* the average temperature between p_1 and p_2; $\vec{k}$ the unit vector in the vertical direction; and R and f are the gas constant for dry air and Coriolis parameter, respectively. In contrast, the latitudinal velocity u to the south of the zone should be superposed by an eastern component as the gradient in SSTs in the south regions is reverse to that in the north ones. As a result, the RV, as is expressed by $\varsigma_p = \left(\frac{\partial v}{\partial x}\right)_p - \left(\frac{\partial u}{\partial y}\right)_p$, in the regions to the north of the zone of higher temperature will be decreased (at the higher level) since the term of $-\left(\frac{\partial u}{\partial y}\right)$ becomes smaller with the term of $\left(\frac{\partial v}{\partial x}\right)_p$ having a minor change in this case. At the same time, the RV in the regions to the south of the zone of higher temperature will be increased owing to the reversed gradient in SSTs or T_m there.

Taking the definition of ITCZ in terms of positive RV into account, we might expect that the part of the ITCZ to the north of the zone of high temperature will tend to weaken and even disappear as the result of reduction in RV there and, on the contrary, the part of the initial ITCZ to the south will enhance and even extend south further (see Fig. 5 for reference). That is able to be used to explain why the ITCZ migrates south apparently, as is relevant to the second factor of the ITCZ variabilities above.

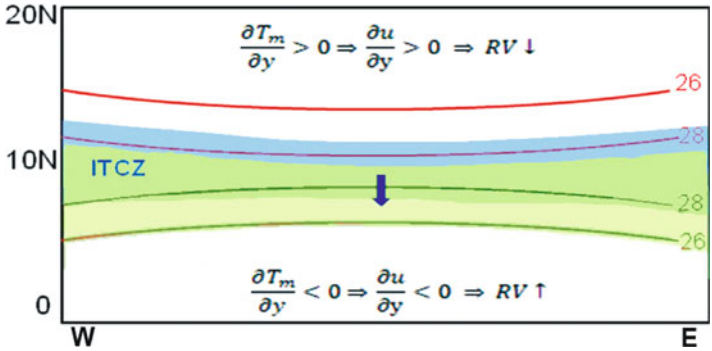

Fig. 5 The diagrammatic sketch for the proposed mechanism for a southern shift of the ITCZ coupled with RV which is contributive to the reduction in TC counts around the WNP (see the text for further details). The red lines represent SSTs showing sketchily the opposite temperate gradients (and the potentially-forced average temperature gradients $\frac{\partial T_m}{\partial y}$ within the immediate layer above the sea surface) in the both sides of the maximum SSTs

4 Conclusive Remarks

As well-known to all, the necessary conditions for TC genesis are not equally important and, among them dynamical factors such as low level vorticity and vertical wind shear play a more important role than thermodynamic factors such as SST and moist instability as suggested on some simulative results (Sugi et al. 2002; McDonald et al. 2005; Chauvin et al. 2006). This study shows that, warmer SSTs in the WNP even caused fewer TCs, that is, warmer SSTs as one of the necessary conditions do not definitely lead to an increase in TC numbers, which might be attributed to the heterogeneous effects of complicated pattern of SSTs on RV as implied by the second law of thermodynamics with the thermal wind principle taken into account. This study further proves that low level vorticity associated with ITCZ variations should be a fundamental factor for TC genesis. Based on the analyses in this chapter, a new way of understanding the mechanism responsible for the causality among SSTs and TC occurrence frequency over the WNP is then suggested. As a matter of fact, the WNP is only used as an example in this study and, the principle of the methodology illustrated herein is universal. This analysis can be also applied to the other oceanic basins worldwide than the WNP.

Acknowledgment This work has been jointly supported by 973 Program (2009CB421500), the National Natural Science Foundation of China under Grants 40633016, 40875029, 40775038 and 40975036, as well as the Basic Research Project of the State Key Laboratory of Severe Weather, Chinese Academy of Meteorological Sciences (2008LASWZI01).

Some Related Support Websites

http://www.ncdc.noaa.gov/oa/climate/severeweather/extremes.html
http://www.ncdc.noaa.gov/ncdc/data.ncep.reanalysis.derived.pressure.html

References

Bates JR (1970) Dynamics of disturbances on the intertropical convergence zone. Quart J Roy Meteor Soc 96:677–701

Bjerknes J (1969) Atmospheric teleconnections from the equatorial Pacific. Mon Wea Rew 97: 163–172

Cerveny RS, Lawrimore J, Edwards R, Landsea C (2007) Extreme weather records. Bull Am Meteorol Soc 88:853–860

Chan SC, Evans JL (2002) Comparison of the Structure of the ITCZ in the West Pacific during the boreal summers of 1989–93 using AMIP simulations and ECMWF reanalysis. J Clim 15:3549–3568

Charney JG (1971) Tropical cyclonegenesis and the formation of the intertropical convergence zone, in mathematical problems of geophysical fluid dynamics. In: Reid WH (ed) Lectures in applied mathematics, vol 13. American Mathematical Society, 383 pp

Chauvin F, Royer J–F, Déqué M (2006) Response of hurricane-type vortices to global warming as simulated by ARPEGE-climate at high resolution. Clim Dyn 27:377–399

CMA (1949–2007) Tropical cyclone annals. China Meteorological Press, Beijing, 150 pp (each)

De Groot SR, Mazur P (1962) Non-equilibrium thermodynamics. North-Holland, Amsterdam, The Netherlands, 510 pp

Easterling DR, Evana JL, Grosman PY, Karl TR, Kunkel KE, Ambenje P (2000) Observed variability and trends in extreme climate events: A brief review Bull Am Metor Soc 81:417–425

Elsner JB, Jagger TH (2009) Hurricanes and climate change, Springer, New York 380 pp

Graham NE, Barnett PT (1987) Sea surface temperature, surface wind divergence and convection over tropical oceans. Science 238:657–659

Gray WM (1967) Global view of the origin of tropical disturbances and storms. Mon Wea Rev 96:669–700

Ho C-R, Yan X-H, Zheng Q (1995) Satellite observations of upper-layer variabilities in the western Pacific warm pool. Bull Am Meteor Soc 76:669–679

Holton JR, Wallace JM, Young JA (1971) On boundary layer dynamics and the ITCZ. J Atmos Sci 28:275–280

Holton JR (1992) An introduction to dynamic meteorology. Academic, New York 535 pp

Kalnay E et al. (1996) The NCEP/NCAR 40-year reanalysis project. Bull Am Meteor Soc 77:437–471

Karl TR, Kukla G, Razuvayev VN, Changery MJ, Quayle RJ, Heim RT Jr, Easterling DR, Fu CB (1991) Global warming: evidence for asymmetric diurnal temperature change. Geophys Res Lett 18:2253–2256

Lau K-M, Wu HT, Bony S (1997) The role of large-scale atmospheric circulation in the relationship between tropical convection and sea surface temperature. J Clim 10:81–392

Lin Y, Chao JP (1998) The processes of tropical semi-geostrophic adaptation. Sci China Ser D 41:566–573

Lindzen RS, Nigam S (1987) On the role of sea surface temperature gradients in forcing low level winds and convergence in the tropics. J Atmos Sci 44:2440–2458

Liu C, Liu Y (2005) An attempt at improving a global spectral model by incorporating the second law of thermodynamics. Geophys Res Lett 32:L03806. doi:10.1029/2004GL021602

Liu C, Liu Y, Xu H (2006) A physics-based diffusion scheme for numerical models. Geophys Res Lett 33:L12805. doi:10.1029/2006GL025781

Liu Y, Liu C (2007) On the entropy flow properties of a severe tropical storm. Appl Phys Lett 91:014103. doi: 10.1063/1.2753538

Ma, L, Chen L (2009) The relationship between global warming and the variation in tropical cyclone frequency over the western North Pacific. J Trop Meteor 15:38–44

Manton M., Eral J (2001) Trends in extreme daily rainfall and temperature in Southeast Asia and the South Pacific: 1961–1998. Int J Climatol 21:269–284

McBride JL, Ramsay H (2009) Relationship between tropical cyclone activity and sea surface temperature in the southern hemisphere, 2nd International Summit on Hurricanes and Climate Change, May 31–June 5, Corfu, Greece

McDonald RE, Bleaken DG, Creswell DR, Pope VD, Senior CA (2005) Tropical storms: Representation and diagnosis in climate models and the impact of climate change. Clim Dyn 25:19–36

Prigogine I (1955) Introduction to thermodynamics of irreversible processes. Charles C. Thomas, Springfield, IL, 119 pp

Sugi M, Noda A, Sato N (2002) Influence of global warming on tropical cyclone climatology: An experiment with the JMA global model. J Meteorol Soc Jpn 80:249–272. doi:10.2151/jmsj.80.249

Von Storch H (2008) An attempt to homogeneously describe 60 years statistics of TC activity in East Asia, 1948–2007, 2008 Taiwan climate workshop, November 18, Taipei, Taiwan, China

Wang C, Li S-K, Enfield DB (2008) Atlantic warm pool acting as a link between Atlantic multidecadal oscillation and Atlantic tropical cyclone activity. Geochem Geophys Geosys 9:1–17. doi: 10.1029/2007GC001809

Wang SW, Gong DY (2000) Enhancement of the warming trend in China. Geophsys Res Lett 27:2581–2584

Xu H, Liu C (2008) Entropy flow properties of a typhoon as simulated by a meso-scale model. Europhys Lett 83:18001. doi: 10.1209/0295-5075/83/18001

Chapter 13
A Track-Relative Climatology of Eglin Air Force Base Hurricanes in a Variable Climate

Kelsey N. Scheitlin and James B. Elsner

Abstract The evolving hurricane threat to coastal communities is a critical consideration in the face of a changing climate. With a possible increase in hurricane destructive potential, it is important to analyze the climatology of hurricanes at a local, or decision-making, level. This chapter outlines a technique for establishing a climatological hurricane track for Eglin Air Force Base (EAFB) based on the occurrence and intensity of past hurricane events. First a "worst-case" track for a hurricane approaching EAFB is created by averaging distance maps of historical hurricanes. Hurricane characteristics (intensity and translation speed) are assigned to the track by gathering information from past hurricanes that passed nearby a set of points along the track. Then, by limiting the set of hurricanes to those from warm and cool sea surface temperatures epochs, the process is repeated to show the affects a changing climate might have on the hurricane risk to EAFB. The technique can be applied to any coastal location, and serves as a basis for understanding a local-scale hurricane climate and the affects of climate change on future hurricane threats.

Keywords Hurricane tracks · Climatology · Climate change

1 Introduction

The relationship between hurricanes and climate change has received a lot of attention. Current attempts to understand this relationship focus on the affects climate change will have on the frequency and intensity of future tropical cyclones. Some question our ability to discern changes in hurricane frequency due to climate change, as the signals may be masked by large natural variability (Trenberth 2005).

K.N. Scheitlin (✉) and J.B. Elsner
Department of Geography, Florida State University, Tallahassee, FL 32306, USA
e-mail: kscheitlin@fsu.edu; jelsner@fsu.edu

J.B. Elsner et al. (eds.), *Hurricanes and Climate Change: Volume 2*,
DOI 10.1007/978-90-481-9510-7_13, © Springer Science+Business Media B.V. 2010

The intensity of future cyclones is also in question, but findings suggest a 30-year increase in tropical cyclone destruction potential (Emanuel 2005), especially in the strongest hurricanes (Elsner et al. 2008). This increase in destructiveness, coupled with an increase in coastal populations, will result in greater economic loss due to tropical cyclones (Emanuel 2005; Hallegatte 2007). Others suggest there is no basis for making such claims in the present state of knowledge (Pielke et al. 2005; Landsea et al. 2006). Regardless, one can not deny the tremendous coastal devastation in the past decade due to tropical cyclone activity worldwide, and the weariness associated with a potential increase in destruction.

It is important for coastal communities to be prepared for future storms. This can be achieved through sound prediction and mitigation strategies. In this regard, it is useful to assess hurricane risk at a local, or decision-making level. This chapter serves to analyze the hurricane vulnerability of Eglin Air Force Base (EAFB), located on the Florida Panhandle, to help personnel understand the potential for future infrastructure damage (Fig. 1). Utilizing a "point" analysis approach as opposed to the common method of using portions of coastline, provides a resolution suitable for understanding local hurricane vulnerability (Muller and Stone 2001).

The method uses past hurricane events to understand the movement and characteristics of the "typical" strong hurricane affecting EAFB. Through creation of an average track we outline the hurricane climatology of the area. Additionally, we show how past tropical cyclone characteristics can be used to understand the future of EAFB hurricanes in a changing climate. In Section 2, we illustrate our

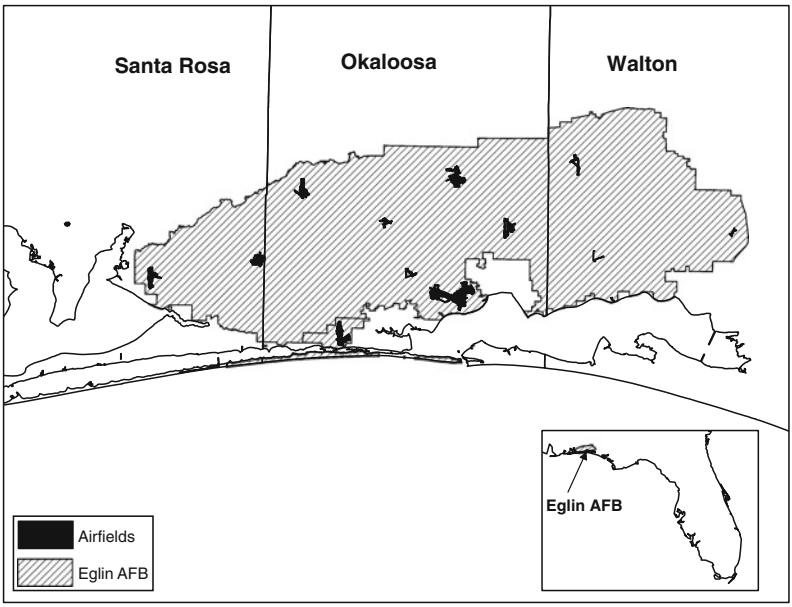

Fig. 1 Study area. Eglin Air Force Base (*hatched*) is located in the Florida Panhandle, in portions of Okaloosa, Walton, and Santa Rosa counties

technique for constructing a climatological hurricane track for a specific area based on the movement of past hurricanes. We create an average track representing the typical EAFB hurricane. In Section 3, average hurricane characteristics (i.e. intensity and translation speed) are found along the track based on past hurricane events. Together, the track and wind characteristics serve as a track-relative climatology of EAFB hurricanes. Further, in Section 4, we construct separate climatologies for years of warm and cool sea surface temperature (SST). This provides a glimpse into the possible future of EAFB hurricanes associated with a change in SST. The methodology can be repeated for any location to help understand the present local-scale hurricane climate, as well as the future of these storms in a changing climate. Section 5 provides the summary and conclusions regarding both the overall methodology and the EAFB-specific analysis.

2 An Average Hurricane Track

Due to the nature of their driving forces, hurricanes move in somewhat predictable patterns (Brettschneider 2008). Thus, hurricanes striking a particular locale are likely to follow similar pathways. It is possible to summarize the behavior of the typical track of hurricanes for a specific location based off of past tropical cyclone events. The goal is to provide a technique for analyzing a local-level hurricane climate, and the affect changing SST may have on the average hurricane. The first step is creating a track for the average hurricane.

When creating a track for the typical EAFB-affecting hurricane, we take into account that the wind effects of a hurricane are largely based on where the cyclone makes landfall relative to a particular location. It is known that the forward right quadrant usually contains the most intense wind speeds (Elsner and Kara 1999) and the greatest storm surge (Simpson and Riehl 1981). Consequently, EAFB is likely to experience the greatest effects from a tropical cyclone striking just to the west. Since this research is interested in those hurricanes that threaten local infrastructure, we analyze EAFB vulnerability relative to those making landfall just west of the base. The remainder of this chapter considers hurricanes making landfall near 30.4°N and 86.8°W, a point on Santa Rosa Island, Florida located approximately 30 km southwest of the EAFB geographic center.

We first create an average hurricane track for EAFB based on past hurricanes making landfall near the selected landfall location on Santa Rosa Island. The hurricane data are an hourly-interpolated version of the HURDAT data set (1851–2008). As described in Jagger and Elsner (2006), spline interpolations are used to create hourly estimations from the six-hourly HURDAT observations. Using hourly-interpolated data reduces the chance of missing a hurricane passing through a small area relative to the chance when using six-hourly data. Moreover, at an area the size of EAFB, higher temporal resolution is not needed.

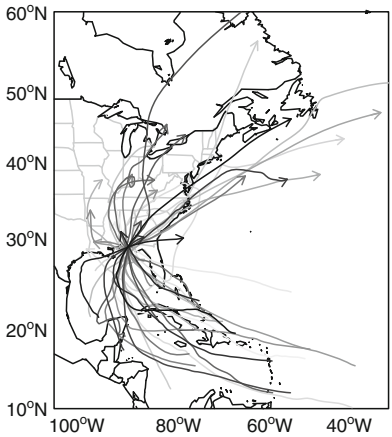

Fig. 2 Tracks of hurricanes affecting Eglin Air Force Base (EAFB). All 26 tracks came within 100 km of Santa Rosa Island, FL (30.4°N and 86.8°W) based on data from 1851 to 2008. The *gray shading* is proportional to the distance the track came to the landfall location. *Darkest tracks* are those that passed nearest the island

Figure 2 shows the 26 tracks that have come within a 100 km radius of EAFB over the period 1851 through 2008. The tracks have gray shading to reflect their closest great-circle distance to the chosen location of interest; the darker the track the closer it came to the location. Each of the tropical cyclones reached winds of hurricane force (33 m s^{-1}) or greater within the radius. We consider an average of these tracks to represent the typical EAFB hurricane track capable of producing catastrophic winds across the region.

The method to obtain an average hurricane track uses a series of distance maps (Scheitlin et al. 2010). The value at any point on the distance map is the length of the shortest route from that point perpendicular to the track, in units of degrees longitude. A distance map is created for each of the 26 hurricanes shown in Fig. 2. The methodology could be made more precise by using great-circle distances in projected coordinates, but for the length of track used here and because we are only interested in relative distances (relative to the track) the use of degrees longitude is acceptable.

In order to find the average track we create an average-distance map. The value at any point on the average-distance map is the mean of the shortest lengths at that point on the individual distance maps (one for each hurricane track). Instead of taking the simple mean of the distance maps, we use an inverse-distance weighted mean based on the distance from the track to the landfall location. The tracks passing closest by the landfall point (the darkest tracks in Fig. 2) are weighted more heavily than those at a farther distance. In this way the search radius used for selecting tracks is not critically important as increasing the search radius only increases the number of hurricanes farther from the landfall point, which have minimal weight in the averaging.

Figure 3 shows the average-distance map based on the 26 hurricanes. The average track is the line down the center of the distance contours. This represents the track of a typical EAFB hurricane. Here the track is drawn within a threshold of

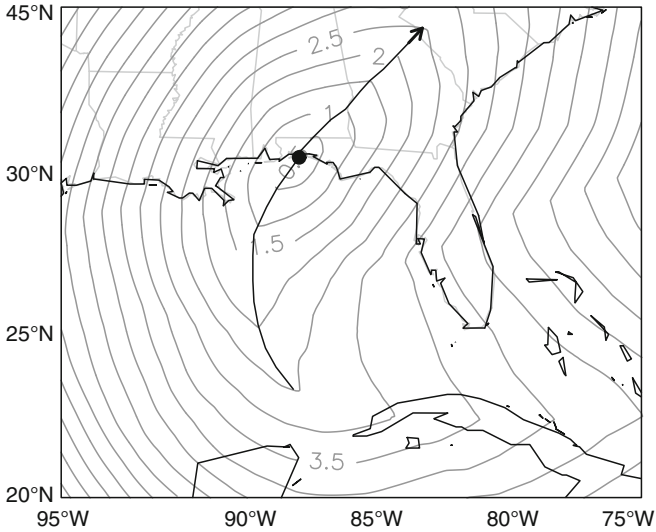

Fig. 3 Average hurricane track for EAFB. The average track is the *solid line* drawn through the minimum distance contours of the average-distance map. The average-distance map is based on 26 hurricanes affecting EAFB over the period 1851–2008

2.5° longitude of distance, but it can be drawn longer or shorter depending on the purpose. Next, we are interested in gathering information about the typical hurricane characteristics along this track.

3 Hurricane Characteristics Along the Track

The previous section described the method for creating a track based on past hurricanes affecting the area. An important additional consideration is the hurricane characteristics along the track, such as intensity and translation speed. In this section, the average track is sampled at equal-distant points, and the data used to characterize each point comes from past hurricanes that passed nearby the sampled points.

Figure 4 shows the average EAFB track represented by points spaced in 100 km intervals before and after landfall. Tracks of all hurricanes passing within a 100 km radius of the point 500 km from landfall are also depicted. The radius about this point contains the most hurricane tracks, with 39 historical hurricanes passing within 100 km. Hurricane characteristics are averaged based on the maximum value obtained from the hourly data as the hurricane passes through the circle. For example, if the hurricane spends 8 h within 100 km of the point, only the single maximum wind speed value is used in the average.

This process is repeated along the track, selecting a set of hurricanes coming within 100 km of each of the track points. The average translation speed and

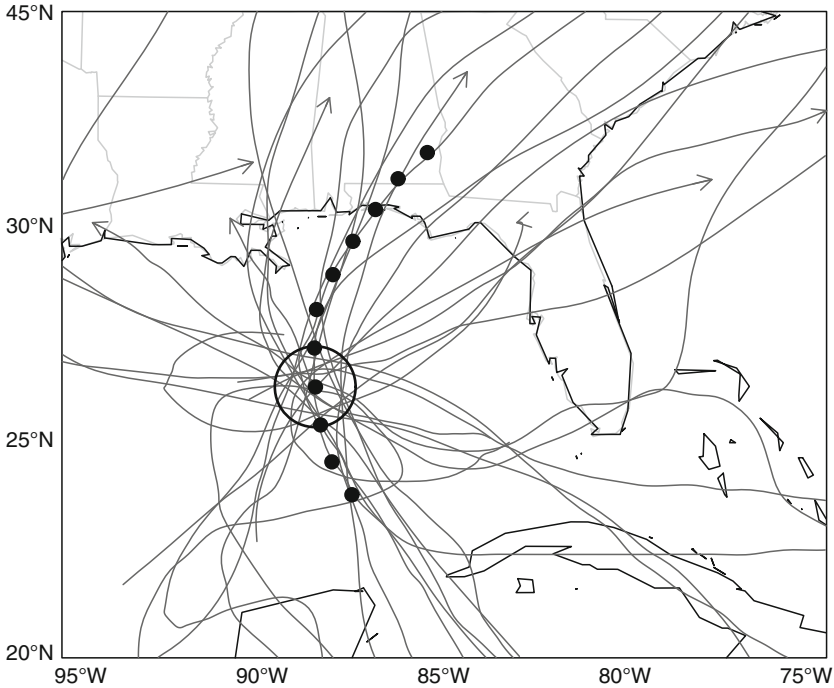

Fig. 4 The average EAFB hurricane track depicted as a series of equal-interval points spaced 100 km apart and centered on the landfall location of EAFB. The tracks of all hurricanes passing within a 100 km radius of the point 500 km from landfall are also depicted. Hurricane characteristics (intensity, forward speed, etc.) are averaged based on the maximum value obtained from the hourly data as the hurricane passes through the circle. The process is repeated for each point

intensity are calculated from the selected hurricanes, again using the maximum hourly-observation within the radii for each event. Information regarding the average decay and intensification behavior is gathered from the change of average intensity over track distance.

Figure 5 shows the profiles of the average hurricane characteristics along the length of the average track. The number of hurricanes used in the average is given inside the horizontal axis. As noted, the frequency peaks at locations 300–600 km from the landfall point. As expected there are fewer hurricanes closer to the coast and over land as tropical cyclones weaken below hurricane intensity.

For the intensity profile, which is based on the maximum wind speed, the dashed line marks the Category 3 (Saffir/Simpson hurricane intensity scale) threshold, which the cyclone maintains for some distance prior to landfall. The hurricane reaches its maximum intensity of approximately 52 ± 2 m s^{-1} (s.e.) 400 km before reaching the coast. After that point, hurricanes approaching EAFB, on average, begin to weaken until making landfall with wind speeds of approximately 45 m s^{-1}, a Category 2 hurricane. The downward slope of the intensity profile provides information about the typical decay rate of hurricanes approaching the coast.

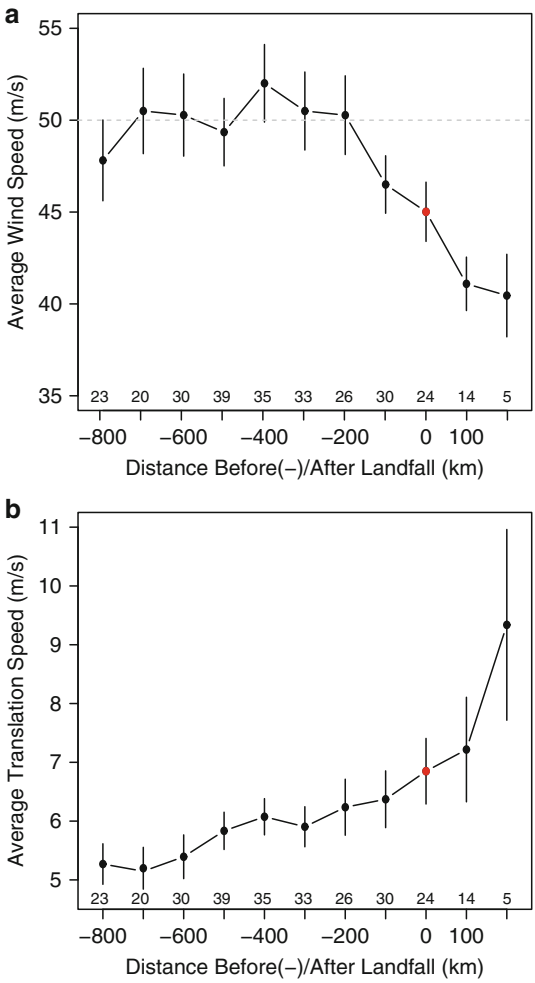

Fig. 5 Hurricane characteristics along the average track. Average (**a**) wind speeds and (**b**) translation speeds at 100 km intervals along the track. Distances in kilometers before (negative) and after landfall are plotted on the *horizontal axis*. Standard errors (s.e.) about the mean are drawn as *vertical lines* and the number of hurricanes used in the averaging are shown above the *horizontal axis*

Although the intensity profile shown in Fig. 5 is based on an average, a similar intensity profile was exhibited by Hurricane Opal in 1995, which affected EAFB. While much more intense than the average EAFB hurricane, Opal experienced rapid intensification in the Gulf of Mexico and subsequent decay prior to landfall, similar to the average cyclone. Approximately 450 km prior to making landfall just west of Santa Rosa Island, Florida, a warm-core ring in the Gulf of Mexico helped Opal

reach Category 4 intensity (Hong et al. 2000). The late onset of intensification surprised forecasters and an unsuspecting coastline. However, the average intensity profile shows that Opal's intensification profile is the rule rather than the exception. Although Opal is a more extreme case, the average EAFB hurricane exhibits some degree of intensification until 500–400 km from landfall before decaying during its final advancement towards the shore.

What is known about Hurricane Opal and other Gulf of Mexico hurricanes can provide insight into the average EAFB hurricane intensity profile. Similar to Opal, it is likely that the increased intensification exhibited by the average hurricane approximately 500–400 km before landfall is due to especially warm SSTs in the Gulf of Mexico. Areas of warm SST are often associated with warm-core rings that separate from the Loop Current and travel across the Gulf of Mexico (Vukovich and Crissman 1986). The Loop Current is a stream of warm upper-ocean water in the Gulf of Mexico that flows northward between Cuba and the Yucatán peninsula into the Gulf of Mexico then exits east through the Florida Straits.

Once a tropical cyclone reaches tropical storm strength, the thermodynamic structure of the upper ocean plays an important role on storm intensity (Emanuel 1999). For Opal and the average EAFB hurricane, the extra heat content of the warm-core ring increases the thermodynamic instability that fuels the hurricane as it travels northward toward the Gulf coast.

While the intensification of the average EAFB hurricane is easily interpreted, the decay of the hurricane as it approaches inland has a more complex explanation. That being said, it is no surprise that the hurricane decays in such a manner. Hurricane Opal experienced similar pre-landfall decay, and Vickery and Wadhera (2008) note that this 12–24 h pre-landfall decay is common in, and exclusive to, hurricanes making landfall along the Gulf Coast. Levinson et al. (2009) add that this pre-landfall weakening is more prominent in stronger Gulf of Mexico hurricanes.

There are at least three factors associated with the pre-landfall decay of the EAFB hurricane. One obvious factor is the movement of the hurricane away from the warmest waters associated with the warm-core rings of the Loop Current. Second, the entrainment of dry continental air works to "fill in" a hurricane as a portion of it begins to reach the coast (Levinson et al. 2009). This will affect larger storms first, as they will interact with the drier air earlier than smaller storms as they approach landfall. A third, lesser-known factor in the pre-landfall decay is the effect of continental aerosols near the coast. Khain (2008) found that aerosols decrease the convective intensity in the center of a simulated hurricane leading to weakening. These three factors help explain the pre-landfall weakening.

In addition to intensity, the average EAFB hurricane translation speed is also gathered from the historical data set. Figure 5b displays the translational speed profile along the average track. On average, hurricanes are accelerating as they approach EAFB. And the acceleration rate increases, especially after landfall. For a large portion of the track, the average forward speed is in the range of 6–7 m s^{-1}. Extrapolating from a constant translation speed of 6.5 m s^{-1} from the location of maximum intensity, the hurricane is estimated to reach EAFB in about 17 h. This

extrapolation would error on the wrong side for coastal communities and EAFB employees as the tendency is for an acceleration of the hurricane resulting in an arrival earlier than anticipated.

4 Warm Versus Cool SST Years

A major concern about hurricane risk is the possibility that the risk will change in a warming world. Once again, it is useful to take a local-scale approach to this research in order to provide information at the decision-making level. This also allows us to account for different affects of climate change based on location, as previous studies have shown that intense hurricanes in different ocean basins are affected somewhat differently by a warming environment (Elsner et al. 2008). Here we analyze how SST variability has affected past EAFB hurricane characteristics. This may provide information regarding the affects of future SST changes on local hurricane activity.

SST data are obtained from the Caribbean SST Index provided by NOAA Earth System Research Laboratory (2009). The data set contains monthly SST anomalies for the Caribbean Sea from 1951 to 2006. For this analysis, an August–September –October anomaly average is calculated each year. The yearly averages are divided into thirds (terciles), with the top third representing warm years, and the bottom third representing cool years. The lower tercile is a −0.060°C temperature anomaly with a minimum value being a −0.374°C anomaly. The upper tercile is a 0.194°C temperature anomaly with a maximum value being a 0.472°C anomaly. Intensity and translation speed profiles are created for cool and warm years by finding the average maximum values for each cyclone passing within 100 km of each track point during the appropriate years. The track stops 100 km inland due to decreasing sample size.

Figure 6 displays the EAFB intensity profile for the cool (a) and warm (b) years, along with the standard error of the mean. It is important to note that the time frame for these graphs is 1951–2006, differing from that of Fig. 5, which is based on data over the period 1851–2008. The number of events used to calculate the means are given above the horizontal axis. Larger samples during the cooler years mean that since 1951, more tropical cyclones have passed nearby the average track in cooler years than warmer years. However, the warmer years exhibit greater wind speeds at each location. The highest average wind speed for warm years is 50 m s^{-1} (threshold for a Category 3 hurricane), occurring 800 km before landfall. The large standard error associated with the warm years suggests the possibility of much greater intensities. The warm years also exhibit the largest range of wind speeds along the track. During cooler years the average wind speed peaks at 42 m s^{-1} (a Category 2 hurricane), 600 km prior to landfall. On average, the hurricane makes landfall at category 1 intensity for warm and cool years.

Figure 7 shows the average translation speed for the (a) cool and (b) warm years. There is little difference in forward speed of the average hurricane approaching

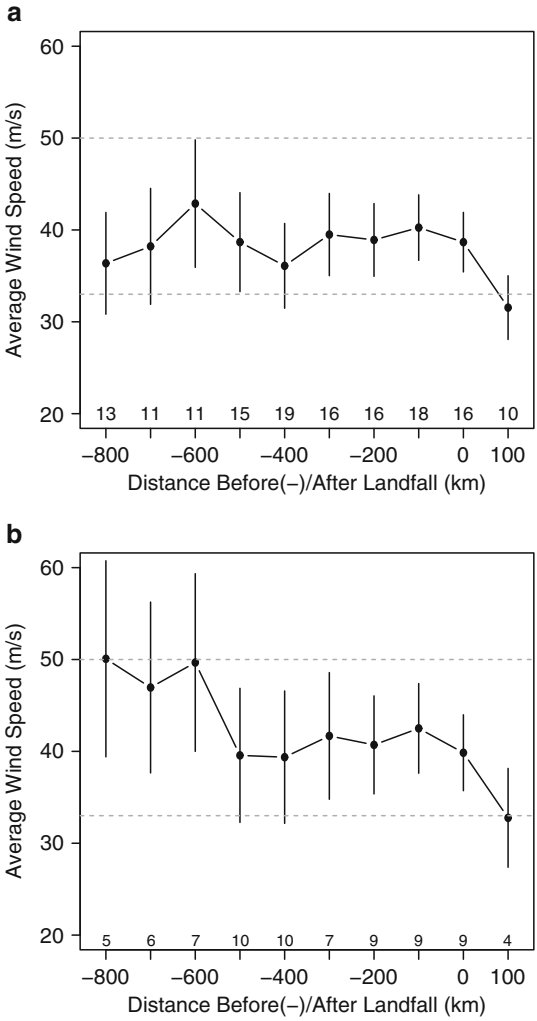

Fig. 6 Average hurricane intensities along the average track for hurricanes during (**a**) cool and (**b**) warm SST years. Distances in kilometers before (negative) and after landfall are plotted on the *horizontal axis*. Standard errors (s.e.) about the mean intensities are drawn as *vertical lines* and the number of hurricanes used in the averaging are shown above the *horizontal axis*

EAFB between warm and cool years. The exception is near the coast. On average the warm years feature slower moving hurricanes as they approach and cross the coast. This can amplify the damage potential, as the slightly more intense hurricane will move more slowly over an area. While it is difficult to draw conclusions from such a small sample size, these data suggest that more destruction may be expected from hurricanes occurring in warm years, or in a warming environment.

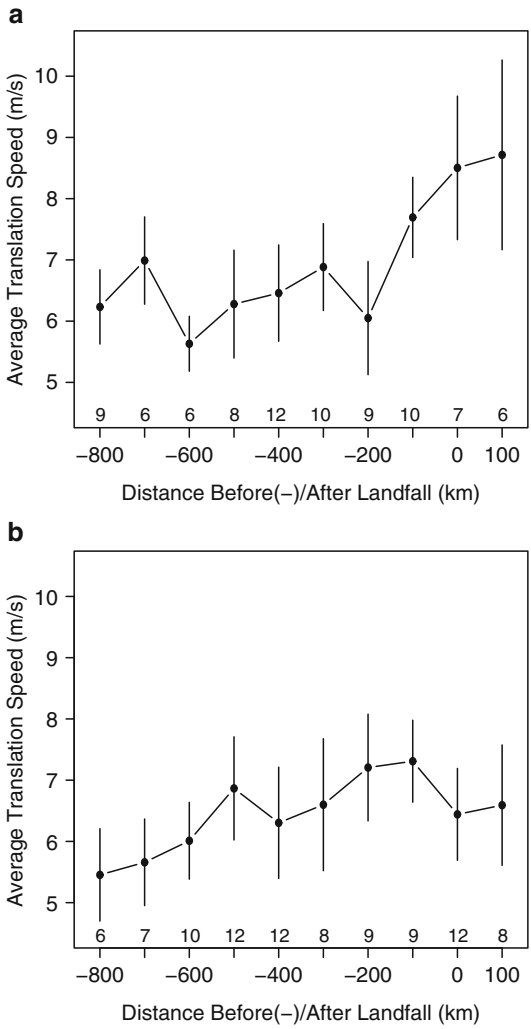

Fig. 7 Average hurricane forward speed along the average track for hurricanes during (**a**) cool and (**b**) warm SST years. Distances in kilometers before (negative) and after landfall are plotted on the *horizontal axis*. Standard errors (s.e.) about the mean translation speed are drawn as *vertical lines* and the number of hurricanes used in the averaging are shown above the *horizontal axis*

5 Summary and Conclusion

This chapter provides a methodology for developing a local-scale hurricane climatology and assessing the impact of SSTs on hurricane characteristics. Using Eglin Air Force Base (EAFB) as an example, an average hurricane track is created, and the average characteristics along the track are attained based off of past hurricane events. The process is repeated for warm and cool SST years. The results

are a track-relative climatology of the average EAFB hurricane, as well as the average warm- and cool-year EAFB hurricanes.

First, we create an average EAFB hurricane track based off of past hurricanes. A landfall point just west of EAFB on Santa Rosa Island, Florida is chosen because it places EAFB in the front right quadrant of the cyclone. Historical hurricanes (1851–2008) coming within 150 km of this point are selected, resulting in 26 hurricanes. A distance map is created for each hurricane, the values of which display the distance from the hurricane track to any point on the map. The distance maps are averaged using an inverse-distance weighted approach favoring the hurricanes that passed nearest the landfall point. A line down the center of the averaged distance map is the climatological EAFB hurricane track.

Next, we obtain hurricane characteristics along the average track. The track is represented by a series of equal interval points, spaced in 100 km intervals before and after landfall. Past hurricanes coming within 100 km of these points are selected, and their maximum hourly-observation within the radii are averaged to represent the mean characteristics for that location. The average intensity and translation speed are shown in the form of track profiles, creating a track-relative climatology. The average EAFB hurricane reaches its maximum intensity of 52 ± 2 m s^{-1} (s.e.) 400 km prior to landfall. The cyclone continues to travel towards the coast at approximately 6.5 m s^{-1}, before making landfall with winds of 45 m s^{-1}.

The characteristics along the track are determined, this time using only those hurricanes occurring in warm or cool SST epochs. The lack of Caribbean SST data prior to 1951 makes it difficult to discern the impact of SSTs on EAFB hurricanes. However, since 1951, warm-year hurricanes have exhibited slightly higher wind speeds and moved a slower pace than their cold-year counterparts. In addition to increased wind speed, higher storm surge should also occur with warmer SSTs for two reasons. First, greater wind speeds result in a higher surge. Second, storm surge is best correlated with wind speeds further from the coast, rather than wind speeds at landfall (Jordan and Clayson 2008). Thus, the relatively larger difference between the pre-landfall wind speeds in warm versus cool years will likely result in large differences of surge damage. Since an increase in surge and wind speeds will cause more destruction, the economic impacts of warmer SSTs should be further analyzed.

While EAFB is likely to accrue greater hurricane damages per hurricane in a warmer climate, it may be especially worthwhile to look at strongest storms. Since the most intense hurricanes are the most destructive, and are already exhibiting strengthening in the North Atlantic (Elsner et al. 2008), it would be useful to analyze the affect of changing SSTs on major hurricanes. Currently, we provide a methodology for obtaining a local-scale hurricane climate and the basis for understanding the affects of SSTs on the hurricane characteristics. The technique can be made more useful with additional variables such as storm surge and economic loss, and by employing return levels to look at the most extreme events.

Acknowledgements The authors thank Thomas Jagger for developing the computer code used to gather hurricane information locally, and Shawn Lewers for his assistance in cartography. This

research was supported by the U.S. Department of Defense, through the Strategic Environmental Research and Development Program (SERDP), Project SI-1700. Views expressed within do not necessarily reflect the opinions of the funding agency. All spatial and statistical analyses were performed using the software environment R (http://www.r-project.org).

References

Brettschneider B (2008) Climatological hurricane landfall probability for the United States. J Appl Meteor Climatol 47:704–716

Elsner JB, Kara AB (1999) Hurricanes of the North Atlantic: climate and society. Oxford University Press, New York, pp 488

Elsner JB, Kossin JP, Jagger TH (2008) The increasing intensity of the strongest tropical cyclones. Nature 455:92–95

Emanuel KA (1999) Thermodynamic control of hurricane intensity. Nature 401:665–669

Emanuel K (2005) Increasing destructiveness of tropical cyclones over the past 30 years. Nature 436:686–688

Hallegatte S (2007) The use of synthetic hurricane tracks in risk analysis and climate change damage assessment. J Appl Meteor Climatol 46:1956–1966

Hong X, Chang SW, Raman S, Shay LK, Hodur R (2000) The interaction between Hurricane Opal (1995) and a Warm Core Ring in the Gulf of Mexico. Mon Wea Rev 128:1347–1365

Jagger TH, Elsner JB (2006) Climatology models for extreme hurricane winds near the United States. J Climate 19:3220–3226

Jordan M, Clayson C (2008) A new approach to using wind speed for prediction of tropical cyclone generated storm surge. Geophys Res Lett 35, L13802, doi: 10.1029/2008GL033564

Khain A, Cohen N, Lynn B, Pokrovsky A (2008) Possible aerosol effects on lightning activity and structure of hurricanes. J Atmos Sci 65:3652–3677

Landsea CW, Harper BA, Hoarau K, Knaff JA (2006) Can we detect trends in extreme tropical cyclones? Science 28:452–454

Levinson DH, Vickery PJ, Resio DT (2009) A climatology of landfalling hurricane central pressures along the Gulf of Mexico coast. Eleventh international workshop on wave hindcasting and forecasting and 2nd coastal hazard symposium, October 18–23, 2009

Muller RA, Stone GW (2001) A climatology of tropical storm and hurricane strikes to enhance coastal vulnerability prediction for the southeast U.S. coast. J Coast Res 17:949–956

NOAA Earth Systems Research Laboratory, Physical Sciences Division (2009) Monthly Caribbean SST Index (CAR), http://gcmd.nasa.gov/records/GCMD_NOAA_NWS_CPC_CAR.html

Pielke RA Jr, Landsea C, Mayfield M, Laver J, Pasch R (2005) Hurricanes and global warming. Bull Am Meteorol Soc 86:1571–1575

Scheitlin KN, Elsner JB, Malmstadt JC, Hodges RE, Jagger TH (2010) Towards increased utilization of historical hurricane chronologies. J Geophys Res 115:D03108, doi:10.1029/2009JD012424

Simpson RH, Riehl H (1981) The hurricane and its impact. Louisiana State University Press, London, pp 398

Trenberth K (2005) Uncertainty in hurricanes and global warming. Science 308:1753–1754

Vickery PJ, Wadhera D (2008)Statistical models of Holland pressure profile parameter and radius to maximum winds of hurricanes from flight-level pressure and H*Wind data. J Appl Meteor Climatol 47:2497–2517

Vukovich FM, Crissman BW (1986) Aspects of warm rings in the Gulf of Mexico. J Geophys Res 91:264–2660

Chapter 14
Estimating the Impact of Climate Variability on Cumulative Hurricane Destructive Potential Through Data Mining

Roshanak Nateghi, Steven M. Quiring, and Seth D. Guikema

Abstract In this chapter, we assess the relationship between climate variability and hurricane hazard in the U.S. using data mining techniques. Regression trees are developed to investigate the relationship between seventeen climate variables (with their quarterly and annual averages) on the yearly cumulative destructive potential of U.S. land-falling hurricanes. The U.S. coast is divided into three separate sections: the Atlantic Coast excluding Florida, Florida, and the Gulf Coast excluding Florida. Each region is analysed separately as well as the aggregate of all the regions in an effort to better understand the factors that drive the frequency and intensity of hurricanes making landfall in the U.S. The results indicate that a large number of climate variables contribute to the observed historical variations in hurricane activity. This insight is validated by demonstrating that the models outperform previously published models that are based on only two climate variables. The results show that geographic partitioning is essential in both understanding the pattern of past hurricane activity and forecasting future hurricane hazard. The analysis of variable importance shows that temperature-related variables are useful for explaining hurricane activity, even though their importance differs between regions.

Keywords Classification and regression trees · Hurricane hazard · Climate variability · Data mining

1 Introduction

The concern over the impacts of climate variability and climate change on human lives and the environment has escalated over the past two decades. Past efforts examining the relationship between climate variability, climate change and hurricane

R. Nateghi (✉) and S.D. Guikema
Department of Geography and Environmental Engineering, Johns Hopkins University, Baltimore, MD 21211, USA
e-mail: rnategh1@jhu.edu

S.M. Quiring
Department of Geography, Texas A&M University, College Station, TX 77843, USA

J.B. Elsner et al. (eds.), *Hurricanes and Climate Change: Volume 2*,
DOI 10.1007/978-90-481-9510-7_14, © Springer Science+Business Media B.V. 2010

hazard include Yonetani and Gordon (2001), Emanuel (2005), Michaels et al. (2005), Elsner et al. (2008), Knutson et al. (2008), Webster et al. (2005) and Saunders and Lea (2008). However, these previous studies considered a limited number of climate variables for their analysis, limiting the strength of the inferences that can be drawn.

The objective of this chapter is to investigate the potential impact of climate variability on the frequency and intensity of hurricanes by utilizing a large number of climate variables and employing distinctly different statistical modeling approaches to the ones that have been used in the past. In our study, regression trees were built in order to determine which set of variables is most important in capturing the variability of past patterns of hurricane hazard in the U.S. We start in Section 2 with a brief overview of the past research in the field. In Section 3 we introduce the data used in our analysis. Section 4 presents the methods for developing regression trees. In Section 5, we summarize the results of fitting regression trees and discuss the implications of our results. To conclude we provide a summary in Section 6.

2 Background Information

Numerous previous studies have investigated climate variables to determine which are the most important factors influencing hurricane occurrence rate and intensity. For example, Sabbatelli and Mann (2007) used Poisson regression and binary classification schemes to examine the link between El Niño /Southern Oscillation (ENSO), Main Development Region Sea Surface Temperature (MDR SST), North Atlantic Oscillation (NAO) and tropical cyclone counts and concluded that only ENSO and MDR SST were essential to take into account for forecasting future hurricane counts.

A number of studies such as Knutson and Tuleya (2004), Emanuel (2005), Pielke et al. (2005) and Elsner et al. (2008) argued that sea surface temperature (SST) is a critical explanatory variable in explaining hurricane frequency and intensity. For instance, Emanuel (2005) stated that net hurricane power dissipation is highly correlated with tropical SST and hence a warmer world in the future will see an increase in the potential intensity of tropical cyclones. A statistical analysis concluded that every 0.5°C increase in SST is associated with 40% increase in hurricane frequency and activity in the Atlantic basin (Saunders and Lea 2008). Model-based research has suggested insights different to the ones stated above. For example, a physics-based model suggested that environmental changes in circulation or atmospheric moisture are more important than sea surface temperatures in determining future hurricane activity (Knutson et al. 2008). Their models suggest that the frequency of Atlantic hurricanes and tropical storms will likely be reduced in the future (Knutson et al. 2008). Results obtained by downscaling IPCC AR4 simulations also suggest a reduction in the global frequency of hurricanes in a warmer future climate scenario, with a potential increase in intensity in some locations (Emanuel et al. 2008). However, there still exists a considerable degree of uncertainty and disagreement

regarding the climate factors that drive hurricane intensity and frequency and the potential impact of climate change on hurricane hazards. Moreover, none of the previous research has investigated an extensive range of climate variables. In this paper, we will explore the potential links between climate variability and climate change on hurricane destructive potential by including a large number of climate variables in our analysis.

3 Data

A chronological list of all hurricanes that made landfall in the continental United States from 1948 through 2007 was obtained from the National Oceanic and Atmospheric Administration website (NOAA 2008: www.aoml.noaa.gov/hrd/hurdat/ushurrlist.htm). The U.S. coast was then subdivided into the following three distinct sections as shown in Fig. 1:

1. Region one: the Gulf Coast excluding Florida
2. Region two: Florida
3. Region three: the Atlantic Coast excluding Florida

Florida was treated as a separate coastal segment because it experiences a unique hurricane environment with hurricanes approaching from both the Atlantic and the Gulf of Mexico.

Rather than simply using hurricane counts or occurrence rates as our response variable as some have done (e.g., Elsner et al. 2001), we use a measure that incorporates both hurricane occurrence rates and hurricane intensity, because it is a better

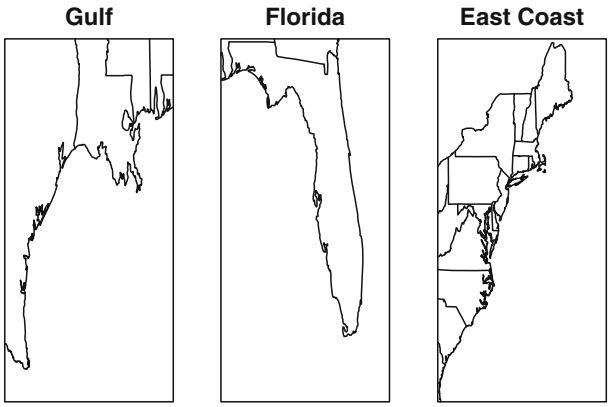

Fig. 1 Regions used as the basis for developing the regression tree models. Texas through Alabama is Region one (*left figure*), Florida is region two (*middle figure*), and the rest of the Atlantic Coast north of Florida is Region three (*right figure*). Maps are not drawn to scale

indicator of hurricane damage than counts. Hurricane damage is generally modelled as a function of hurricane wind speed, and hurricane wind speed is proportional to the square root of the central pressure difference of hurricanes. Consequently, we used the following equation to calculate our measure of the hurricane hazard in a given region in a given year:

$$V_y = \sum_{h \in Y} \sqrt{(P_{h,n} - P_{h,c})} \tag{1}$$

where V_y is the cumulative hurricane hazard for year y, $P_{h,n}$ and $P_{h,c}$ are ambient and central pressures for hurricane h respectively, and Y is the set of hurricanes occurring in the region in year y. We used 1,005 mb for $P_{h,n}$ for all years and all hurricanes in accordance with Holland (1980). This approximate measure of yearly hurricane hazard was used as our response variable in fitting regression trees. We fit regression trees using quarterly averages and annual averages of the climate variables. We included a total of 73 exploratory variables (described below) in our models. It should be noted that modelling this high dimension data set with conventional regression-based methods such as a simple regression or a compound Poisson approach is challenging, and the results would be difficult to interpret. This is because (1) the number of covariates (73) exceeds the number of our records (60) and (2) there is a high degree of collinearity among the covariates. PCA transformation could potentially be implemented to reduce the number of dimensions and transform the covariates to an orthogonal space, however interpreting the importance of the significant beta values when transformed back to the original space is challenging.

Previous studies have modelled the occurrence or intensity of Atlantic tropical cyclones using at most four climate variables (e.g., Jagger and Elsner 2006; Sabbatelli and Mann 2007). Jagger and Elsner (2006) developed a model of maximum hurricane wind speeds in the Atlantic basin using El Niño/Southern Oscillation (ENSO), Atlantic Multi-decadal Oscillation (AMO), North Atlantic Oscillation (NAO), and global temperature. Sabbatelli and Mann (2007) predicted the occurrence of Atlantic tropical cyclones based on ENSO, NAO, and August–October sea surface temperatures (SST) over the main development region (MDR) in the tropical Atlantic. This paper includes additional candidate predictors that were selected because they are known to influence hurricane development, intensity, and movement or because they have been previously considered in similar studies. Table 1 lists the 17 climate variables that were used and they are described briefly below. Quarterly averages (e.g. January–February–March (1), April–May–June (2), July–August–September (3), October–November–December (4)) were calculated for each variable and they were used to develop regression trees.

ENSO has been shown to play an important role in modulating hurricane activity in the Atlantic Basin (Elsner et al. 2001; Jagger and Elsner 2006). ENSO conditions can be represented using equatorial Pacific SST. The Niño 3.4 index SST averaged over the region (5°N–5°S & 170°W–120°W) is one of the SST indices commonly used (Sabbatelli and Mann 2007; Trenberth 1997). El Niño (La Niña) is associated with large positive (negative) SST anomalies.

Table 1 Variables used in our models: we used the values of quarterly averages as well as the annual values for all the variables listed below except for aerosol, volcanic and solar forcing for which only the annual values were used

Variable (abbr.)	Source
Niño-3.4 (ENSO)	ftp.cgd.ucar.edu/pub/CAS/TNI-N34
North Atlantic Oscillation (NAO)	www.cru.uea.ac.uk/ftpdata/nao.dat
Pacific Decadal Oscillation (PDO)	jisao.washington.edu/pdo/PDO.latestl
Atlantic Multidecadal Oscillation (AMO)	www.cdc.noaa.gov/Correlation/amon.us.long.data
Quasi-Biennial Oscillation (QBO)	www.cdc.noaa.gov/Correlation/qbo.data
Sahel Standardized Rainfall (Sahel)	jisao.washington.edu/data-sets/sahel/sahelrain18982004
North Tropical Atlantic SST (NTA)	www.cdc.noaa.gov/Correlation/NTA.data
Caribbean SST (CAR)	www.cdc.noaa.gov/Correlation/CAR.data
Tropospheric Aerosol Forcing (AF)	www.meteo.psu.edu/ mann/eos06/tropoAer.dat
Volcanic Forcing	ftp.ncdc.noaa.gov/pub/data/paleo/climate-forcing/mann2005/
Solar Forcing	ftp.ncdc.noaa.gov/pub/data/paleo/climate-forcing/mann2005/
Main Development Region (MDR) Sea-level Pressure (SLP)	www.cdc.noaa.gov/cgi-bin/Timeseries/timeseries1.pl
Main Development Region (MDR) Zonal Wind (925 mb) (ZW)	www.cdc.noaa.gov/cgi-bin/Timeseries/timeseries1.pl
Main Development Region (MDR) Specific Humidity (600 mb) (H)	www.cdc.noaa.gov/cgi-bin/Timeseries/timeseries1.pl
Hadley CRU global land and ocean temperature anomalies (CRU)	www.cru.uea.ac.uk/cru/data/temperature/hadcrut3gl.txt
Sunspot numbers (SSN)	www.ngdc.noaa.gov/stp/SOLAR/ftpsunspotnumber.html
Wind shear (W)	www.cdc.noaa.gov/cgi-bin/Timeseries/timeseries1.pl

North Atlantic Oscillation (NAO) is calculated based on the normalized sea level pressure differences between Gibraltar (or Lisbon, Portugal) and Iceland. The positive phase of the NAO corresponds to below-normal heights and pressure across the high latitudes of the North Atlantic and above-normal heights and pressure over the central North Atlantic, the eastern United States and western Europe. Positive NAO is associated with an enhanced polar vortex, stronger westerlies, and above normal temperatures over Eurasia and central North America, and below normal temperatures in eastern North America (Marshall et al. 2001).

Pacific Decadal Oscillation (PDO) is the leading EOF (Empirical Orthogonal Functions) of monthly SST anomalies in the North Pacific Ocean, pole-ward of

20°N. The positive (or warm) phase of the PDO is associated with above normal SSTs along the west coast of North America and in the tropical Pacific and below normal SSTs in the central north Pacific (Mantua and Hare 2002).

The Atlantic Multi-decadal Oscillation (AMO) is a 65–80 year cycle in North Atlantic sea surface temperatures (SST). It is associated with SST differences between the warm and cold phases that are on the order of 0.4°C throughout the North Atlantic basin. AMO warm (or positive) phases occurred from 1860 to 1880 and 1940 to 1960, and cool (or negative) phases occurred from 1905 to 1925 and 1970 to 1990 (Enfield et al. 2001).

Quasi-Biennial Oscillation (QBO) is a stratospheric (30 mb) oscillation of equatorial zonal trade winds with a period of 26–30 months. The positive (negative) phase is associated with easterly (westerly) winds. The negative phase of QBO (e.g., westerly winds) is associated with decreased hurricane activity in the Atlantic basin (Gray 1984).

Sahel standardized rainfall departures are calculated based on stations between 8°–20°N and 20°W−10°E. Above normal Sahel rainfall is associated with increased Atlantic hurricane activity (Landsea et al. 1999; Lehmiller et al. 1997).

Sea surface temperatures (SST) in the Caribbean and North Atlantic (60°W to 20°W, 6°N to 18°N and 20°W to 10°W, 6°N to 10°N respectively) were also included. Previous research has shown that SST has a strong positive influence on hurricane activity (Emanuel 2005; Mann and Emanuel 2006; Sabbatelli and Mann 2007).

Other factors that were considered include solar forcing, volcanic radiative forcing, and tropospheric aerosol forcing (Mann and Emanuel 2006). Increased concentrations of tropospheric aerosol can lead to cooling over the MDR, and this cooling is associated with decreased hurricane activity (Mann and Emanuel 2006). Although the influence of solar variability and volcanic forcing on Atlantic hurricane activity is not well understood, it is considered potentially important.

Atmospheric conditions in the main development region (10°–20°N, 20°–60°W) have also been shown to influence hurricane activity (Landsea et al. 1999; Michaels et al. 2005; Saunders and Lea 2008). This paper considers mean (area weighted) sea-level pressure (mb), zonal wind (u) at 925 mb, and specific humidity at 600 mb.

The potential influence of increasing global temperatures on Atlantic hurricane activity is incorporated by considering Hadley CRU global land and ocean temperature anomalies. Previous studies have shown that global surface temperatures are useful for predicting Atlantic SST and hurricane activity (Elsner 2006; Sabbatelli and Mann 2007).

4 Theory and Methods

We constructed regression trees using the data described in Section 3 to understand which variables are most important to include in modelling past patterns in hurricane destructive potential and to develop fitted models using the past data. In

the following discussion we closely follow the presentation of classification and regression trees of Breiman et al. (1998). Regression trees are built by recursive binary partitioning of the data space at nodes. The following sections describe the process of building and validating a regression tree. At each node t of a tree, a set of binary questions of the form $x_j \leq t$ and $x_j > t$ (i.e., a binary partitioning of the data based on splitting covariate j at value t), generate a set of splits; those cases in node t answering yes to the questions go to the left; otherwise they go to the right. The best splits are the ones that maximize the decrease in re-substitution error R(t) given by Eq. 2:

$$\triangle R(s,t) = R(t) - R(t_L) - R(t_R) \tag{2}$$

where R(t) is a measure of fit such as the sum of squared errors or absolute deviation within node t.

At any given point in the tree, splits (i.e., which variable to split on and where to split that variable) are chosen from the large set of possible splits to minimize the re-substitution error at that node. That is, a greedy algorithm is used that looks only at the current split and does not attempt to look deeper into the developing tree. The tree re-substitution error, R(T), decreases as the number of terminal nodes increases. In this respect, R(T) is similar to R^2 in regression in that the more independent variables are included, the higher the value of R^2 even though the variables may add little additional information. Similarly, the higher the number of terminal nodes, the lower the value of R(T), even though the additional splits may not extract any extra information.

Regression trees use a stopping rule to determine how large to build a tree for a given data set and then prune (reduce) this large tree back to a smaller tree that should give more accurate predictions. We use the standard stopping rule of splitting the data space recursively until each terminal node contains no more than a certain predefined minimum number of records. The average or median value of the records in the training data set classified into a given terminal node is then assigned as the value to be used as the prediction for all future records ending in that terminal node (Breiman et al. 1998).

Trees are pruned after growing maximum trees (T_{max}) to avoid over-fitting (Breiman et al. 1998). The standard approach for pruning a tree, termed minimal cost complexity pruning, involves iteratively removing nodes from the tree such that the node removed at any iteration is the one that contributes the least to model fit. The cost complexity measure $R_\alpha(T)$ given in Eq. 3 is used as basis for this determination, and it takes into account both the cost of misclassification and the cost for the terminal nodes.

$$R_\alpha(T) = R(T) + \alpha|\tilde{T}| \tag{3}$$

The complexity parameter $\alpha \geq 0$ is a real number and $\tilde{T}$ stands for terminal nodes. In pruning, for each value of α, the sub-tree that minimizes the cost complexity measure is found. The final result is a series of trees of decreasing size such that $T_1 > T_2 > \cdots > T_k$ (while $T_1 = T_{max}$). T_k is the smallest sub-tree of T_{max}, the largest tree built, that minimizes $R_\alpha(T)$.

To compare the different trees in this series of trees and choose the best tree for inference and prediction, we used v-fold cross validation. With this approach, the learning sample S is randomly divided into v subsets of almost equal sizes with the vth learning sample denoted $S^{(v)} = S - S_v$ for $v = 1 \cdots v$ with S_v consisting of the data in the vth holdout. First, v trees are grown together with a specified maximum size tree where the vth tree is grown using the learning sample $S^{(v)}$. $S^{(v)}$ consists of all of the data except the data in S_v, which will be used for validation purposes. The least squares v-fold-cross validation error is computed as given in Eq. 4:

$$R^{CV}(T_k) = \frac{1}{N} \sum_{v=1}^{v} \sum_{(x_n, y_n \in l_v)} \left(y_n - d_k^{(v)}(x_n) \right)^2 \tag{4}$$

where N is the total number of cases, y_n is our data point and $d_k^{(v)}(x_n)$ is the prediction from the regression rule from the tree fitted to $S^{(v)}$. The relative cross validation error is then given by Eq. 5:

$$RE^{CV}(T_k) = \frac{R^{CV}(T_k)}{R(\overline{y})} \tag{5}$$

where $\overline{y}$ in the equation represents replacing the fitted tree with the mean value from the training data set. If least absolute deviation is used as the error measure rather than squared error, the same procedure applies except that the squared error term in Eq. 4 is replaced by an absolute value of the error. In both cases, the tree with minimum cross validation error is chosen as the optimal tree.

Our implementation of regression trees was done through Salford system's CART package. This approach uses surrogate splits to handle missing data and correlated data and to rank variables based on their importance. For each split s on x_m, a surrogate split $\tilde{s}$ is found on a variable other than x_m such that whenever a case has the variable x_m missing, it can be classified using the surrogate. Variable importance for regression trees is calculated using Eq. 6:

$$M(x_m) = \sum_{t \in T} \triangle R(\tilde{s}, t) \tag{6}$$

where $M(x_m)$ is the variable importance and $\triangle R(\tilde{s}, t)$ is change in re-substitution error via the surrogate split $\tilde{s}$ for node t. Since the importance of variables relative to each other is of interest, variable rankings are normalized so that the most important variable(s) has a value of 100. This normalization is given by Eq. 7:

$$\frac{100 M(x_m)}{max_m M(x_m)} \tag{7}$$

In our analysis we fitted regression trees to the entire data set to detect the climate variables that are most important in explaining hurricane intensity and

frequency. In order to minimize fit and cross validation errors the method of least-absolute deviation was used to develop the regression tree for region one, and the method of least-squares was used to develop regression trees for region two, three and aggregate of all regions. In order to determine the importance of including a large number of climate factors relative to simpler models with pre-selected sets of variables we developed regression trees using only a subset of the total of seventeen climate variables that we originally included in our analysis. First we included only NTA3 (third quarter North Tropical Atlantic SST) and ENSO3 (third quarter ENSO) in this reduced set as they were reported to be the most critical explanatory variables by Sabbatelli and Mann (2007). It should be noted that these variables are similar, but not identical, to the variables used by Sabbatelli and Mann (2007). The correlation between MDR SST and NTA3 is 0.89 and the correlation between MDR ENSO and ENSO3 is 0.90. In the second reduced model we included ZW3 (zonal wind for the months of July–September) and NTAO3 as they were the explanatory variables that were closest to the ones included in Saunders and Lea (2008). The correlation between the August–September–October zonal wind variable used by Saunders and Lea (2008) and our ZW3 variable is 0.86. A comparison of these previously published models to our models provides a means for quantifying the improvement achieved by including additional climate variables.

5 Results

5.1 Model Fit and Predictive Ability

Our models yielded very good fits for each region as well as the combined region when judged by the root mean square error (RMSE) and mean absolution deviation (MAD). For example, the ratios of MAD to the mean annual cumulative destructive potentials were 0.21, 0.53, 0.36, and 0.31 for regions one through three and the aggregate of all regions, respectively (Table 2).

This suggests that these models fit the past hurricane record with reasonable accuracy, though there is still unexplained variability in the fitted values. When the results given in Table 2 are compared with those from the models fits with only two climate variables (Tables 3 and 4), we see that both MAD and RMSE are substantially higher in these two-variable models. The errors of the fitted trees based on the full set of climate variables are substantially smaller than those of the fitted trees

Table 2 Regression tree fitting results for hurricane cumulative destructive potential by region

Region of interest	RE^{CV}	RMSE	MAD	Mean of observation
Region one	1.4 ± 0.1	2.2	0.8	3.8
Region two	0.6 ± 0.2	3.8	1.8	3.4
Region three	2.0 ± 0.5	2.1	1.0	2.8
Aggregate of regions	1.5 ± 0.2	5.6	3.1	10

Table 3 Results from fitting regression trees for hurricane cumulative destructive potential using only NTA3 and ENSO3

Region of interest	RE^{CV}	RMSE	MAD	Mean of observation
Region one	1.4 ± 0.1	3.5	2.1	3.8
Region two	1.1 ± 0.2	4.5	2.3	3.4
Region three	1.7 ± 0.3	3.6	2.2	2.8
Aggregate of regions	1.3 ± 0.2	6.0	4.3	10

Table 4 Results from fitting regression trees for hurricane cumulative destructive potential using only ZW3 and NTA3

Region of interest	RE^{CV}	RMSE	MAD	Mean of observation
Region one	1.2 ± 0.1	3.4	1.8	3.8
Region two	1.1 ± 0.2	4.4	2.5	3.4
Region three	2.1 ± 0.4	3.2	1.6	2.8
Aggregate of regions	1.4 ± 0.3	5.8	4.4	10

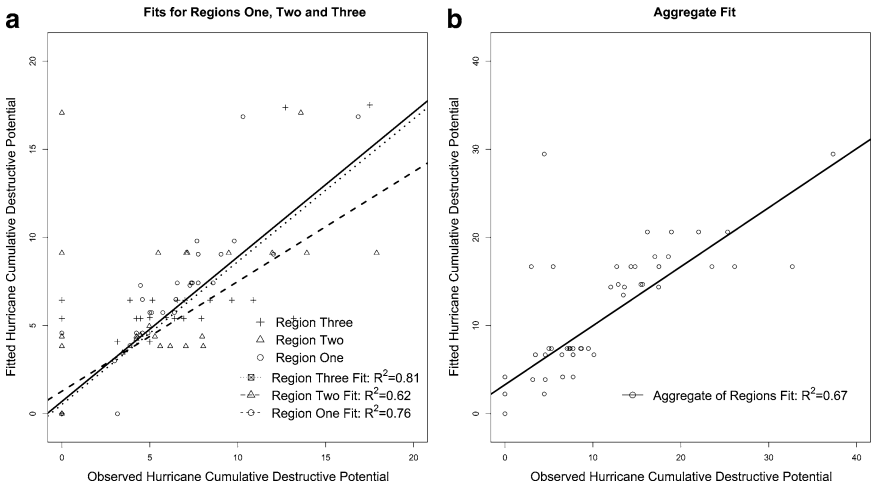

Fig. 2 Fitted values vs. actual values for the trees fitted for each separate region (**a**) and the aggregate of all regions together (**b**)

based on only two climate variables. A small set of variables alone does not suffice. Hence our results indicate the importance of incorporating a wide range of climate variables to reproduce the past variability of hurricane activities when using CART. This is the advantage that CART offers since we cannot use a wide range of climate variables with traditional regression-based approaches without both variable reduction and variable transformation to address collinearity. As discussed above, this impedes interpretation of the results of the analysis.

Graphs of the fitted values against the observed values shown in Figs. 2–4 help visualize the extent to which we succeeded in reproducing the variability in the past

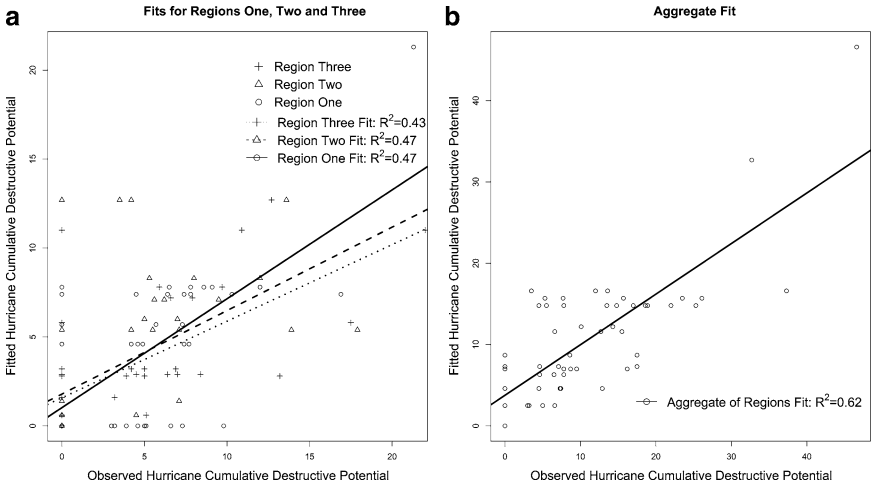

Fig. 3 Fitted values vs. actual values for regression trees fitted to the entire data set for each separate region (**a**) and the aggregate of all regions together (**b**) and using only two climate variables of NTA3 and ENSO3 as independent variables

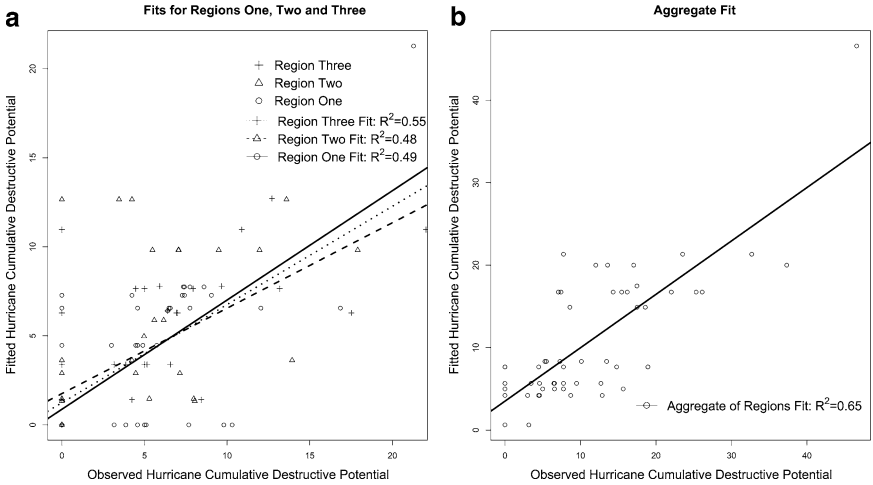

Fig. 4 Fitted values vs. actual values for regression trees fitted to the entire data set for each separate region (**a**) and the aggregate of all regions together (**b**) and using only two climate variables of NTA3 and ZW3 as independent variables

data. The value of R^2 for a linear regression of fitted values against actual values ranges from 0.62 to 0.81 for the models utilizing all of the climate variables. These results indicate good model fits in general, and better fits for each geographic region individually than for the aggregate of all the regions together. Once the coast

has been segmented appropriately, it is possible to model past hurricane patterns with high degrees of accuracy if appropriate climate variables are used. However, as can be seen in Figs. 3 and 4, the R^2 percentages for the models using only two climate variables have dropped to 0.43–0.65, further indicating that including just two climate variables is not sufficient to capture the past patterns in hurricane variability.

In examining the RE^{CV} values in Tables 2–4, recall that a relative cross validation error value below one indicates that the fitted model should, on average, yield better predictions than using the mean. The cross validation errors of our fitted models are one or above in every case except for regression trees for the entire data set for region two (see Tables 2–4). We did select for comparison those trees that yielded the best fit, not those that yielded the lowest RE^{CV}. However, even the trees with the lowest RE^{CV} values had similar problems. Despite the fact that our models fit the past data very well, we should not expect accurate future predictions from these models, except, perhaps, for region 2 when using the entire data set. This highlights the fact that accurate prediction of future hurricane destructive potential is a difficult problem. Past efforts to statistically model long-term hurricane patterns have also had similar problems with achieving accurate predictions. This poses a significant unanswered research problem.

5.2 Variable Importance

There are three basic goals that can underlie the development of a statistical model for hurricane hazard: explaining the past hurricane record on the basis of explanatory variables (model fitting), accurately predicting future hurricane hazards on the basis of explanatory variables, and drawing inferences about which variables are most important in explaining or predicting hurricane hazard. The previous section addressed fit and prediction. In this section we discuss variable importance based on the approach given by Eqs. 6 and 7.

The variable importance rankings for the fitted regression trees show that a large number of climate variables are needed to adequately capture the variability in the past hurricane destructive potential. Table 5 lists the 10 most important climate variables for each region.

The results show that a range of climate variables are important, and that variable importance differs by region. This suggests that it is important to include a large number of climate variables in statistical analyses as opposed to including only a limited number as has been done in the past. We next examine the variable importance results by region in more detail, focusing in particular on areas where our results support or disagree with results previously reported in the literature. Since the climate variables that contribute to hurricane activity differ by region (Ballenzweig 1959), the regions are discussed separately.

Table 5 List of the 10 most important variables for each region. The variable names are defined in Table 1, and the numbers indicate the quarter. The dimensionless variable importance is given as a measure of the relative improvement in model fit due to inclusion of that variable

List of variables	Region one	Region two	Region three	Aggregate
W2	71.9			
W3	100.0			
ZW2	84.1			
CRU1	28.8			
CRU3		18.4		51.2
CRU4		34.1		36.6
CRUANN		16.7		30.2
QBO4	57.8	39.5		63.4
QBOANN	64.1	40.8		65.6
NTA4	51.2	100		100.0
SLP3			53.6	
SLP4		9.6		
SAHEL4		57.1		36.4
SAHELANN		57.1		50.6
AMO1		47.2		59.1
SSN1			85.6	
SSN2	71.5		100.0	
SSN3	59.3		85.6	
SSN4	76.3			
SSNANN	76.3		85.6	
PDO2			53.6	
PDO3			53.6	
PDOANN			53.6	
CAR4			83.9	
NAO1				29.9
NAOANN			76.4	

5.2.1 Region One

The regression tree for Region One, the Gulf Coast excluding Florida, suggests that hurricane activity in this region is primarily dependent on wind parameters, temperature anomalies and sunspot numbers. The significance of QBO agrees with Shapiro (1989), Gray et al. (1992) and Lehmiller et al. (1997) in that the QBO is associated with hurricane activity because it modulates the strength of the coupling between the troposphere and the lower stratosphere. Previously, Lehmiller et al. (1997) also identified the QBO as an important predictor of hurricane activity in the Gulf of Mexico.

Zonal wind (ZW) and wind shear (W) were identified as important factors for explaining cumulative hurricane intensity. Our findings are supported by Saunders and Lea (2008) who also found that it is important to include measures of the wind field over the main development region given that this influences cyclonic

vorticity and vertical wind shear. Previous work has also suggested that solar forcing is associated with changes in hurricane activity over the Caribbean and Gulf of Mexico (Elsner et al. 2008), again in agreement with our model results. North Tropical Atlantic SST (NTA) and Hadley Climate Research Unit global land and ocean temperature anomalies (CRU) were also found important in agreement with the previous literature in that higher temperatures are associated with increased hurricane activity (Elsner 2006).

Inspection of the structure of the regression trees (shown in the Appendix) illustrates how CART generates splits on the data space by primarily trying to separate all the years with zero hurricane activity to the left and the more active years to the right. Hence the variables that appear to the right of the tree are more indicative of the variables that are associated with hurricane activity. For Region One it can be seen that higher global temperatures are associated with increased hurricane activity, and that higher solar forcing is associated with decreased hurricane activity (Elsner 2006; Elsner et al. 2008).

5.2.2 Region Two

Our models suggest that hurricane cumulative destructive potential in the state of Florida (region two) is influenced primarily by wind parameters, temperature, and Sahel rainfall anomalies. NTA is of primary importance and, as expected, higher temperatures are seen to be associated with increased hurricane activity (Emanuel 2005; Elsner 2006). The importance of Sahel rainfall anomalies is also not surprising since years of increased rainfall are known to be associated with increased hurricane activity in the Atlantic basin as the pressure troughs generated by storms over Africa can become the seeds needed to generate hurricanes (Landsea and Gray 1992). Our model also suggests that above (below) normal NAO anomalies are associated with decreased (increased) hurricane activity, in agreement with the results of Elsner et al. (2001) who found that coastal hurricane activity increases when NAO is weak.

5.2.3 Region Three

Our results suggest that sunspot number is the most important variable in Region Three (Atlantic Coast north of Florida). The influence of sunspot numbers on hurricane destructive potential agrees with Elsner et al. (2008) in that years with higher sunspot numbers are associated with lower levels of hurricane activity. Similarly, our model suggests that NAO is important in agreement with the literature. Both sea surface and air temperature variables (NTA, AMO, CRU, CAR, and PDO) are also important in the region. The one anomaly is that higher values of NTA in the second quarter are found to be associated with decreased hurricane destructive potential. The reason for this remains an open question.

The importance of a climate variable that is removing an outlier should be treated carefully. Looking at the regression tree for this region (please refer to Appendix, Fig. 9) we can see that PDO is important in identifying the outlier. When the regression tree is re-developed with the outlier removed, PDO not seem to be a critical predictive variable. We can conclude that PDO for this region is a key factor in identifying the anomalous year.

5.2.4 Aggregate of All Regions

When considering the aggregate of all regions together, the temperature parameters, Sahel rainfall, wind parameters and solar forcing are the most important variables in the regression tree. As discussed above, higher temperatures (NTA, CRU) are associated with an increase in hurricane activity as expected. The one exception for this is that CRU tends to be associated with decreased hurricane cumulative destructive potential, though this variable is of lower importance in the tree than the other temperature variables. Higher PDO values are also associated with increased hurricane activity. As expected (Landsea and Gray 1992), above normal rainfall in the Sahel is associated with increased hurricane activity. Higher NAO values are associated with decreased hurricane activity in agreement with the literature as discussed above for individual regions.

6 Conclusion

We have demonstrated that regression trees can be used to accurately fit complicated historical patterns in annual hurricane hazard. It is worth mentioning that similar results are achieved when a different measure of hurricane destructive potential (i.e. $V_y = \sum_{h \in Y} \sqrt{(P_{h,n} - P_{h,c})^3}$) is used as the response variable in developing the regression trees. We have also shown that a range of climate variables is needed to achieve accurate model fits. Small subsets of variables, as have tended to be used in the past, are generally insufficient to capture the inherent complexity in hurricane patterns. For example, the regression trees developed based on the pairs of variables used by Sabbatelli and Mann (2007) and Saunders and Lea (2008) perform poorly in comparison to regression trees developed based on all of the climate variables considered in this paper. While future research is needed to increase the predictive accuracy of these statistical models, they offer a promising direction for future developments. These results also suggest that regardless of the statistical methods used, a suite of climate variables should be investigated in future modelling efforts rather than determining a small subset of variables to use a priori.

Acknowledgement This work was funded by the Office of Science (Biological and Environmental Research) of the U.S. Department of Energy under grant number DE-FG02-08ER64644. This support is gratefully acknowledged, but the results of this work are those of the authors and do not reflect the position of the U.S. Department of Energy.

Appendix

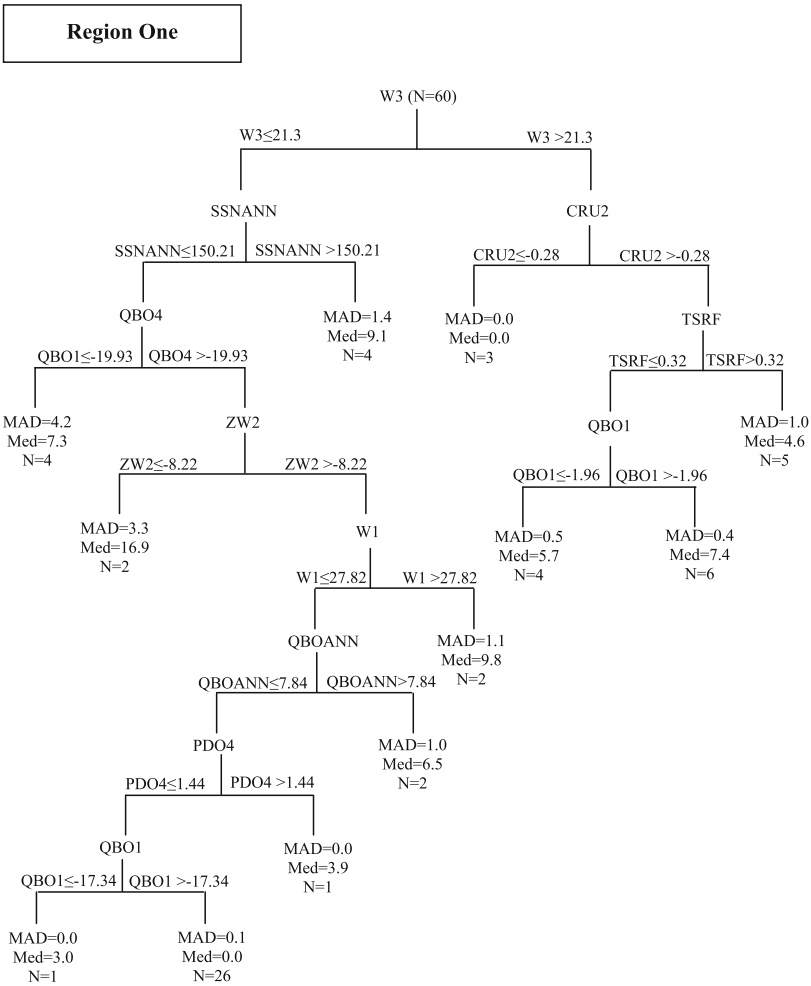

Fig. 5 Regression tree developed for region one

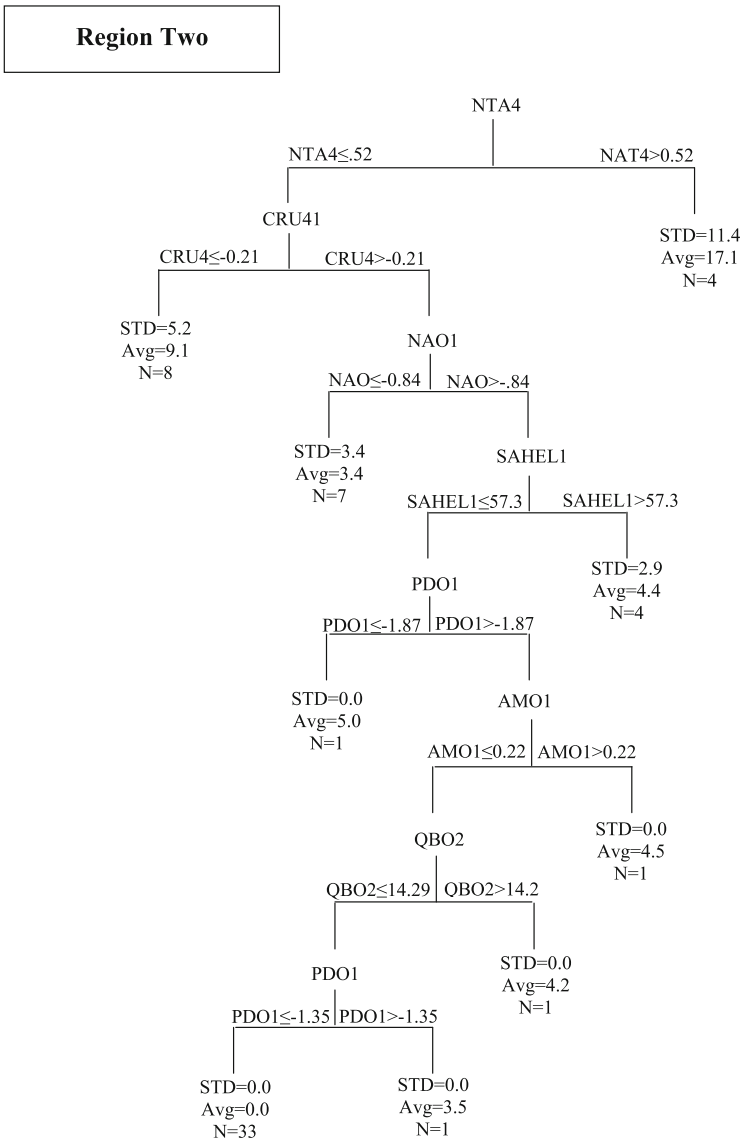

Fig. 6 Regression tree developed for region two

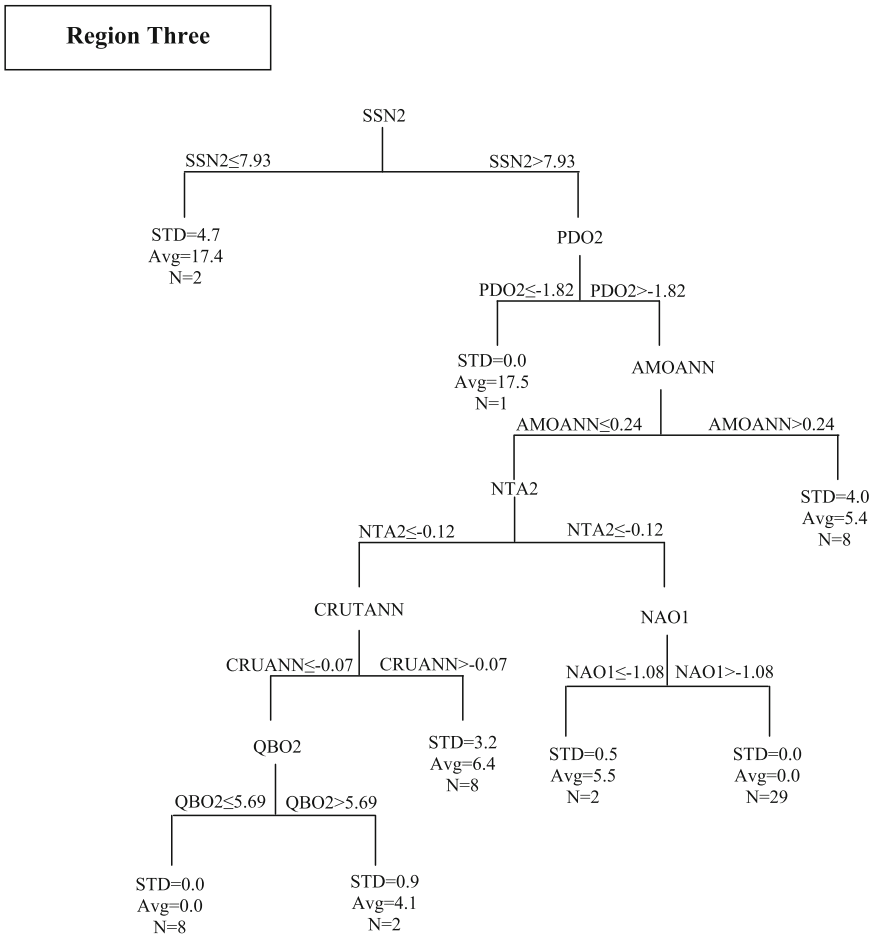

Fig. 7 Regression tree developed for region three

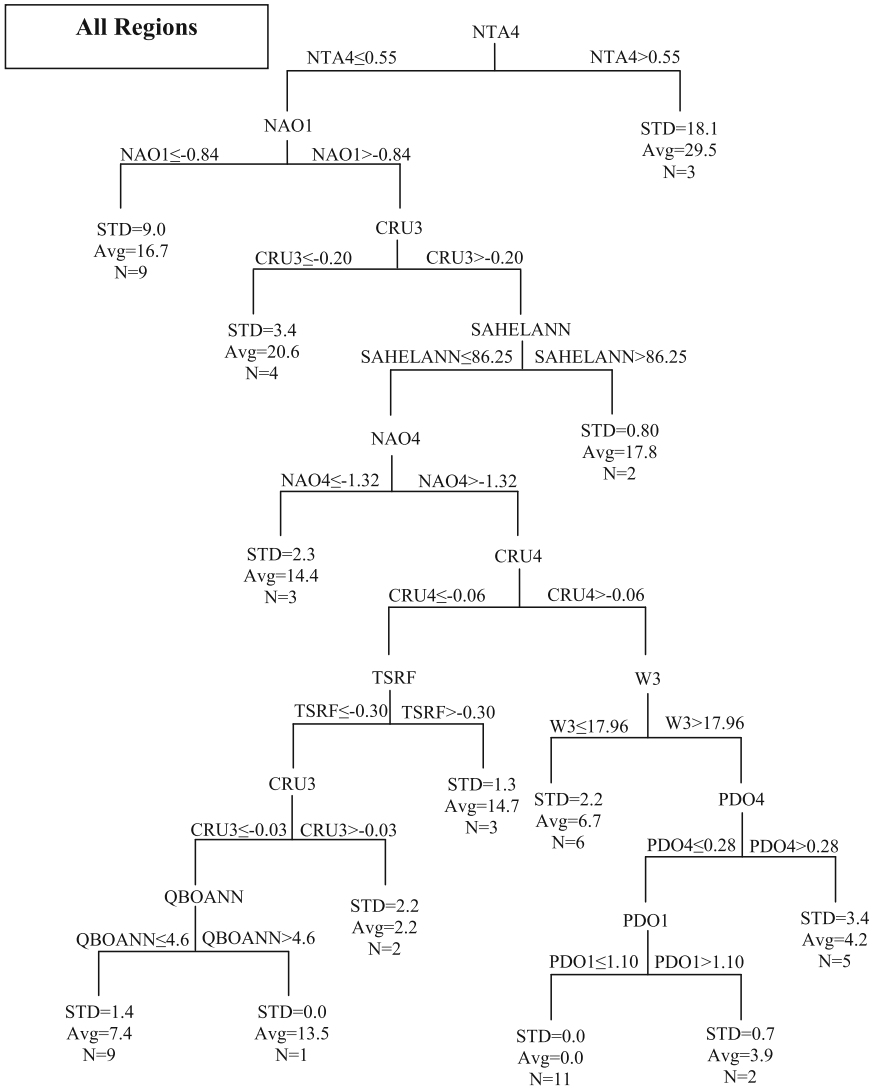

Fig. 8 Regression tree developed for the aggregate of all regions

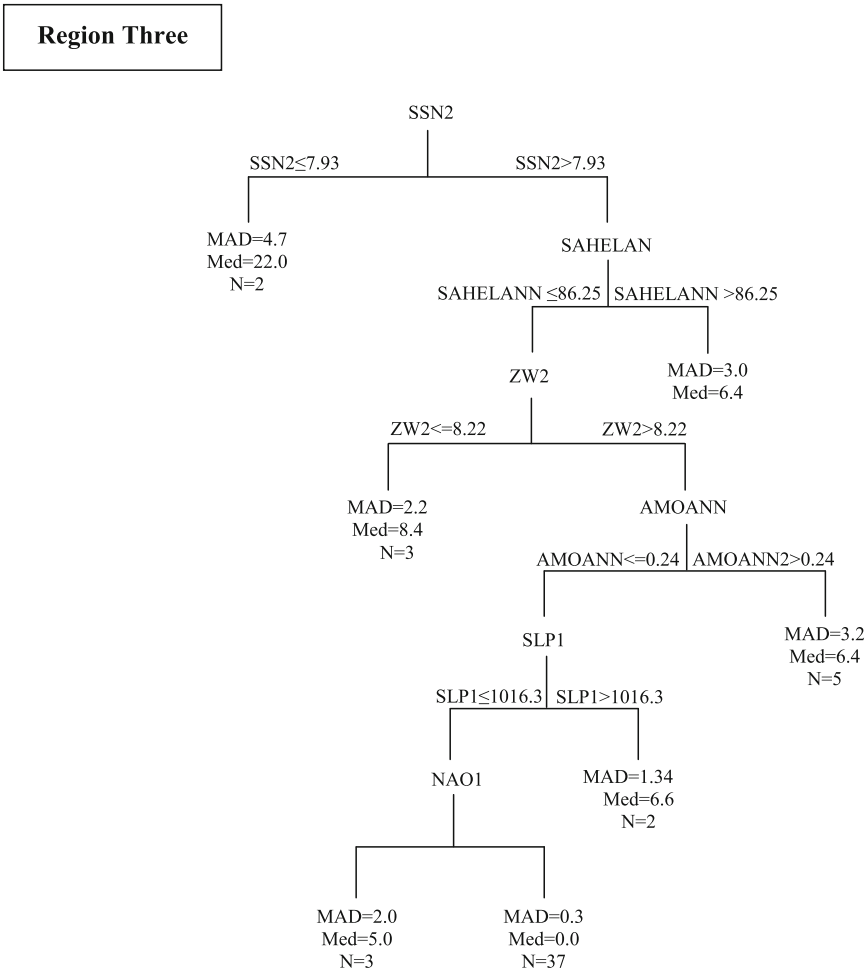

Fig. 9 Regression tree developed for region three with the outlier removed

References

Ballenzweig EM (1959) Relation of long-period circulation anomalies to tropical storm formation and motion. J Meteor 16:121–139

Breiman L, Friedman JH, Olshen RA, Stone CJ (1998) Classification and regression trees. CRC, New York, 358 pp

Elsner JB (2006) Evidence in support of the climate change-Atlantic hurricane hypothesis. Geophys Res Lett 33:L16705

Elsner JB, Bossak BH, Niu X (2001) Secular changes to the ENSO-U.S. hurricane relationship. Geophys Res Lett 28:4123–4126

Elsner JB, Kossin JP, Jagger TH (2008) The increasing intensity of the strongest tropical cyclones, Nature, 455:92–95

Elsner JB, Jagger TH, Dickinson M, Rowe D (2008) Improving multiseason forecasts of North Atlantic hurricane activity. J Climate 21:1209–1219

Emanuel KA (2005) Increasing destructiveness of tropical cyclones over the past 30 years. Nature 436:686–688

Emanuel KA, Sundararajan R, Williams J (2008) Hurricanes and global warming: Results from downscaling IPCC AR4 simulations. Bull Amer Meteor Soc 89:347–367

Enfield DB, Mestas-Nuez AM, Trimble PJ (2001) The Atlantic multidecadal oscillation and its relation to rainfall and river flows in the continental U.S. Geophy Res Lett 28:2077–2080

Gray WM (1984) Atlantic seasonal hurricane frequency. Part I: El Niño and 30 mb stratospheric Quasi-Biennial Oscillation influences. Mon Wea Rev 112:1649–1668

Gray WM, Landsea CW, Mielke Jr PW, Berry KJ (1992) Predicting Atlantic seasonal hurricane activity 6-11 months in advance. Wea Forecasting 7:440–455

Holland G J (1980) An analytical model of the wind and pressure profiles in hurricanes. Mon Wea Rev 108:1212–1218

Jagger TH, Elsner JB (2006) Climatology models for extreme hurricane winds near the United States. J Climate 19:3220–3236

Knutson TR, Tuleya RE (2004) Impact of CO_2-induced warming on simulated hurricane intensity and precipitation: Sensitivity to the choice of climate model and convective parameterization. J Climate 17:3477–3495

Knutson TR, Sirutis JJ, Garner ST, Vecchi GA, Held IM (2008) Simulated reduction in Atlantic hurricane frequency under twenty-first-century warming conditions. Nat Geosci 1:359–364

Landsea CW, Gray WM (1992) The strong association between western Sahelian monsoon rainfall and intense Atlantic hurricanes. J Climate 5:435–453

Landsea CW, Pielke Jr RA, Mestas-Nuez AM, Knaff JA (1999) Atlantic basin hurricanes: indices of climatic changes. Climatic Change 42:89–129

Lehmiller GS, Kimberlain TB, Elsner JB (1997) Seasonal prediction models for North Atlantic basin hurricane location. Mon Wea Rev 125:1780–1790

Mann ME, Emanuel KA (2006) Atlantic hurricane trends linked to climate change. EOS 87:233–239

Mantua NJ, Hare SR (2002) The Pacific decadal oscillation. J Oceanogr 58:35–44

Marshall J, et al (2001) North Atlantic climate variability: phenomena, impacts and mechanisms. Int J Climatol 21:1863–1898

Michaels PJ , Knappenberger PC, Landsea CW (2005) Comments on impacts of CO_2-induced warming on simulated hurricane intensity and precipitation: sensitivity to the choice of climate model and convective scheme. J Climate 18:5179–5182

Pielke Jr RA, Landsea CW, Mayfield M, Laver J, Pasch R (2005) Hurricanes and global warming. Bull Amer Meteor Soc 86:1571–1575

Sabbatelli TA, Mann ME (2007) The influence of climate variables on Atlantic Tropical Cyclone occurrence rates. J Geophys Res 112:D17114

Saunders MA, Lea AS (2008) Large contribution of sea surface warming to recent increase in Atlantic hurricane activity. Nature 451:557–559

Shapiro LJ (1989) The relationship of the quasi-biennial oscillation to Atlantic tropical storm activity. Mon Wea Rev 117:2598–2614

Trenberth KE (1997) The definition of El Niño. Bull Amer Meteor Soc 78:2771–2777

Webster PJ, Holland GJ, Curry JA, Chang HR (2005) Changes in tropical cyclone number, duration and intensity in a warming environment. Science 309:1844–1846

Yonetani T, Gordon HB (2001) Simulated changes in the frequency of extremes and regional features of seasonal/annual temperature and precipitation when atmospheric CO_2 is doubled. J Climate 14:1765–1779

Index

A
Accumulated cyclone energy (ACE), 82–86, 138, 141–143, 145–147
ARPEGE, 40, 42–51, 53–55, 57–77

B
Bayesian modeling, 111, 112

C
Caribbean, 58, 62–67, 69, 72, 73, 75, 76, 122, 123, 132, 150–158, 160–163, 165, 167, 168, 170, 171, 176, 177, 182–186, 191–194, 198, 199, 202, 225, 228, 235, 236, 244
Characteristic scale, 89, 90, 92
Climate model, 1–22, 26–28, 33–35, 59, 70–76, 176, 186
Convective yearly genesis parameter (CYGP), 41–55
Critical phenomenon, 81–97
Criticality, 89–94, 97
Cyclogenesis, 20, 27, 39–55, 60, 123
CYGP. *See* Convective yearly genesis parameter

D
Damage losses, 101–118
Data mining, 231–250
Decay rate, 199–202, 222
Dissipated energy, 81, 85

E
EAFB. *See* Eglin Air Force Base
Earthquakes, 88–90, 92–94
East Coast, 233
Eastern North Pacific (ENP), 121–135
Eglin Air Force Base (EAFB), 217–228
El Nino, 27, 36, 151
El Niño Southern oscillation (ENSO), 41, 59, 106, 129, 150–153, 156–158, 160, 161, 165, 167–171, 177, 179–180, 186, 232, 234, 235, 239
Energy distribution, 92
ENP. *See* Eastern North Pacific
ENSO. *See* El Niño Southern oscillation
Expectation-maximization algorithm, 140, 141
Expected loss, 110–113, 117

F
Florida, 69, 72, 73, 103, 176, 191–202, 218, 219, 223, 224, 228, 233, 243, 244
Frequency, 4, 28, 33–36, 59, 60, 95, 101, 102, 106, 109–111, 113–115, 117, 121–135, 138, 143, 145, 151, 152, 156–158, 160, 167, 170, 176, 178, 179, 181–183, 189, 191–202, 205–213, 217, 222, 232, 233, 239

G
Gaussian, 138, 139, 141, 143
General circulation model (GCM), 6, 17, 34, 40, 59, 71, 153, 156, 164
Generalized Pareto distributions (GPD), 111, 113–115, 196, 197
Genesis potential index (GPI), 6, 7, 20, 41–43, 45, 47–55
Global cloud-system-resolving model, 25–36
Global frequency, 34, 232
Global Precipitation Climatology Project (GPCP), 60–70, 76
GPD. *See* Generalized Pareto distributions
GPI. *See* Genesis potential index

Gulf of Mexico, 58, 62–64, 67, 69, 72, 73, 75, 76, 123, 150, 176, 182–186, 191–194, 202, 223, 224, 233, 243, 244

H

Hexagon binning, 181–184, 186
HURDAT. *See* North Atlantic-basin hurricane database

I

Insurance, 102, 103, 114, 117, 192, 201
Intensity, 2–4, 6, 7, 20, 34, 41, 58, 59, 62, 72, 101, 102, 104, 106, 108, 117, 121–123, 126, 127, 129, 138, 141, 143–146, 150–155, 161, 175–189, 191–202, 206–208, 210, 217–219, 221–226, 228, 232–234, 238, 243
Intertropical convergence zone (ITCZ), 28, 152, 154, 168, 171, 206–213
Intra-Americas (Caribbean) low-level jet, 168

L

Lifespan, 138, 145
Loss prediction, 102, 111, 115

M

Maximum potential intensity (MPI), 5–7, 44, 45, 122, 123, 129, 182, 188, 189
Mg II, 127, 128
Mid-summer drought (MSD), 152–155, 157, 161, 167, 168
Model, 25–36, 40–51, 53–55, 59, 61, 70–77, 88, 92, 95, 101, 102, 106–118, 123, 124, 130–135, 138–141, 143, 150, 153, 156, 161, 162, 164, 170, 171, 176–179, 186–189, 192, 196–198, 201, 202, 206, 232–237, 239–245
Model intercomparison, 1–22, 156
MPI. *See* Maximum potential intensity
MSD. *See* Mid-summer drought

N

NATL. *See* Tropical North Atlantic
North Atlantic, 17, 34–36, 51, 57–77, 84, 96, 97, 101, 106, 123, 124, 129, 132, 134, 138, 150, 151, 153, 154, 171, 178–184, 186, 188, 228, 235, 236
North Atlantic oscillation (NAO), 106–108, 110, 112, 113, 116, 117, 124, 129–132, 135, 152, 179, 232, 234, 235, 244, 245
North Atlantic-basin hurricane database (HURDAT), 123, 124, 176, 177, 184, 192, 219

O

Observations, 4, 6, 7, 17, 20, 27–29, 31, 33, 34, 36, 42, 57–77, 91, 113, 123, 124, 139, 141, 146, 171, 182–186, 192, 200, 206, 219, 222, 228, 239, 240
Outgoing long wave radiation (OLR), 28, 30, 155
Ozone, 122, 123, 127

P

Pacific decadal oscillation (PDO), 153, 235, 236, 243–245
PDI. *See* Power dissipation index
Poisson, 102, 110, 113–115, 124, 125, 196, 197, 232, 234
Poisson model, 124, 131, 132, 134
Power dissipation index (PDI), 82–87, 95–97, 145
Power-law distribution, 83–93

Q

Quantile regression, 176, 178, 179, 187, 192, 198, 200–202
Quasi-biennial oscillation (QBO), 235, 236, 243

R

Rainfall, 31, 57–77, 89, 93, 94, 97, 138, 154, 157, 168, 235, 236, 244, 245
Reanalysis, 9, 19, 27, 29, 57–77, 157, 206, 208
Regional climate model, 3, 19–20
Regression trees, 232–234, 236–250
Return levels, 115–117, 192, 196–198, 228
Return periods, 113, 115, 117, 192, 196–198

S

Sea-surface temperatures (SST), 3, 27, 36, 39–55, 71, 106–108, 110, 112, 113, 116, 117, 122–127, 129–135, 151, 152, 154–156, 161–163, 165, 167, 170, 176, 177, 179–180, 186, 188, 189, 192, 193, 198, 199, 205–213, 219, 224–228, 232, 234–236, 239
Solar cycle, 102, 122, 123, 128

SST anomalies, 39–55, 71, 106, 107, 125, 151, 152, 154, 155, 161, 170, 177, 193, 198, 199, 225, 234, 235
Sunspots, 106, 108, 112, 113, 117, 122, 124, 125, 127–129, 135, 179, 235, 243, 244

T
TC. *See* Tropical cyclone
TCPE. *See* Tropical cyclone precipitation efficiency
Thermodynamics, 122, 123, 127, 131, 188, 210, 211, 213, 224
Tracks, 2, 3, 8, 9, 14, 27, 28, 32–36, 40, 60–61, 70–73, 77, 82, 84, 123, 124, 132, 137–147, 151, 177, 192, 199, 217–228
Translation speed, 219, 221, 223–225, 227, 228
TRMM. *See* Tropical Rainfall Measurement Mission
Tropical cyclone (TC)
  frequency, 36, 138, 143, 151, 160, 205–213
  genesis, 14, 28, 35, 54, 206, 207, 213
  track, 26, 28, 33, 138, 139, 143
Tropical cyclone precipitation efficiency (TCPE), 69–70, 73–77
Tropical North Atlantic (NATL), 57–77, 84–87, 95, 153, 155, 156, 159, 165, 167, 170, 171
Tropical Rainfall Measurement Mission (TRMM), 59, 60, 62–70, 73, 75, 76
Typhoon, 84, 86, 87, 137–147, 206, 207

U
Ultraviolet (UV) radiation, 122, 123, 127–129, 134
US hurricanes, 122, 131

W
Warming SSTs, 207, 208
West North Pacific (WNP), 48–50, 53, 54, 59, 138, 139, 142, 144, 145, 151, 205–213
Wind speed, 2–4, 7, 26–28, 33–35, 42, 106, 118, 121, 123, 124, 142, 145, 151, 157–159, 162–164, 170, 177–179, 182, 187, 192–202, 219, 221–223, 225, 228, 234